CHARACTERIZATION OF SOFT CLAYS AND THE RESPONSE OF SOIL-FOUNDATION SYSTEM FOR OFFSHORE APPLICATIONS

A Dissertation

by

MADHURI MURALI

Submitted to the Office of Graduate and Professional Studies of
Texas A&M University
in partial fulfillment of the requirements for the degree of

DOCTOR OF PHILOSOPHY

Chair of Committee	Giovanna Biscontin
Co-Chair of Committee,	Charles Aubeny
Committee Members,	Stefan Hurlebaus
	Frederick Chester
Head of Department,	Robin Autenrieth

August 2015

Major Subject: Civil Engineering

ABSTRACT

The overwhelming bulk of our population, about 4 billion people, are concentrated along or near a coastline (within 250 miles). It is recognized that a mix of energy sources will be required to meet mainstream energy needs of this growing coastal population and bring about the benefits of a diversified energy portfolio. The oceans are teeming with energy, whether it be the more established offshore oil and gas fields or the newer renewable sources such as tidal, wave and offshore wind. This dissertation focussed on contributing to the field of offshore geotechnics in two ways: first, to aid in offshore site characterization by developing a framework for correlating soil strength with geophysical measurements for shallow sediments; and second, to study the ultimate capacity of caisson foundations subjected to loads typically encountered in offshore wind tower installations in water depths up to 30 m.

The research project describes a laboratory testing program of CK_oU triaxial tests along with bender element measurements carried out at Texas A&M University for correlation of soil strength with stiffness. A new framework for correlating stiffness and strength is proposed, based on void ratio and over consolidation ratio (OCR). Although site specific correlations between soil strength and various geophysical measurements is required, the formulation provides a convenient way of estimating both absolute value and trends of behavior at different void ratios and OCRs. This experimental program also allows for the investigation of the small strain response of soils at shallow depths which was previously unstudied.

The project also describes a centrifuge testing program carried out at Rensselaer Polytechnic Institute. Model caisson foundations with aspect ratios of two were subjected to combined vertical, horizontal and moment loads usually experienced by offshore wind tur-

bine foundations. This dissertation focuses on the ultimate capacity of the pile response to lateral load, to ensure the foundation has sufficient strength in an extreme loading event.

ACKNOWLEDGEMENTS

I would like to thank my advisor Dr. Giovanna Biscontin for her unwavering support and help in completing this work, and my co-advisor Dr. Charles Aubeny for his guidance and direction when I needed it. I would also like to express gratitude to my committee members, Dr. Stefan Hurlebaus and Dr. Fred Chester for their valuable comments and timely assistance.

A big thank you to Mike Linger, Sammy Pirano and Charles Pivonka for all the help in design, fabrication and troubleshooting. This research would not have been possible without their help. I would also like to thank all the personnel at the NEES facility at Rensselaer Polytechnic Institute, specifically John Lawler, Panagiota Kokkali, Michael Bretti and Jason Thomas for their time and assistance. I also acknowledge the support provided by the Aerospace department at Texas A&M University, specifically Rodney Inmon for his help with 3D printing.

I want to express my sincere gratitude to all the Geotechnical Engineering graduate students for the amazing time spent at Texas A&M. In particular, I would like to thank my office mates: Ryan Beemer, Francisco Grajales and Ajay Shastri for their constant company, conversations and craziness during grad school. I also want to thank my friends in College Station and Houston for helping me relax when I needed to, and my roommate, Nandita Kohli for being there the whole time and listening to all my complaints.

To my family, Muralidharan K., Vanitha Murali, Mayuri Murali and Varenya Kumar, I want to express my love and appreciation for supporting me throughout my journey and helping me grow. I could not have done it without you all.

This research was supported by the Naval Facilities Engineering Service Center (NAVFAC ESC) project Material Uncertainties in Assessing Soil Strength from Geophysical

Surveys, BAA number: N6258312R0708 and the National Science Foundation, Network for Earthquake Engineering Simulation Research (NEESR-CR) project Capacity and Performance of Foundations for Offshore Wind Towers, Award Number: 1041604.

TABLE OF CONTENTS

Page

LIST OF FIGURES

FIGURE Page

LIST OF TABLES

TABLE Page

1. INTRODUCTION

Recent studies have shown that the overwhelming bulk of our population, about 4 billion people, are concentrated along or near a coastline (within 250 miles). It is recognized that a mix of energy sources will be required to meet mainstream energy needs of this growing coastal population and bring about the benefits of a diversified energy portfolio. The oceans are teeming with energy, whether it be the more established offshore oil and gas fields or the newer renewable sources such as tidal, wave and offshore wind.

Offshore wind has the potential to provide substantial amounts of energy, and is, after onshore wind, the nearest to market renewable energy source. Although the benefits of harnessing wind at sea are already firmly established at all levels (Bruijne et al., 2005), as with any new technology, there are challenges to be overcome. The cost of foundations has been estimated to be about 35% of the total installation cost (Byrne and Houlsby, 2003) for an offshore wind farm project and decreasing the cost can be an important part of making wind a viable source of energy.

The current activities in offshore wind energy are built on the experiences of two fields of engineering: those of wind energy and of offshore oil and gas, with smaller but significant input from the field of coastal engineering. However, an offshore wind farm differs from oil&gas development in some key aspects:

- An offshore oil & gas field generally has a small number of structures, some of very large size. This is unlike an offshore wind farm, which consists of several separately founded wind energy turbines distributed over the wind farm area (Toolan, 2001). Thus, the site investigation for an offshore wind farm would differ significantly simply because of the vast area required to install multiple foundations as compared to a single platform. A means of correlation of soil properties with geophysical mea-

surements would greatly aid in estimating and extrapolating across large areas of the seabed.

- In the case of a foundation structure supporting a wind turbine, there will be significant horizontal loads and moments, but relatively low vertical loads applied to the foundation. The relative magnitudes of these loads are very different from those experienced by oil and gas structures, and therefore there is little guidance to be gained from the established database.

Different structural configurations have been developed for offshore wind turbine applications. Monopile or gravity based structures are existing solutions for water depths shallower than 30 m and jacket structures (with multiple footing options) are used for slightly deeper water depths (Byrne and Houlsby, 2005; Moe et al., 2007). Floating options are being investigated for deep water foundations, as it is economically not feasible to have structures resting directly on the seabed beyond a certain water depth (Frye, 2011). Most of the already existing offshore wind energy converters are founded on monopiles (Achmus et al., 2009).

Villalobos et al. (2009) and Byrne and Houlsby (2003) presented research on suction caissons as an alternative foundation for offshore wind turbines. Also known as bucket foundations or skirted foundations because of their lower aspect ratio (L/D $<$ 6), suction caissons are highly advantageous as they can be installed in great water depths exceeding the feasibility limits of driving piles, provide larger holding capacities than drag anchors, can be installed reliably at pre-selected locations with good precision and minimum seafloor disturbance, and in various soil conditions, and can be retrieved for reuse by pressurizing the interior (Tjelta, 2001). In addition, suction caissons can be less expensive to fabricate and require less expensive installation equipment and shorter installation periods (Andersen and Jostad, 1999).

There has however, been relatively little research on the use of caissons as foundations rather than as anchors. The main difference is the nature of the applied loading. Suction caisson anchors are designed to carry a combination of compression and tensile loading whereas for caisson foundations the loading consists of vertical and horizontal compression loads as well as moments. A principal aspect of pile response to lateral load that requires assessment is the ultimate lateral pile capacity, to ensure the foundation has sufficient strength in an extreme loading event (Zhang et al., 2011).

Site investigation for offshore structures is necessary to acquire data that will facilitate successful foundation design, site or route selection, choice of foundation type, dimensioning, installation and operational integrity of the proposed structure. A large part of the commercial and operational risk involved relates to uncertainties about the properties of the soil at the site. It is therefore necessary to perform sufficient investigations to evaluate these risks thoroughly. A geophysical survey is required for two reasons, first to aid a rapid and economical choice between a number of alternative sites for a proposed project, prior to a detailed investigation and, secondly, as part of the detailed site assessment at the chosen location. They are vastly useful as a means of interpolating between, and extrapolating from, borehole data.

Along with geophysical surveys, it also necessary to define site specific geotechnical data such as strength parameters, consolidation characteristics, permeability. These can be assessed from in-situ tests (traditionally Cone Penetrometers) or offshore and onshore laboratory tests on cored samples. In the case of laboratory tests profiles of triaxial compression/extension and undrained shear strength values are determined on representative samples, for offshore foundation design in soft clays (Lunne et al., 1976; Andersen et al., 2005).

Different foundation solutions require investigations to different depths. The soil data needed for bucket foundations or monopile design is generally not more extensive than for

deep piles. As caisson foundations are relatively shallow, deep borings are not needed, but more detailed information at shallow depths is required for caissons and low aspect ratio monopiles (Andersen and Jostad, 1999).

Before site specific correlations between soil strength and various geophysical measurements can be achieved, a controlled laboratory study is required to highlight variability in these correlations for a range of geotechnical materials. Shallow sediments or sediments within 7 m of the seafloor are targeted for this research. Apart from aiding in site characterization for wind farms, an important application for this work also lies in the area of sub-sea pipelines. They traverse across vast areas of the seafloor and require detailed strength and deformation properties of shallow sediments.

1.1 Research objectives

The area of offshore geotechnics uses an integrated approach in which geophysical data are combined with other information, such as regional geology, past experience of soil and foundations, in order to obtain the best performance of the proposed foundation.

The aim of this dissertation is to contribute to this field in two ways: first, to aid in offshore site characterization by developing a framework for correlating soil strength with geophysical measurements for shallow sediments; and second, to study the ultimate capacity of caisson foundations subjected to loads typically encountered in offshore wind tower installations in water depths up to 30 m.

Correlating the sediment strength to geophysical measurements, consists of two major components: (1) Laboratory experimental testing; and (2) Correlations between geophysical and geotechnical data obtained.

1. Laboratory experimental testing: Perform high quality triaxial tests accompanied by shear and body wave velocity measurements to generate a matrix of tests relating geophysical data to soil strength over a range of soil types, stress levels, stress

history, and density for soils found in the top 7 m of the seafloor.

2. Correlations: As a starting point, the database of measurements generated in this research is fitted to previously published correlations; these correlations are refined to fit the new database. A framework for correlating sediment strength with small strain shear modulus or stiffness is developed for shallow offshore sediments.

    - Clays: Shear wave velocity is correlated to shear modulus which in turn is correlated to undrained shear strength of 4 different types of clays.
    - Sand: Shear wave velocity is correlated to void ratio which correlates to friction angle for both round and angular sand.

This experimental program allows for the investigation of the small strain response of soils at shallow depths which was previously unstudied. This will also provide insight into the difference in the stiffness behavior of natural and remolded marine clays and the difference in the stiffness behaviour of round and angular sands.

Performance of the caisson foundation system is assessed for a combination of loads particularly moment, and horizontal forces by carrying out centrifuge tests (at 70 gs) at Rensselaer Polytechnic Institute (RPI). The centrifuge experimental testing consists of the following components:

1. Design and construction of testing tool to be used in sync with the in-flight robot at RPI to apply required loads in collaboration with Beemer et al. (2015).

2. Centrifuge testing of model caissons in soft clay (kaolin) at 70 g over a range of eccentricities, loading sequences and displacement amplitudes.

Two issues are relevant in characterizing the behavior of any offshore foundation: performance during extreme events, and fatigue performance under the application of many

cycles of low amplitude loads. This dissertation focuses on the ultimate capacity of the caisson foundation.

1.2 Dissertation outline

The research plan outlined above is presented in 8 sections. Section 2 describes the background and previous work on relevant topics with the goal of unifying concepts in the work performed for this project. The small strain shear modulus and its relevance in relating soil strength and geophysical measurements is discussed. A review of the existing correlations is also presented. Background on existing concepts of offshore wind turbine foundations is provided and important soil response characteristics are examined. A brief discussion on centrifuge testing and its limitations is presented.

Sections 3, 4 and 5 present the work carried out on correlating sediment strength with geophysical measurements. The methodology including the experimental setup and materials used are described in Section 3. Section 4 presents the strength and geophysical results on all the samples tested, this includes results from triaxial tests and shear wave and compression wave velocity results from bender and piezo crystals. Section 5 provides a discussion and interpretation on various correlations obtained from the data in this testing program.

Sections 6 and 7 present the work on characterizing the caisson foundation for offshore wind turbines. Section 6 describes the development of the equipment required for centrifuge testing and the procedures for carrying out centrifuge tests. Properties of the centrifuge test bed is also presented in this section. Section 7 presents the results and interpretation of tests carried out to study the performance of the model caisson foundations.

A summary is presented in Section 8 along with a direction for future work. The appendices provide methods for data reduction, necessary calculations, calibration and drawings.

2. LITERATURE REVIEW

2.1 Site characterization

Knowledge of seabed soils is essential if offshore and nearshore structures are to be safely designed and properly built. A large part of the commercial and operational risk involved relates to uncertainties about the properties of the soil at the site. It is therefore necessary to perform sufficient investigations to evaluate these risks thoroughly. Many geophysical techniques are available to the engineer to perform such investigations which are a lot faster and cheaper to conduct, compared to soil borings. Thus for wind farms with large areas, it would be more economical to make the most of geophysical surveys.

Several sensors currently provide geophysical information without requiring direct contact with the seafloor. Sub-bottom Profiling, swath bathymetry, electro-resistivity, seismic refraction, and electromagnetic sensors are all examples of these techniques, several of which are frequently utilized with Autonomous Underwater Vehicles (AUV) and Remotely Operated Vehicles (ROV) (NAVFAC, 2011). Typically, a combination of techniques such as echosounding, side scan sonar, reflection seismic systems and electrical resistivity systems are used. The data required includes site-specific information (Toolan, 2001) on:

- Seabed topography and morphology
- Nature of the soils and rocks, their stratification and variability
- Soil strength, deformation and consolidation characteristics
- The influence of specific factors such as cyclic loading, rate of loading, soil sensitivity and thixotropy

- The possibility of scouring

There are two basic types of offshore site surveys (Campbell and Hough, 1986): reconnaissaince survey and site specific survey, of which the latter is of great importance for offshore wind farms. Geophysical data provides information on any structural complexities or geohazards within the shallow geology that affect design criteria for the wind-turbine installations (Jenner et al., 2002). An assessment of natural and man-made seabed features within the area is also critical to the design layout of the turbines and choice of cable routes. With up to 40% of the as-installed cost of a project being directly attributed to the foundation (Byrne and Houlsby, 2003), comprehensive geophysical and geotechnical investigations are essential to understand the behaviour of the soil at a given site. Westgate and DeJong (2005) provides guidance to the offshore wind industry with respect to the site investigation program and provides an insight into the current research developments in offshore wind turbine foundations.

Along with geophysical surveys, it also necessary to define site specific geotechnical data such as strength parameters, consolidation characteristics, permeability, etc, all of which are usually carried out by either in situ tests (traditionally Cone Penetrometers) or offshore and onshore laboratory tests on cored samples. Profiles of triaxial compression/extension and undrained shear strength values are determined on representative samples, for offshore foundation design in soft clays (Lunne et al., 1976; Andersen et al., 2005).

2.1.1 Strength testing

The shear strength of soil is measured in terms of a limiting resistance to deformation offered by a soil mass or a test specimen when subjected to loading or unloading (Head, 1998). This limiting shearing resistance corresponds to the condition generally referred to as 'failure' which can be defined in several different ways. Skempton (1960) defined shear

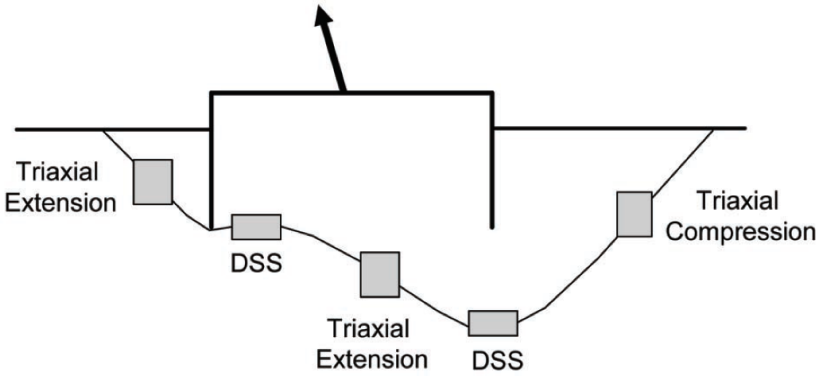

Figure 2.1: Principle of need for profiles of $Su_{CKoUC}, Su_{DSS}, Su_{CKoUE}$ (Lunne and Andersen, 2007).

strength as the maximum shear stress the soil could withstand, whereas Hvorslev (1949) defined shear strength as the shear stress on the failure plane of the soil at the moment of failure.

Following the approach used by Norwegian Geotechnical Institute (NGI) for several decades, for any offshore foundation design in soft clays (Lunne et al., 1976; Andersen et al., 2005; Murff et al., 2005), it is necessary to define profiles of triaxial compression, direct simple shear (DSS) and triaxial extension strengths (Su_{CKoUC}, Su_{DSS}, Su_{CKoUE}) respectively, since shear strength depends on different modes of shearing (Refer Figure 2.1). Triaxial compression tests were carried out to determine the undrained shear strengths in this project.

The triaxial test was initially developed by A. Casagrande (Casagrande, 1936) in the 1930s to overcome the limitations of the direct shear test. It is now a standard test procedure that provides a high amount of control during the test (ASTM Standard D4767, 2011). Some of the major advantages of the triaxial test are that drainage can be controlled and the failure plane is not constrained by the design of the apparatus to occur on a specific plane (Bishop and Henkel, 1962).

The test can also be modified to restrict lateral strain of the soil sample simulating the in situ conditions, called K_o. True K_o consolidation requires application of many small increments of vertical and radial stress in order to follow a stress path that is dictated by the specimen deformation. Germaine and Ladd (1988) discuss a simplified method for manual K_o consolidation. The specimen is first isotropically consolidated to σ'_s (see Figure 2.2), and then follows a drained stress path of decreasing K_o (path B in Figure 2.2), as it approaches the normally consolidated condition (the true $\mathrm{K_o}$ stress path A is shown in Figure 2.2). For actual manual K_o consolidation, increments must be sufficiently small to minimize straining due to undrained shear and must remain long enough to allow full consolidation. At the end of each increment the change in length and volume are used to calculate the present area to determine if the selected K_o, is too high or too low. Based on this information a new K_o, value is estimated and the next increment is applied.

Berre and Bjerrum (1973) presented the technique shown as stress path C in Figure 2.2 in which the specimen is isotropically consolidated to the final radial effective stress, and then the vertical stress is increased such that K_o equals the estimated K_o value. This stage is equivalent to drained triaxial compression and must be performed relatively slowly. Once at the K_o value, the vertical stress must be maintained for one cycle of secondary compression prior to undrained shear. This process dramatically decreases the testing period and labor requirements compared to stress path A. This procedure can be used only if the K_o value is already known.

The results of both compression and extension tests on Drammen clay (Berre and Bjerrum, 1973) confirm that the simplified method, while not perfect, yields data comparable to true $\mathrm{K_o}$ consolidation. However isotropic consolidation well beyond the yield envelope may cause a significant change in the structure of the soil. Hence a better approach would be to select a path similar to B in Figure 2.2 which was followed for this research program. For additional information on strength testing see Murali (2011).

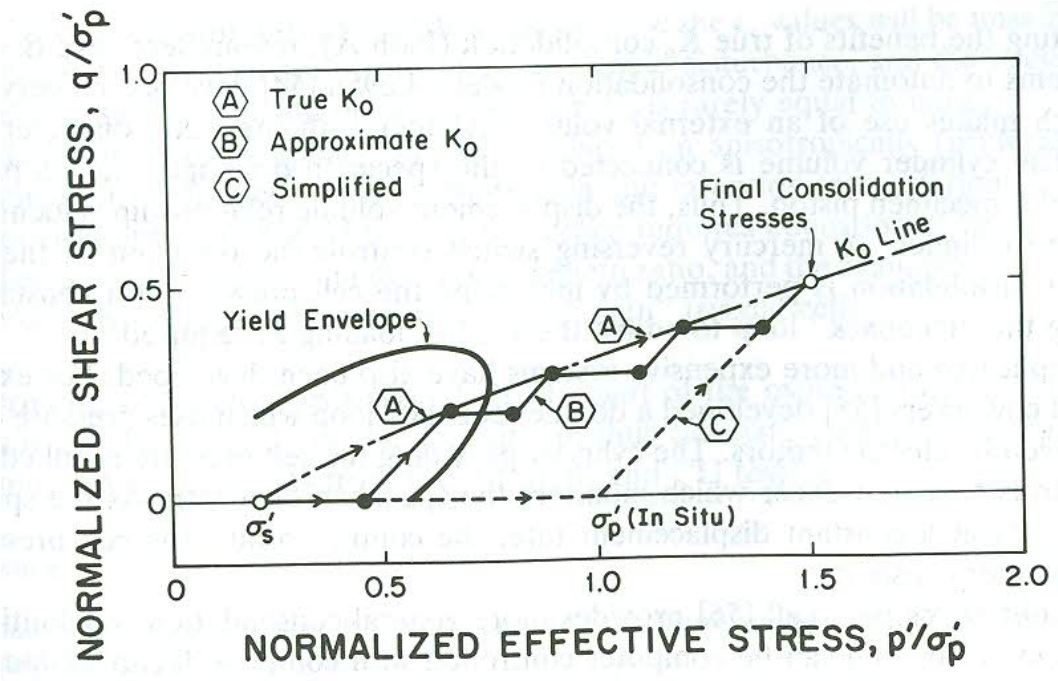

Figure 2.2: Techniques for anisotropic consolidation to OCR=1 (Germaine and Ladd, 1988).

2.1.2 Small strain shear modulus

The shear modulus plays an important role in prediction of soil behavioral response and soil structure development and degradation in several different loading conditions (Burland, 1989; Burland and Georgiannou, 1991; Youn et al., 2008). It is used for a variety of geotechnical design applications (Dyvik and Madshus, 1985). Soil strength can also be related to geophysical measurements using the small strain shear modulus (G_o) which is an indicator of the stiffness of soil when the soil response is linear elastic.

Bates (1989) early on realised in the importance of measuring shear modulus in the laboratory to supplement the range of tests possible offshore during site investigation. G_o is especially critical in analyses such as those for predicting soil behavior or soil-structure interaction during earthquakes, explosions, machine or traffic vibrations. It is representative

of many other soil properties such as density, fabric, and can be correlated with sample disturbance by comparing laboratory and field measurements (Guldur, 2010). Small strain cyclic loading induced by wind or waves also have to be analyzed using $\mathrm{G_o}$.

Small strain shear modulus is measured within the elastic limit of the response of the soil that is tested, and is typically computed from the soil density (ρ) and measured shear wave velocity (V_s) through the soil.

$$G_o = \rho V_s^2 \tag{2.1}$$

where, G_o is the maximum small strain shear modulus within the elastic range (kPa), ρ_s is the bulk density of the soil (kg/m^3) and V_s is the shear wave velocity (m/s).

There are several factors affecting small strain shear modulus: strain level, effective stress state, Over Consolidation Ratio (OCR), void ratio, soil macro- and micro-structure, cyclic behavior, damping, consolidation and ageing (Guldur, 2010; Jones, 2009; Landon et al., 2007). It is known that $\mathrm{G_o}$ is a function of soil matrix, and since waves transmitted thorough solid media travel faster, lower soil void ratios lead to higher shear modulus values. For all soils, shear modulus rises with confining stress.

There are several empirical equations which relate $\mathrm{G_o}$ with known soil parameters such as void ratio, OCR and stress state for deep sediments which are discussed in Section 2.1.4 (Hardin and Black, 1968; Hardin and Richart, 1963; Marcuson and Wahls, 1972; Houlsby and Wroth, 1991; Jamiolkowski et al., 1994; Shibuya et al., 1997). There is however, a lack of information in the literature about the small strain properties of shallow saturated sediments or soil in the top 7 m of the seafloor. The correlation of stiffness (G_o) with soil strength is not understood in these low confining pressures.

Jamiolkowski et al. (1991) stated the need to operate in laboratory on undisturbed samples which preserve, to the highest extent possible their original structure, using the

reconsolidation techniques that do not cause destructuring. The paper also highlights the importance of comparing the stiffness characteristics of a natural well structured soil with its remolded state.

Edil and Luh (1980) performed resonant column tests (Section 2.1.2.1) on clay samples to observe the effect of soil structure on G_o. They found that clay mineral type, pore fluid chemistry and effective stress history affect clay behavior at small strains. Based on their findings they also concluded that the soil microstructure plays an important role in dynamic soil measurements. Later, Diaz-Rodrigues and Lopez-Flores (1997) used resonant column tests to observe how G_o is affected by the changes in the microstructure of soil. They monitored the changes in G_o values with respect to time under several confinement pressures.

2.1.2.1 Determining $\mathrm{G_o}$

The value of $\mathrm{G_o}$ can be determined either in situ using a variety of methods, or in the laboratory using resonant column test or bender elements.

In situ methods include: seismic refraction; crosshole, downhole and uphole Spectral Analysis of Surface Waves (SASW); suspension compression and shear wave logging; and the Seismic Cone Penetration Test (SCPT). Figure 2.3 shows how these methods are performed on the site and the measurement that these procedures provide (Schneider et al., 1999).

The resonant column test is the traditional means for laboratory determination of G_o. In this test, one end of a confined cylindrical (triaxial) soil specimen is excited in a fundamental mode of vibration developed by torsional or longitudinal excitation. Resonant frequency and amplitude of vibration are measured when the fundamental mode of resonance frequency is established. Later, this frequency and amplitude are used to determine wave velocities and strain amplitudes. An advantage of this test is that it provides both the

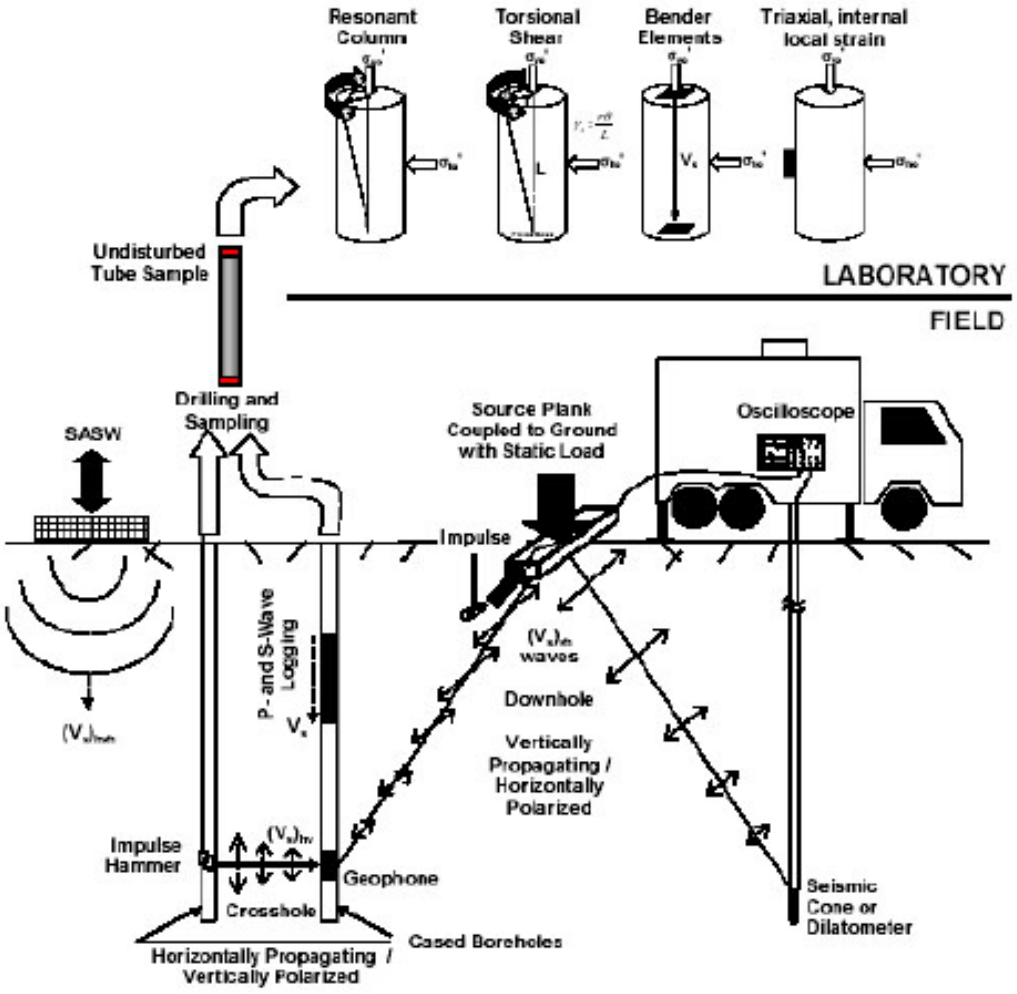

Figure 2.3: Field and Laboratory Methods for Determining Shear Wave Velocity and Shear Modulus (Schneider et al., 1999)

dynamic modulus and the damping ratio of the soil (Lo Presti et al., 1993).

The other laboratory method for determining G_o is through the use of piezoceramic plates, known as bender elements. Bender elements have been used to measure shear wave velocity in soils starting the 1970s (Shirley and Hampton, 1978; Dyvik and Madshus, 1985; Viggiani and Atkinson, 1995a; Brignoli et al., 1996; Santamarina et al., 2001; Pennington et al., 2001; Landon et al., 2007). Piezoelectric plates generate a voltage when mechanically stressed and they oscillate when excited by a voltage source. This technique is explained further in Section 2.1.3

The advantage of bender element testing is that it is simpler and more direct compared to resonant column testing; at the same time it provides a non-destructive measure of shear wave velocity of a soil. Bender elements can be mounted on many geotechnical testing devices, and the shear wave velocity may be monitored in conjunction with other soil parameters (Landon et al., 2007).

2.1.3 Bender elements

Bender elements consist of two thin piezoceramic plates rigidly bonded to a central metallic plate. Two thin conductive layers, electrodes, are glued externally to the bender. The polarization of the ceramic material in each plate and the electrical connections are such that when a driving voltage is applied to the element, one plate elongates and the other shortens. The net result is a bending displacement. On the other hand, when an element is forced to bend, an electrical signal can be measured through the wires leading to the element (Shirley and Hampton, 1978).

Based on this principle the bender elements are placed on the two ends of the triaxial sample, a shear wave or compression wave pulse is generated by bender elements at one end (bottom) and this wave propagates along the specimen length; a receiver element at the other end (top) of the sample picks up the wave and generates an output voltage (Dyvik

and Madshus, 1985). A variable voltage (either a square or sine wave) is sent to the transmitting bender element in order to generate mechanical oscillation. The transmitted wave travels through the soil and causes the receiving bender element to oscillate with the motion of the shear wave and this mechanical movement creates a voltage output.

There are two possible versions, differing only in the electrical connection of the two polarized plates: a series or a parallel connection (Figure A.1). The series version gives a higher output for a given distortion and is better used as a receiver. The parallel version has an additional electrode between the piezoceramic plates and is better used as transmitter because it gives the largest distortion for a given input (Dyvik and Madshus, 1985). These piezoelectric plates are very sensitive and can be easily damaged if exposed to excessive mechanical stress, temperature or voltage because any of these may result in depolarization of bender elements (Van Randeraat and Setterington, 1974; Waanders, 1991).

The travel time of the shear wave is calculated by calculating the time difference between the transmitted and the received wave. Since the specimen length is already known, this bender element measurement directly gives a measurement of shear wave velocity, V_s from which G_o can be determined using equation 2.1 (Dyvik and Madshus, 1985).

Clayton and Heymann (2001) measured the stiffness behaviour of three widely different materials: Bothkennar clay, London clay and chalk and found that stiffness measured in the triaxial apparatus at small strains was similar to those obtained using field geophysical techniques, despite assumptions of isotropy and the influence of sampling.

The transmitter and receiver element can be placed in various soil testing devices, such as oedometer, simple shear test device or, as in this project, in the bottom and top cap of a conventional triaxial device. Although a combination of a parallel element as sender and a serial element as receiver would improve the signal quality, in the frame of this research only series connected elements are used. This gives the opportunity to change the pulse direction in the sample without the element configuration influencing the receiving signal.

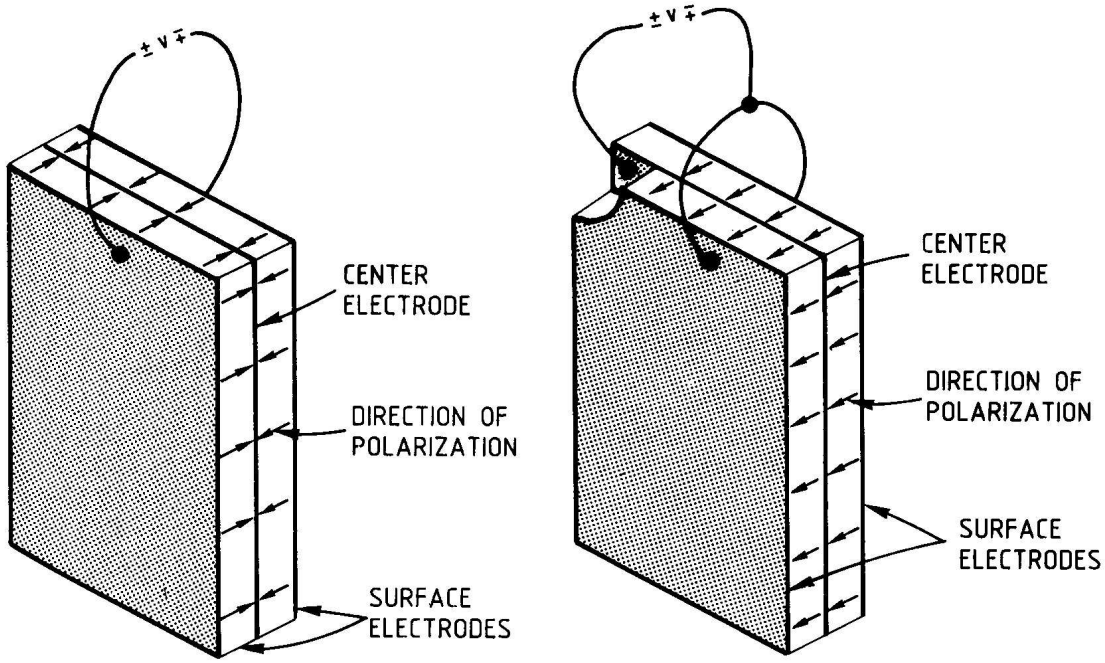

Figure 2.4: (a) Series and (b) parallel connected piezoceramic elements (Dyvik and Madshus, 1985)

It means the received signals should have the same shape independently of the sending direction.

The physical orientation of bender elements are important while receiving and transmitting a shear wave because transmitted and received waves need to be in phase (Pennington et al., 2001). In order to prevent additional electrical interference, bender elements have to be shielded and grounded with conductive paint and shielding cables to avoid electromagnetic coupling and cross-talking of electric signals (Santamarina et al., 2001).

Square, sine or modified sine waves can be used for excitation of bender elements. Dyvik and Madshus (1985) recommended use of square waves with an amplitude of 10 volts to 20 volts. Later, Reimer et al. (1998) and Lohani et al. (1999) proposed using sine waves instead of square wave. This is because square waves are composed of an infinite number of frequencies that makes the interpretation of shear wave more complicated. Pennington et al. (2001) suggested use of modified sine waves for simplifying received wave interpretation.

Some difficulties lie with using the bender elements which have been discussed in detail in Viggiani and Atkinson (1995a); Brignoli et al. (1996); Gordon and Clayton (1997). One important issue is in accurately evaluating the travel time of the shear wave from the source bender to the receiver, as the distance is accepted as the tip-to-tip distance between the benders, which can be accurately measured.

Many methods exist for the determination of the travel time of the shear and compression wave such as: travel time by direct arrival, travel time between characteristic points, travel time by cross-correlation, travel time using multiple arrivals, wavelet analysis, phase detection analysis (Brignoli et al., 1996; Viggiani and Atkinson, 1995a; Jovicic et al., 1996; Arulnathan et al., 1998; Bonal et al., 2012; Airey and Mohsin, 2013). Cross correlation was found to give the most accurate and consistent results and was adopted

for this research. Airey and Mohsin (2013) discusses in detail the procedure, pulse type and frequency, for evaluating the shear wave velocity from bender elements using cross-correlation method and addresses the calibration and issues of the method. The various methods to obtain the travel time of the shear and compression wave velocities are detailed in Appendix B.

Chan et al. (2010) investigated the effects of bender element installation on the measurement of shear wave velocity. The effects of penetration rate of the bender, size of sample and consolidation pressure during the test were examined and it was determined that the benders did not cause soil disturbance.

2.1.4 Existing correlations

The concept of normalized behavior has been used extensively in soil mechanics and it provides a useful framework for comparing and relating behavioral characteristics of cohesive soils. Normalization is also central to critical state soil mechanics and has led to the development of the stress history and normalized soil engineering properties (SHANSEP) design method (Ladd and Foott, 1974). It again proves to be a useful concept in correlating shear modulus with other soil parameters for both clays and sands as described in the following sections.

2.1.4.1 Clays

Hardin and Black (1968) started the research on the effects of confining stress and void ratio on shear modulus ($\mathrm{G_o}$) on a normally consolidated kaolin (edgar kaolin). Based on theoretical elastic stress strain relationships by Rowe (1971) and empirical equations by Janbu (1963), Hardin (1978) expressed the G_o values of clays subject to isotropic consolidation with the following equation:

$$G_o = Af(e)\sigma_c^n \sigma_r^{(1-n)} OCR^k \tag{2.2}$$

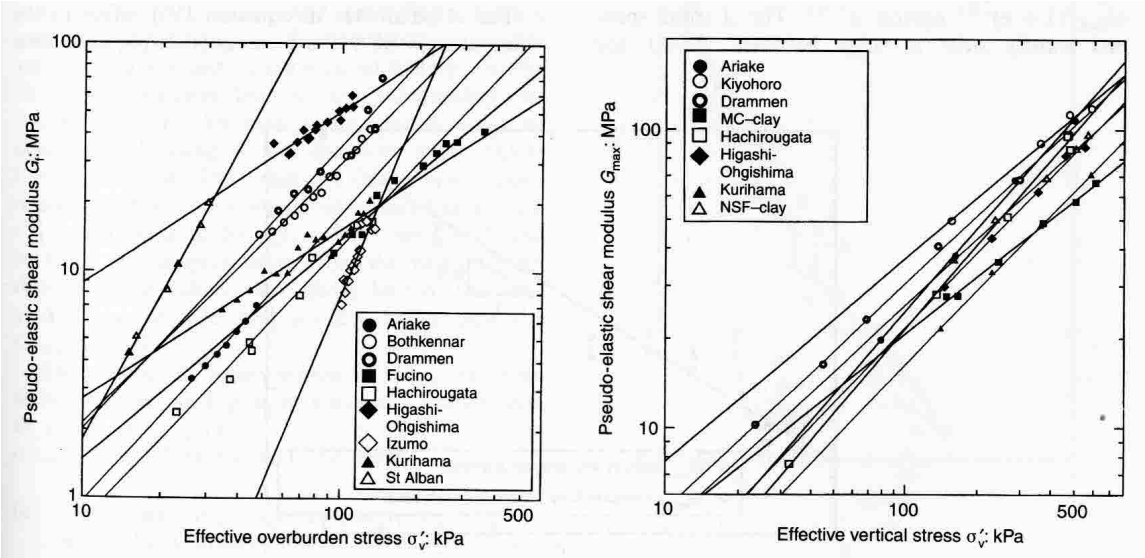

Figure 2.5: Normalized maximum shear modulus versus mean effective stress (Shibuya et al., 1997).

Where A is an empirical constant, $f(e)$ is a function of void ratio, σ_c is the confining stress, σ_r is a reference stress, OCR is over consolidation ratio, and n and k are empirical power exponents.

Roesler (1979), Ni (1987), Stokoe et al. (1994) and Shibuya et al. (1997) suggested the use of mean stress in place of confining stress in equation 2.2 when the soil is subjected to an anisotropic stress state. Jamiolkowski et al. (1994) expressed G_o for an anisotropic stress state by the following expression:

$$G_o = S_v f(e) \sigma_r^{(1-nv-nh)} \sigma^{(nv)_v} \sigma_h^{(nh)} \tag{2.3}$$

Where S_v is a material constant characteristic of the soil structure, σ'_v is the effective vertical stress, σ'_h is the effective horizontal stress and nv and nh are empirically determined exponents.

The relation between G_o and mean effective stress has been well established. Shibuya

et al. (1997) compiled field and laboratory data from a number of papers (Shibuya et al., 1996; Hight et al., 1992; Lunne et al., 1976; Associazione Geotechnica Italiana, 1991; Lefebvre et al., 1994) and presented Figure 2.5 where shear modulus ($\mathrm{G_o}$) varies with mean effective stress for both natural deposits and reconstituted samples. Viggiani and Atkinson (1995b) carried out bender element triaxial compression tests on reconstituted samples of Specswhite kaolin and undisturbed and reconstituted samples of London clay by varying the over consolidation ratio and mean stress. They developed an empirical relationship between mean stress and $\mathrm{G_o}$ given by Equation 4.1.

$$(G_o/p_r) = A(\sigma'_m/p_r)^n \tag{2.4}$$

Where A and n are empirical constants varying with soil type and p_r is a reference pressure (equal to 1 kPa) used for normalization. Jovicic and Coop (1998) also tested Specswhite Kaolin with his data fitting the same equation. Viggiani and Atkinson (1995b) extended his study to include the effect of OCR on reconstituted Specswhite kaolin and London clay and obtained Equation 4.3:

$$G_o/p_r = A(\sigma'_m/p_r)^n OCR^m \tag{2.5}$$

The influence of OCR on the variation of stiffness was also studied by Houlsby and Wroth (1991) using a power function expressed in Equation 2.6.

$$(G_o/p')_{oc} = (G_o/p')_{nc} OCR^m \tag{2.6}$$

A number of researchers (Hardin and Richart, 1963; Hardin and Black, 1968; Marcuson and Wahls, 1972; Jamiolkowski et al., 1991; Shibuya et al., 1997) have studied the effect of void ratio on $\mathrm{G_o}$ and developed void ratio functions to describe the relationship

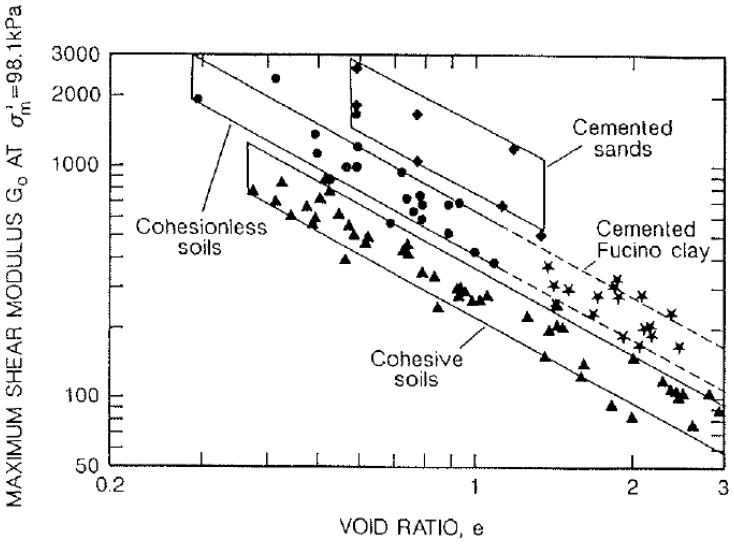

Figure 2.6: Normalized maximum shear modulus versus void ratio (Jamiolkowski et al., 1991).

as given in Equations 2.7, 2.8, and 2.9. Figure 2.6 gives a sense of how void ratio affects G_o for a different soil types (Jamiolkowski et al., 1991).

Hardin and Richart (1963)

$$f_1(e) = (2.17 - e)^2/(1 + e) \tag{2.7}$$

Jamiolkowski et al. (1991)

$$f_2(e) = e^{-1.3} \tag{2.8}$$

Shibuya et al. (1997)

$$f_3(e) = (1 + e)^{-2.4} \tag{2.9}$$

To relate the elastic shear modulus and shear strength of clays, Houlsby and Wroth (1991) also described a method where the rigidity index (G/s_u) which plays an important role in many engineering analysis, was expressed using a power function of the OCR given

by Equation 2.10.

$$(G_o/S_u)_{oc} = (G_o/S_u)_{nc} OCR^{n-\lambda} \tag{2.10}$$

where the exponent $(n - \lambda)$ was determined to be -0.25.

2.1.4.2 Sands

The small strain response of sands have been well studied with particular attention to machine vibrations, earthquake ground response analyses and liquefaction potential evaluations (Richart et al., 1970; Andrus, 2000; Yang and Yan, 2009; Gu et al., 2013)

For sands, $\mathrm{G_o}$ is primarily controlled by the density and confining pressure (Hardin and Richart, 1963; Seed and Idriss, 1970; Pestana and Salvati, 2006) given by Equation 2.11.

$$\frac{G_o}{p_{at}} = G_b f(e) f(\frac{p}{p_{at}}) \tag{2.11}$$

Salvati (2002) reviewed all the formulations developed between 1960 and 2000 describing the effect of confining pressure on shear modulus ($f(p/p_{at})$ in Equation 2.11). Most of the formulations prescribe an exponent for the power law which is in range of 0.4-0.6. Pestana and Whittle (1995) suggested using 0.33 as the exponent.

Hardin and Richart (1963) and Jamiolkowski et al. (1991) proposed their formulations describing the influence of void ratio (Refer to Equations 4.13 and 2.8) for clays as well as sands. In addition to these, Pestana and Whittle (1995) presented Equation 2.12.

Pestana and Whittle (1995)

$$f_2(e) = (1 + e)/e \tag{2.12}$$

Pestana and Salvati (2006) carried out experiments on Monterey sand and found the

void ratio function by Jamiolkowski et al. (1991) fit their data best.

2.2 Offshore wind turbine foundations

In application to offshore wind turbines, different structural configurations have been developed (Byrne and Houlsby, 2005; Moe et al., 2007). Monopile or gravity based structures are existing solutions for water depths shallower than 30 m. Jacket structures (with multiple footing options) are used for slightly deeper water depths. Floating options are being investigated for deep water foundations, as it is economically not feasible to have structures resting directly on the seabed beyond a certain water depth.

The loads are distributed to the foundation differently depending on the sub-sea structure. If a jacket sub-sea structure is adopted with a multiple footing, the loading will be comprised of horizontal loading along with compressional and tensile vertical loading. In case of a monopod structure supporting a wind turbine, there will be significant horizontal loads and moments but relatively low vertical loads applied to the foundation (Byrne et al., 2002; Byrne and Houlsby, 2003). The magnitudes of these loads are very different from those experienced by oil and gas structures, and so therefore there is little guidance to be gained from the established database. Existing values for the ratio of vertical load to horizontal load (V/H) for offshore wind turbines in the literature are found to be ranging from 2.1 to 5.8 (Argyriadis et al., 2005; Lesney and Wiemann, 2005).

The monopile is a simple design in which the wind tower, made up of steel pile, is supported either directly or through a transition piece. It mainly consists of a large diameter steel pipe pile of around 5-6 m in diameter with wall thicknesses as much as 0.15 m. The monopile is usually driven into the seabed by either large impact or vibratory hammers, or they are grouted into sockets and drilled into rock depending on the subsurface conditions. It is considered to have minimal and localized environmental impact (Malhotra, 2009).

Suction caissons have been studied by various investigators as an alternative founda-

tion for offshore wind turbines (Villalobos et al., 2009; Byrne and Houlsby, 2006). They have been referred to as bucket foundations, skirted foundations, skirt piles, suction piles, and suction anchors (Tjelta, 2001).

The aspect ratio (length-to-diameter ratio) of suction caissons reported to be used for offshore structures ranges from less than one to ten (Tjelta, 2001) depending on the type of structure and soil conditions. Suction caissons can be installed in great water depths exceeding the feasibility limits of driving piles and at pre-selected locations with good precision and minimum seafloor disturbance, provide larger holding capacities than drag anchors, and can be retrieved for reuse by pressurizing the interior. In addition, suction caissons can be less expensive to fabricate and require less expensive installation equipment and shorter installation periods (Andersen and Jostad, 1999). Therefore, the use of suction caissons for anchorage of offshore structures has gained wide acceptance and is used all over the world, including the Gulf of Mexico, Brazil, West Africa, North Sea, Norwegian Sea, and West of Shetland (Tjelta, 2001).

There has been relatively little research on the use of caissons as foundations rather than as anchors. The principal difference is the skirt length-to-diameter ratio as well as the nature of the applied loading. For foundations the skirt length-to-diameter ratio is about one, and the loading consists of vertical and horizontal loads as well as moments.

2.2.1 Soil response

The soil data needed for bucket foundations or monopile design is generally not more extensive than for deep piles. As caisson foundations are relatively shallow, deep borings are not needed, but more detailed information at shallow depths is required for caissons and low aspect ratio monopiles (Andersen and Jostad, 1999).

The major foundation design aspects for structures subjected to wave and wind loading according to Andersen (2004) are (1) ultimate bearing capacity; (2) cyclic displacements;

(3) equivalent soil spring stiffnesses; (4) settlements due to cyclic loading, both from increased shear strains due to cyclic loading and from dissipation of cyclically induced pore pressure, and (5) soil reactions against the structure.

A principal aspect of the pile response to lateral load that requires assessment is the ultimate lateral pile capacity, to ensure the foundation has sufficient strength in an extreme loading event (Zhang et al., 2011). This dissertation focusses on the ultimate bearing capacity behaviour for horizontal, moment and combined loading.

The most commonly used method for calculating limiting lateral pile capacity is that recommended by American Petroleum Institute (2000), which is based on the work of Matlock (1970) from field experiments. The API method adopts a limiting resistance of N_p = 9, with lower values applying close to the ground surface. API provides a nonlinear resistance-deflection (P-y) relationship in which 50% of the limiting resistance is mobilized at a deflection of y_{50}/D = 2.5 ϵ_{50}, where ϵ_{50} = strain at which 50% of the soil strength is mobilized in a compression test

One of the earliest work on laterally loaded piles was carried out by Broms (1964) who presented methods for the calculation of the ultimate lateral resistance and lateral deflection of single piles driven in cohesive soils.

Randolph and Houlsby (1984) presented a two-dimensional limit analysis solution for assessing ultimate capacity assuming a deep flow mechanism. This analysis leads to limit bearing factors, N_p, for different values of pile roughness, in the range 9.14 (smooth)-11.94 (rough) (Randolph and Houlsby, 1984; Martin and Randolph, 2006). This flow around solution corresponded to conditions with no-gap formation behind the caisson.

Murff and Hamilton (1993) proposed an upper bound analysis for assessing ultimate capacity based on a 3 dimensional collapse mechanism comprised of a wedge mechanism near the soil surface and a flow around failure (Randolph and Houlsby, 1984). They computed the bearing capacity factors from the relationship:

$$N_p = \frac{\Delta F}{s_u D \Delta L} \tag{2.13}$$

where s_u is the undrained shear strength, D is the caisson diameter, ΔL is the incremental increase in length of caisson, and ΔF is the increase in lateral capacity for pure translation of the caisson.

Their study also showed that predicted lateral resistance profiles for translating and rotating caissons have similar results, consistent with methods based on equivalent p-y curves or semi empirical models (Matlock, 1970; Reese et al., 1975). Murff and Hamilton (1993) also compared their bearing factors to centrifuge data carried out by Hamilton et al. (1991) and found good agreement.

Aubeny et al. (2001) presented a simplified upper bound analysis for estimating the lateral capacity of suction caissons in uniform and linearly varying undrained shear strength profiles. The results can also be applied to other rigid laterally loaded foundation elements such as caisson foundations and short piles, as tested in this paper. This was extended to estimate the inclined lateral load capacity (Aubeny 2003).

Failure envelopes have been studied in detail for piles with aspect ratios of one Gourvenec (2007) and five Zhang et al. (2011) based on finite element results and centrifuge tests, respectively. The ultimate capacity under monotonic load for aspect ratio of 5 was found to be comparable with calculations based on existing design methods, including theoretical plasticity solutions and empirical methods Zhang et al. (2011). Jeanjean (2009) carried out centrifuge tests on a laterally loaded conductor and validated theoretical curves derived via finite element analysis.

Based on the literature, there is a gap in understanding the bearing capacity response of short aspect ratio monopiles, this dissertation aims to address it by studying monopiles of aspect ratio of 2 in the centrifuge environment.

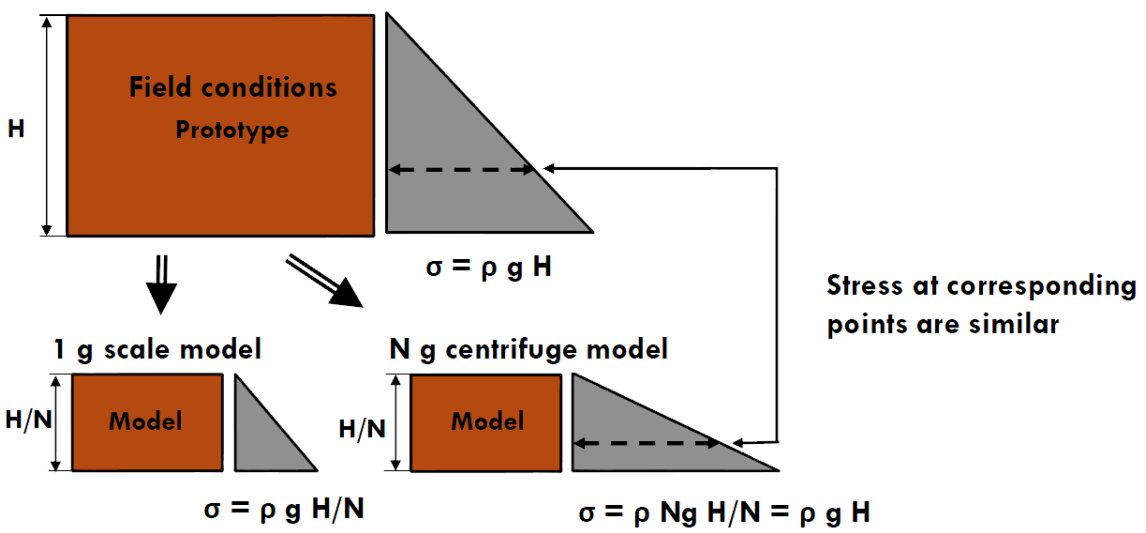

Figure 2.7: Principle of centrifuge modelling

2.2.2 Centrifuge testing

The principles of centrifuge modeling have been discussed and thoroughly verified through numerous trials (Taylor, R. N. (ed.), 1995; Garnier and Gaudin, 2007). It is an extremely useful tool to model self-weight stresses and gravity dependent processes as they are accurately reproduced and observations from small scale models can be related to the full scale prototype situation using well established scaling laws.

Figure 2.7 shows a sketch of how the centrifuge reproduces real world stresses on the scale of the model. Table 2.1 lists all the typical scaling relationships (Taylor, R. N. (ed.), 1995). The variable N refers to the g-level that the model experiences in the centrifuge environment.

This research was carried out at the Geotechnical Centrifuge Research Facility at Rensselaer Polytechnic Institute (NEES@RPI) which houses a 150 g-ton centrifuge designed and manufactured by Acutronic of France. It has a nominal radius of 2.7 m which is the distance between the center of payload and the centrifuge axis. Usable load capacity

Table 2.1: Scaling relationships for centrifuge modeling (Taylor, R. N. (ed.), 1995).

Parameter	Centrifuge (model units)	Full scale (prototype units)
Length	1/N	1
Area	$1/N^2$	1
Moment of Inertia	$1/N^4$	1
Stress	1	1
Strain	1	1
Displacement	1/N	1
Volume	$1/N^3$	1
Density	1	1
Mass	$1/N^3$	1
Force	$1/N^2$	1
Time (diffusion)	$1/N^2$	1
Acceleration	N	1
Frequency	N	1
Velocity	N	1
Elastic modulus	1	1
Flexural Rigidity	$1/N^4$	1
Strain rate (dynamic)	N	1
Strain rate (diffusion)	N^2	1

and acceleration are defined at this radius. The centrifuge was used along with the in-flight robot which was designed to perform multiple tasks while the centrifuge is spinning. The in-flight robot was used to apply lateral loads and also used to operate the T-bar to characterize the strength of the model (Section 2.2.3). For additional information on the equipment and facility see (nees.rpi.edu).

2.2.3 T-bar testing

The shear strength of the clay bed was characterized in flight by using a T-bar penetrometer developed at the University of Western Autralia available at NEES@RPI (Stewart and Randolph, 1991). The tests were carried out using a T-bar that was 5 mm in diameter and 20 mm in length, at a penetration rate of 2 mm/s. This rate provided undrained conditions in kaolin (Einav and Randolph, 2005). Figure 2.8 shows a picture of the T-bar

used at RPI.

The T-bar makes use of the plasticity solution for the limiting pressure acting on a cylinder moving laterally through a purely cohesive soil based on a local flow-around failure method (Randolph and Houlsby, 1984). The shear strength is determined based on the T-bar load cell given by Equation C.7.

$$s_u = \frac{P}{N_{tbar} d} \tag{2.14}$$

where s_u is the undrained shear strength, P is the force per unit length acting along the cylinder, d is the diameter of the cylinder and N_{tbar} is the bar factor.

The bar factor, N_{tbar}, is a function of surface roughness. Theoretical and numerical solutions have been developed to determine appropriate N_{tbar} factors for estimating undrained shear strength (Randolph, 2004; Einav and Randolph, 2005; Randolph and Andersen, 2006; Martin and Randolph, 2006; White et al., 2010). Based on the existing research a T-bar factor, N_{tbar} of 10.5 was selected for computing shear strength below a depth of 1.4 m. The data from shallow depths was computed based on a different failure mechanism as shown in Figure 2.9 (White et al., 2010). An adjustment was also introduced to correct for rate penetration effects of the T-bar (Yafrate and DeJong, 2007; DeJong et al., 2011).

Figure 2.8: Picture of the T-bar at RPI

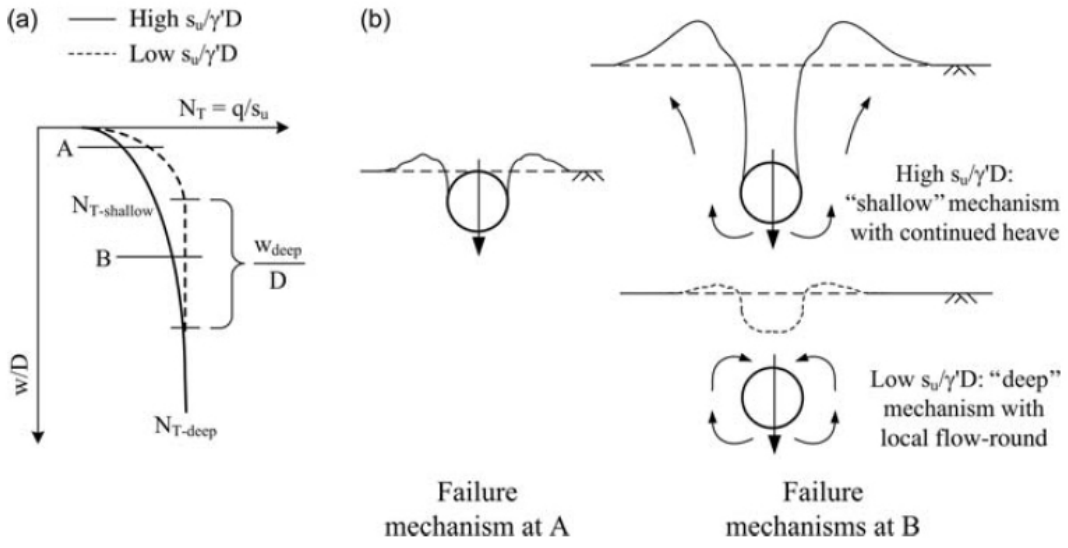

Figure 2.9: T-bar failure mechanisms (White et al., 2010)

3. METHODOLOGY FOR STRENGTH-STIFFNESS CORRELATIONS

The following section describes the materials and the testing capabilities of the equipment used, the procedures followed for sample preparation, and the laboratory testing program to characterize the soils. The methodology for all the laboratory tests is also discussed.

3.1 Materials

This testing program consists of tests on 4 different types of clayey soils and 2 different types of sandy soils with a range of index properties. Index properties are considered as void ratio limits (maximum and minimum void ratio) for sands and Atterberg limits (liquid limit, plastic limit, plasticity index) for clays.

3.1.1 Clay

Four different types of clays were tested in this project: natural Gulf of Mexico (GoM-N), reconstituted Gulf of Mexico (GoM-R), Red Art (RA) and Kentucky Special kaolin (KS). As seen in the Figure 3.1, natural Gulf of Mexico clay is an olive greenish grey clay that was sampled in and around the Green Canyon near the Sigsbee Escarpment from the Gulf of Mexico using jumbo piston cores (Rutherford, 2011). This clay was first tested intact, reconstituted by adding water and then tested again. Also seen in the figure is Red Art clay which is a silty red clay, and Kentucky Special which is a standard kaolin both obtained from Armadillo Clay & Supplies in Austin, TX in dry powder form.

3.1.2 Sand

Two different types of sands were tested: Ottawa sand and Mystic White sand. Both are poorly graded sands with an average grain size of 0.6 mm. Figure 3.2 shows a picture of the sands used. The main difference in the two types of sands is the particle angularity,

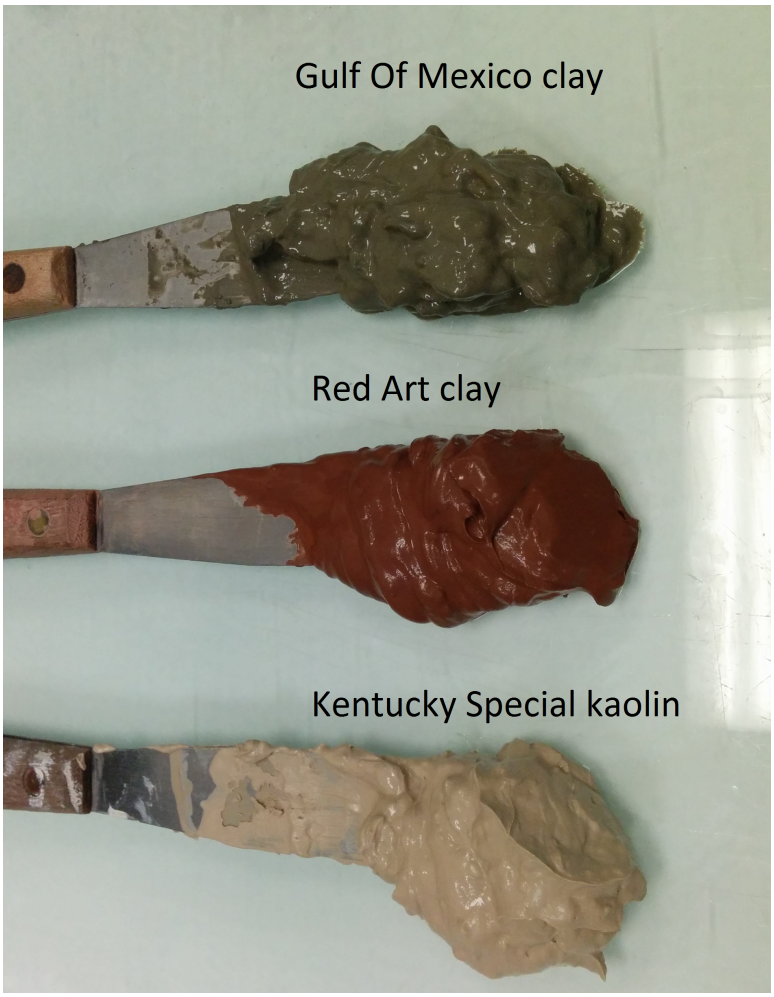

Figure 3.1: Clays tested in this research program.

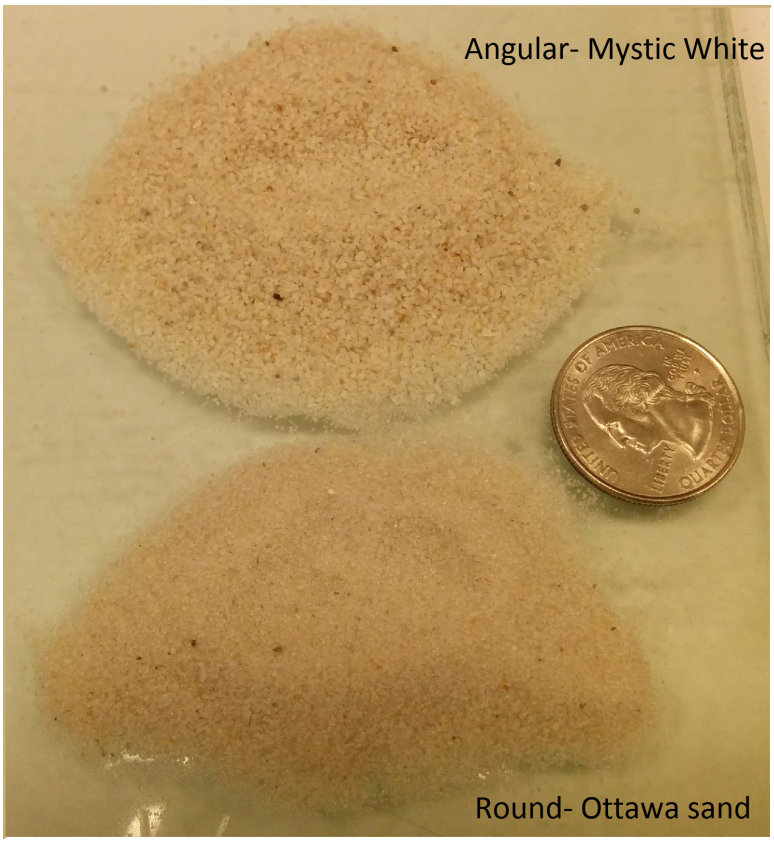

Figure 3.2: Sands tested in this research program.

Ottawa sand is extremely round whereas Mystic White sand was selected because of its extreme angularity.

3.2 Equipment

3.2.1 GEOTAC triaxial testing device

The triaxial testing system used for this research was the GeoTAC TruePath system (Figure 3.3), which consists of the axial load frame, cell and pore pressure-volume flow pumps (PVP), instrumentation, data acquisition and control hardware and software. The axial load frame has a capacity of 4.45 kN (1,000 lb), and also provides deformation control with a calibrated screwjack. The position of the platen is recorded when the test is

started and the change in platen position used to calculate deformation. The pore pressure-volume pump continuously measures the volume change in the sample during consolidation and by comparing axial and volumetric deformations, a feedback loop can automatically enforce K_o conditions (zero lateral strain) by varying the cell pressure and vertical load. Combinations of vertical and volumetric deformation rates can be used to control strain paths (Bishop and Wesley, 1975; Germaine and Ladd, 1988; Berre and Bjerrum, 1973).

Transducers which are monitored by the data acquisition system and recorded using the GeoTAC system software, are used for monitoring and controlling the test progress. The sensors used in this setup include: a linear strain conversion transducer (LSCT) for axial displacement; force transducer for axial force; and three pressure transducers, one each for cell pressure, back pressure at the pore pressure-volume pump and pore pressure within the sample. The system is operated by a control and data acquisition software which has a graphical user interface to enable the user to input test parameters and monitor the test. See Murali (2011) for more details.

3.2.2 Bender and piezo-crystal testing caps

Two sets of caps for the triaxial samples were equipped with piezoelectric transducers. The systems were manufactured by GCTS Testing Systems and fit the GEOTAC setup with some modification. Bender elements and p-crystals are installed in one set of caps, while both p- and s-crystals are installed on the other set. While the bender elements protrude from the caps, the s-crystals are mounted under the surface of the cap. The water lines align with the ports in the bottom plate of the triaxial chamber, enabling undrained testing.

The system is completed by a Tectronix arbitrary function generator AFG320, a Tectronix oscilloscope TD3014B and TDS3GV and a Piezosystems PiezoLinear Amplifier as shown in Figure 3.3, the schematic of connections is shown in Figure 3.4.

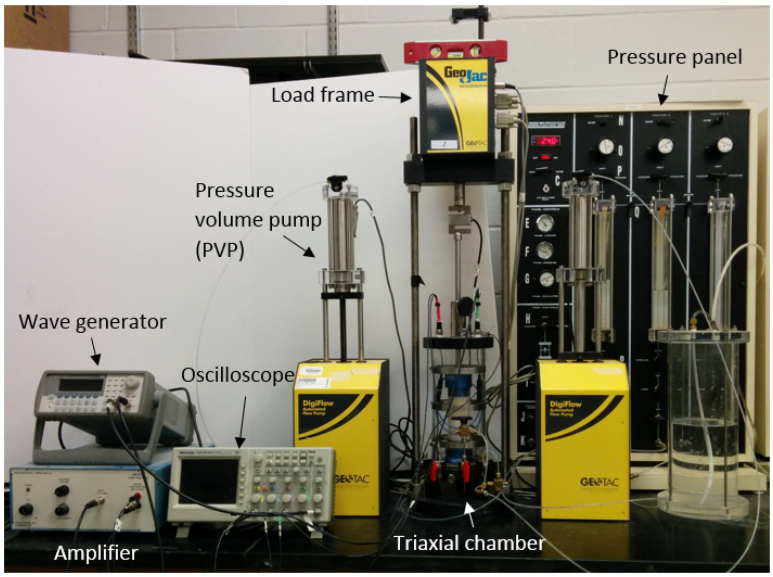

Figure 3.3: Triaxial test setup with bender caps.

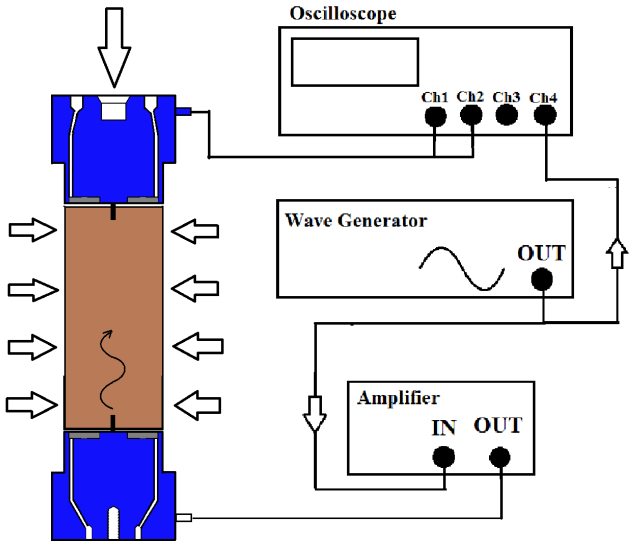

Figure 3.4: Schematic of test setup showing connections.

The bender caps and piezo caps allow the s- wave velocity and p- wave velocity through the soil specimen to be measured with some ease. Two elements are used: a receiver and a transmitter as the top and bottom cap respectively. A voltage is applied to the transmitter element causing it to vibrate in the direction normal to the face of the ceramic plates. The shear wave produced by the vibration is sent through the sample and detected by the receiver element. The time difference between the input and the output wave represents the travel time of the shear wave. It is captured and displayed by a digital oscilloscope, so that the shear wave velocity, v_s can be measured.

The function generator provided a burst sine output signal at a frequency of 50 kHz. It was found to give the least amount of electrical interference with the other devices in the laboratory. The driving signal was amplified and served as the input for the bottom cap bender element. The receiver signal from the top cap was sampled by the oscilloscope.

Details on the bender elements and interpretation of the signals is given in Appendix A.

3.3 Laboratory testing program

A comprehensive soil testing program was carried out on all the different samples for material characterization. This section describes the index tests, testing plan and procedures for the strength tests carried out on both clays and sands.

3.3.1 Preliminary tests

3.3.1.1 Clay

Three to five Atterberg limit tests were carried out in order to obtain an average liquid and plastic limit for each type of clay. The liquid and plastic limits were conducted in accordance with ASTM Standard D4318 (2010). Specific Gravity tests were also performed in accordance with ASTM Standard D854 (2010). The results are reported in Table 3.1.

Figure 3.5 shows the plasticity chart and plots all the samples of clay tested. Almost all

Table 3.1: Index properties and classification for the three types of clay.

Type of Clay	Liquid Limit	Plastic Limit	Plasticity Index	Specific Gravity	Soil type
GoM-R	86	41	45	2.76	CH
KS	61	32	29	2.6	MH
RA	39	23	16	2.75	CL

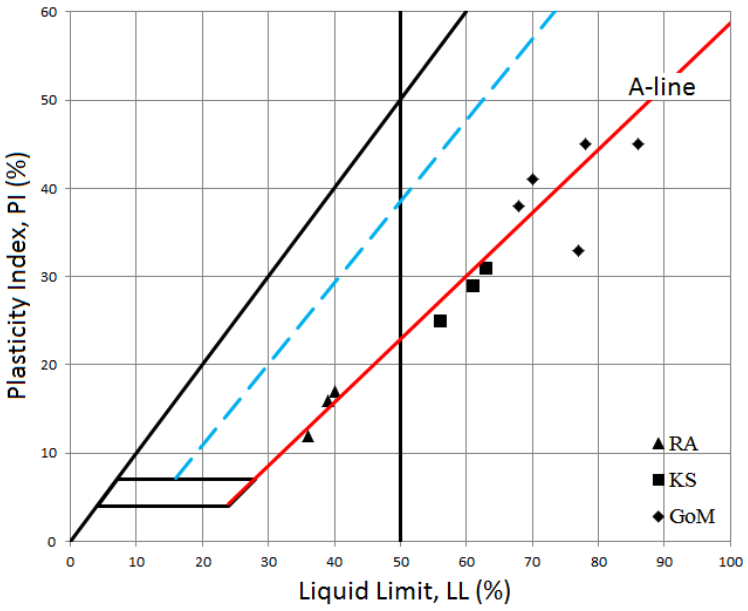

Figure 3.5: Casagrande plasticity chart with the three types of clay.

the samples lie around the A line of the chart. Their classification according to the Unified Soil Classification System (USCS) is also given in Table 3.1. The plasticity of the clays varies widely with GoM being a relatively high plasticity clay and RA on the other hand approaching the behavior of silty clays.

3.3.1.2 Sand

Gradation curves are presented in Figure 3.6 for Ottawa sand (R) and Figure 3.7 for Mystic White sand (A). Mystic White sand was sieved to obtain a similar gradation as that

of Ottawa sand. This was carried out to order to to remove the influence of gradation and compare the two sands purely based on particle angularity.

Relative density was also assessed for both sands. The maximum density (e_{min}) was determined by densifying the sands in a 6 in compaction mold. The sand was placed in five layers by pouring from a set drop height. The base of the mold was then hammered 10 times on each of its four sides and the process repeated for each layer.

The minimum density (e_{max}) was obtained by depositing sand very gently within a graduated cylinder. The process consisted of placing a known weight of sand in the cylinder while it was horizontal. The cylinder was then rotated to its upright position extremely slowly so as to minimize the energy input and produce the loosest state.

The tests were repeated 5 times to check for consistency and the results averaged. The results for the tests are in Table 3.2. The values obtained by these methods are in agreement with the values found in the literature for these types of sands.

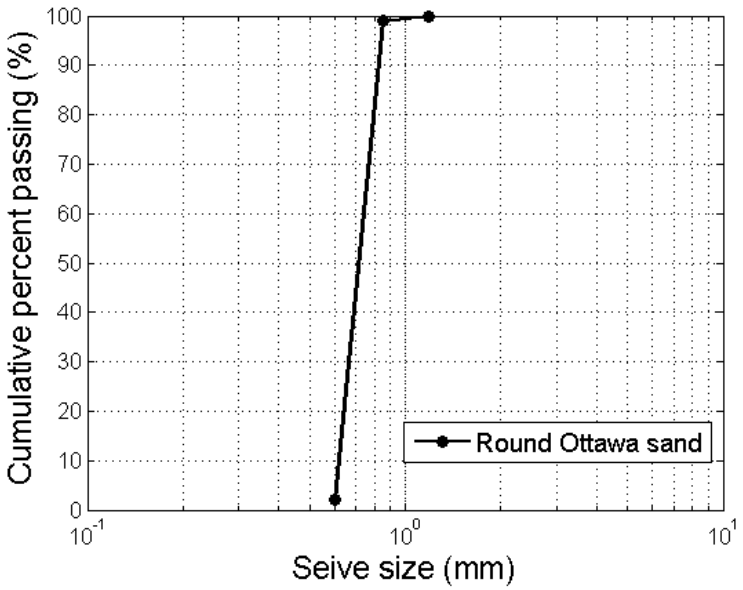

Figure 3.6: Gradation curve for Ottawa Sand.

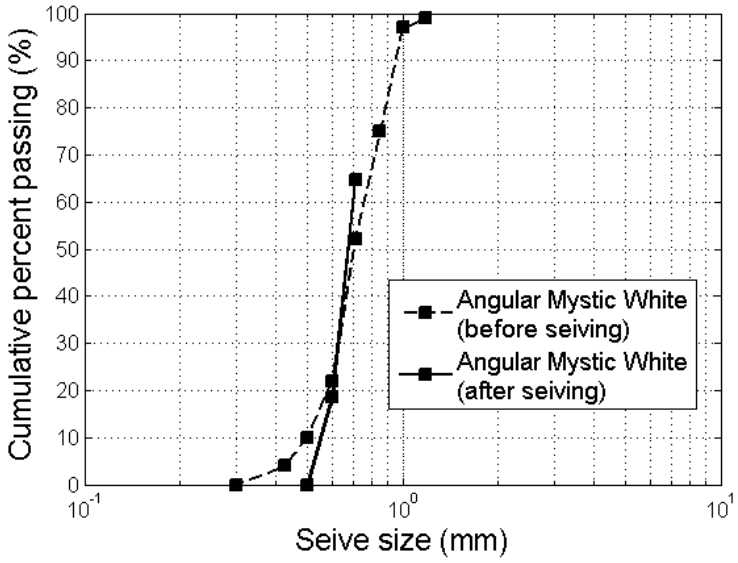

Figure 3.7: Gradation curve for Mystic White Sand.

Table 3.2: Maximum and minimum void ratios for the sands.

Sand type	Minimum void ratio (e_{min})	Maximum void ratio (e_{max})
Ottawa Sand	0.49	0.79
Mystic White Sand	0.80	1.10

Table 3.3: Coefficients of Consolidation and Compression Indexes for Three Clay Types.

Soil type	Strain rate %/hr	Coefficient of Consolidation C_v ($\mathrm{ft}^2/\mathrm{day}$)	Compression Index C_c
GoM	2	0.004	0.731
	5	0.02	0.806
KS	5	0.006	0.543
	7	0.03	0.708
RA	5	0.015	0.226
	7	0.02	0.333
	7	0.03	0.333
	10	0.06	0.530

3.3.2 Consolidation tests

Constant rate of strain (CRS) consolidation tests were carried out for all the clay samples (ASTM Standard D4186, 2006) with strain rates varying from 2% to 10% depending on the hydraulic conductivity of the clay. The specimens were prepared by mixing a ratio of soil and water resulting in an initial water content of approximately 1.5 times the liquid limit of the clay. Since the clays were consolidated from a slurry state, the clay was placed into the steel ring in stages, as shown in Figure 3.8. Once the sample was prepared (Stage 4), it was placed into the cell and CRS consolidation tests started. These clays were tested at strain rates varying from 2% to 10% depending on the hydraulic conductivity of the clay so as to develop a small amount of excess pore pressures during the consolidation. This test was mainly selected to determine the coefficient of consolidation (C_v) for all the clays to help determine the sample preparation time for the strength tests. Figure 3.9 shows the results of the CRS tests on the three different clays and Table 3.3 lists the coefficients of consolidation and compression indices of the clays.

Figure 3.8: Sample preparation for CRS test.

3.3.3 Strength tests

Table 3.4 lists the test matrix for each type of soil and Table 3.5 lists the intervals for body and shear wave measurements along with other properties in the testing program. A set of 6 K_o consolidated undrained (CK_oU) triaxial compression tests were carried out at OCRs of 1, 2, 4 and 8 on clays. K_o consolidated drained (CD) triaxial compression tests were carried out at various stress levels on sand at two different relative densities, dense and loose. Body and shear wave measurements accompanied all tests before and after the test and during the shearing phase.

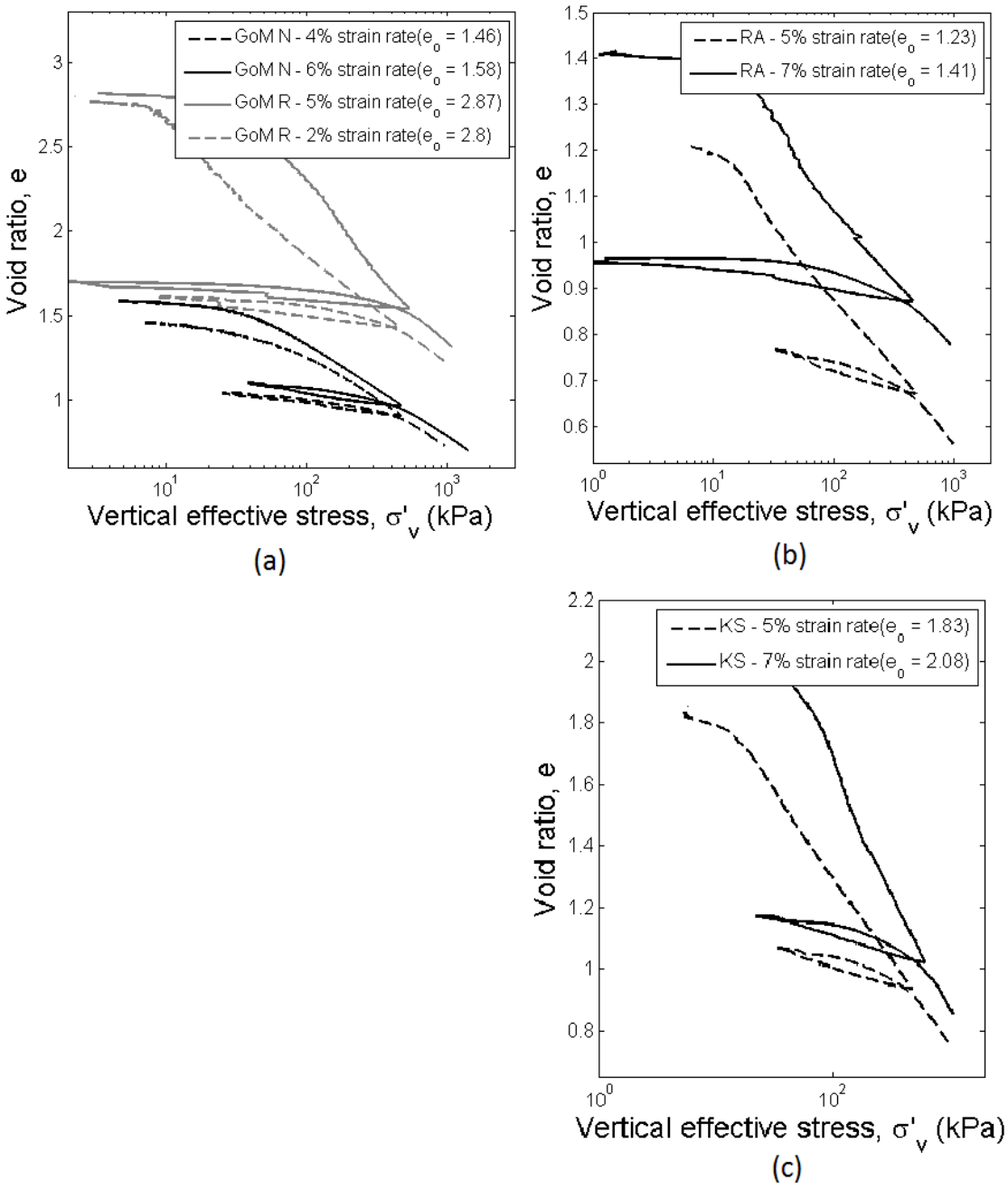

Figure 3.9: CRS test results for (a) Gulf of Mexico, (b) Red Art and (c) Kentucky Special kaolin at different strain rates.

Table 3.4: Test matrix for all soils.

Soil type	Test drainage	Stress level (kPa)	OCR	Relative density
Clay	Undrained	45	1	-
	Undrained	60	1	-
	Undrained	30	2	-
	Undrained	15	4	-
	Undrained	7.5	8	-
	Undrained	60 (repeat)	1	-
Sand	Drained	60	-	Dense (>60)
	Drained	30	-	
	Drained	15	-	
	Drained	5	-	
	Drained	60	-	Loose (<30)
	Drained	30	-	
	Drained	15	-	
	Drained	5	-	

3.3.3.1 Clay - Consolidated Undrained

The GoM-N samples were treated like regular triaxial specimens, the soil was first extruded from the pipe sections using a soil sample ejector combined with a hydraulic hand pump (ENERPAC; Model P-80). These samples of clay were then trimmed very carefully into dimensions of 5 cm diameter and 10-12 cm length. The tests on GoM-N samples were carried out on specimens from different elevations and tested at various stress levels (Chapter 4 Table 3.6).

The GoM-R, KS and RA clay samples were reconstituted by prepared by mixing dry powdered clay or trimmings from previous tests in the case of GoM-R, with water in a bread mixer to produce a slurry (Germaine, 1982). The slurry was scooped into a 5 cm inner diameter PVC split mold fitted with a membrane and closed at the both end with porous stones. Samples were bench consolidated by incrementally loading the split molds with dead weights until the desired vertical effective stress for each test was reached (Fig-

Table 3.5: Soil type and interval for measurements.

Soil	Test Drainage	e, n w, ρ	$\sigma - \epsilon$	p-wave	s-wave
Gulf of Mexico (GoM)	Undrained	BA	BCSA	BCSA	BCSA
Kentucky Special (KS)	Undrained	BA	BCSA	BCSA	BCSA
Red Art (RA)	Undrained	BA	BCSA	BCSA	BCSA
Ottawa sand (R)	Drained	BA	BCSA	BCSA	BCSA
Mystic White sand (A)	Drained	BA	BCSA	BCSA	BCSA

BA - Before and after

BCSA - Before, after and continuous monitoring

ure 3.10). A load increment of 1 kg (9.81 N) was used, with each load being maintained for at least one week to ensure the completion of primary consolidation. Since these samples were prepared from slurry, the time required for consolidation was quite long. Once the target stress was achieved, the load was removed. The sample encased in the membrane was then removed from the split mold and treated as an undisturbed specimen for testing. The results from the CK_oU tests show that resedimented specimens exhibit similar behavior to intact specimens, especially in undrained shearing.

In addition to these three clays consolidated in split molds, Red Art clay samples were also prepared using a clay pugging machine. The dry Red Art clay powder was added to the soil pugging and extruding machine along with a measured volume of water. The pugger mixes the soil and water under a vacuum and extrudes clay logs which can then be trimmed similarly to the natural samples. Strength tests were also carried out on these 'extruded' samples and the results compared with the consolidated Red Art clay samples.

Once the prepared sample was installed in the triaxial chamber, the steps for all tests were identical. A seating pressure of 5 kPa, equivalent to a seating load of 6.67 N (1.5 lbf) was applied. After back saturation, the test proceeded to the consolidation phase if the B-value was greater than 0.95. Otherwise the sample was again back pressured for an-

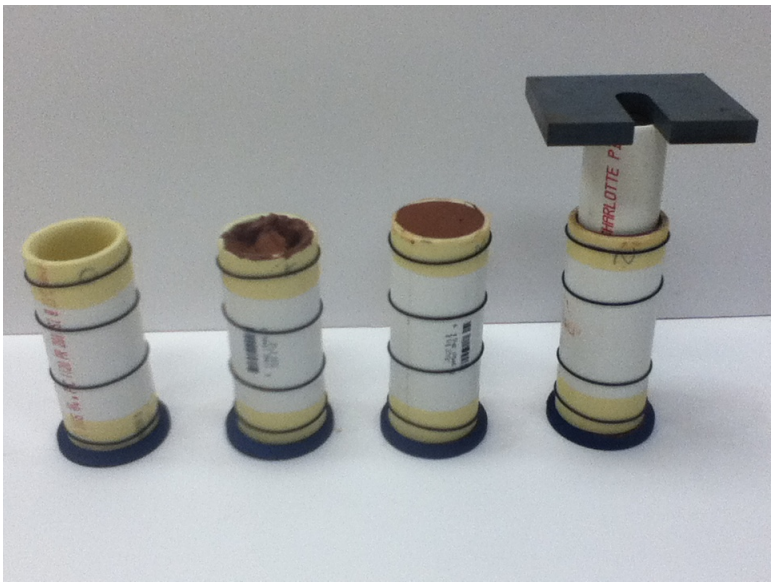

Figure 3.10: Sample preparation for strength tests.

other 12 hrs and its B-value was checked again. This step was extremely important as the presence of air pockets in the sample diminishes the output signal on the oscilloscope as wave propagation is very sensitive to saturation. Since the bender and ultrasonic caps could not be immersed in water (Figure 3.11), air was used as confining pressure within the triaxial chamber applied using the pressure panel (Figure 3.3). Thus, the consolidation part of the test was controlled manually as the pressure panel was not automated with a feedback loop.

To simulate soil conditions that are encountered in nature, K_o consolidation was carried out, implying consolidation of the soil sample with no radial strain. The value of K_o (σ'_h/σ'_v) for each of the three types of clays was first determined by carrying out one test (without bender caps) where the consolidation phase was completely automated using the cell pressure-volume pump for control with water as the confining pressure. The K_o unload stress path until an OCR of 8 was also determined and is plotted in Figure 3.14 for all clays.

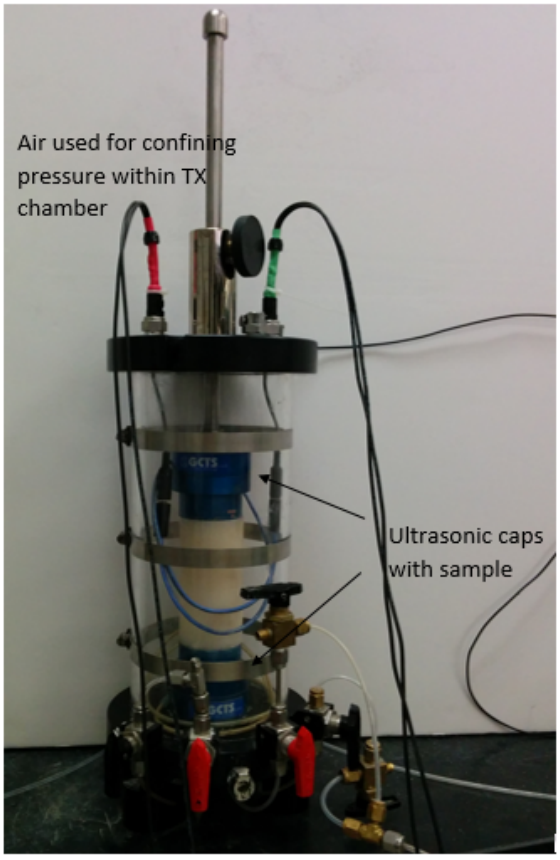

Figure 3.11: Triaxial chamber with bender caps and sample.

Once the K_o values were determined the procedure followed was similar to that proposed by Germaine and Ladd (1988). Manual consolidation was carried out by increasing the vertical effective stress and horizontal effective stress incrementally based on the determined K_o value. The loads were applied in 3 to 4 increments and allowed to equilibrate after each increment. The K_o value during each of these increments was calculated and the ratio of confining pressure and vertical load was adjusted accordingly. The axial strain of the sample was compared with the volumetric strain to ensure minimal radial strain during consolidation. The specimens to be tested at various OCRs were then unloaded manually to the desired stress level depending on the K_o value. Figures 3.12 and 3.13 show examples of strain vs time and strain vs vertical effective stress curves during the manual consolidation process. The strain rate used was approximately 1% per hour, which resulted in a consolidation time of 4 days. The OC samples took longer, about 5-6 days, depending on the OCR.

After consolidation and rebound, when needed, all specimens were sheared in compression at a strain rate of 5%/hr. During this phase p- and s- wave velocity readings were recorded at specific strain intervals.

3.3.3.2 Consolidated Drained

Specimens were created initially by dry pluviation. A membrane was stretched inside a split mold set around the bottom cap of the triaxial cell. Sand was then rained down from a designated height and into the membrane. The mesh size and drop height depended on the size and type of soil particles. As sand filled up the mold, the pluviator was also raised to maintain consistent impact energy. For dense specimens the sand was poured from a height of 7 cm from a funnel. For loose specimens a wire mesh (sieve size 10, equal to 2 mm). was placed on the bottom cap, sand was poured slowly from the funnel through a small diameter (6.35 mm) tube. The small diameter ensures the sand pours

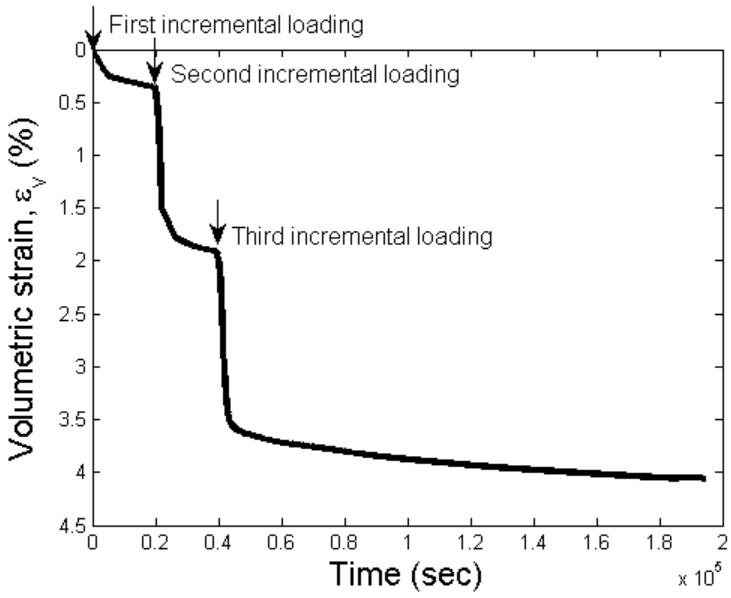

Figure 3.12: Incremental loading during consolidation phase showing vertical strain versus time.

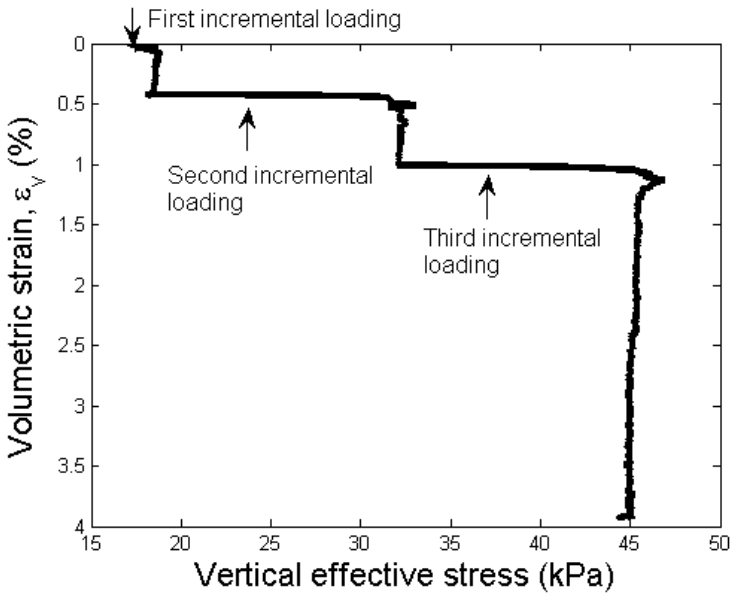

Figure 3.13: Incremental loading showing vertical strain versus vertical stress.

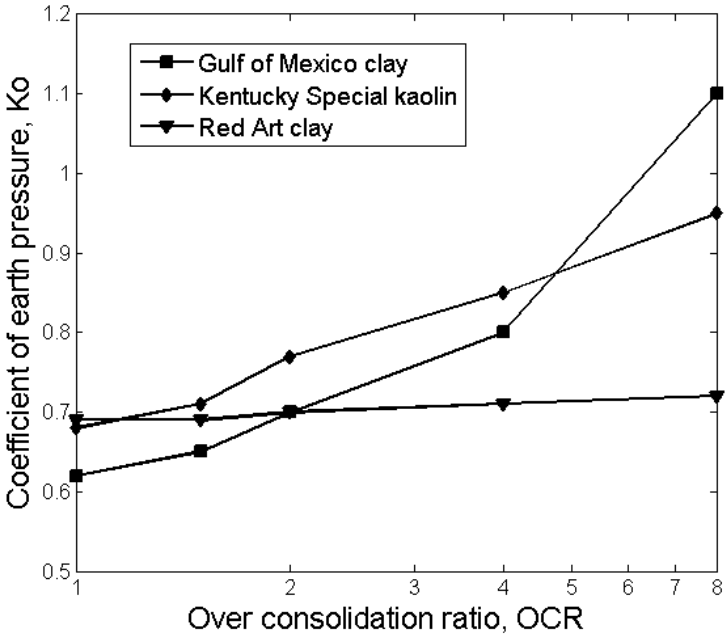

Figure 3.14: Variation of K_o with over consolidation ratio during the unload phase.

out slowly giving more control while preparing the sample. In order to minimize pour height the end of the tubing was always kept at the surface of the sand and was slowly raised as the sand filled the mold. Once the mold was filled to the desired height the mesh was raised through the sand, increasing the void ratio even further. Once the top cap was placed and the membrane sealed by O-rings, the specimen was subjected to a small vacuum (5 kPa) to minimize disturbance due to handling and mounting the specimen. This was especially important for the loose samples. The specimen was then saturated by maintaining a vacuum of 5 kPa at the top and connecting the bottom cap to a de-aired water tank at atmospheric pressure, letting de-aired water flow into the sample from the bottom upwards and filling all the voids. The weight of sand rained in for each sample was recorded and the void ratio for each specimen was computed.

Once the specimen was filled with water, the sample was back saturated in increments

of 20 kPa up to a back pressure of 140 kPa and an effective pressure of 3 kPa to remove any air bubbles still in the sample. A B-value check was carried out to ensure the sample was fully saturated and the effective stress then increased up to the required confining pressure for the sample to be sheared.

The cell pressure was increased to the required value assuming K_o to be 0.4 for all the sand tests. Once the sample equilibrated shearing was carried out in drained conditions at a strain rate of 5%/hour.

3.4 Strength characteristics

The following section presents the strength results from $CK_o - U/D$ triaxial tests carried out on all the types of clays (GoM-N, GoM-R, KS, RA, and RA-E) and all the sands (Round and Angular). The chapter also includes a brief interpretation of the strength results for all the samples.

3.4.1 Clay

3.4.1.1 Gulf of Mexico (GoM)

Figures 3.15 and 3.16 illustrate the undrained triaxial compression behavior of natural GoM (OCR 1 to 8) sheared at a rate of 5%/hr. The depths of the each sample tested is given in Table 3.6. The normally consolidated samples were tested from depths of 7 m (45 kPa test) and 8.5 m (60 kPa test) with estimated pre-consolidation pressures to be 36 kPa and 44 kPa respectively (Table 3.6).

The stress strain behavior becomes more ductile with increasing OCR as larger axial strains are required to mobilize the peak resistance (Figure 3.15). No strain hardening or softening is observed from the stress strain curves for GoM-N samples.

During undrained loading of a normally consolidated (NC) clay, excess pore pressure is generated in the sample which causes the stress path to decrease (move to the left in Figure 3.16). At failure, the normally consolidated GoM-N specimens do not show as much of

Table 3.6: Depth of natural GoM samples.

Depth (m)	Estimated pre-consolidated pressure (kPa)	Test stress level
7.01	36.38	45kPa OCR = 1
8.53	44.29	60kPa OCR = 1
9.14	47.15	30kPa OCR = 2
9.44	49.03	15kPa OCR = 4
9.75	50.6	7.5kPa OCR = 8
10.05	52.2	60kPa OCR = 1 (repeat)

an increase in excess pore pressure as expected (Figure 3.16). The age and storage of the natural samples is thought to be the reason for causing the natural clay to behave as if it were slightly overconsolidated than what is usually expected for samples from these depths. Storage of samples causes a certain amount of desiccation or loss of saturation leading to an over consolidated behavior where the samples do not generate as much pore pressure as expected.

Increasing OCR causes a decrease in the peak value of strength normalized by the maximum vertical effective stress (σ'_v) and an increase in the axial strain needed to mobilize peak strength (ϵ_{af} = 4%, 6% and 6.5% for OCR = 2,4 and 8). The GoM-N sample tested at OCR of 8 begins to develop negative excess pore pressure as expected. The figure shows the effective stress failure envelope at an angle of 29^o.

Figures 3.17 and 3.18 illustrate the undrained triaxial compression behavior of reconstituted GoM (OCR 1 to 8) sheared at a rate of 5%/hr. The figures show that NC GoM-R reaches peak strength at relatively small axial strain (0.2%), followed by slight softening; and the development of positive pore pressures causes the effective stress path to decrease significantly along the x-axis. Similar to GoM-N, increasing OCR causes a decrease in the peak value of strength normalized by the maximum vertical effective stress (σ'_v) and an increase in the axial strain at failure (ϵ_{af} = 0.5%, 4% and 6% for OCR = 2,4 and 8).

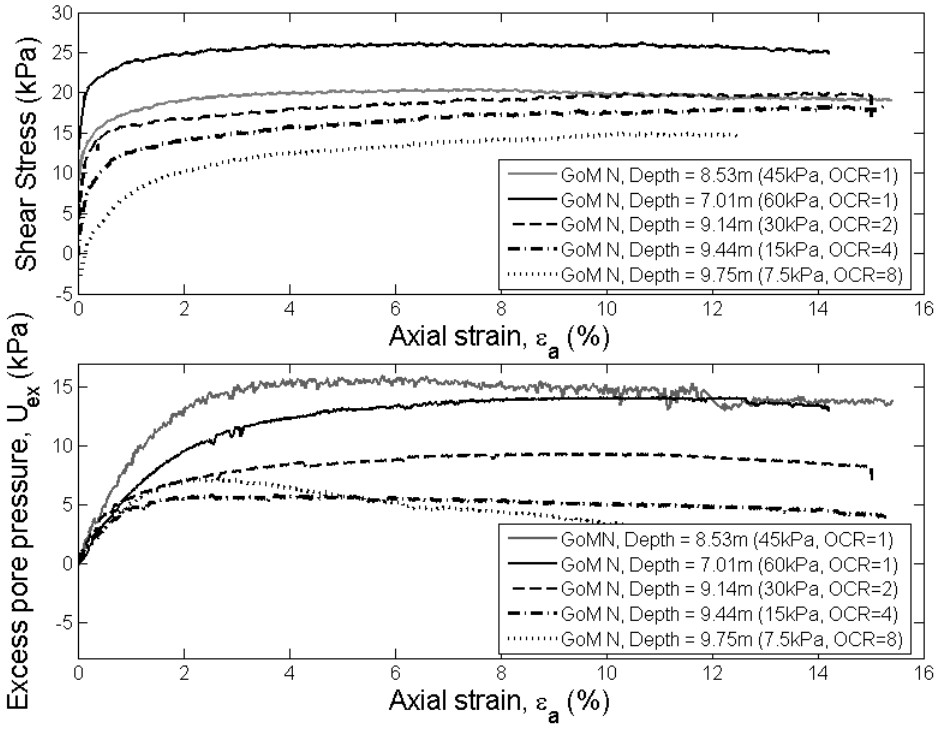

Figure 3.15: Stress strain behavior and excess pore pressure for natural GoM clay.

On comparing the GoM-N sample OCR = 1 (Figure 3.16) and GoM-R sample OCR = 2 (Figure 3.18) we observe a similarity in their stress path, reinforcing the supposition that the natural Gulf of Mexico clay may be slightly over consolidated due to loss of saturation and/or ageing. This similarity can also be observed on comparing the GoM-N samples OCR = 2 and OCR = 4 with the GoM-R samples OCR = 4 and OCR = 8, respectively. At larger strains, the effective stress paths approach a common failure envelope at an angle of 25^o. The higher friction angle of the failure envelope for GoM-N samples is thought to be due to the difference between reconstituted and a structured clay deposit.

Figure 3.19 summarizes the observations of the axial strain needed to mobilize peak shear stress (ϵ_f) in each of the triaxial tests on Gulf of Mexico clay along with the best fit

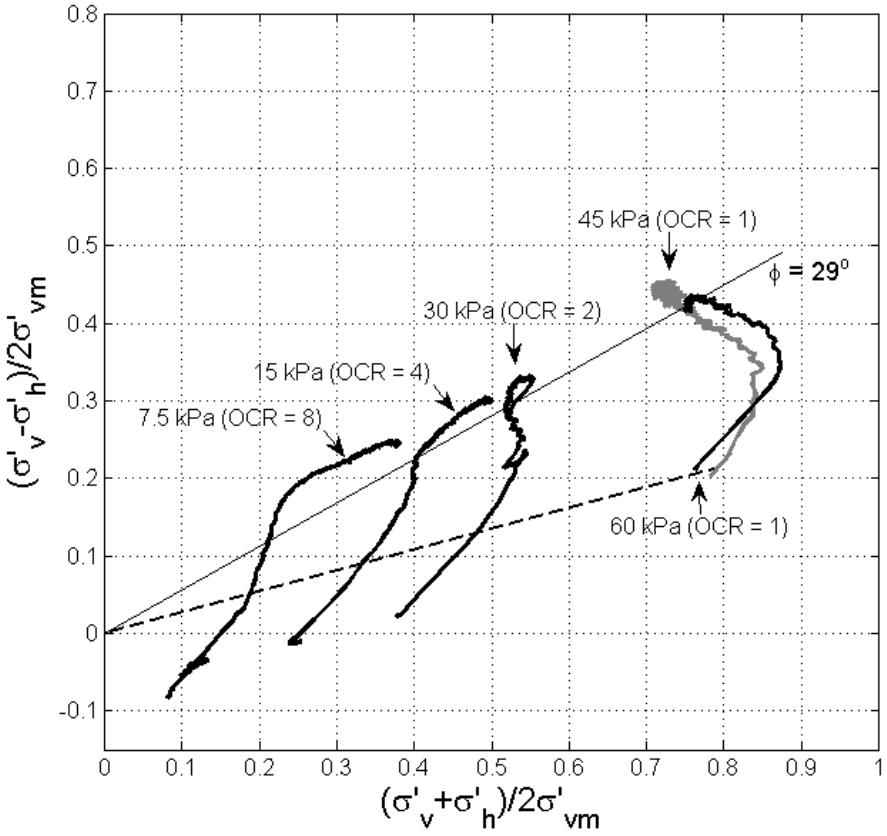

Figure 3.16: Effective stress paths for natural GoM clay.

curve using the data. As the OCR increases from 1 to 8 there is a significant rise in ϵ_f from 1.5% to 6.5% for GoM-N and from 0.3% to 6% for GoM-R. Also evident from the figure is that the failure strain needed to mobilize peak strength is higher in the natural samples compared to the reconstituted samples.

Figure 3.20 shows the normalized undrained strength ratios (s_u/σ'_v) as a function of OCR for all the GoM tests, together with the derived SHANSEP parameters $(s_u/\sigma_v)_{oc} = S(OCR)^m$ of S and m. On observing Figure 3.20 a comparison can be made between the normalized undrained strength ratio for GoM-N OCR = 1 and GoM-R OCR = 2. Simi-

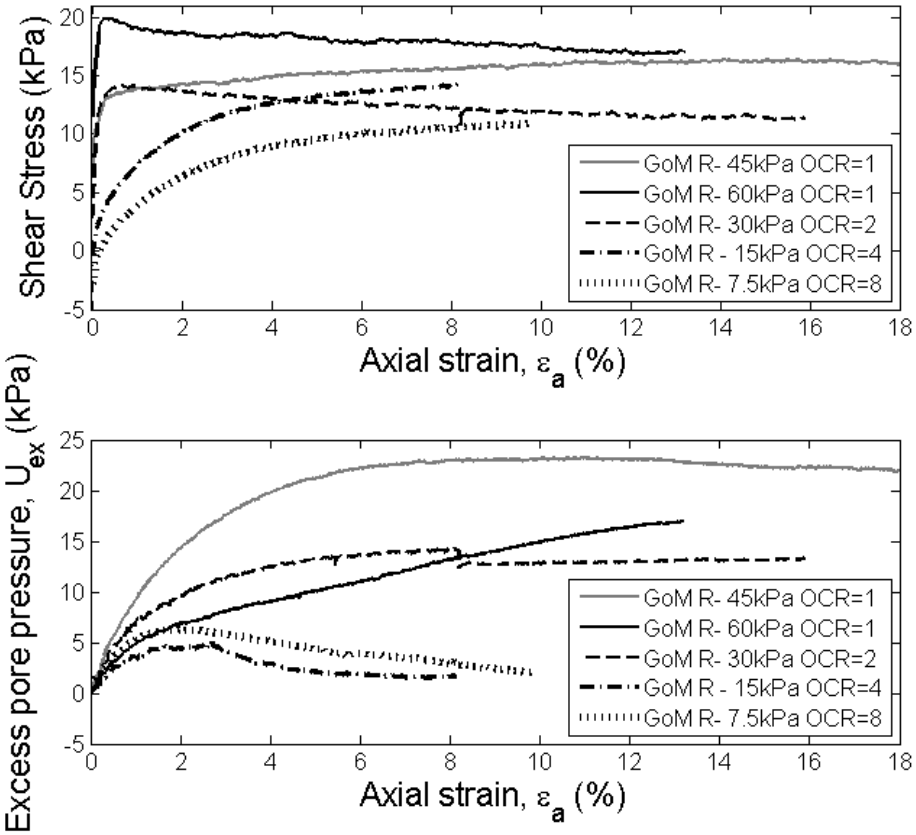

Figure 3.17: Stress strain behavior and excess pore pressure for reconstituted GoM clay.

larly s_u/σ'_v for GoM-N OCR = 2 and 4 can be compared with GoM-R OCR = 4 and 8 respectively. The exponent, m is found to be quite similar between the two sets (0.632 for GoM-N and 0.625 for GoM-R), however the true value of parameter, S, ($(s_u/\sigma'_v)_{nc}$) is obtained from the NC GoM-R sample equal to 0.32. Ladd et al. (1977) showed that the OCR exponent parameter, m, is typically equivalent to 0.8$\pm$ 0.05. The lower, m, value is thought to be due to the samples tested at low confining pressures. Based on both the effective stress paths and the SHANSEP parameters it can be inferred that due to a combination of age, storage and loss of saturation of the clay, all of the natural GoM-N samples

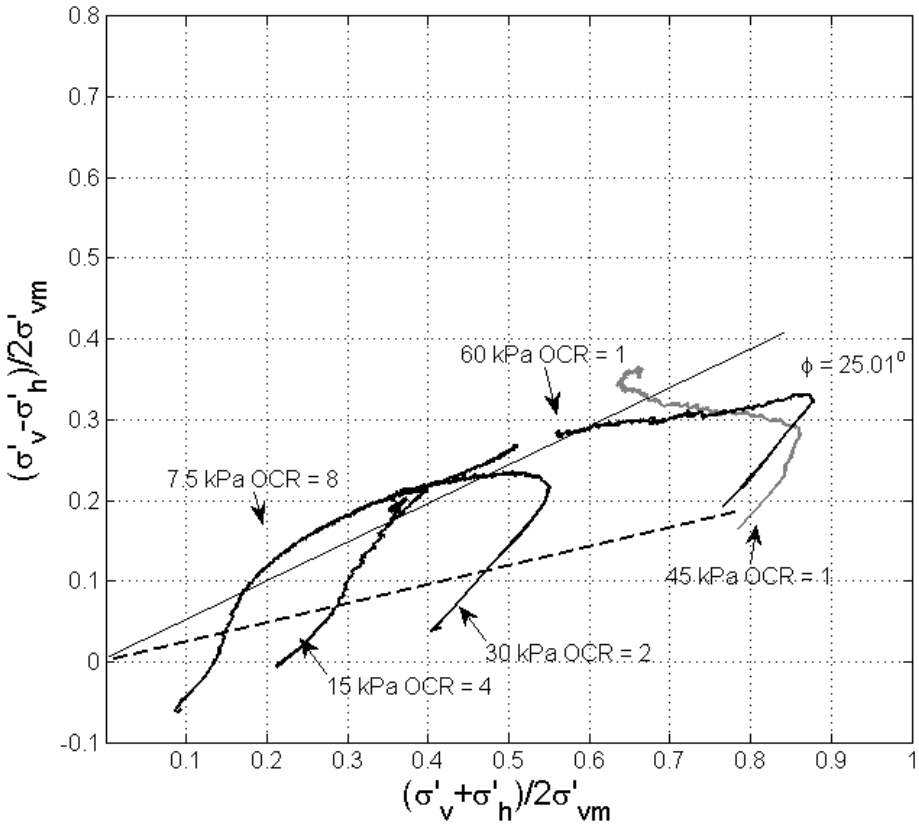

Figure 3.18: Effective stress paths for reconstituted GoM clay.

were slightly more over-consolidated than estimated.

Figures 3.21a and 3.21b show the normalized undrained secant modulus, i.e., Young's modulus over maximum vertical stress ratio (E_u/σ'_{vmax}), versus axial strain, (ϵ_a) on a log log plot for natural and reconstituted GoM samples respectively. The measurements were performed using external LVDT, thus the estimates of secant modulus are only considered reliable for ϵ_a greater than 0.03%-0.1%. The data shows that all samples exhibit significant nonlinearity at small strains for both GoM -N and -R. The decrease in modulus becomes more pronounced once the soil yields or reaches its peak strength and the rate of decrease

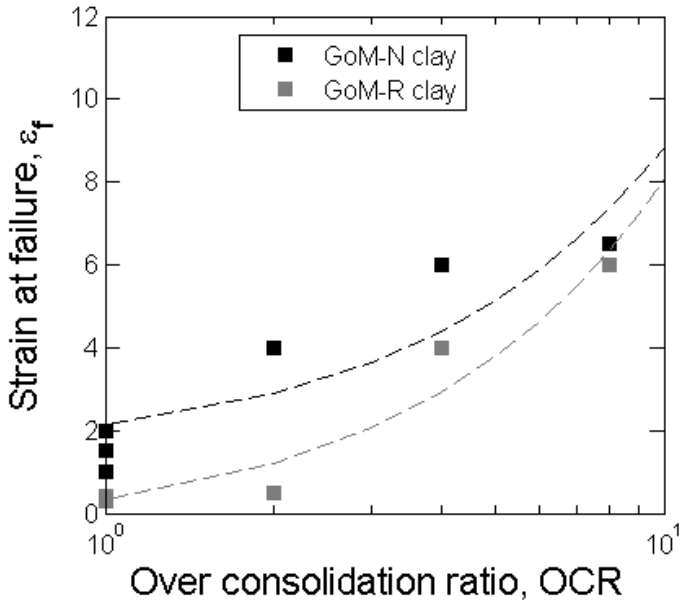

Figure 3.19: Axial strain at failure as function of OCR for GoM clay.

is constant for the GoM-N samples. Also obvious from the figures is that the normalized modulus for the NC samples is almost the same and it increases as the OCR increases for both GoM -N and -R. Similar behavior has been observed by Abdulhadi et al. (2012) and Santagata et al. (2005) after testing Boston Blue clay.

3.4.1.2 Kentucky Special kaolin (KS)

Figures 3.22 and 3.23 illustrate the undrained triaxial compression behavior of KS kaolin (OCR 1 to 8) sheared at a rate of 5%/hr. The figures show that NC KS samples develop very high pore pressures with increase in axial strain causing the stress path to decrease significantly along the x-axis. Increasing OCR causes a decrease in the peak value of strength normalized by the maximum effective stress (σ'_v) and a decrease in the amount of excess pore pressure generated. At larger strains, the effective stress paths

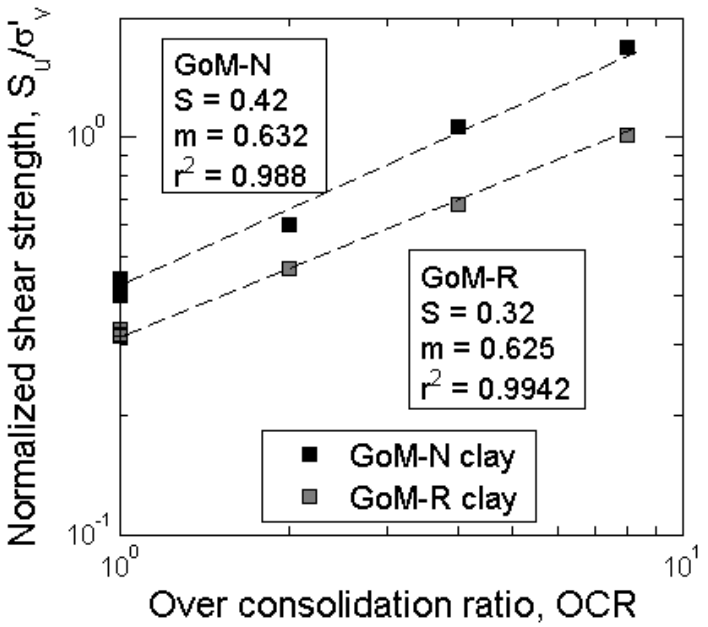

Figure 3.20: Undrained strength ratio as a function of OCR for GoM clay.

approach a common failure envelope with a slope of 24.8^o.

Figure 3.24 summarizes the observations of the axial strain needed to mobilize peak shear stress (ϵ_f) in each of the triaxial tests on Kentucky Special kaolin. Similar to the GoM samples, as the OCR increases from 1 to 8 there is a significant rise in ϵ_f from 1% to 4%.

Figure 3.25 shows the normalized undrained strength ratios (s_u/σ'_v) as a function of OCR for all the KS tests, together with the derived SHANSEP parameters of S and m. As seen in the figure, parameter S is equal to 0.30 and exponent, m is 0.85 and compares well with the values in the literature for kaolin (Ho, 1985; Atkinson et al., 1987).

Figure 3.26 shows the normalized undrained secant modulus, i.e., Young's modulus over maximum vertical stress ratio (E_u/σ'_{vmax}), versus axial strain, (ϵ_a) on a log log plot for KS samples. Similar to GoM samples, the data shows that all samples exhibit nonlinearity

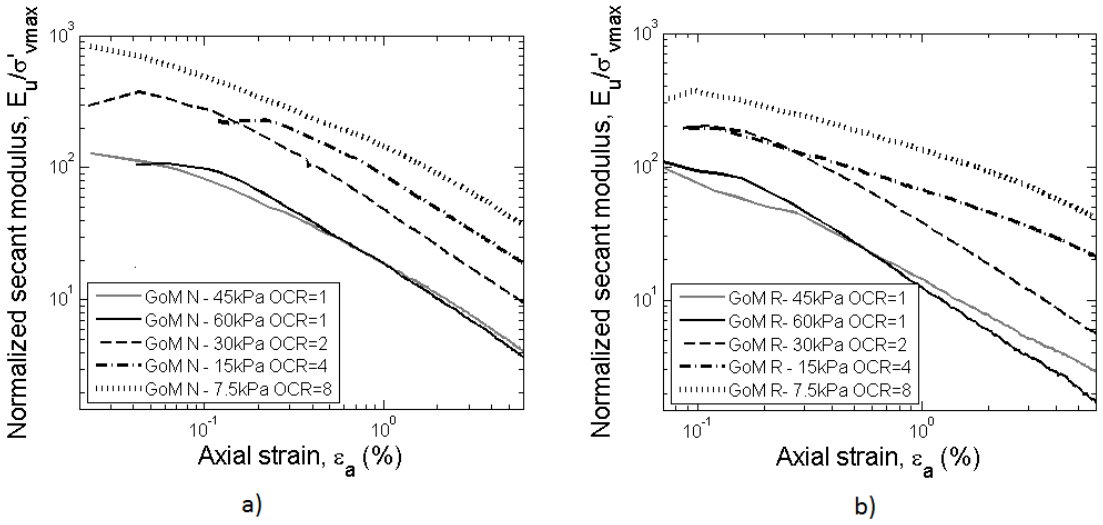

Figure 3.21: Normalized undrained secant modulus versus axial strain for (a) GoM-N clay, (b) GoM-R clay.

at small strains. The normalized Young's modulus is similar for the NC samples and increases with increase in OCR.

3.4.1.3 Red Art clay (RA)

Figures 3.27 and 3.28 illustrate the undrained triaxial compression behavior of RA clay (OCR 1 to 8) sheared at a rate of 5%/hr. As observed in the figure, RA clay appears to exhibit strain hardening response. Since there is no well defined peak "failure" for RA clay is considered to be the value of shear stress when the slope of the stress-strain curve changes. The yield point here is determined by the intersection of the two straight lines that best fit the experimental curve at the beginning and at the end of the curve (Graham et al., 1982).

The figures show that NC RA samples yield at relative small axial strains (0.25%). The combination of the strain harding behavior and the plateauing of the excess pore pressures of the NC samples causes the effective stress path to decrease along the x-axis initially

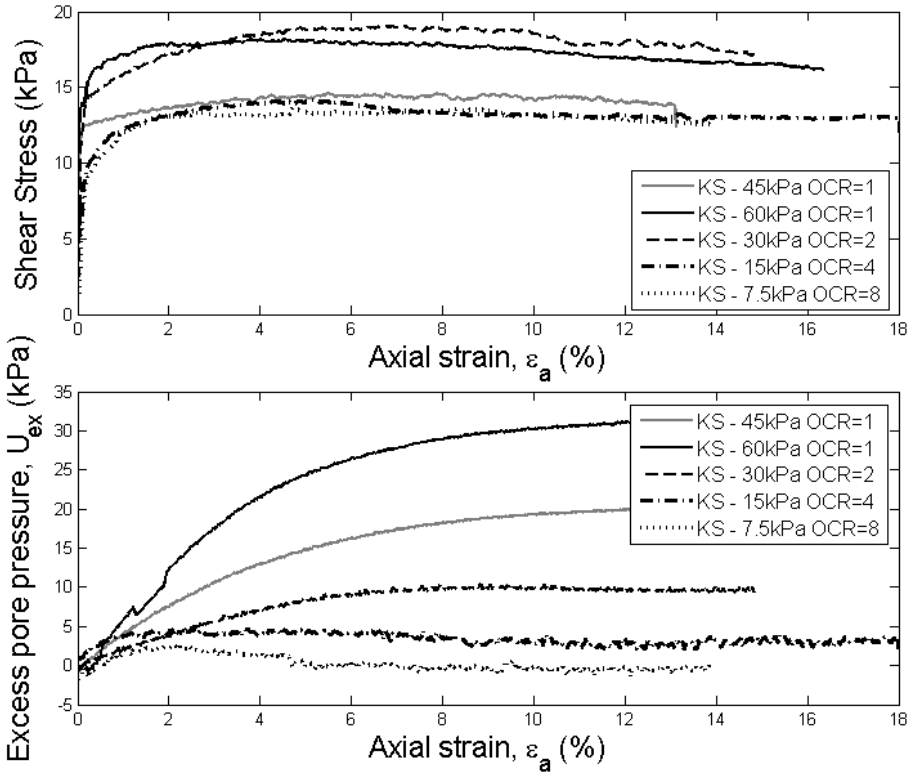

Figure 3.22: Stress strain behavior and excess pore pressure for KS kaolin.

and then exhibit silty behavior by dilating (Figure 3.28). OC RA samples show a gradual increase in shear stress after the initial failure, also characteristic of silty clays. At larger strains, the effective stress paths approach a common failure envelope with slope of 25.7^o.

Figures 3.29 and 3.30 illustrate the undrained triaxial compression behavior of Red Art clay (OCR 1 to 8) samples prepared using the clay extruder, RA(E) sheared at a rate of 5%/hr. These samples behave similarly to the samples consolidated outside the triaxial cell. However, the extruded clay samples are prepared at a water content below the liquid limit and mixed in a chamber under vacuum. This process does not allow to establish a clear stress history correlated to the initial water content of the specimens. The figures show that NC RA(E) samples yielded at very small axial strains (0.15%). These samples

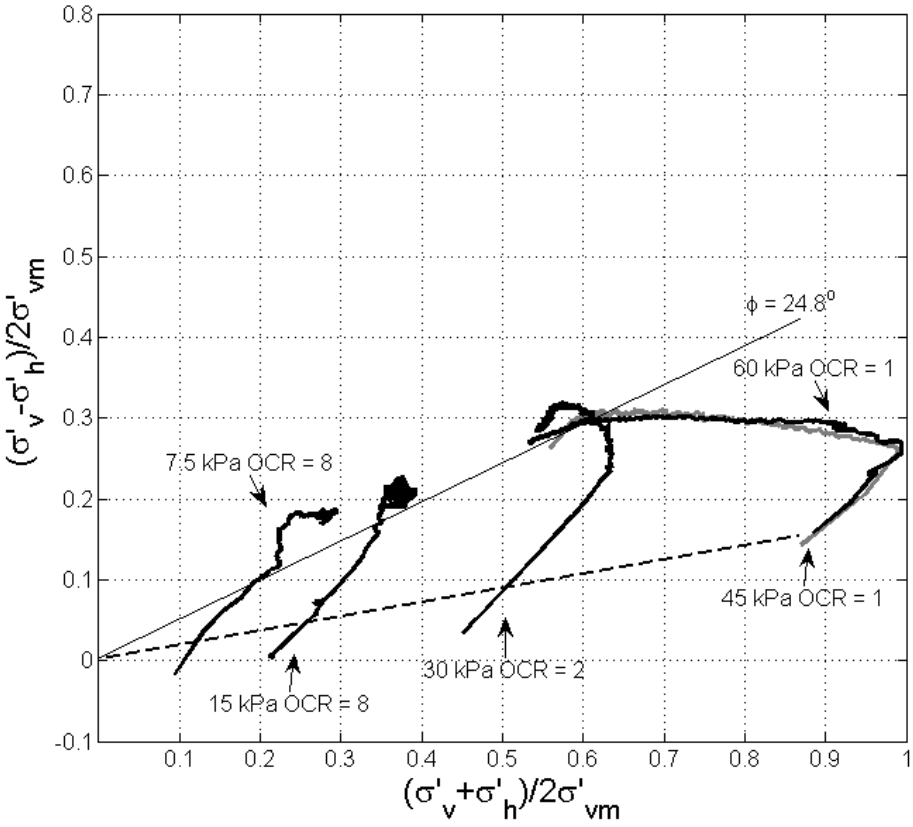

Figure 3.23: Effective stress paths for KS kaolin.

also exhibit silty behavior in the stress paths and stress-strain plots. The effective stress failure envelope for the RA(E) clay is at an angle of 26.5^o.

Figure 3.31 summarizes the observations of the axial strain needed to mobilize "failure" shear stress (ϵ_f) in each of the triaxial tests on Red Art clay. As the OCR increases from 1 to 8, there is a significant rise in ϵ_f from 0.25% to 2.5% for RA clay and from 0.1% to 0.5% for RA-E clay. Also observed, is that the failure strains for the extruded samples much lower than that of the split mold consolidated samples. It should be noted that clear failure planes were observed in all samples of RA(E) clay while the mode of failure for the other samples was bulging. Due to the nature of sample preparation of the RA(E) samples,

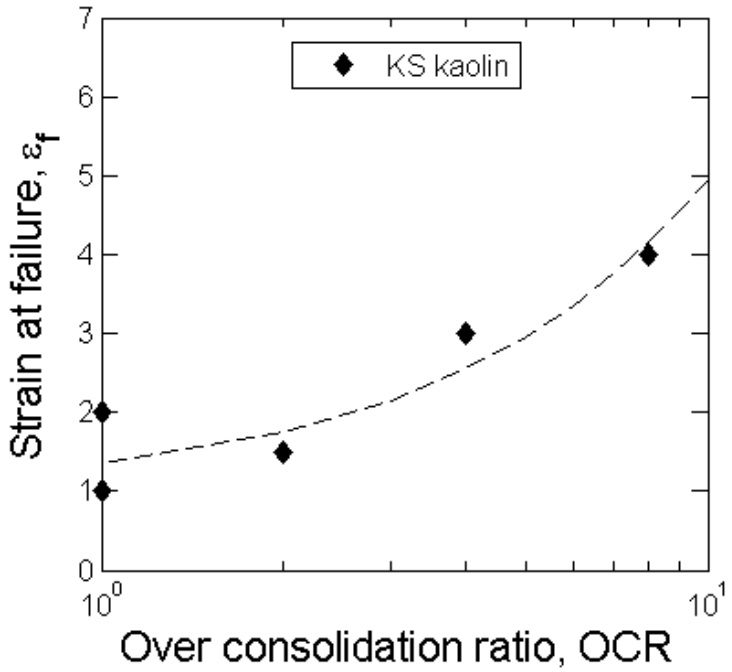

Figure 3.24: Axial strain at failure as function of OCR for KS kaolin.

the "pugging" process might induce the fabric to be more prone to the formation of slip surfaces. This would explain the lower values of ϵ_f for the RA(E) samples as compared to RA samples.

Figure 3.32 shows the normalized undrained strength ratios (s_u/σ'_v) as a function of OCR for all the RA tests, together with the derived SHANSEP parameters ($(s_u/\sigma_v)_{oc} = S(OCR)^m$) of S equal to 0.31 and exponent, m equal to 0.75. Although the fabric of the "pugged" clay samples might not be uniform and idealized like the remolded samples, the SHANSEP results indicate that they also show normalized stress behavior and can be used in data analysis with some degree of confidence.

Figures 3.33a) and 3.33b) show the normalized undrained secant modulus, i.e., Young's modulus-vertical stress ratio (E_u/σ'_{vmax}), versus axial strain, (ϵ_a) on a log-log plot for RA

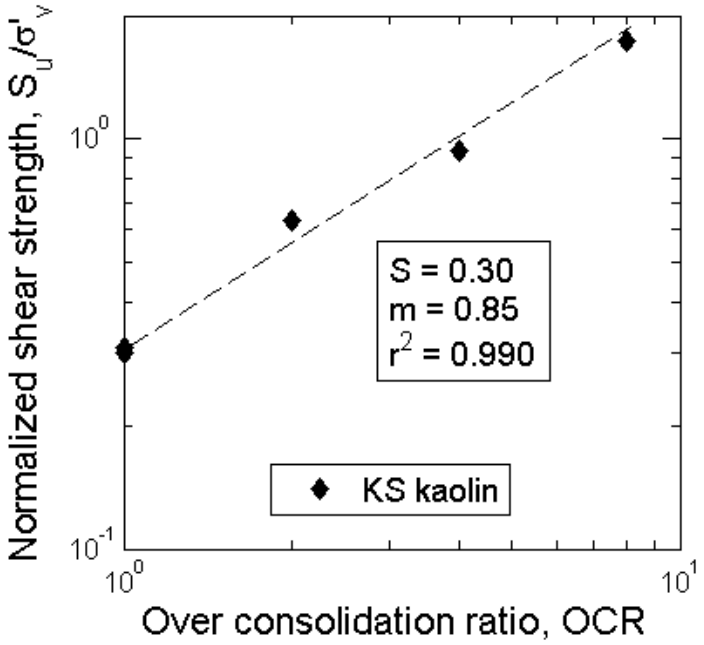

Figure 3.25: Undrained strength ratio as a function of OCR for KS kaolin.

and RA(E) samples respectively. The data shows that the normalized Young's modulus for the NC clays are similar for both RA and RA(E) samples and like the previous clays an increase in OCR leads to an increased value of modulus.

3.4.2 Sand

As mentioned before, both round (Ottawa) and angular (Mystic White) sands were tested at a range of low confining pressures. The sands were tested at different relative densities, dense (>60%) and loose (<30%). A list of the tests with information on confining stress, initial void ratios and peak friction angle is given in Table 3.7.

Table 3.7: Summary of tests on sands

Sand	Confining stress (kPa)	Initial void ratio e_o	Relative density $\%$)	Peak friction angle ϕ
Ottawa Sand	60	0.64	60.2	37.1
	30	0.53	90.0	39.5
	15	0.53	90.0	40.3
	60	0.80	0	27.5
	30	0.71	30.0	29.5
	15	0.80	0	33.3
	5	0.73	23.3	38.6
Mystic White Sand	60	0.84	85.3	40
	30	0.89	69.9	44.2
	15	0.84	87.3	46.2
	60	1.01	30.0	34.6
	30	1.02	26.6	36.5
	15	1.01	30.0	33.3

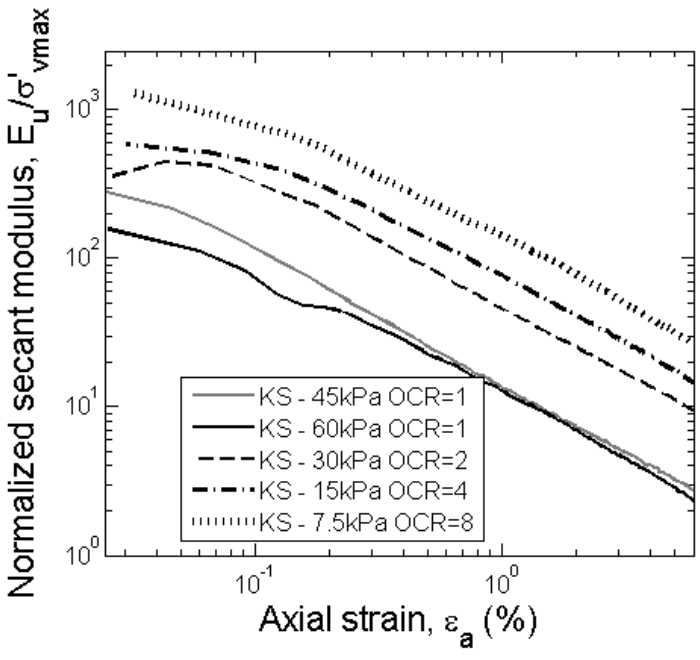

Figure 3.26: Normalized undrained secant modulus versus axial strain for KS kaolin.

3.4.2.1 Round sand

Figure 3.34 shows the shear stress (τ) vs axial strain (ϵ_a) and volumetric strain (ϵ_v) vs axial strain (ϵ_a) plots for the dense Ottawa sand tests at various confining pressures. The samples behave as expected with dilation occurring with increase in axial strain and the shear strength increasing with higher confining pressure. The extent of dilation increases with decrease in confining pressure. These results are in agreement with Dakoulas and Yuanhui (1992) tests on fine Ottawa sand.

Figure 3.35 shows the shear stress (τ) vs axial strain (ϵ_a) plots for loose Ottawa sand tests at various confining pressures. Similar to the dense samples the shear strength increases with increase in confining pressure. Volumetric data was unavailable for this set of sand tests.

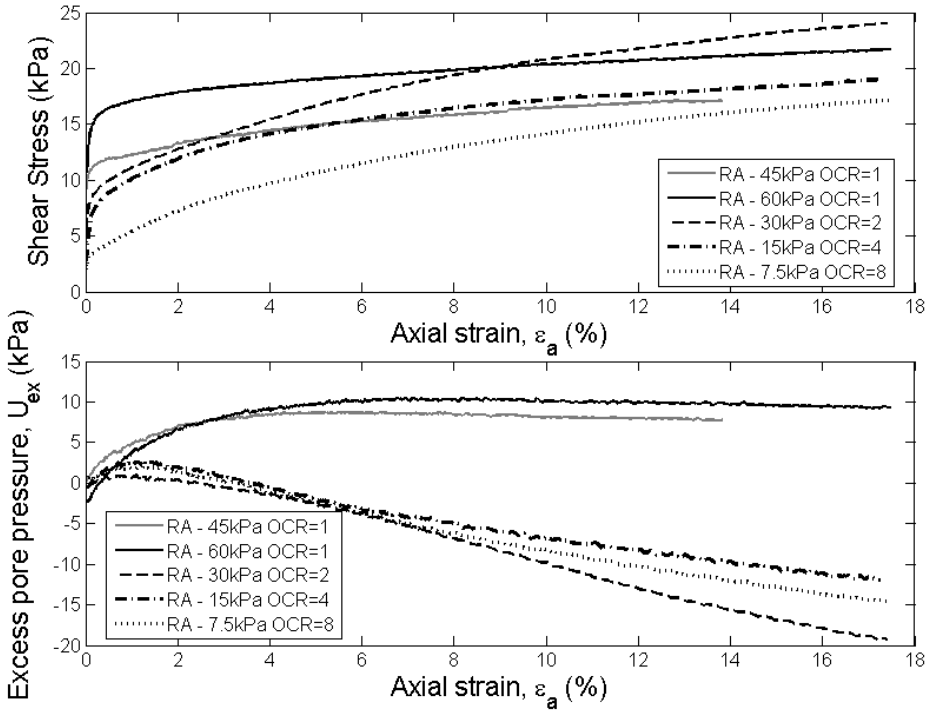

Figure 3.27: Stress strain behavior and excess pore pressure for RA clay.

3.4.2.2 Angular sand

Figure 3.36 shows the shear stress (τ) vs axial strain (ϵ_a) and volumetric strain (ϵ_v) vs axial strain (ϵ_a) plots for dense angular Mystic White sand tests at various confining pressures. Similar to the round dense samples the peak shear strength increases with increase in confining pressure and all the samples show increase in dilation with decrease in confining pressure.

Figure 3.37 shows the shear stress (τ) vs axial strain (ϵ_a) and volumetric strain (ϵ_v) vs axial strain (ϵ_a) plots for loose Mystic White sand tests at various confining pressures. Although these samples were considered loose, they were tested at very low confining pressures, leading to dilation during drained shear (Lee and Seed, 1967). The extent of

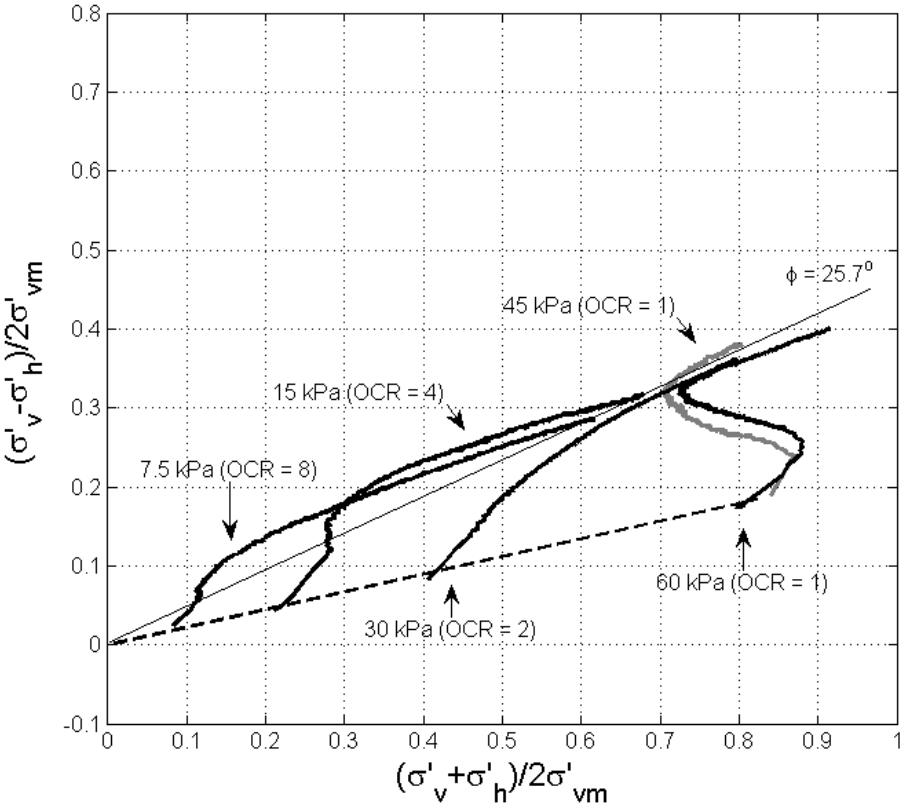

Figure 3.28: Effective stress paths for RA clay.

dilation increases with decrease in confining pressure as expected.

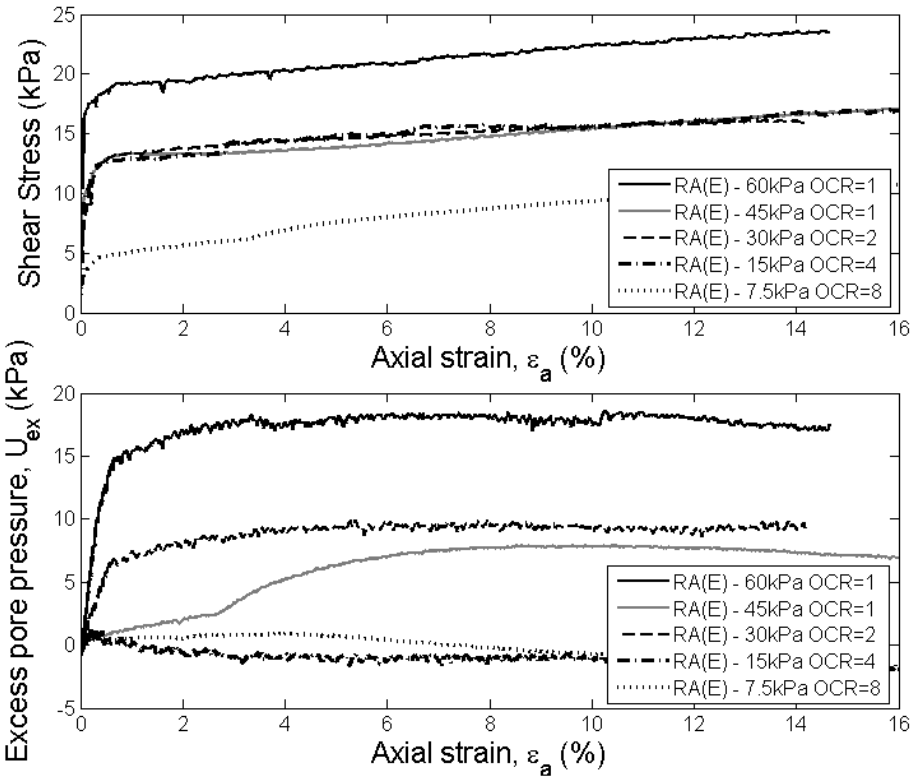

Figure 3.29: Stress strain behavior and excess pore pressure for RA(E) clay.

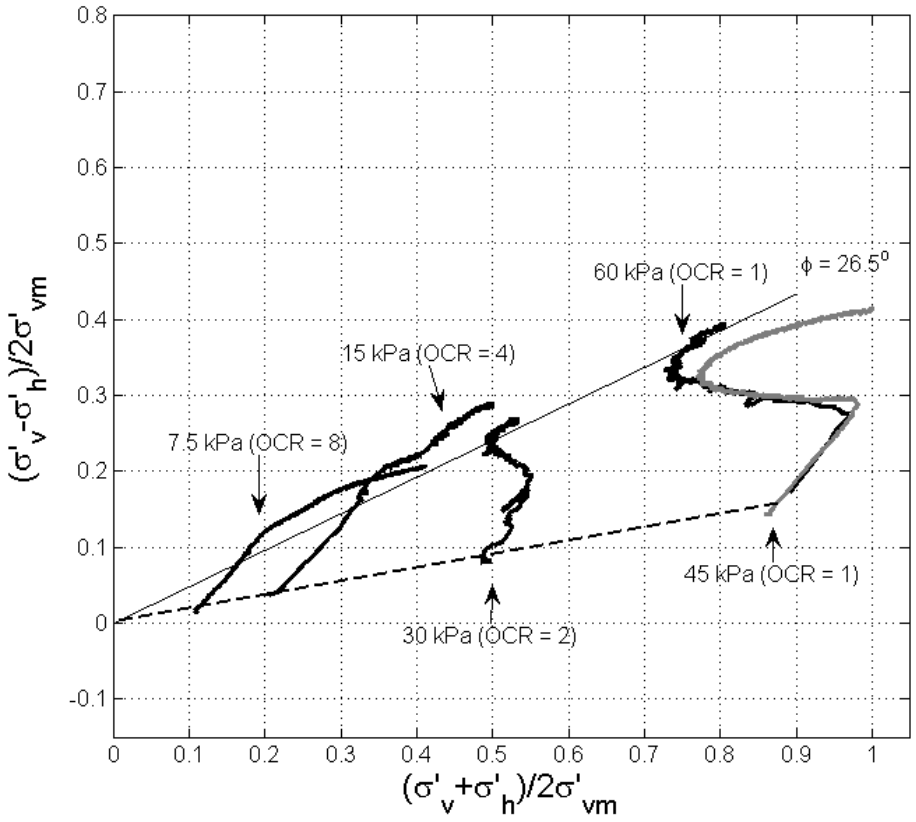

Figure 3.30: Effective stress paths for RA(E) clay.

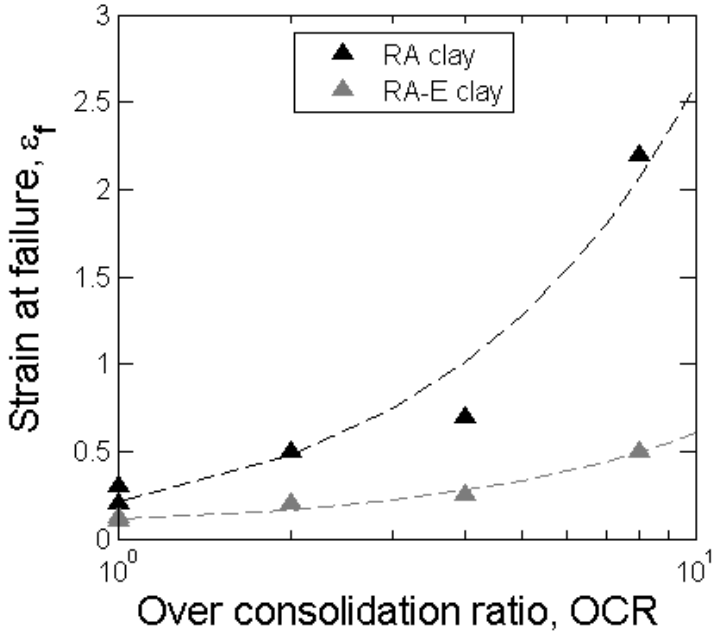

Figure 3.31: Axial strain at failure as function of OCR for RA clay.

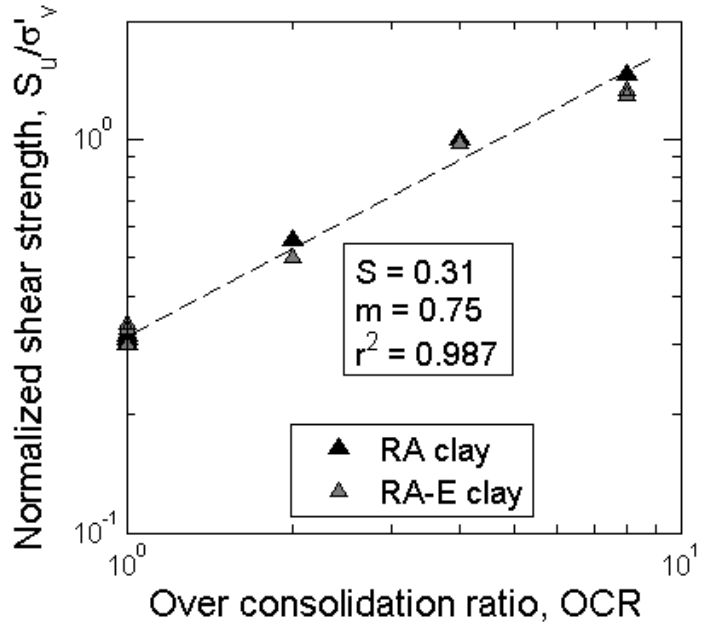

Figure 3.32: Undrained strength ratio as a function of OCR for RA clay.

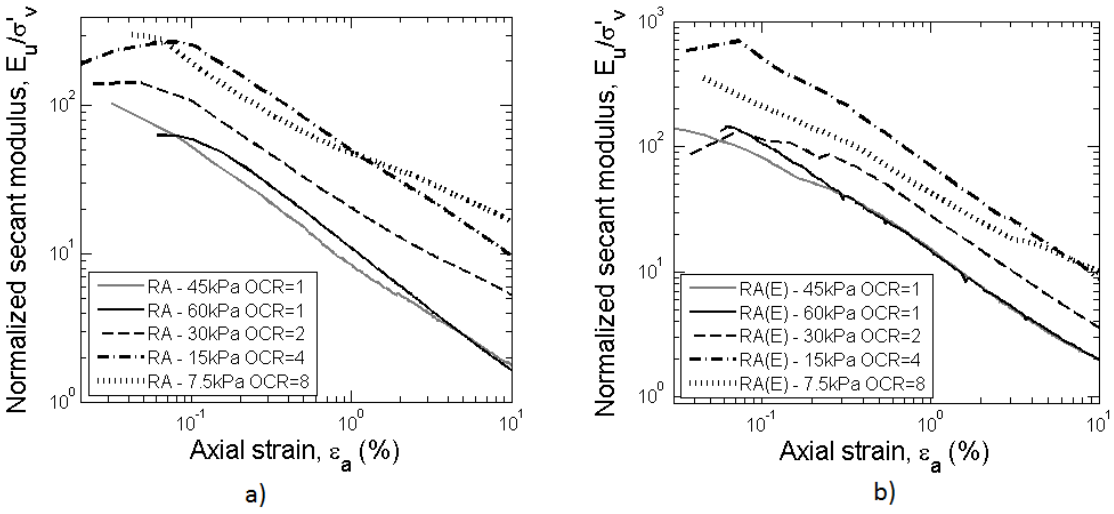

Figure 3.33: Normalized undrained secant modulus versus axial strain for RA clay.

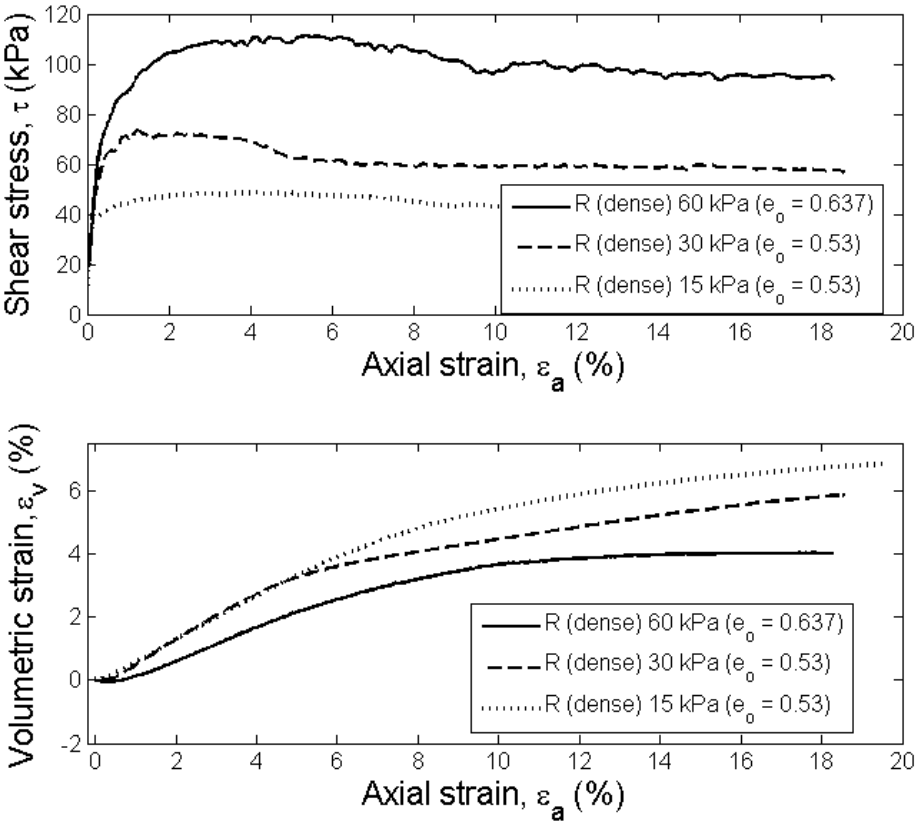

Figure 3.34: Triaxial tests on dense Ottawa sand.

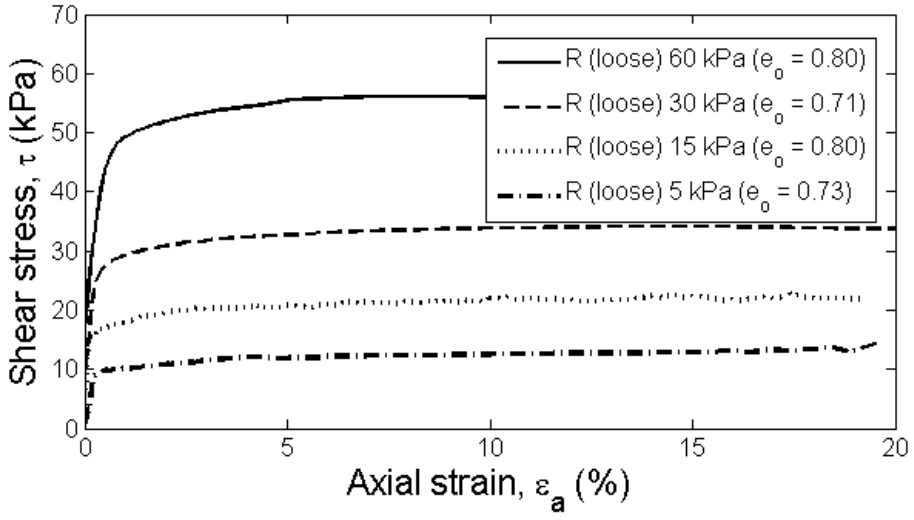

Figure 3.35: Triaxial tests on loose Ottawa sand.

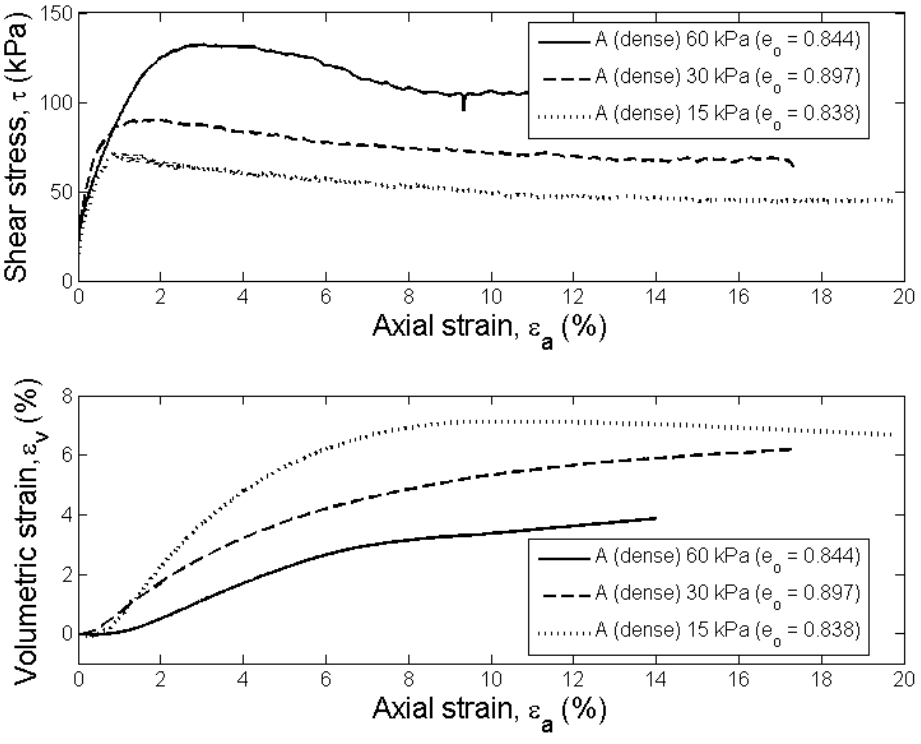

Figure 3.36: Triaxial tests on dense Mystic White sand.

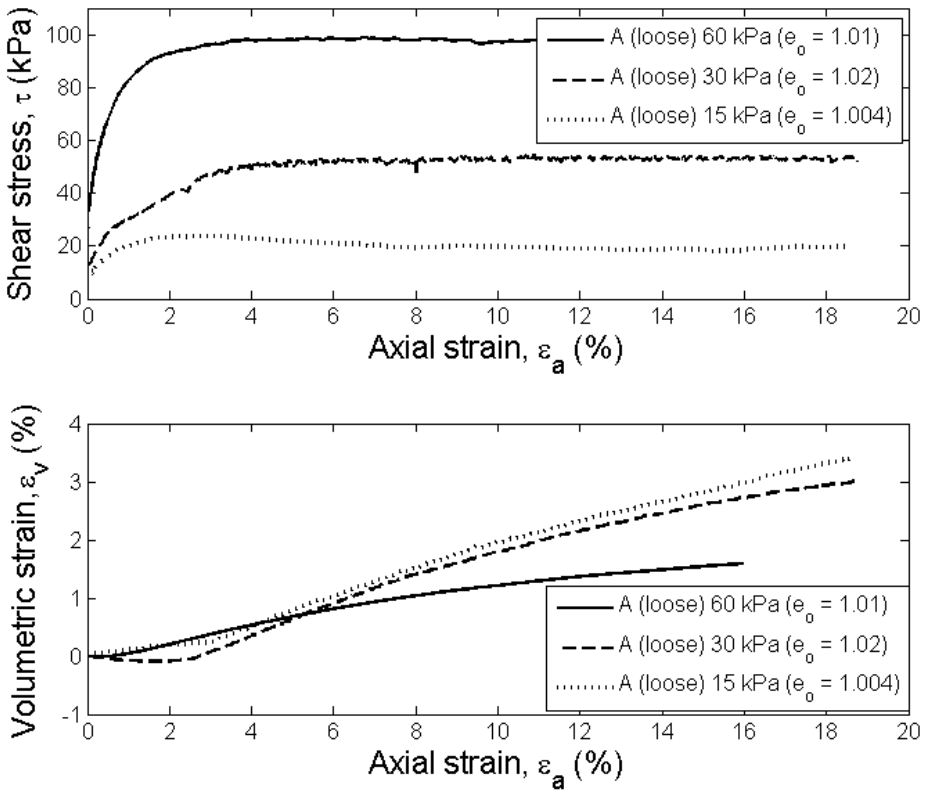

Figure 3.37: Triaxial tests on loose Mystic White sand.

4. STIFFNESS FROM GEOPHYSICAL METHODS

This section presents the stiffness ($\mathrm{G_o}$) results of all the samples and the geophysical correlations developed using the data.

4.1 Clay

The geophysical data was correlated with the mean stress, void ratio, OCR and compared with published research. A framework for correlating the geophysical data with measured strength values is also developed.

The density for each sample was calculated based on the void ratio of the sample just before shearing. The mean stress for each sample is computed as the average of the principal stresses.

4.1.1 Geophysical characteristics

4.1.1.1 Gulf of Mexico clay (GoM)

Figure 4.1 shows the variation of the shear modulus (G) and bulk modulus (K) with respect to axial strain (ϵ_a) during the undrained shear phase for each sample of GoM clay. The shear modulus values almost overlap for the NC samples tested at the same confining pressure, while the values decrease with increasing OCR. The rate of decrease of shear modulus at larger strains is almost constant in all the samples. The bulk modulus remains relatively constant during the entire shearing process.

Figure 4.2 shows the variation of the shear modulus (G) and bulk modulus (K) with respect to axial strain (ϵ_a) during the undrained shear phase for each sample of GoM-R clay. The shear modulus values decrease with increasing OCR and the bulk modulus remains relatively constant during the entire shearing process.

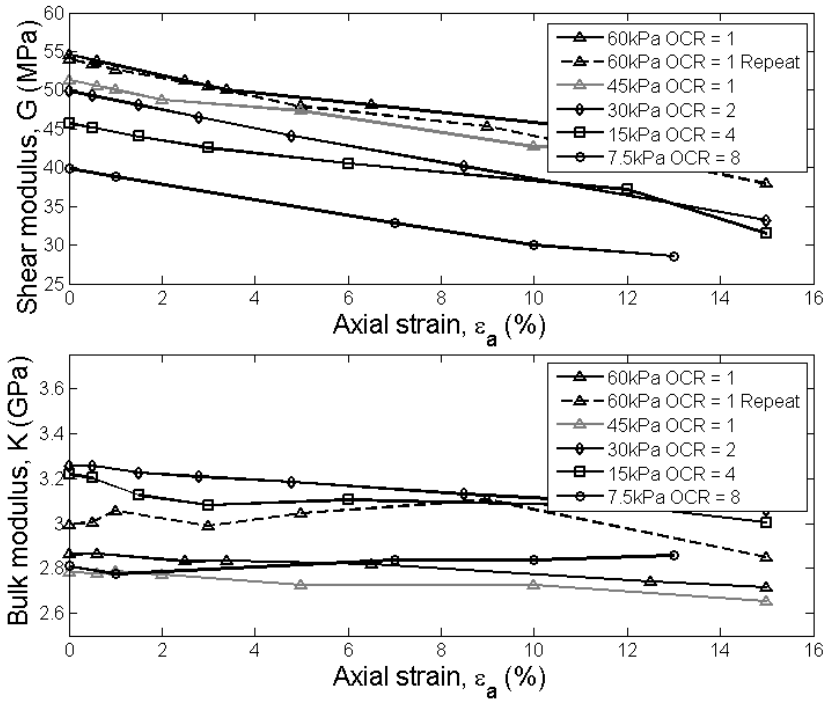

Figure 4.1: Shear modulus and bulk modulus for natural GoM clay.

4.1.1.2 Kentucky Special kaolin (KS)

Figure 4.3 shows the variation of the shear modulus (G) and bulk modulus (K) with respect to axial strain (ϵ_a) during the undrained shear phase for each sample of KS kaolin. The shear modulus values decrease with increasing OCR and also decrease with decrease in confining pressure for the NC samples. The bulk modulus remains relatively constant during the entire shearing process.

4.1.1.3 Red Art clay (RA)

Figure 4.4 shows the variation of the shear modulus (G) and bulk modulus (K) with respect to axial strain during the undrained shear phase for each sample of RA. This clay also follows a similar trend as the previous clays, the moduli values decrease with increase

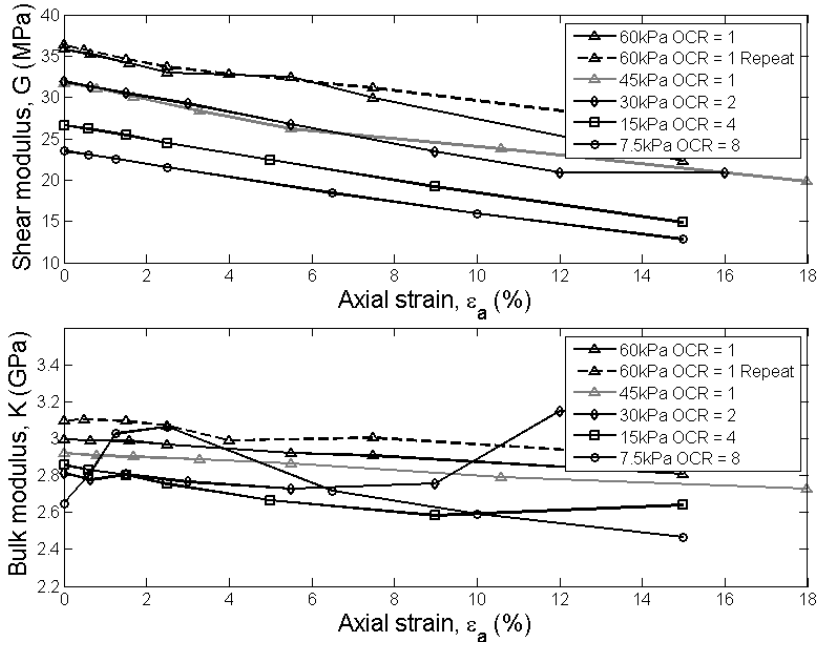

Figure 4.2: Shear modulus and bulk modulus for reconstituted GoM clay.

in shear strain. There is a decrease in shear modulus values with increasing OCR, this decrease is however not very prominent in these samples as compared to the previous clays. The bulk modulus remains relatively constant during the entire shearing process.

Figure 4.5 shows the variation of the shear modulus (G) and bulk modulus (K) with respect to axial strain during the undrained shear phase for each sample of RA(E) clay. Similar to the previous clays, the moduli values decrease with increase in shear strain. There is a decrease in shear modulus values with increasing OCR, this decrease is also not very prominent in RA(E) samples as compared to the previous clays. The bulk modulus remains relatively constant during the entire shearing process.

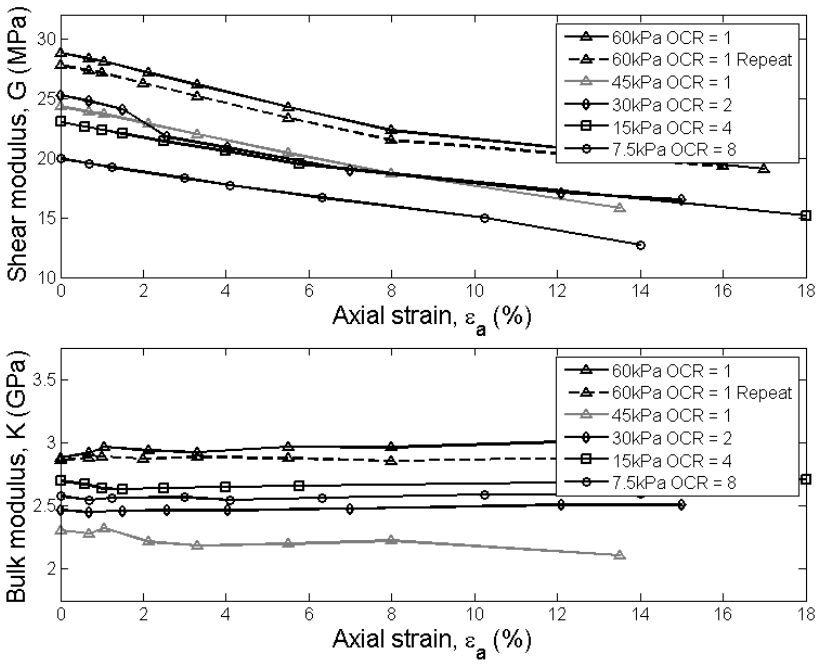

Figure 4.3: Shear modulus and bulk modulus for KS kaolin.

4.1.1.4 Shear modulus with axial strain

Figure 4.6 compares the shear modulus values at large axial strains for GoM-N and GoM-R. The intact samples tested at the same confining pressures are found to have higher values of shear modulus as compared to the reconstituted samples. This is presumably due to the higher initial void ratio of the reconstituted samples influencing the magnitude of shear modulus (Jamiolkowski et al., 1994; Shibuya et al., 1997). However on observing the slopes of the lines, it is found that the rate of decrease of shear modulus is the same for -N and -R clays, independent of void ratio, confining pressure and OCR.

Figure 4.7 (a, b and c) illustrates the variation in the range of shear modulus normalized with respect to initial shear modulus, G/G_o versus axial strain (ϵ_a) for all the clays. With the same scaling on the axis, the trend of decreasing shear modulus with axial strain is

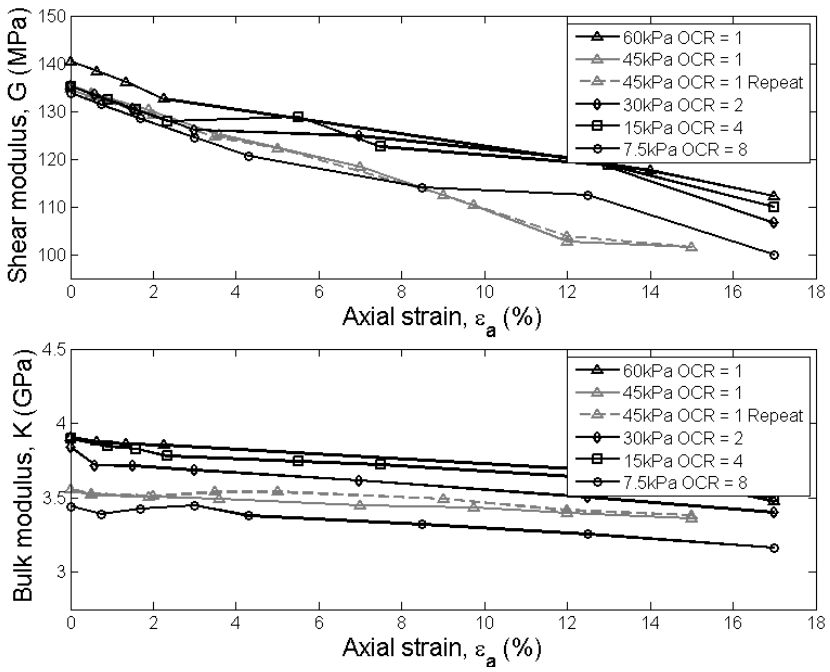

Figure 4.4: Shear modulus and bulk modulus for RA clay.

easily comparable between the clays. It is observed that at relatively smaller strains (¡2%) the rate of decrease of normalized shear modulus is almost the same and varies between clays at higher strains. Also seen in the figure, the rate of decrease of shear modulus is highest for GoM clays, followed by KS and RA respectively. This is specially significant for large deformation failures such as sub-sea slope failures.

4.1.2 Correlations with mean stress and void ratio

Figure 4.8 shows the mean effective stress (σ'_m) and initial shear modulus ($\mathrm{G_o}$) for all the clay samples tested in this project. Although not very apparent in this figure due to the large scale of the y axis, the NC samples have decreasing shear modulus with decrease in σ'_m.

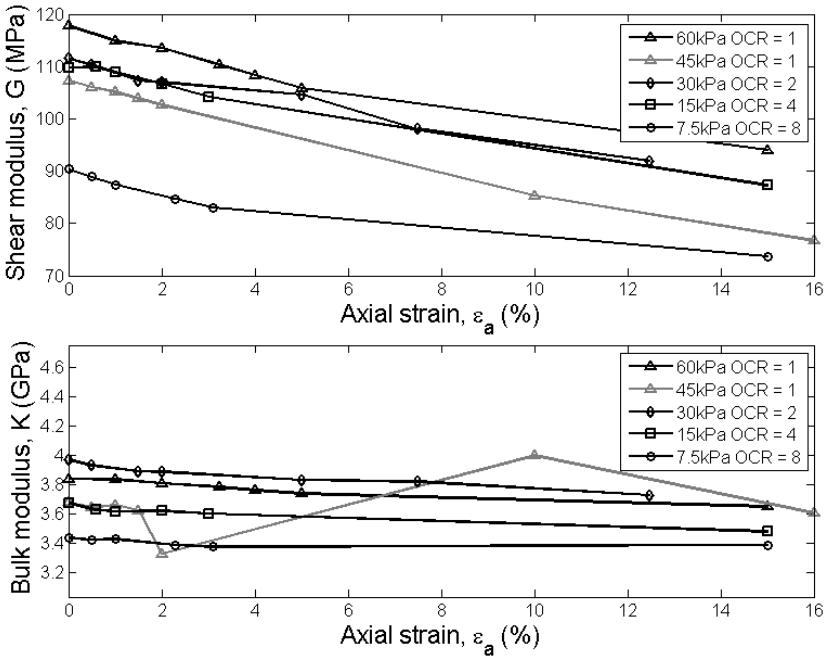

Figure 4.5: Shear modulus and bulk modulus for RA(E) clay.

Viggiani and Atkinson (1995b) carried out bender element triaxial compression tests on reconstituted samples of Specswhite kaolin and undisturbed and reconstituted samples of London clay by varying the over consolidation ratio and mean stress. Due to the type of tests carried out with a similar experimental setup it was easy to compare the data of Specswhite kaolin with the data of KS kaolin obtained from this project. The tests on London clay was helpful in interpreting the geophysical data obtained by tests on samples of GoM clay.

Figure 4.9 shows a log-log plot of normalized mean effective stress (σ'_m/p_r) and normalized shear modulus (G_o/p_r) both normalized with respect to a reference pressure, p_r, for KS samples along with the results of Specswhite kaolin (Viggiani and Atkinson, 1995b). The reference pressure (p_r) was taken as 1 kPa to be consistent with the paper. The NC kaolin data points fall close to a perfectly straight line given by Equation 4.1 after

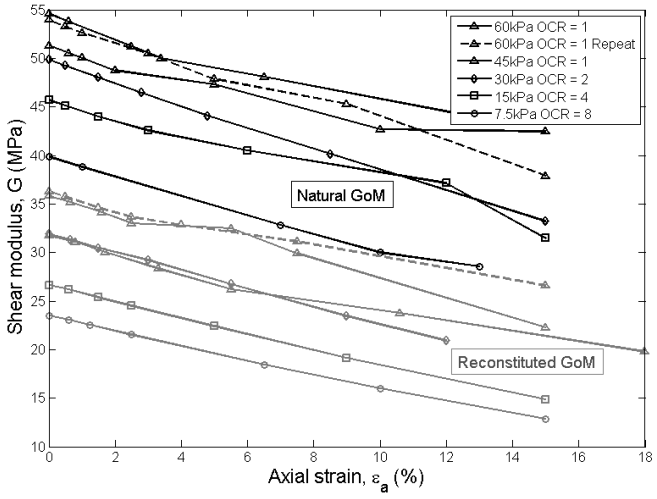

Figure 4.6: Shear modulus for all samples of Gulf of Mexico clay.

Viggiani and Atkinson (1995b):

$$(G_o/p_r) = A(\sigma'_m/p_r)^n \tag{4.1}$$

or

$$\log(G_o/p_r) = \log(A) + n\log(\sigma'_m/p_r) \tag{4.2}$$

Where A and n are empirical constants varying with soil type. The values of A and n are given in Table 4.1 comparing the data of Specswhite kaolin to Kentucky Special kaolin. The values of A and n depend on the value taken for the reference pressure. Jovicic and Coop (1998) also tested Specswhite Kaolin with similar results.

Viggiani and Atkinson (1995b) also studied the effect of OCR on reconstituted Specswhite kaolin. On extending Equation 4.1 to include the influence of over consolidation, we obtain Equation 4.3:

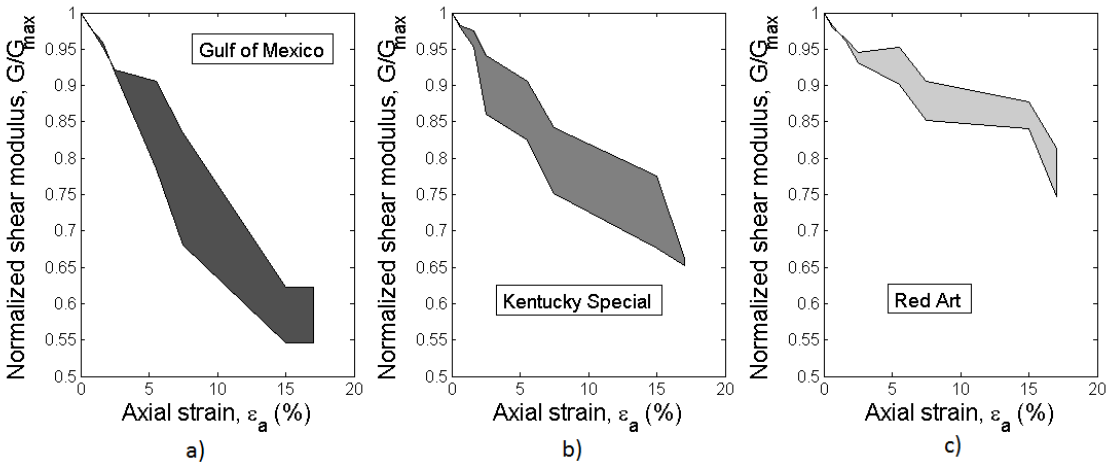

Figure 4.7: Range of normalized shear modulus for all clays.

$$G_o/p_r = A(\sigma'_m/p_r)^n OCR^m \tag{4.3}$$

The exponent for OCR, m, is easily determined by plotting the variation of normalized $\mathrm{G_o}$, $((G_o/p_r)/A(\sigma'_m/p_r)^n)$ with OCR for all the clay samples, normalized with respect to their corresponding values of A and n, as shown in Figure 4.10. The slopes of the straight lines represent the exponent m and its value for all the clays are also given in Table 4.1. This trend of $\mathrm{G_o}$ increasing with increasing OCR is similar to that reported by Houlsby and Wroth (1991) (Refer Equation 2.6 in Section 2.1.4). The figure also illustrates that OCR affects the shear modulus for different clay types with varying degrees. KS kaolin is more affected by OCR whereas RA and RA(E) samples are barely influenced by mechanical over consolidation.

Figure 4.11 shows a log-log plot of normalized mean effective stress (σ'_m/p_r) and normalized shear modulus (G_o/p_r) for GoM-N and GoM-R samples along with the results of London clay (Viggiani and Atkinson, 1995b). General trend lines are drawn for the NC

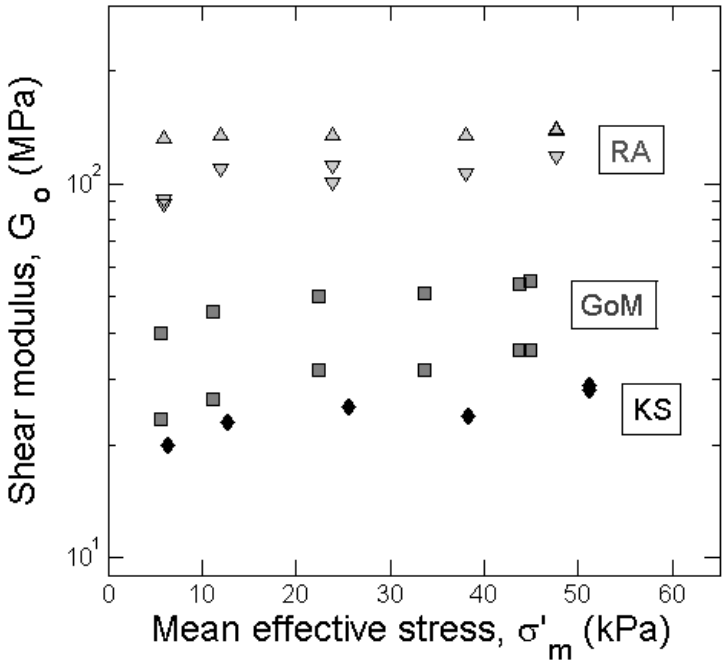

Figure 4.8: Mean effective stress versus shear modulus for all clay samples.

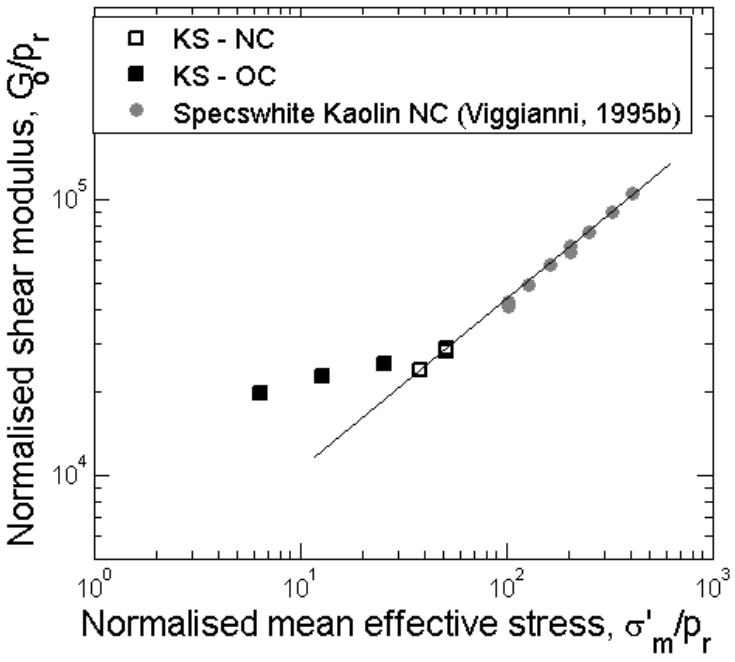

Figure 4.9: Normalized mean stress versus normalized shear modulus for KS kaolin plotted along with data for Specswhite kaolin after Viggiani and Atkinson (1995b).

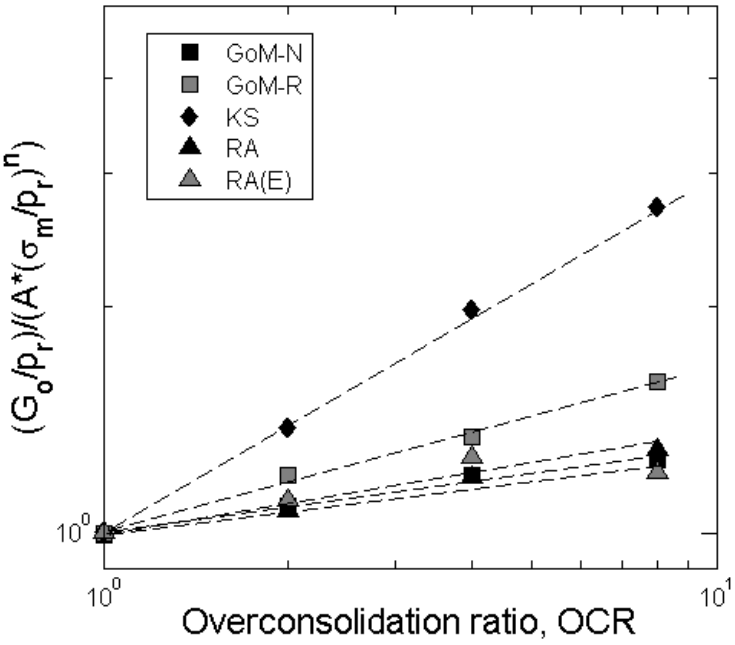

Figure 4.10: Influence of OCR on G_o for all clays.

samples of Gulf of Mexico. As expected the G_o values for the over consolidated samples are higher than the normally consolidated samples for both GoM -N and -R clays. The coefficients A and n for GoM are given in Table 4.1. Similar to London clay, at the same mean effective stress the values of shear modulus for natural clay are higher than the values of shear modulus for reconstituted clay. Viggiani and Atkinson (1995b) found that the differing G_o values between natural and remolded clays was due to the current state of the sample dependent on both current stress and OCR, and seemingly independent of structure and fabric. However Jamiolkowski et al. (1994) and Shibuya et al. (1997) stated that different void ratios and differing structure contributes to difference in magnitude of shear modulus for samples tested at the same mean effective stress. The influence of void ratio is studied in Section 4.1.3. The dependency on OCR is shown in Figure 4.10 and the exponent m is presented in Table 4.1. It is found to be slightly higher for GoM-R

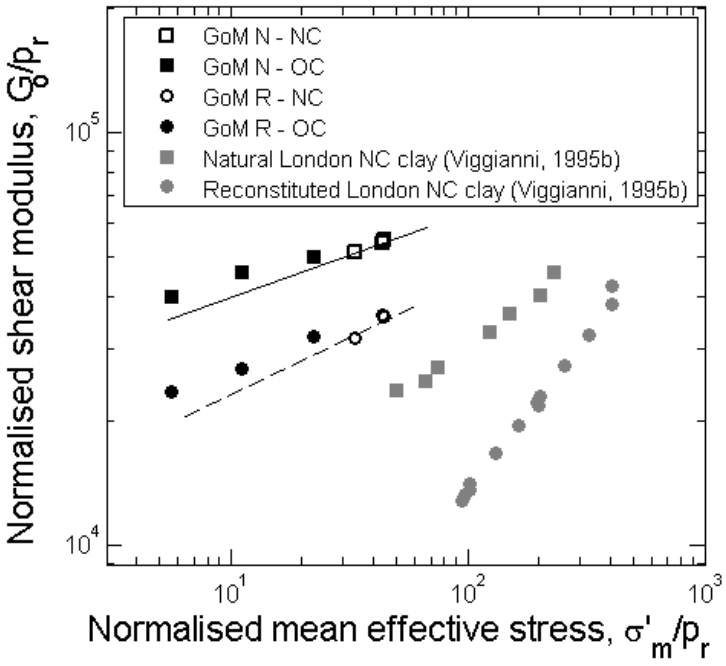

Figure 4.11: Normalized mean effective stress versus normalized shear modulus for GoM clay plotted along with London clay after Viggiani and Atkinson (1995b).

compared to GoM-N.

Figure 4.12 shows a log-log plot of normalized mean effective stress (σ'_m/p_r) and normalized shear modulus (G_o/p_r) for all the samples of RA and RA(E) clay. Trend lines are drawn for the NC samples and they have decreasing shear modulus with decreasing mean effective stress. As mentioned before, from Figure 4.12 it is seen that for RA samples the shear modulus is very negligibly influenced by mechanical over consolidation of the clay. All of these OC samples had the same pre-consolidation pressure of 60 kPa before they were rebounded to OCRs of 2, 4 and 8. The empirical constants A, n and m are given in Table 4.1.

Table 4.1: Comparing coefficients A, n and m values of all clays with Viggiani and Atkinson (1995b).

Clay	G_s	W (%)	A ($\sigma_r = 1\ kPa$)	n	m	Reference
Specswhite kaolin	2.6	-	2088	0.653	0.196	
Intact London clay	-	-	3000	0.5	-	Viggiani and Atkinson (1995b)
Reconstituted London clay	-	-	350	0.6	-	
KS	2.6	72-84	2177	0.657	0.45	
GoM-N	2.75	47-64	20274	0.3	0.043	
GoM-R	2.75	80-92	4988	0.51	0.3	this research
RA (split mold)	2.76	19-21	74890	0.16	0.21	
RA (pugged)	2.76	25-29	48630	0.22	-	

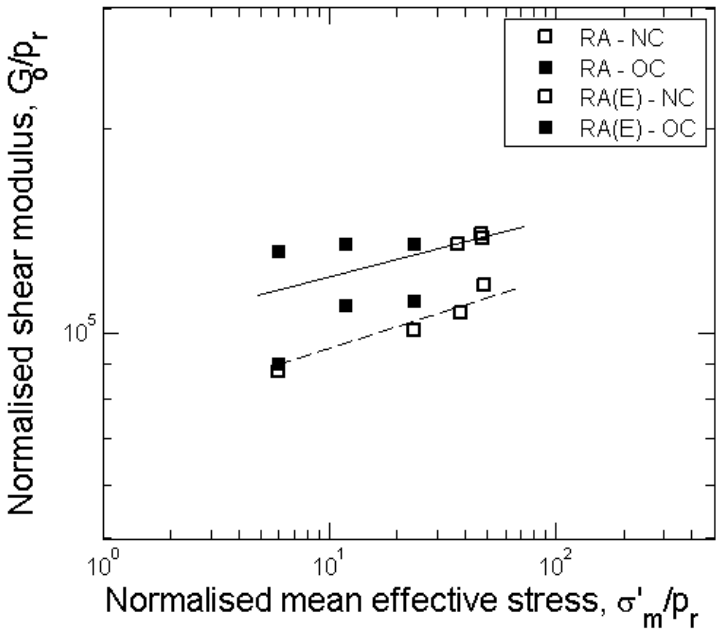

Figure 4.12: Normalized mean effective stress versus normalized shear modulus for Red Art silty clay.

4.1.3 Correlations with void ratio

A number of researchers (Hardin and Richart, 1963; Hardin and Black, 1968; Marcuson and Wahls, 1972; Jamiolkowski et al., 1991; Shibuya et al., 1997) have published research correlating void ratio with $\mathrm{G_o}$. Figure 4.13 shows a log-log plot of maximum shear modulus normalized by 101 kPa ($\sigma_{atm} = 1\ atm$) for all the clays tested in this research program along data for cohesive soils presented by Jamiolkowski et al. (1991). The dependence of void ratio on shear modulus is clearly shown, while it is impossible to observe an influence of OCR. The data presented by Jamiolkowski et al. (1991) was carried out through resonant column tests thus the magnitudes cannot be compared, however a similar trend is observed in the data with modulus decreasing with increase in void ratio.

Figure 4.14 illustrates the effect of void ratio on shear modulus by removing the influ-

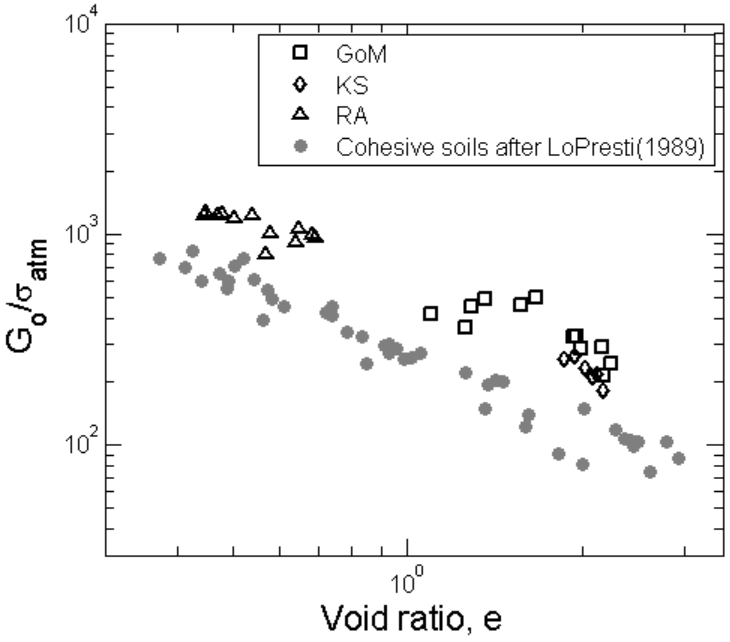

Figure 4.13: Normalized G_o plotted versus void ratio for all clays.

ence of mean effective stress by plotting $(G_o/p_r)/(\sigma'_m/p_r)^n$ versus void ratio (e), where p_r is the reference pressure equivalent to 1 kPa and the values of n are as mentioned in Table 4.1. The formulations by Jamiolkowski et al. (1991) and Hardin and Richart (1963) are also plotted, along with the best fit curve for this experimental data. The coefficient A is dependent on the value of the reference pressure.

Based on the plot it is found that void ratio plays a significant role in influencing stiffness and the function of void ratio that best represents the data is given by Equation 4.4

$$f(e) = 1/e^{2.4} \tag{4.4}$$

On combining the different influencing factors (σ'_m, OCR, and e), the empirical equation that best relates the shear modulus obtained through experimental testing in this re-

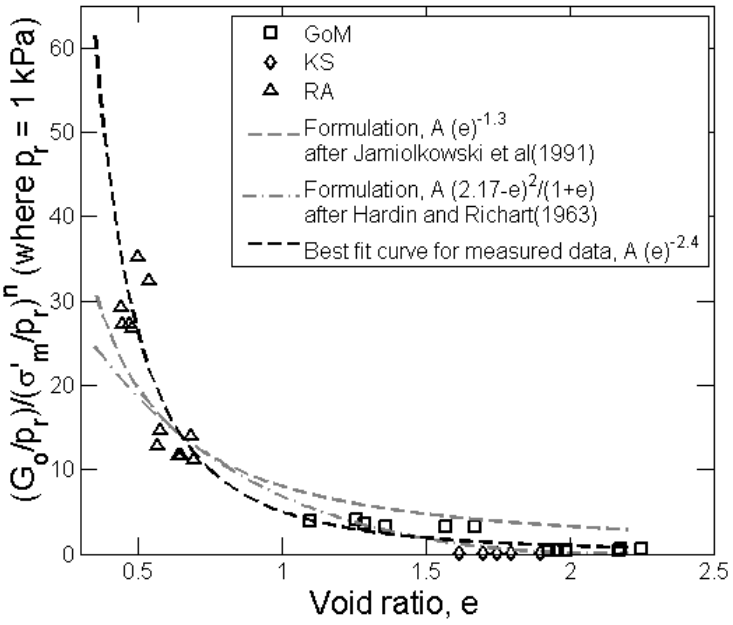

Figure 4.14: Influence of void ratio on the shear modulus of clays.

search program is given by equation 4.5.

$$G_o/p_r = Af(e)(\sigma'_m/p_r)^n OCR^m \tag{4.5}$$

4.1.4 Correlations with strength

The shear strength values (s_u) were obtained from each sample's stress strain curve during shearing as shown in Section 3.4. 'Failure' was considered to be the maximum value from each stress strain curve. In the case of tests where the peak shear stress is not defined clearly (eg. RA samples) failure was considered to be the value of shear stress when the slope of the stress-strain curve changes. Figure 4.15 shows the shear strength plotted against the initial shear modulus for all the samples tested in this project. The figure gives a sense of the range of $\mathrm{G_o}$ variation between the different clays. There is a general trend where the shear modulus increases with increase in normalized shear strength.

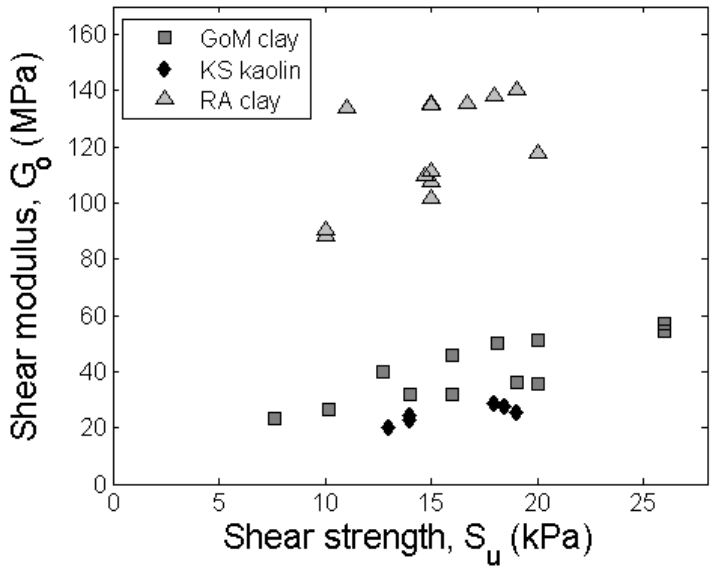

Figure 4.15: Shear strength versus shear modulus for all clays.

Similar to SHANSEP ($(S_u/\sigma'_v)_{OC} = (S_u/\sigma'_v)_{NC}OCR^m$), Houlsby and Wroth (1991) proposed an equation using shear modulus in place of shear strength based on the tests carried out by Webb (1967).

$$(G_o/\sigma'_v)_{OC} = (G_o/\sigma'_v)_{NC}OCR^k \tag{4.6}$$

Where G_o is the initial shear modulus, σ'_v is the current vertical effective stress and OCR is over consolidation ratio. Figure 4.16 presents the variation of initial shear modulus normalized by vertical effective stress (G_o/σ'_v) with OCR, along with values of the exponent, k from the Equation 4.6 for all three clays. Normalization of stiffness is highly convenient as it provides a measure of initial shear modulus with an estimate of σ'_v and OCR. Table 4.2 presents the values of $(G_o/\sigma'_v)_{nc}$ and the k for all clays. Values of the SHANSEP parameter, m is also included in Table 4.2 to compare m and k.

Another advantage of normalizing G_o is that it can easily be related to normalized

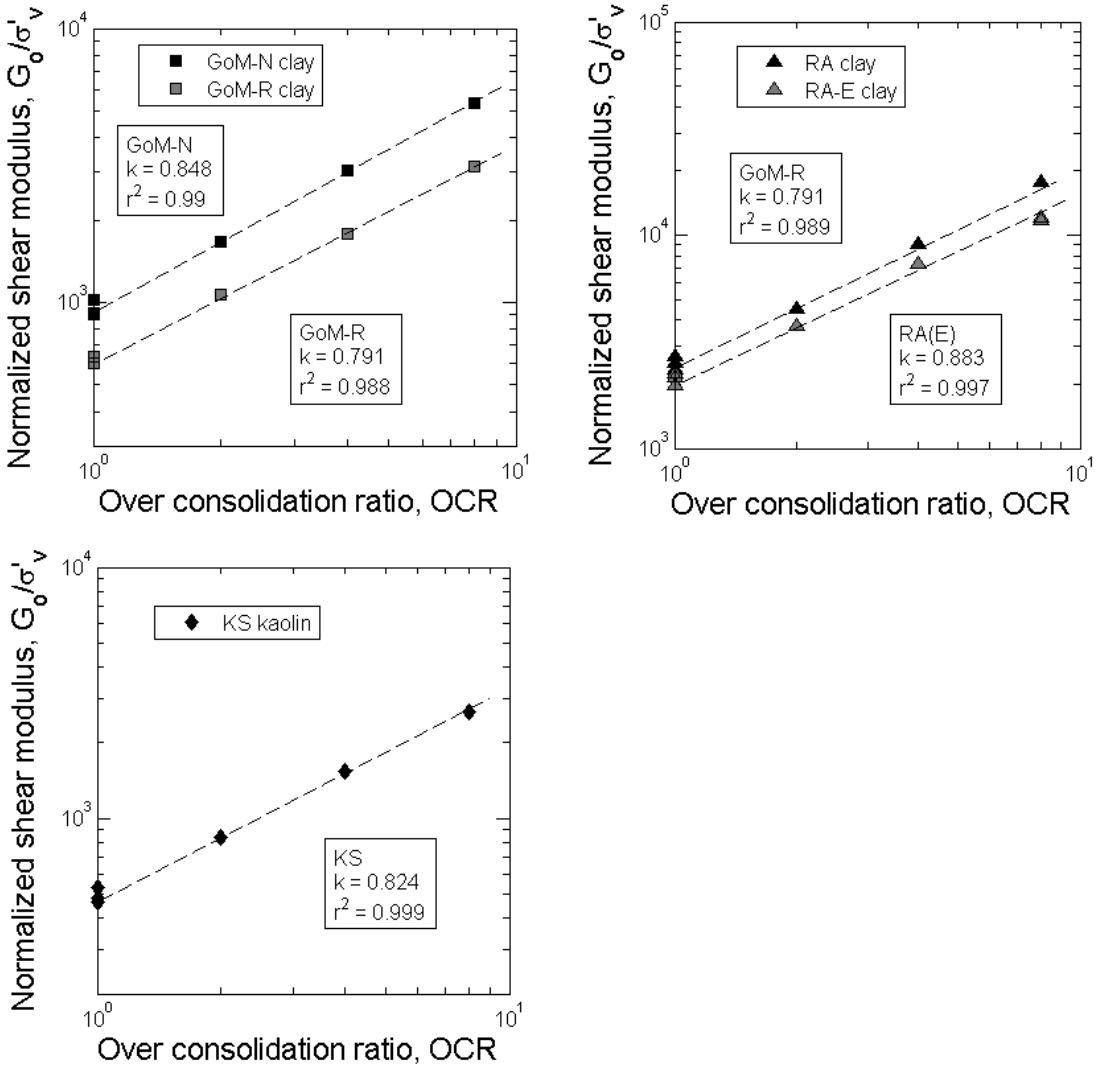

Figure 4.16: Normalized G_o versus OCR for all clays.

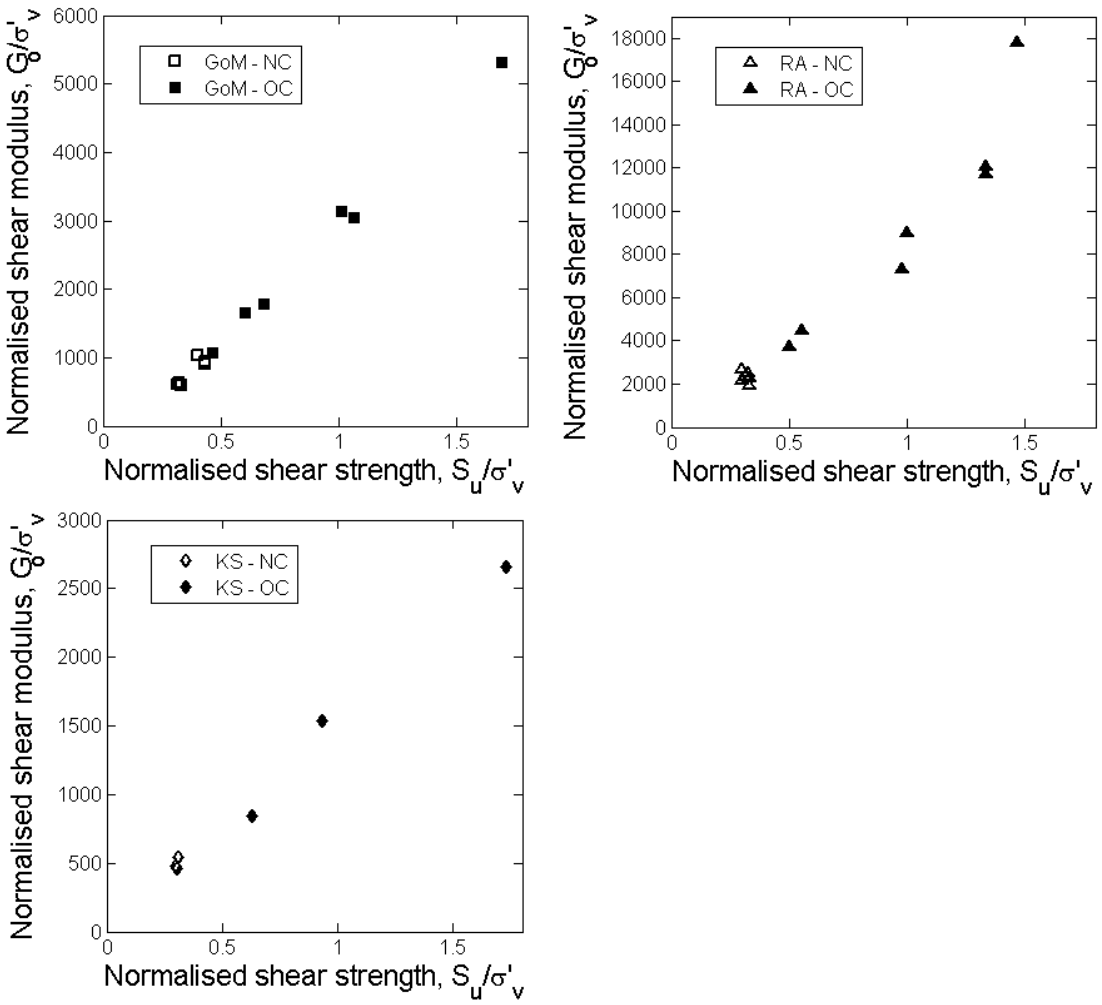

Figure 4.17: Normalized shear strength versus normalized shear modulus for all clays.

undrained shear strength by combining Equation 4.6 and SHANSEP. Figure 4.17 plots undrained shear strength (s_u) versus shear modulus ($\mathrm{G_o}$), both normalized with respect to vertical effective stress (σ'_v) for GoM, RA and KS clays. From all the figures it can be seen that the NC specimens lie in a cluster around the same region and the OC data points fall on a straight line with slightly varying slopes. It is observed that the relation between $\mathrm{G_o}$ and s_u is linear in nature.

Figure 4.18 shows the variation of G_o/s_u with OCR for all clays. As seen in the figure

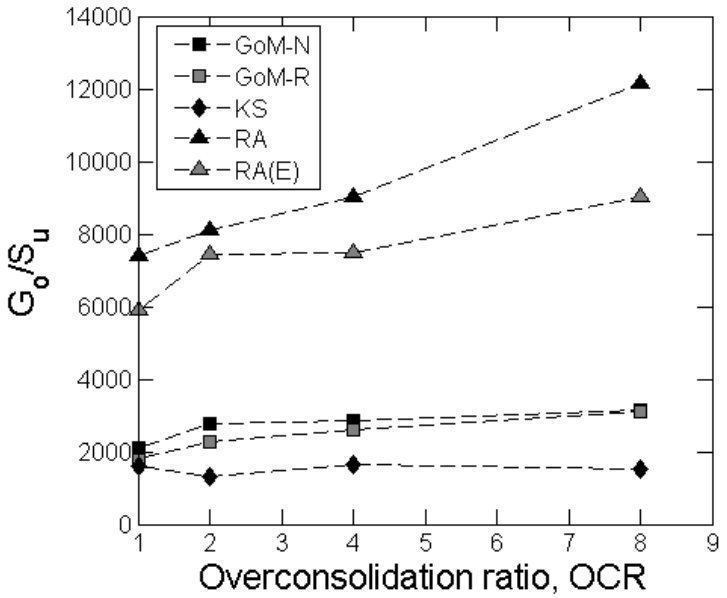

Figure 4.18: G_o/s_u plotted against OCR.

there appears to be a small contribution from the influence of OCR. This can be expressed using the Equation 4.7.

$$G_o/s_u = C * OCR^p \tag{4.7}$$

Where C is a constant that depends on the clay type measured by $(G_o/s_u)_{nc}$, p is the exponent that varies depending on the slope of the line in Figure 4.18. Values for the exponent p are given in Table 4.2 . As seen in the Figure 4.18 the influence of OCR appears to be almost negligible for KS samples, in such cases the Equation 4.7 reduces to:

$$G_o = Cs_u \tag{4.8}$$

Also observed in Figure 4.18 is that the coefficient C is not identical for the same clay type (comparing RA and RA(E); GoM-N and GoM-R). On comparing the corresponding

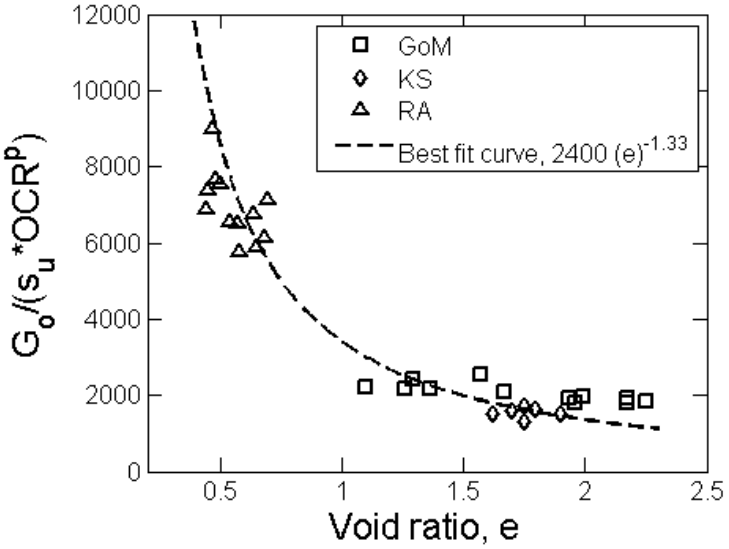

Figure 4.19: Normalized G_o plotted against void ratio.

samples it was found that the only variable (quantifiable) involved was void ratio (e). Figure 4.19 was plotted between $G_o/(s_u * OCR^p)$ (or coefficient C from Equation 4.7) and void ratio, where the exponent, p, for each clay is given in Table 4.2. A trend is observed between C and void ratio and the best fit curve shown in Figure 4.19 describes the influence of void ratio ($f(e)$) on stiffness.

A new equation is proposed to correlate initial shear modulus and undrained shear strength based on SHANSEP principles, Houlsby and Wroth (1991)'s Equation 4.7 and the experimental data carried out in this research program, given by:

$$G_o = 2400e^{-1.33}s_u OCR^p \tag{4.9}$$

Where $\mathrm{G_o}$ is the initial shear modulus, s_u is the undrained shear strength, e is the void ratio, OCR is over consolidation ratio and p is the exponent for OCR as presented in Table 4.2. Units for strength and modulus are in kPa for the constant value of 3400.

Table 4.2: Comparing parameters of $(G_o/\sigma'_v)_{nc}$, k, p and $(G_o/s_u)_{nc}$ for all clays.

Clay	$(G_o/\sigma'_v)_{nc}$	k	m	p	C = $(G_o/s_u)_{nc}$
GoM-N	945	0.845	0.63	0.179	2286
GoM-R	610	0.791	0.62	0.255	1894
KS	494	0.824	0.85	0.0119	1612
RA	2514	0.974	0.79	0.2309	7525
RA(E)	2115	0.883	0.71	0.186	6332

The equation presented above provides a convenient way of estimating both absolute value and trends of behavior at different void ratios and OCRs. It is emphasized that this equation does not provide a means to directly estimate the undrained shear strength based on geophysical measurements and that suitable site specific correlations will have to be developed for estimating strength for design purposes.

4.2 Sand

The geophysical data was correlated with the mean stress, void ratio and compared with published research. A framework for correlating the geophysical data with measured drained strength values is developed.

4.2.1 Geophysical characteristics

4.2.1.1 Round sand

Figure 4.20 shows the variations of the shear modulus (G) with respect to axial strain (ϵ_a) during the drained shear phase for each sample of Ottawa sand. There is a general increase in shear modulus with increase in confining pressure and increase in relative density. As seen in the figure, the dense samples have higher values of shear modulus as compared to the loose samples at the same confining pressure. Another trend observed is a gradual decrease of shear modulus with increase in axial strain.

Figure 4.21 shows the variations of the bulk modulus (K) with respect to axial strain

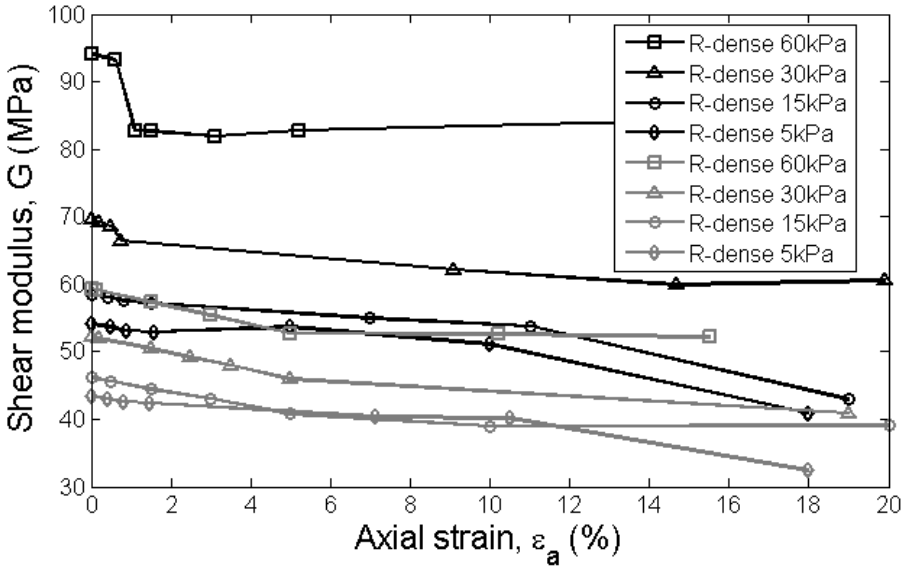

Figure 4.20: Shear modulus for round Ottawa sand.

(ϵ_a) during the drained shear phase for each sample of round Ottawa sand. The bulk modulus remains relatively constant for the entire shearing process.

4.2.1.2 Angular sand

Figure 4.22 shows the variations of the shear modulus (G) with respect to axial strain (ϵ_a) during the drained shear phase for each sample of Mystic White sand. There is a general increase in shear modulus with increase in confining pressure and increase in relative density. Similar to the round sand, the dense samples have higher values of shear modulus as compared to the loose samples at the same confining pressure. There is also a gradual decrease of shear modulus with increase in axial strain.

Figure 4.23 shows the variations of the bulk modulus (K) with respect to axial strain during the drained shear phase for each sample of angular Mystic White sand. The bulk modulus remains relatively constant for the entire shearing process.

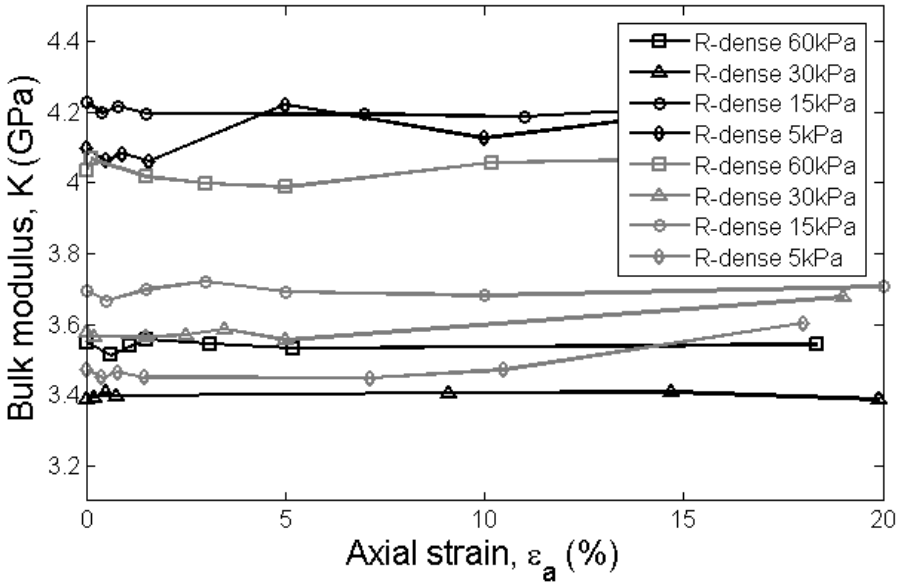

Figure 4.21: Bulk modulus for round Ottawa sand.

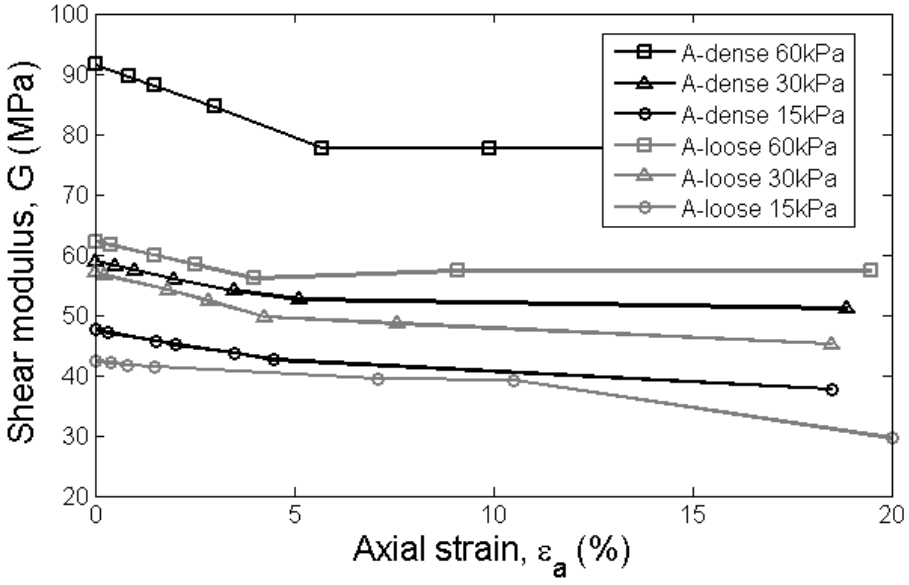

Figure 4.22: Shear modulus for angular Mystic White sand.

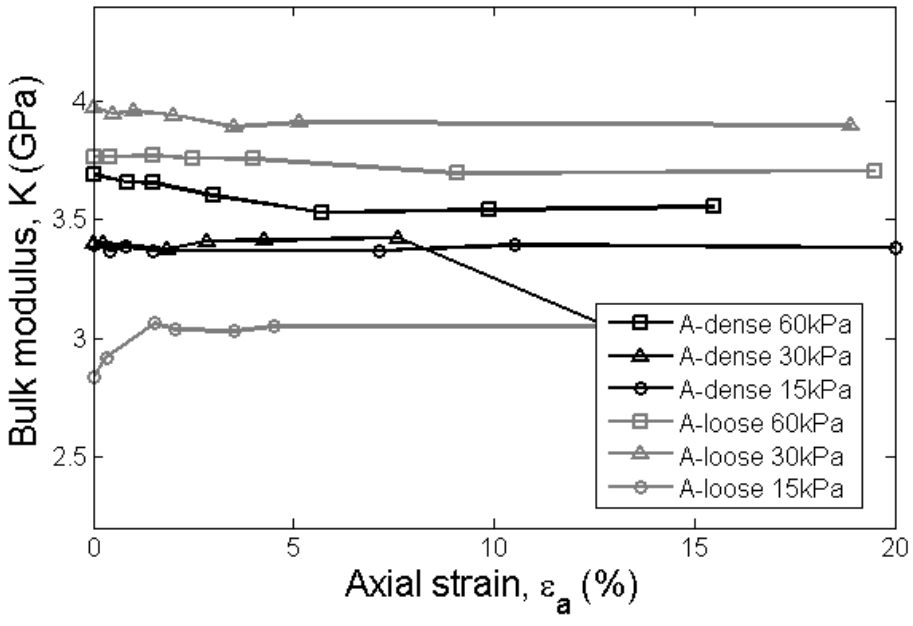

Figure 4.23: Bulk modulus for angular Mystic White sand.

4.2.2 Correlations with mean stress and void ratio

Based on the formulations for shear modulus available in the literature, it is evident that $\mathrm{G_o}$ is controlled primarily by the relative density and confining pressure (Hardin and Richart, 1963; Seed and Idriss, 1970; Pestana and Whittle, 1995; Pestana and Salvati, 2006). Pestana and Salvati (2006) proposed a general formulation for $\mathrm{G_o}$:

$$G_o/p_{atm} = G_b.f(e).f(\sigma'_m/p_{atm}) \tag{4.10}$$

Where σ'_m is the mean effective stress, p_{atm} is the atmospheric pressure, $f(e)$ is a function dependent on the void ratio and G_b is the material constant varying for each soil type. The mean stress function ($f(\sigma'_m/p_{atm})$), void ratio function ($f(e)$) and material constants (G_b) are computed for the data from this research and compared with the published data

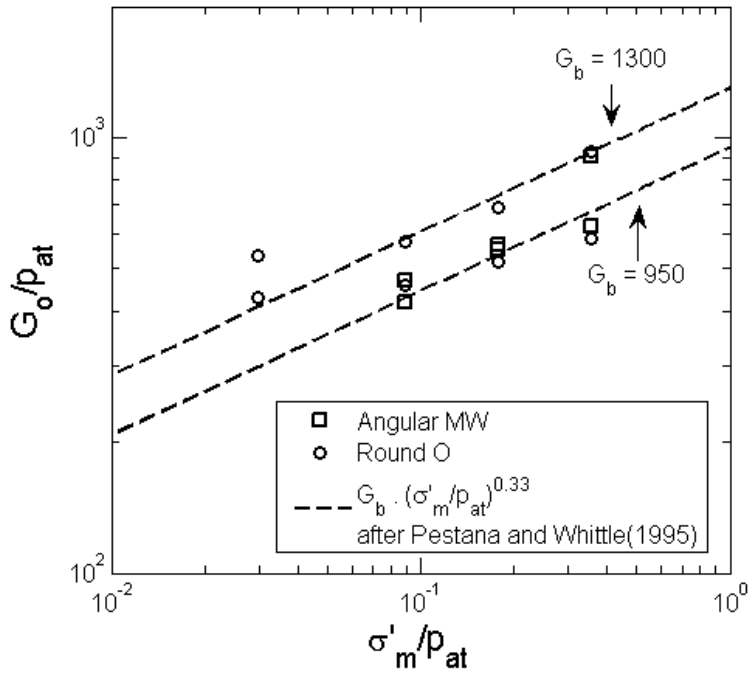

Figure 4.24: Effect of mean stress on $\mathrm{G_o}$ for Ottawa and Mystic sands.

by Pestana and Salvati (2006).

Salvati (2002) reviewed all the formulations developed between 1960 and 2000 describing the effect of confining pressure on $\mathrm{G_o}$. Most of the formulations prescribe an exponent for the power law which is in range of 0.4-0.6. Pestana and Whittle (1995) suggested using 0.33 as the exponent.

Figure 4.24 compares the predictions of $\mathrm{G_o}$ using the power law exponent equal to 0.33 with measured values of $\mathrm{G_o}$ for Ottawa sand and Mystic White sand. Pestana and Whittle (1995)'s exponent of $n = 0.33$ was chosen as it fit the data the best. The material constant G_b varies for Ottawa and Mystic White sands and is discussed below.

Figure 4.25 plots $(G_o/p_{atm})/(\sigma'_m/p_{atm})$ versus void ratio and presents the data from this research along with two types sand (Ottawa-round and Toyoura-angular) tested by Pestana and Salvati (2006). The figure also shows the following three functions describing

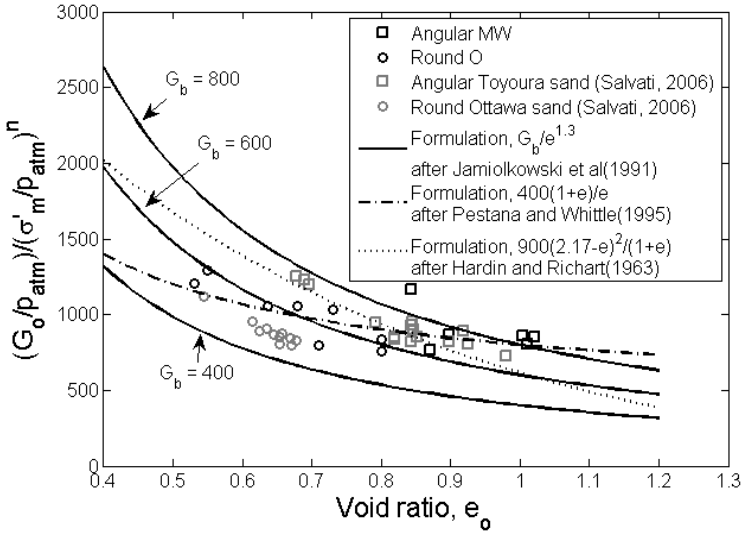

Figure 4.25: Effect of void ratio on G_o for Ottawa and Mystic sands after Pestana and Salvati (2006).

the effects of void ratio on G_o :

Jamiolkowski et al. (1991)

$$f_1(e) = e^{-1.3} \tag{4.11}$$

Pestana and Whittle (1995)

$$f_2(e) = (1+e)/e \tag{4.12}$$

Hardin and Richart (1963)

$$f_3(e) = (2.17-e)^2/(1+e) \tag{4.13}$$

Again, to remain consistent with Pestana and Salvati (2006), the values of the material constant G_b were taken as a range of values from 400 to 800. The trend of the experimental data is best matched by the formulation presented by Jamiolkowski et al. (1991). Within

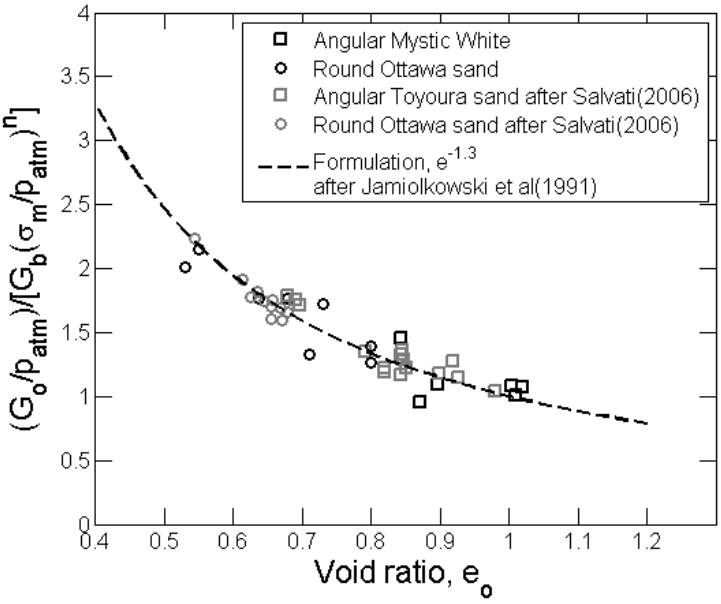

Figure 4.26: Effect of void ratio on normalized G_o for Ottawa and Mystic sands after Pestana and Salvati (2006).

a well chosen range of material constants (G_b) all the different types of sands can be described.

Figure 4.26 shows a plot of all the G_o from this research normalized by their confining pressure and the G_b for the material. The formulation proposed by Jamiolkowski et al. (1991), $f_1(e) = e^{-1.3}$ is also presented in the same plot. The data is found to fit relatively well.

The values of the material constant, G_b, angularity, uniformity coefficient for the sands tested in this research along with values in the literature for some round and angular sands are presented in Table 4.3.

Figure 4.27 shows the shear modulus, G, normalized by the mean stress and the same value of material constant (G_b) at various axial strain intervals during the drained shear phase of the test. The figure shows G at axial strain intervals of 0%, 0.5%, 1%, 2% and

Table 4.3: Selected parameters for Ottawa and Mystic White sands

Sand	Reference	Angularity	C_u	G_b
Ottawa sand	this project	R	1.18	600
Mystic White sand	this project	A	1.32	800
Ottawa sand	Hardin et al. (1994)	R	1.2	475 - 500
Sacramento	Salvati (2002)	SA-SR	1.3	400
Toyoura	Lo Presti et al. (1993)	SA	1.5	700 - 720
Dog's Bay	Jovicic and Coop (1997)	A	2.4	1800

15%. It is evident from the figure that G_b decreases with increase in axial strain for both Mystic White and Ottawa sands. This decrease of G_b with strain is shown in Figure 4.28.

Figure 4.29 shows the same plot as Figure 4.27, except for the value of the material constant (G_b) used to normalize the shear modulus (G) is decreased with axial strain. All the normalized shear modulus values are found to fit relatively well with the formulation by Jamiolkowski et al. (1991).

4.2.3 Correlations with strength and friction angle

The peak shear values (τ_f) were obtained from each sample's stress strain curve during shearing. 'Failure' was considered to be the maximum value of shear stress from each test. Figure 4.30 shows the peak strength plotted against the shear modulus values for all the sand samples tested in this project.

A general trend of increase in shear modulus with increase in failure strength is observed in all the sands. Figure 4.31 show the same shear modulus values plotted against peak strength along with their trend lines for round Ottawa sand and angular Mystic White sand respectively. The influence of relative density in determining the shear modulus is much higher in angular sands as compared to rounded sands. This is clearly seen with different slopes of the trend lines drawn for the 'loose' and 'dense' samples of both angular and round sands.

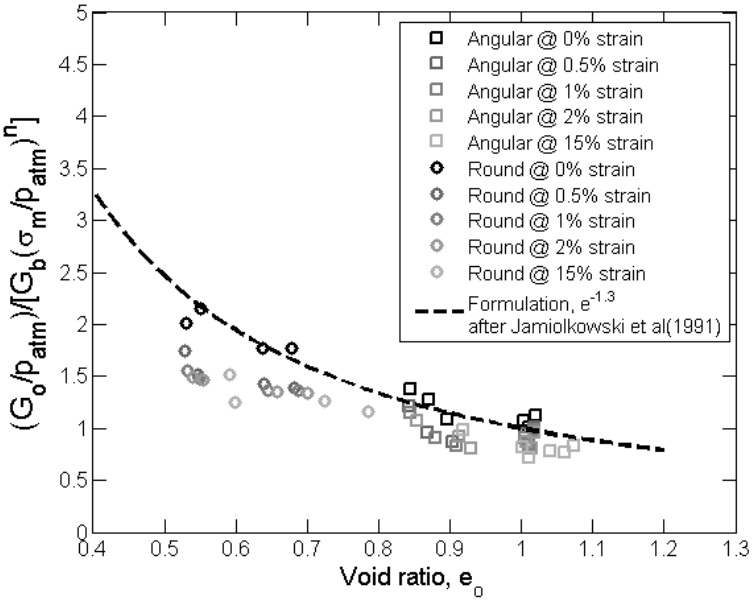

Figure 4.27: Effect of void ratio on normalised G at intervals of axial strain for Ottawa and Mystic sands.

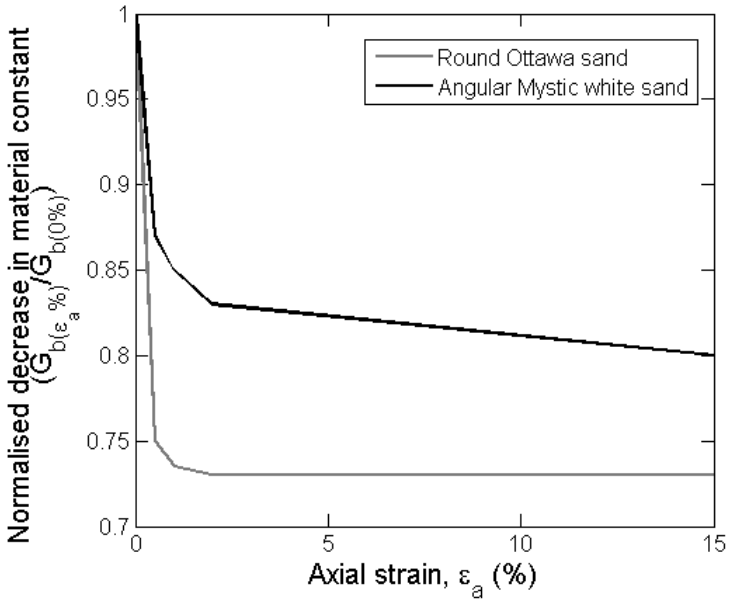

Figure 4.28: Normalised decrease in G_b with strain for Ottawa and Mystic sands.

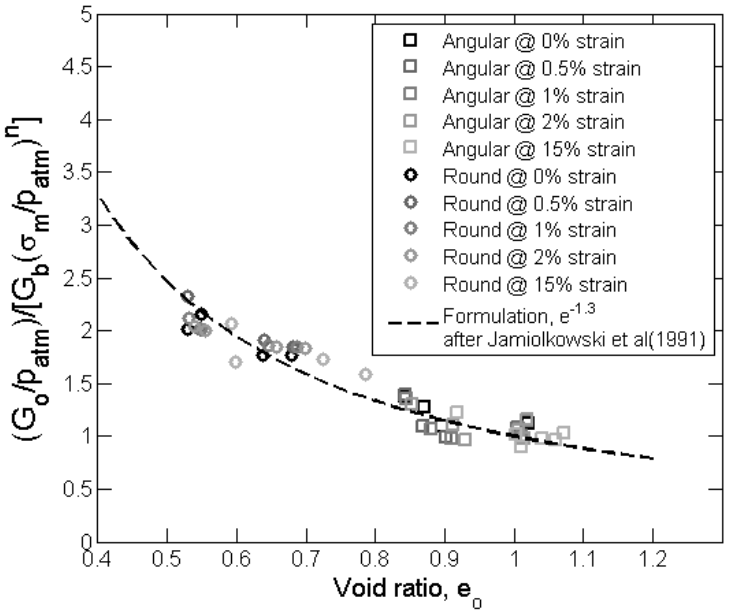

Figure 4.29: Effect of void ratio on normalised G at intervals of axial strain for Ottawa and Mystic sands.

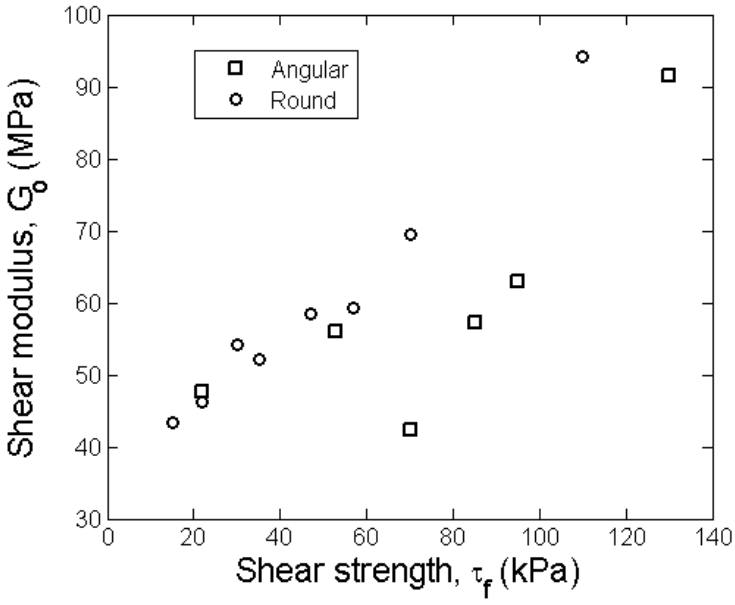

Figure 4.30: Peak shear strength versus shear modulus for all sands.

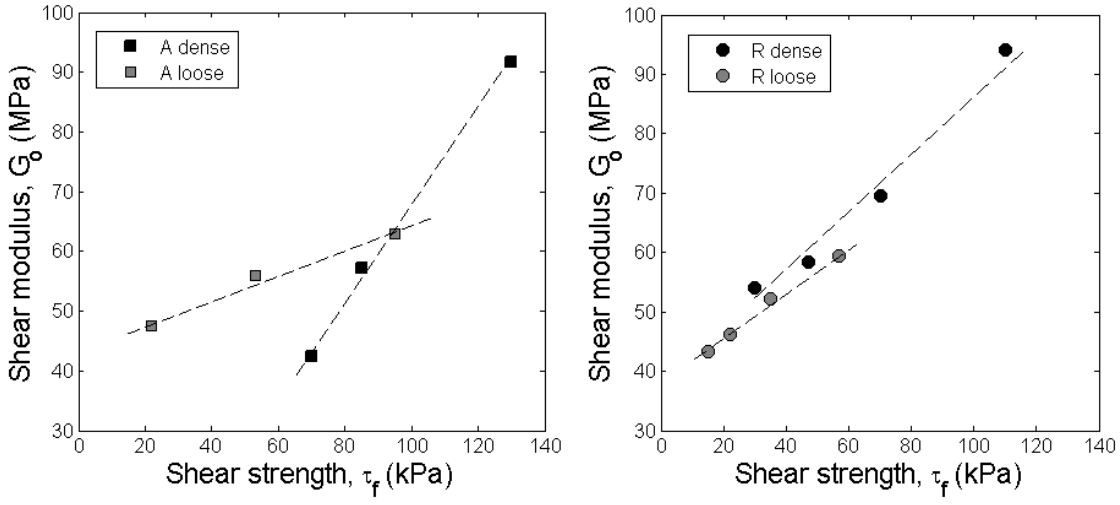

Figure 4.31: Peak shear strength versus shear modulus for angular and round sands.

Figure 4.32 shows the shear modulus, G_o for all the sand tests versus the friction angle, ϕ. The shear modulus appears to be decreasing with increase in friction angle for most samples. Also observed in the figure, is that the decrease of shear modulus with friction angle is more prominent in the dense samples as compared to the loose samples. However due to the limited number of sand tests carried out in this research program no significant conclusion can be made from the trend observed between G_o and ϕ.

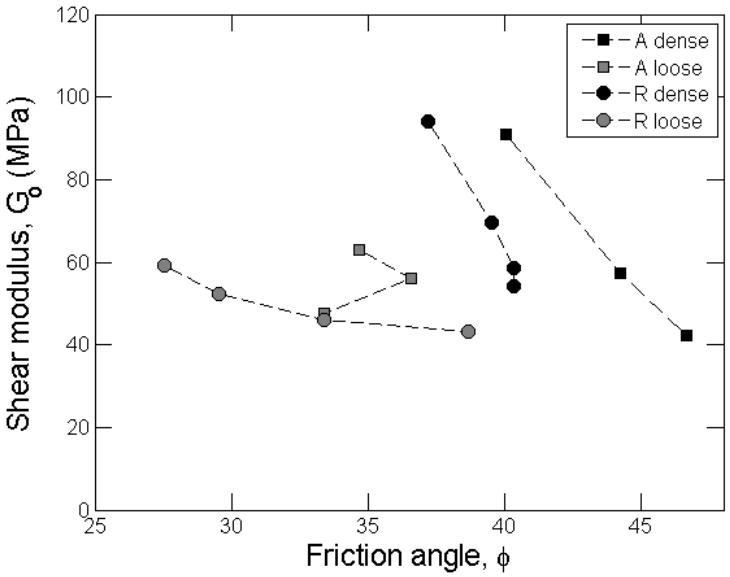

Figure 4.32: Friction angle versus shear modulus.

5. EXPERIMENTAL MODEL FOR CENTRIFUGE TEST

This section describes the methodology for the centrifuge tests including design and fabrication of the equipment used, construction of the test bed, and the soil bed properties. The centrifuge testing was carried out at the Network for Earthquake Engineering Simulation (NEES) facility at Rensselaer Polytechnic Institute (RPI) (nees.rpi.edu). The 150 g-ton centrifuge comprises of a swinging basket with a nominal radius of 2.7 m, which is the distance between the center of payload and the centrifuge axis. Loads were applied on the model foundations using the 4-degree of freedom in-flight robot using a customized tool. Figure 5.1 shows a picture of the centrifuge used at RPI (nees.rpi.edu).

5.1 Design and fabrication of model pile and connectors

When lateral load is applied on a wind turbine foundation, a combination of translation and rotation takes place (Figure 5.2). Two different types of connections were designed to separate these movements and measure displacement and load.

The customized tool consists of an adaptor that was designed and fabricated to latch onto the in-fight robot. This metal adaptor was 3D printed using an alloy of stainless steel and bronze by Shapeways Inc. and was used with 2 different types of pile caps to achieve both pinned and rigid connectors (Figure 5.3). The connectors to transfer the load from the in-flight robot onto the short monopile was designed and fabricated by keeping the different types of motion in mind: rotation and translation.

1. A ball and socket joint was developed with a spherical ball on the top of the pile cap and a cylindrical socket in the adaptor allowing the pile to rotate freely for a pinned joint (Figure 5.4 a). The pinned connection was designed to apply moment with 4 different eccentricities; 1.2D, 1.5D, 2.5D and 3.5D. Eccentricity is defined as the distance between the mudline and the point of application of load (Figure 5.5).

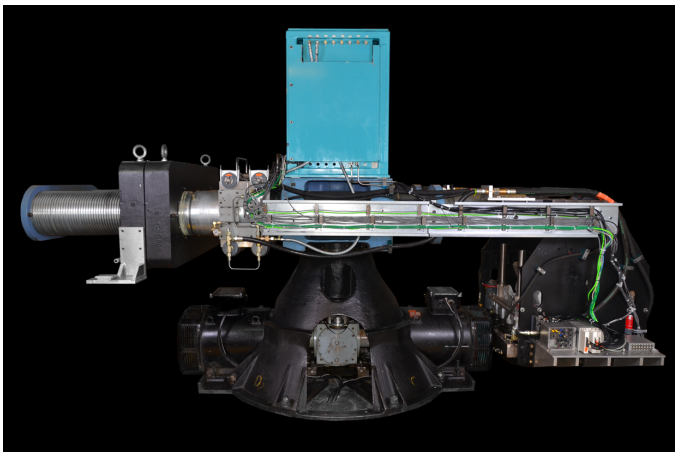

Figure 5.1: Centrifuge at RPI used for experimental testing (nees.rpi.edu).

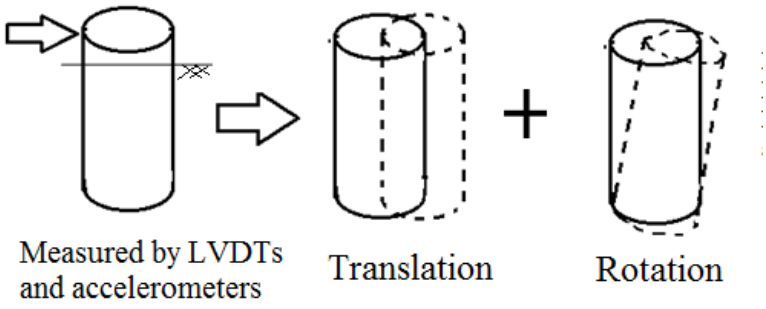

Figure 5.2: Types of motion (exaggerated) on applying a lateral load to a pile.

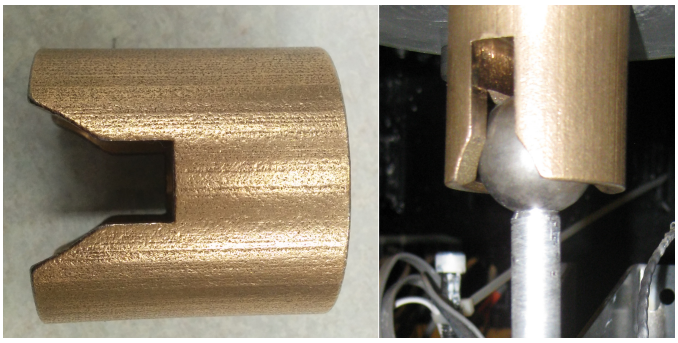

Figure 5.3: 3D printed metal adapter.

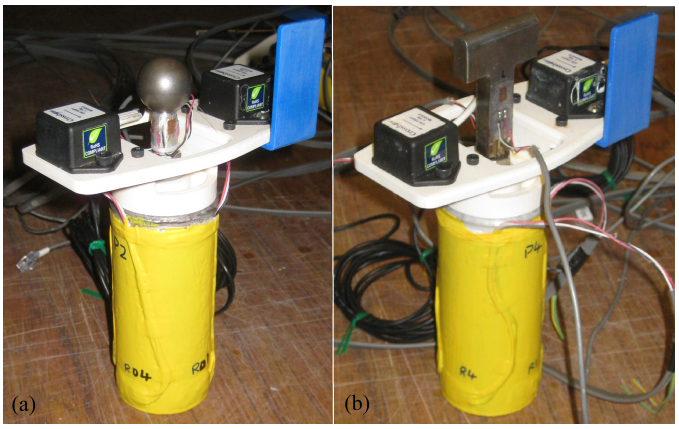

Figure 5.4: a) Ball and socket joint on pile to allow rotation ; b) Rigid connector on pile for pure translation.

2. A rigid locking connection was designed with a flat plate on top of the pile cap to fit into a groove in the adapter providing a rigid connection (Figure 5.4 b).

The rigid and pinned connectors were machined out of steel to be as rigid as possible. Since multiple piles were tested in a single clay bed, the adaptor and pile caps had to be connected in-flight. It was found to be highly advantageous to fabricate the adaptor such that visual alignment between the pile cap and adaptor was possible. As seen in Figure 5.3 bevelled edges were used to guide the adaptor into place. The adaptor and the two connectors had to be as smooth as possible to prevent seizing of the parts in-flight. The adaptor was not designed to constrain the pile vertically. Vertical movement was not restricted during any of the tests.

Monopile foundations in the field range from diameters of 4 m to 6 m with diameter to thickness ratios (D/T) ranging from 100 to 500 (Achmus et al., 2008; Saigal et al., 2007; Lesney and Wiemann, 2005). The prototype in the 70-g centrifuge environment was required to simulate similar stresses and strains as found in the field. The flexural rigidity (EI) of the prototype was matched as closely as possible to a representative field monopile,

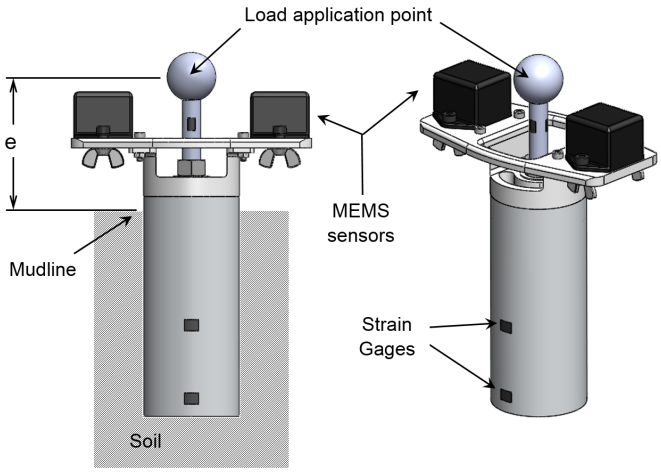

Figure 5.5: Sketch of ball and socket connector (Beemer, 2015).

since it was required for bending moment calculations.

The model piles were fabricated from hollow aluminum tubes with an outer diameter of 49.6 mm (3.47 m in prototype, for the test acceleration of 70 g), thickness of 0.609 mm (0.042 m in prototype) and an effective embedment length of 101.6 mm (7.1 m in prototype) using the appropriate scaling laws (Garnier and Gaudin, 2007). The height available in the centrifuge basket was fixed limiting the maximum effective length of the model pile that could be tested in the centrifuge without considerable boundary conditions, thus the model pile was limited to an aspect ratio (L/D) of 2. Table 5.1 presents all the model pile properties along with comparisons of the stiffness (EI) of the prototype and representative field dimensions. Autocad drawings of the pile and connectors are presented in Appendix C.

5.2 Instrumentation

Figure 5.6 shows a schematic of monopile foundation under lateral load. The total displacement measured at the top of the monopile foundation is a combination of bending of the stem (δ_{bend}) and rotation of the pile setup (δ_{rotate}) for the momentless tests and a com-

Table 5.1: Model, prototype and field pile specifications

Property	Model	Prototype	Field
Material	Aluminum	Aluminum	Steel
Young's Modulus, E (GPa)	69	69	200
Outer diameter, D (m)	0.0496	3.47	4
Thickness, t (m)	6×10^{-4}	0.042	0.013
Effective length, L_e (m)	0.101	7.1	$10 - 50$
Area moment of inertia, I (m^4)	1.43×10^{-8}	0.343	0.162
Bending stiffness, EI (Nm^2)	9.8×10^8	23.7×10^9	32.4×10^9

bination of bending of the stem (δ_{bend}) and translation of the rigid connector ($\delta_{translate}$), refer Figure 5.6.

The model was instrumented using an array of sensors to record and observe the behavior of the soil and foundation system based on the Figure 5.6. Pore pressure transducers, Memsic 10-g accelerometers, Linear Variable Differential Transformers (LVDTs) and strain gages on the piles and stems were used. The following section discusses each type of sensor.

5.2.1 Strain gages

Strain gages were chosen and placed to accurately measure both bending along the pile stem and deformation of the pile. The gauges were manufactured by Vishay Micro-Measurements.

- Along the stem of the pinned pile cap, 3 uni-axial strain gages were mounted parallel to the longitudinal axis of the stem, 120° apart. This orientation enables measurement of axial load, bending moment and angle of neutral axis on that level (Tuttle, 1981). Two opposing gages are used on the plate of the rigid connector. The front and back configuration enables measurement of the bending moment on the pile.

- At the bottom of the model pile, 4 uni-axial strain gages were mounted along the

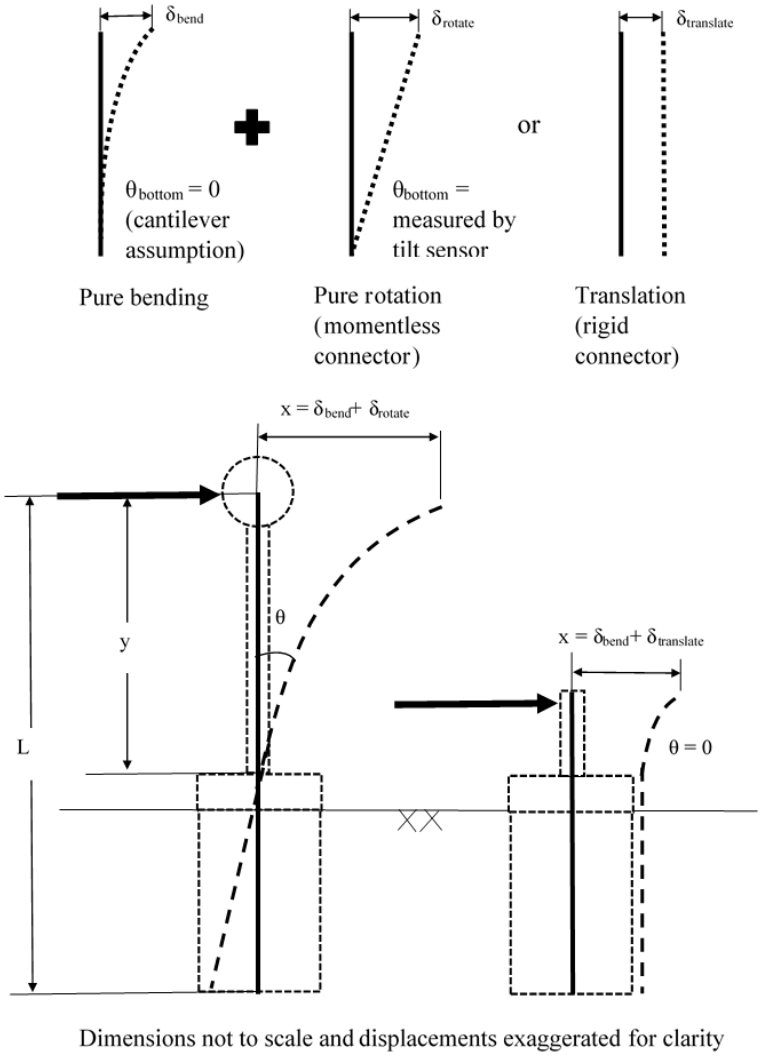

Figure 5.6: Sketch showing rotation and translation combined with bending (exaggerated).

circumference of the pile, 90° apart. This orientation of the gages enables measurement of the ovalization of the thin walled pile. Two of the gages placed along the axis of the load applied would measure compression and the opposite two gages measure elongation.

Figure 5.5 shows a sketch of the model pile with the strain gages on the circumference of the model pile and along the stem. Two types of Vishay Micro-Measurements strain gauges were used: EA-13-125PC-350/E half bridges for ovalization with a resistance on 350 Ohms and EA-06-062AP-120 full bridge for bending with resistances of 120 ohms. Terminals of two sizes, CEG 25C and CPF 75C were used for the gages on the pile and the stem respectively.

Strain gauge wiring was terminated at either a Molex Microfit 3 pin and socket connection or at RJ- 12 connection. It was necessary to use extension cables with the stem strain gauges as they could not accommodate 26 American Wire Gauge (AWG) wire needed for the RJ-12 connectors. The Microfit 3 connectors are lightweight locking connectors compatible with 26 and 30 AWG wire. RJ-12 plugs compatible with the data acquisition system at RPI were at the other end of the extension cables.

5.2.1.1 Strain gage installation

The gauges were installed using recommendations from the manufacturer (Vishay, 2011a; Vishay, 2011b). First, the piles and stems were sprayed with a degreaser and abraded with 300 and 420-grit sand paper. Next, the locations of the gages are measured and marked using a blunt scriber. The surface was conditioned using a light acidic solution and then neutralized using a pH balancing base. The surface is free of foreign substances and corrosion and is now ready for the strain gage to be attached. The gage is laid out on a clean glass plate and cellophane tape is applied to the top of it. The tape is peeled back at a low angle to prevent bending of the gage. The markings on the gage are aligned with

the marking on the metal. Once the gage is aligned the tiny drop of the bonding adhesive to the back of the gage. The tape and gage are lowered into place and pressure is applied for about 10-20 seconds. A sheet of rubber is placed over the tape and gage for protection and a clamp is applied to hold pressure until the glue hardens (approximately 24 hours).

After bonding the gage and terminal to the surface, they are soldered. The connection between the strain gage and the terminal is made using thin magnetic wire and the 26 AWG or 30 AWG wires are soldered onto the terminals. Each gage is checked for connectivity and resistance. Since these gages and wires will be used in the centrifuge environment, to remove the effect of wire pulling on the terminal which might cause errors in the reading or the wire to disconnect in-flight, the wires were tied to the stem or the top of the pile with a thread (Figure 5.7). This transfers all the tension developed in the wire during to spinning from the soldered contact onto the wrapped thread. Once the electrical connections were made and the wires were tied down, the gages and wires are coated with a general purpose protective coating M-coat A. Although this coating was sufficient protection for the gages on the stems, the piles required additional protection since they were embedded in saturated clay. The piles were painted both outside and inside with liquid latex (Plasti-dip) to make it waterproof. Approximately 5-6 coats were applied. Figure 5.4 shows the picture of the piles painted with rubber.

5.2.2 Accelerometers

One or two single dimensional Memsic 10 g accelerometers were mounted to the model foundations with a 3D printed platform (Refer Figure 5.5). These accelerometers are Micro-Electrical-Mechanical Systems (MEMS) capable of measuring constant acceleration while excited. Monopile tilt can be measured by comparing the MEMS measurement to the model gravity. The measured value should be 0 g at 0^o of tilt and theoretically 70 g at 90^o. The accelerometers are oriented in the direction of natural gravity such that

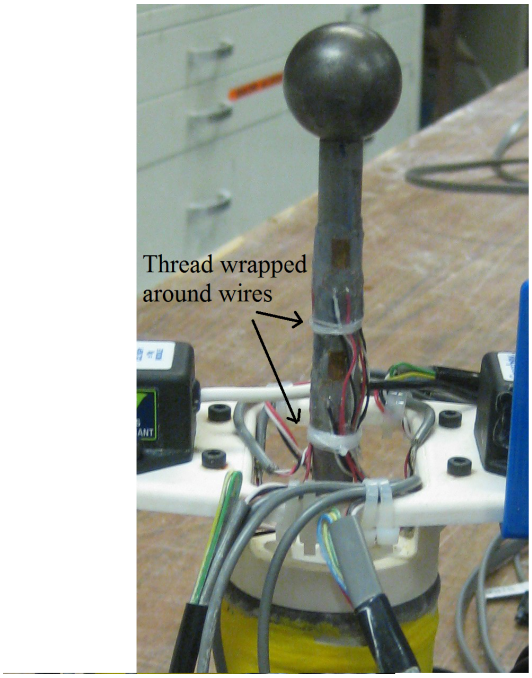

Figure 5.7: Thread tied around the stem and pile head to remove any effects of wire pulling.

they measure 1g at the start of the experiment; this is to avoid variations in acceleration due to orientation of the monopiles with respect to the centrifuges axis. Theoretically, in a 70 g environment 8.2 degrees of tilt with respect to the horizontal can be measured at a sensitivity of 243.9 mV/degree.

The MEMS accelerometers may have an internal alignment error of up to two degrees. This results in a slight, but constant offset during testing. As long as the sensors orientation is not changed between tests this alignment error will not impact data collection. Additionally, the sensors are cross-axis sensitive. The cross-axis sensitivity for the CXL10GP1 is + 5%; this results in a maximum of a 3.5 g offset at 70 g. This offset will change during testing as the acceleration in the z-direction changes during tilting. This is accounted for by running calibration tests at high g (Beemer, 2015). In addition to the 10g MEMS accelerometers, one 100g MEMS accelerometer clamped on a 3D printed mud mat foun-

dation (skirted pile) was placed in the test bed to measure the exact g level at the height of the other MEMS accelerometers placed on the piles to measure tilt. This measurement of the exact g level is required to obtain accurate tilt data from the accelerometers (Beemer et al., 2015). The accelerometers have five pin header jacks which were connected using an extension cable terminating in connectors. The equations for the data processing for these sensors is presented in Appendix C.

5.2.3 Linear Variable Differential Transformers

As mentioned previously, each pile will experience both rotation and translation (Refer Figure 5.2). Thus to separate the components of tilt and displacement both accelerometers and Linear Variable Differential Transformers (LVDT) were used on each pile. LVDTs were used to measure displacement of each monopile by mounting them onto a bracket attached to the edge of the rigid box.

Target flags were used as contact points for the LVDT sensors. These flags were 3D printed from ABS plastic. They were mounted below the MEMS platform with screws and provided a contact area of 5.5 cm by 2.95 cm for the LVDT (Figure 5.8). The LVDTs have a stroke of 25 mm and were calibrated before each use. They were attached to the steel bracket using gorilla glue, the steel bracket was then mounted to the wall of the container using bolts. The LVDT brackets with the sensors were mounted only after the piles were installed. They were positioned in such a way so as to measure displacement in two directions, both the front and back of the monopile. Additional details on this measurement and drawings are given in Appendix C.

5.2.4 Pore pressure transducers

Pore pressure sensors were used to measure the pore pressures induced in the clay during loading. The sensors were installed within the clay layer in two levels: 3 sensors at mid depth and 3 sensors at 2/3rd depths of the pile length. The sensors at mid-depth

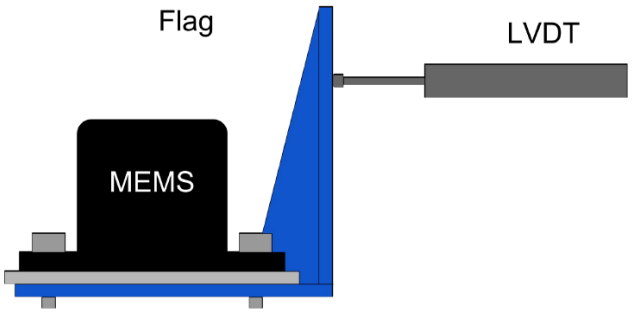

Figure 5.8: Schematic of the LDVT and its target flag attached to the MEMS sensor on the pile (Beemer, 2015).

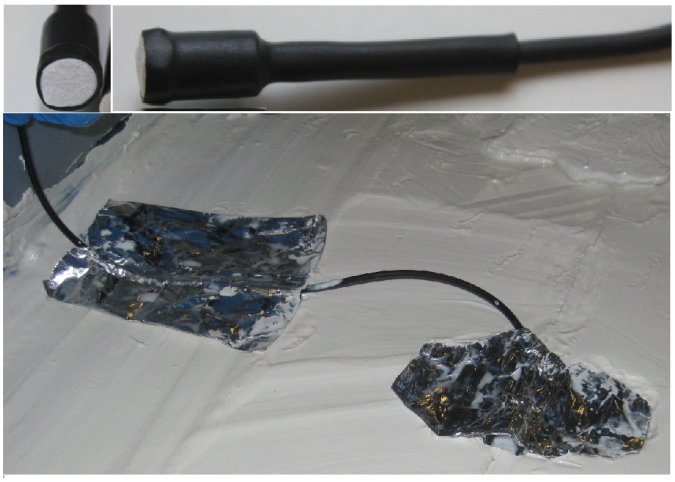

Figure 5.9: GE Druck pore pressure sensor during placement.

were installed to monitor the consolidation process. The sensors at 2/3rd depths of the pile length were placed in the direction of loading along one side of the piles.

The sensors are soaked in water for about 24 hours before use. They contain a ceramic filter that prevents clay infiltration but allows transmission of water pressure. Figure 5.9 shows a picture of the GE Druck sensors used during testing. Installation of the pore pressure sensors is explained in Section 5.3.

5.3 Model construction

The model construction consisted of four main parts: soil placement, consolidation, excavation and pile installation. The following sections describe the model construction steps for a single test bed. Figure 5.10 shows a picture of the sequence of model construction. Three piles were installed and tested in a single test bed.

5.3.1 Soil placement

The model was constructed in the large rigid box available at the NEES facility at RPI with dimensions of 88 cm long, 39 cm wide and 36 cm deep (Figure 5.10 (1)). The box was initially tested for the integrity of all the seals and fasteners. All exposed holes and bolt holes were closed with duct tape. The box was then checked for leaks by filling it with water.

Once the box was ready to be used, it was lined with geotextile on the bottom and sides using duct tape. The clay bed was designed to be doubly drained, plastic sheet was taped on the four side walls over the geotextile to reduce friction during consolidation. This is shown in Figure 5.10 (3).

The test bed consisted of two soil layers; a layer of Nevada sand (1 cm thick) and a layer of kaolinite (32 cm thick). The sand was rained down from a height of 10 cm over the geotextile at a relative density of 35% to serve as the drainage layer. The resultant sand layer was at the desired dry density of $1.62\ g/cm^3$. It was then leveled and saturated slowly by syphoning water onto a sponge placed over the sand to minimize disturbance (Figure 5.10 (4)).

The main soil layer, kaolin was prepared from dry clay powder at a water content of 77% (Refer Appendix B). This clay was placed by hand in the form of pancakes into the rigid box in 3 layers, to a clay height of 32 cm. The clay was placed in 3 layers to ensure proper placement of the pore pressure sensors. The bottom layer was 16 cm thick, after

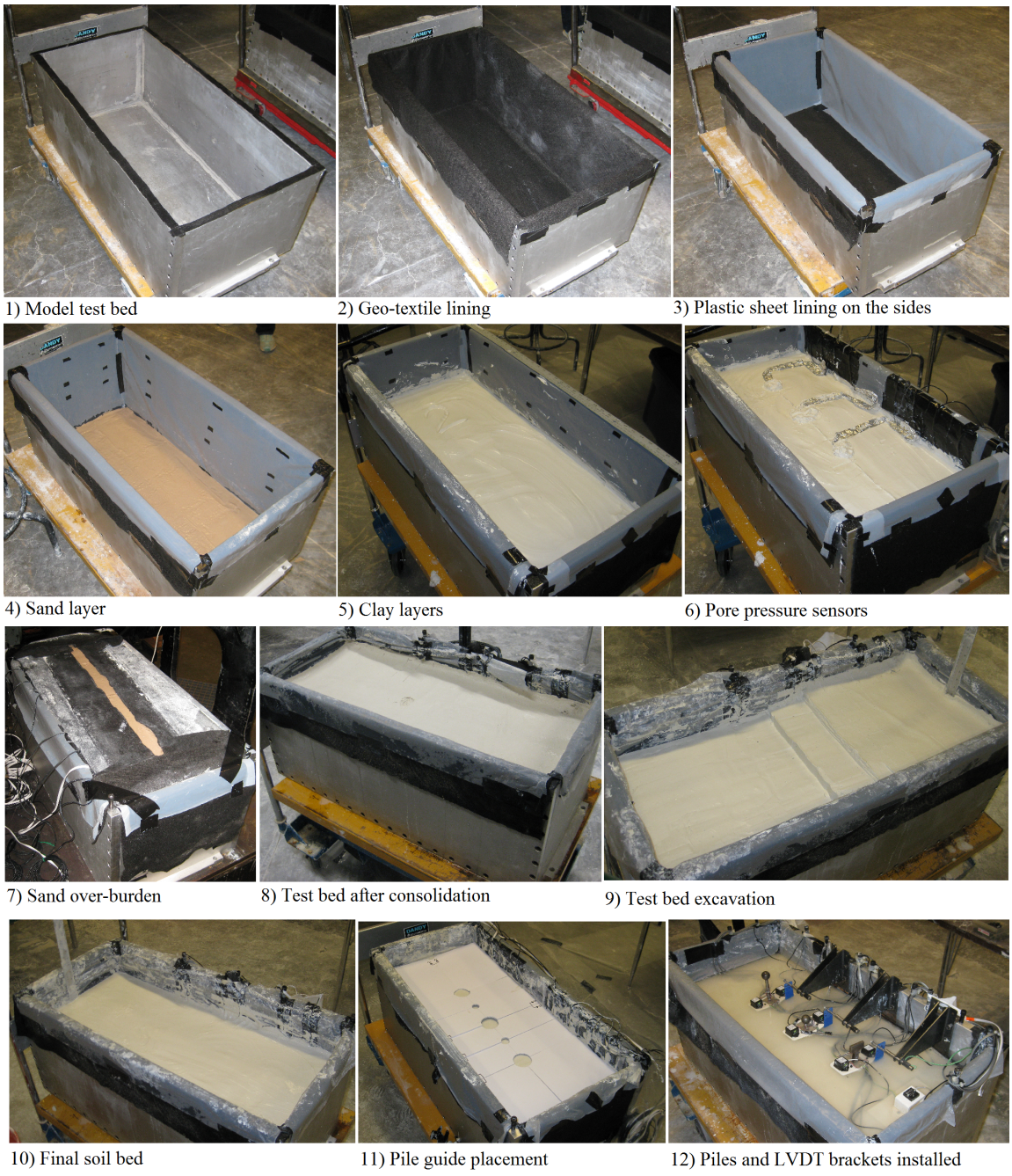

Figure 5.10: Sequence of model construction for a single test bed.

Table 5.2: Soil properties of kaolin used for testing

Property	Value
Manufacturer	BASF
Trade name	ASP 600
Specific gravity (G_s)	2.6
Liquid Limit (LL)	63
Plasticity Index (PI)	33

which all the mid depth pore pressure sensors were placed. Care should be taken while routing the wire of the sensor making sure it doesn't lie in the way of the piles or the T-Bar penetration locations. Sufficient slack should also be given while taping the wires to the plastic sheet on the side of the box to allow for settlement. The next clay layer placed was 6 cm thick, after which the pore pressure sensors at the pile depth were placed in a similar manner. The location of these pore pressure sensors were predetermined based on the location of the piles. The top layer of clay was 10 cm thick. Table 5.2 presents the index properties of the kaolin clay used.

The soil mass was then covered with a geosynthetic layer and sand (Figure 5.10 (7)). The geosynthetic mat acts as a filter to prevent the sand from mixing with the clay. The sand provides overburden to facilitate consolidation. The overburden sand layer is 3 cm thick filling the large rigid box entirely till the top and providing an over burden pressure 47 kPa.

5.3.2 Consolidation

The clay layer was consolidated in the centrifuge under 100g of acceleration. The test bed was doubly drained with pore pressure sensors installed within the clay layer to monitor the progress of consolidation. The degree of consolidation was controlled using the overburden pressure and spin time. To simulate a shear strength profile similar to what is found in the seabed, 40 kPa of pore pressure had to be dissipated at mid depth (pore

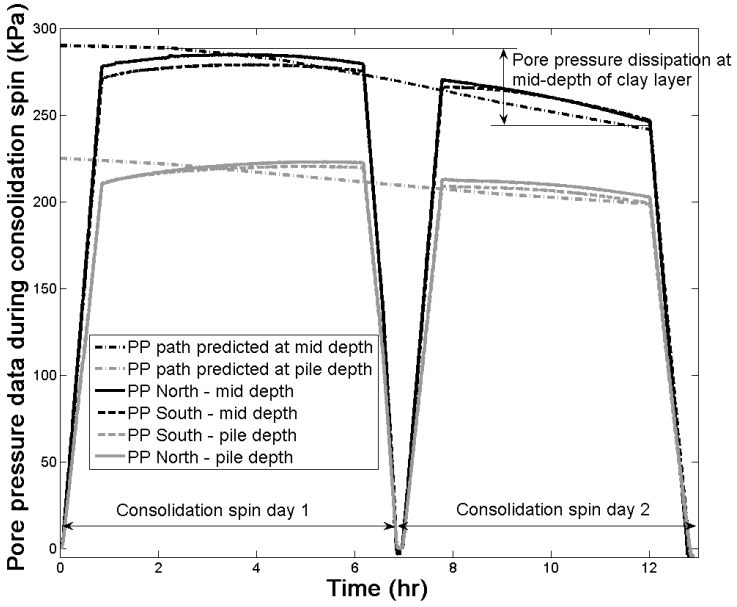

Figure 5.11: Pore pressure data during the consolidation spin.

pressure location) while spinning at 100g. Consolidation was carried out for a period of 12 hours with the test bucket placed along the center line of the centrifuge. Pore pressure and effective stress calculation can be found in Appendix B.

Figure 5.11 shows the measured pore pressure data for a single test bed during the consolidation spin occurring over two days and the expected pore pressure dissipation path calculated assuming a linear initial pore pressure profile. The measured pore pressure path was found to match favourably with the expected path, and consolidation was stopped when approximately 40 kPa of pore pressure dissipated along the mid depth of the clay bed. Small differences in the magnitude of the sensor readings is expected since the pore pressure transducers were placed by hand and small errors in the depth of installation leads to large changes in the reading due to the centrifuge environment.

Figure 5.12: Model test bed with piles installed.

5.3.3 Excavation and pile installation

Once consolidation was complete, the top 4 cm of over consolidated layer was excavated and leveled (Figure 5.10 (9)). The piles were installed manually using a pile guide and level to ensure they were vertical while embedded in the clay (Figure 5.10 (11)). The model piles were placed along the center line of the spinning arm of the centrifuge with a center to center spacing of 18.5 cm (Figure 5.12). This ensured negligible interaction between the piles. This was extremely important since installing the piles away from the center line caused a lateral component of the centrifugal force to act on the piles.

Bolts were installed onto the walls of the test bed and all the wires from the sensors were tied down to the bolts using cable-ties. Enough slack was given to all the wires to prevent pulling of wires in-flight. The LVDT brackets were also mounted to one side of the test bed and fastened using bolts (Figure 5.12). The final soil profile consisted of a layer of kaolin with a thickness of 20 cm (14 m at prototype scale for the test acceleration of 70 g) over a drainage layer of sand with a thickness of 1 cm (0.7 m at prototype scale),

Table 5.3: Sequence of tests carried out

Phase	Date	Major changes from procedure	Quality of data
Calibration	Sept 2013	Sand used as foundation soil Different adaptor used	Usable
Phase One	Jan 2014	No standing water, Thickness of model pile = 1.47 mm, No LVDT used	Soil desiccated during testing
Phase Two	June 2014	-	Good data
Phase Three	Sept 2014	-	Good data

all of which was covered with a 4 cm freeboard of water (2.8 m at prototype scale).

The test bed was loaded onto the centrifuge basket and all the sensors were connected to the data acquisition system. Each sensor was verified to be working properly and the cables were secured.

5.4 Pile test methodology

The pile tests were carried out in different test beds. This section presents the main sequences of tests that were carried out to obtain usable data. The first test at RPI was a calibration carried out by installing multiple piles in a test bed of sand. The clay tests were divided into phases, with modifications being made in each phase based on information obtained from previous tests. Table 5.7 lists the different phases, the major difference from the test setup described in section 5.3.

The aim of the first calibration test was to finalize the design of the adaptor and pile caps to apply lateral load and obtain data using the strain gages. The Phase One test was mainly a ”lessons learned” test based on which the procedure and methodology was finalized and perfected to obtain good quality data. This section presents the testing plan and methodology of Phase Two and Three which resulted in all the data that is presented in this dissertation.

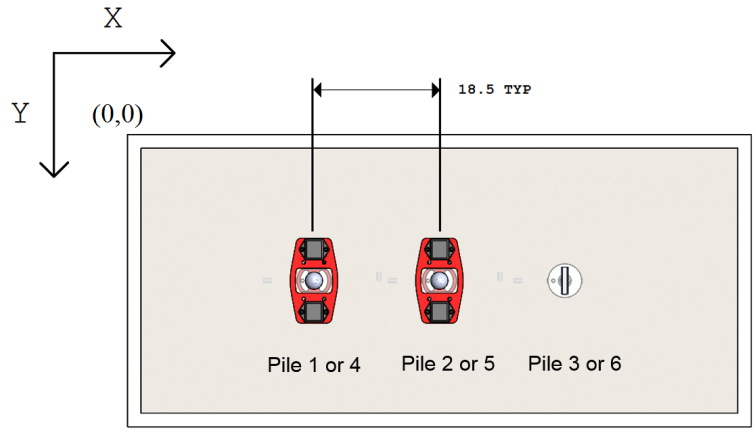

Figure 5.13: Schematic of top view of the testbed with piles installed.

5.4.1 Phase Two

Two sets of experiments were carried out in Phase Two in two separate test beds. Three piles were installed in each test bed as shown in Figure 5.13 thus leading to a total of six monopiles. During the tests connection fixity, eccentricity, displacement amplitude, and type of loading was varied. The aspect ratio (L/D) for the six foundations tested was 2. The test matrix for both sets of experiments is provided in Table 5.4.

Monopiles 1, 2 and 3 were monotonically loaded to failure in the -x direction, the piles were then subjected to 200 cycles of displacement controlled motion with various amplitudes all in the +x direction. After the cyclic loading, all the three piles were again monotonically loaded to failure in the -x direction.

Monopiles 4, 5 and 6 were first subjected to one way cyclic loading in the +x direction with various displacement amplitudes. After the cyclic loading all the three piles were loaded monotonically to failure in the -x direction. All the piles in both experiment 1 and 2, were loaded at a rate of 2 mm/s.

Two T-bar tests (one before and one after each pile test) were also carried out next to

Table 5.4: Test matrix of piles tested in Phase Two.

Test bed	Pile test	Connector type	e	No. of cycles	Displacement amplitude
1	1	Rigid	0	virgin monotonic (-x)	15 mm (30% of D)
				200 cycles (+x)	various
				post cyclic monotonic (-x)	15 mm (30% of D)
	2	Pinned	1.5	virgin monotonic (-x)	15 mm (30% of D)
				200 cycles (+x)	various
				post cyclic monotonic (-x)	15 mm (30% of D)
	3	Pinned	2.5	virgin monotonic (-x)	15 mm (30% of D)
				200 cycles (+x)	various
				post cyclic monotonic (-x)	15 mm (30% of D)
2	4	Rigid	0	200 cycles (+x)	various
				post cyclic monotonic (-x)	15 mm (30% of D)
	5	Pinned	1.5	200 cycles (+x)	various
				post cyclic monotonic (-x)	15 mm (30% of D)
	6	Pinned	2.5	200 cycles (+x)	various
				post cyclic monotonic (-x)	15 mm (30% of D)

each pile to obtain the strength profile of the clay. Coordinates of these tests are given in Table 5.5. All the T bars tests were be carried out along one side of the piles so as to not interfere with the pore pressure transducer wires embedded in the clay.

5.4.2 Phase Three

Similar to Phase Two, two sets of experiments were carried out in Phase Three in two separate test beds. Three piles were installed in each test bed as shown in Figure 5.13 leading to a total of six monopiles. During the tests connection fixity, eccentricity, displacement amplitude, and type of loading was varied. The aspect ratio (L/D) for the six foundations tested was 2. The test matrix for both sets of experiments is provided in Table 5.6.

Monopiles 1, 2 and 3 were monotonically loaded to failure in the -x direction, the piles were then subjected to 200 cycles of displacement controlled motion with various

Table 5.5: T-bar locations for Phase Two

Test bed number	Test number	Pile number	Type	X (mm)	Y (mm)
1	a	1	pre	370	310
	b	1	post	413.1	310
	c	2	pre	560	310
	d	2	post	597.2	310
	e	3	pre	270	310
	f	3	post	227.9	310
2	a	4	pre	190	335
	b	4	post	225	335
	c	5	post	401	335
	d	6	post	590	335

Table 5.6: Test matrix of piles tested in Phase Three.

Test bed	Pile test	Connector type	e	No. of cycles	Displacement amplitude
3	7	Pinned	1.2	virgin monotonic (-x)	15 mm (30% of D)
				50 cycles (+x)	various
				post cyclic monotonic (-x)	15 mm (30% of D)
	8	Pinned	2.5	virgin monotonic (-x)	15 mm (30% of D)
				50 cycles (+x)	various
				post cyclic monotonic (-x)	15 mm (30% of D)
	9	Rigid	0	virgin monotonic (-x)	15 mm (30% of D)
				50 cycles (+x)	various
				post cyclic monotonic (-x)	15 mm (30% of D)
4	10	Pinned	1.2	50 cycles (+x)	various
				post cyclic monotonic (-x)	15 mm (30% of D)
	11	Pinned	2.5	50 cycles (+x)	various
				post cyclic monotonic (-x)	15 mm (30% of D)
	12	Pinned	3.5	50 cycles (+x)	various
				post cyclic monotonic (-x)	15 mm (30% of D)

Table 5.7: T-bar locations for Phase Three

Test bed number	Test number	Pile number	Type	X (mm)	Y (mm)
3	a	1	pre	190	327
	b	1	post	230	327
	c	2	pre	370	327
	d	2	post	406	327
	e	3	pre	535	327
	f	3	post	592	327
4	a	4	pre	190	337
	b	4	post	270	337
	c	5	pre	360	337
	d	5	post	417	337
	e	6	pre	518	337
	f	6	post	598	337

amplitudes all in the +x direction. After the cyclic loading, all the three piles were again monotonically loaded to failure in the -x direction.

Monopiles 4, 5 and 6 were first subjected to one way cyclic loading in the -x direction with various displacement amplitudes. After the cyclic loading all the three piles were loaded monotonically to failure in the -x direction for the post cyclic capacity. All the piles in both experiment 3 and 4, were loaded at a rate of 2 mm/s.

Two T-bar tests (one before and one after the pile tests) were also carried out next to each pile to obtain the strength profile of the clay. Coordinates of these tests are given in Table 5.7. All the T bars tests were be carried out along one side of the piles so as to not interfere with the pore pressure transducer wires embedded in the clay.

The cyclic tests carried out in this research program is presented in a companion thesis by Beemer (2015).

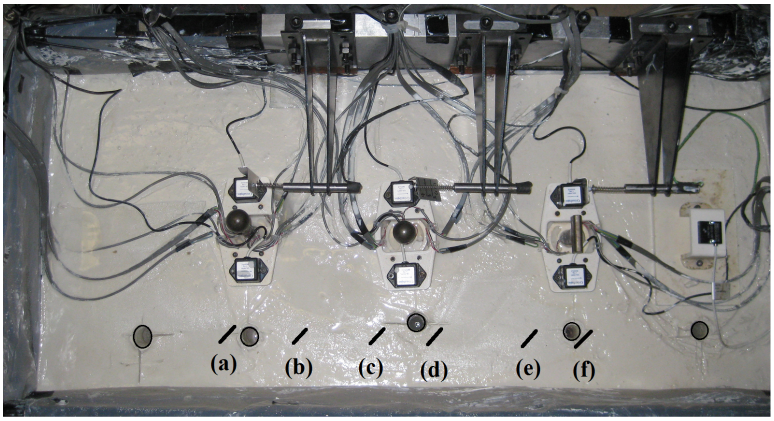

Figure 5.14: Location of water content cores and approximate T-bar test locations.

5.5 Test bed properties

Results in this dissertation are presented from pile tests carried out in 4 different centrifuge test beds: Phase Two - test bed 1, test bed 2 and Phase Three - test bed 3, test bed 4. Each of these test beds is characterized in this section. Water content measurements were taken across the width of each clay bed and T-bar tests were carried out to characterize the strength of the bed.

Figure 5.14 shows the top view of a representative test bed with the location of the water content cores and the approximate location of the Tbar tests. Coordinates of these tests for each test bed are given in Tables 5.5 and 5.7.

5.5.1 Water content profiling

Water contents were measured by extracting tube cores after the test was completed and the centrifuge spun down. Contour plots were made using the cores extracted and plotted to show the water content profiles along the length of each test bed. Figures 5.15, and 5.16 show the water content contour plots for test beds 1, 2, 3 and 4 respectively.

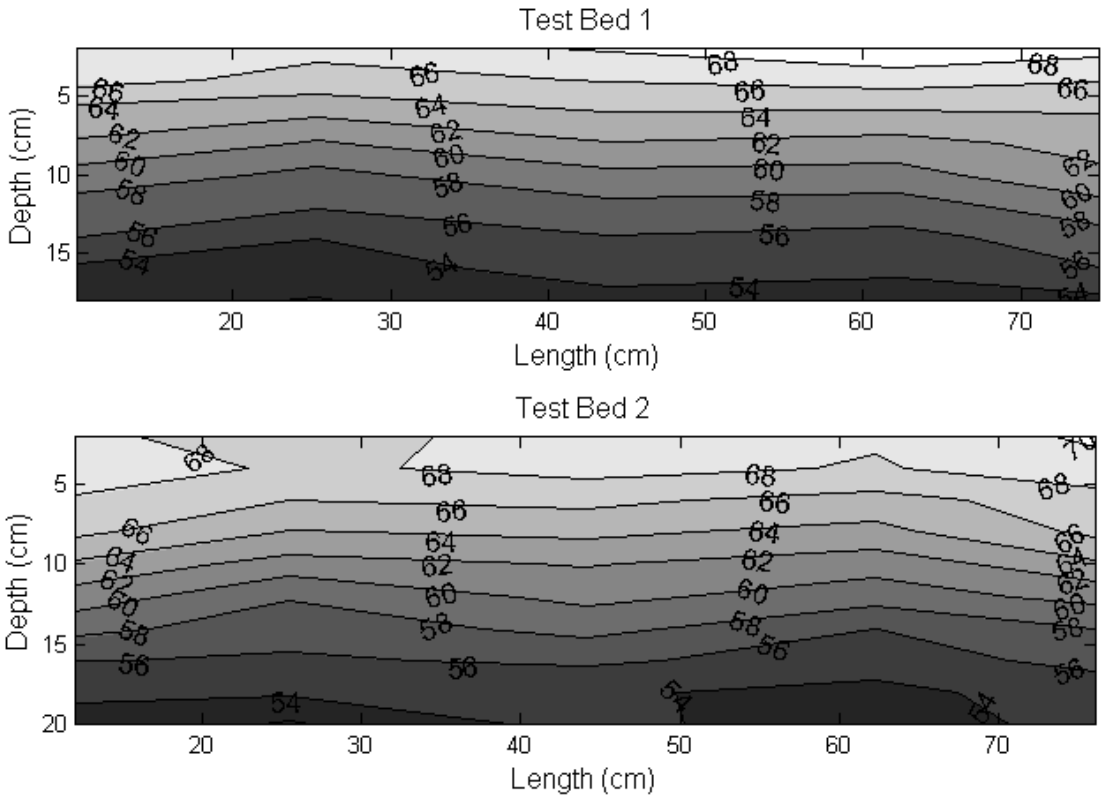

Figure 5.15: Water content contours across the length for test beds 1 and 2.

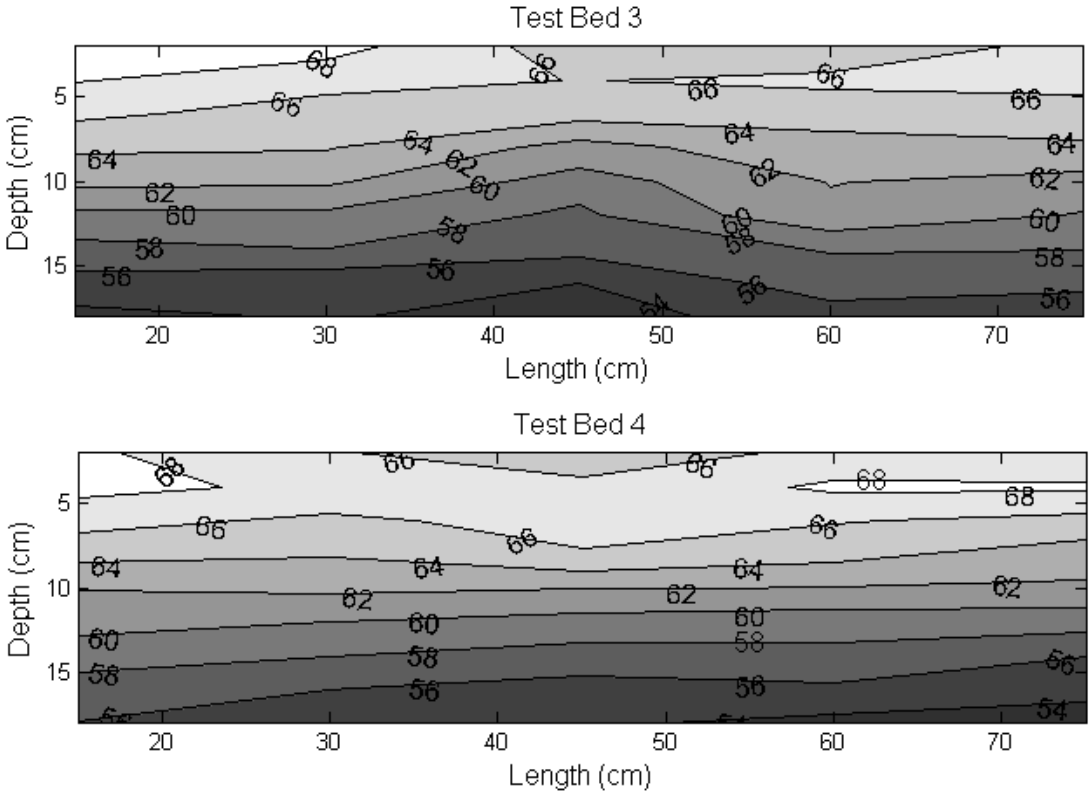

Figure 5.16: Water content contours across the length for test beds 3 and 4.

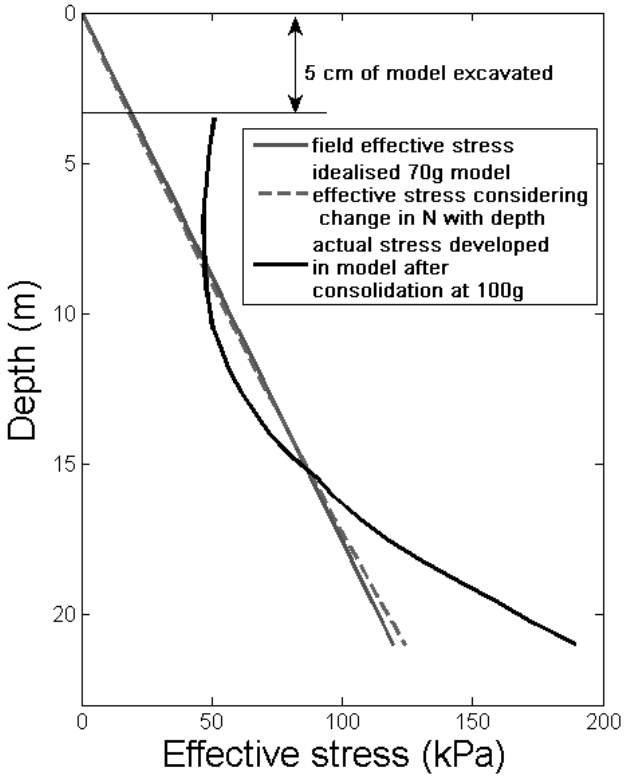

Figure 5.17: Actual stress developed in the model after consolidation at 100 g.

5.5.2 Strength characterization

Figure 5.17 shows the desired field effective stress profile and the expected effective stress profile developed in the model after consolidation at 100 g. The expected effective stress profile was computed assuming a linearly increasing initial pore pressure distribution. The estimated undrained shear strength profile of the clay bed based on effective stress and Stress History And Normalized Soil Engineering Properties (SHANSEP) parameters (Ladd et al., 1977) is computed and plotted in Figures 5.18, 5.19, 5.20, and 5.21.

The shear strength of the clay bed was characterized in flight by using a T-bar penetrometer developed at the University of Western Autralia Stewart and Randolph (1991) available at NEES@RPI (nees.rpi.edu). The tests were carried out using a T-bar that was

5 mm in diameter and 20 mm in length, at a penetration rate of 2 mm/s. This rate provided undrained conditions in kaolin and was also consistent with the rate of pile loading tests.

The T-bar makes use of the plasticity solution for the limiting pressure acting on a cylinder moving laterally through a purely cohesive soil Randolph and Houlsby (1984) based on a local flow-around failure method. Theoretical and numerical solutions have been developed to determine appropriate N_{kt} factors for estimating undrained shear strength Randolph (2004); Einav and Randolph (2005); Randolph and Andersen (2006); Martin and Randolph (2006); White et al. (2010). Based on the existing research a T-bar factor, N_{kt} of 10.5 was selected for computing shear strength below a depth of 1.4 m. The data from shallow depths was computed based on a different failure mechanism White et al. (2010). An adjustment was also introduced to correct for rate penetration effects of the T-bar Yafrate and DeJong (2007); DeJong et al. (2011). Equations for reduction of T-bar data is given in Appendix C.

Figures 5.18, 5.19, 5.20, and 5.21 present all the T-bar test results from four different model clay beds. The shear strength profiles are uniform until a depth of about 6 m below the mudline and gradually increase linearly for deeper sediments. There is good correlation between the measured shear strength profiles and the estimated shear strength profile computed using the effective strength profile. As seen in the figures multiple T-bar tests were carried out spanning a time of approximately 2 hours in the centrifuge, explaining the steady increase in average strength with each consecutive test. At a depth of 7 m (base of the monopile) the strength increases from 8 kPa to 11 kPa from the first T-bar test to the last for the first test bed. For the same soil depth the strength increases from 7 kPa to 9 kPa for the third test bed.

The figures 5.18, 5.19, 5.20, and 5.21 also plot the range of shear strength computed using the range of water content (minimum and maximum measured) values from the multiple cores extracted against prototype depth for the test bucket. The correlation between

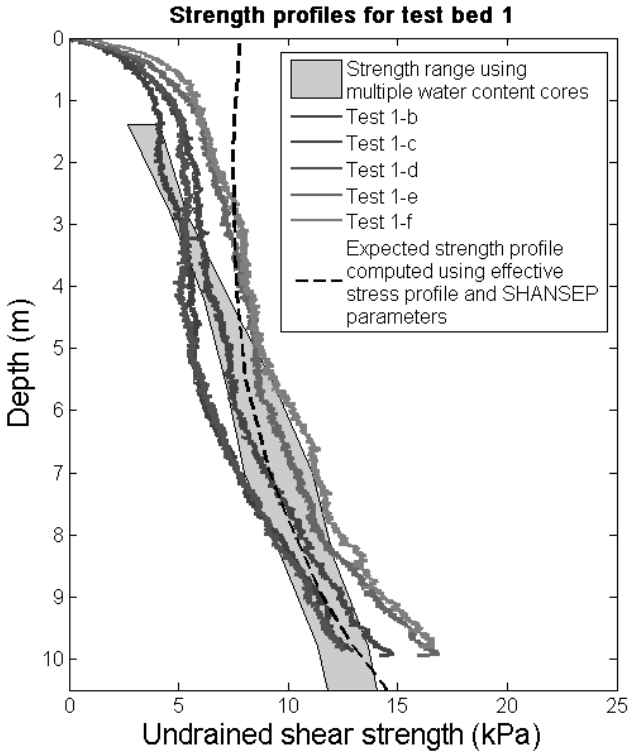

Figure 5.18: Profiles for undrained shear strength for test bed 1 (Phase 2)

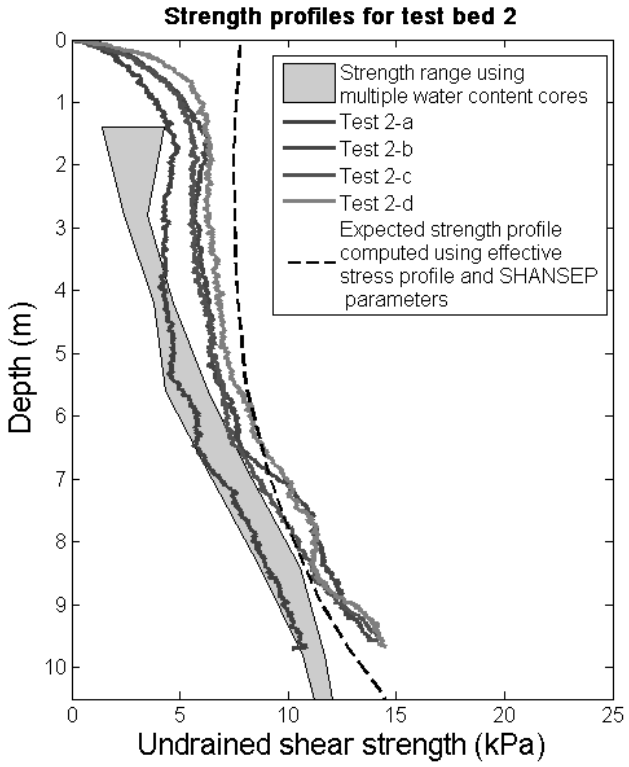

Figure 5.19: Profiles for undrained shear strength for test bed 2 (Phase 2)

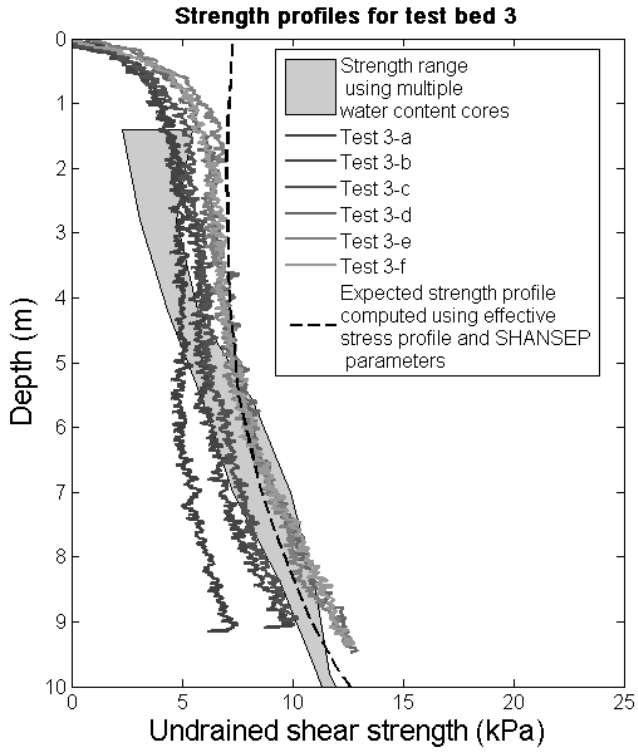

Figure 5.20: Profiles for undrained shear strength for test bed 3 (Phase 3)

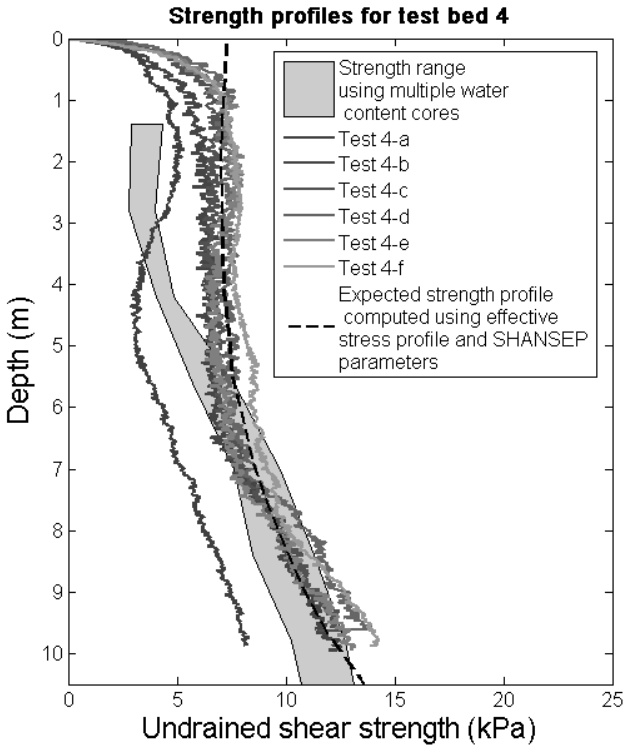

Figure 5.21: Profiles for undrained shear strength for test bed 4 (Phase 3)

water content and strength was computed using Tessari (2012). As observed from the figures all the strength profiles compare very well for all the four test beds.

6. CENTRIFUGE MONOTONIC EXPERIMENTAL RESULTS

This section presents results from pile tests carried out at a centrifugal acceleration of 75 g (at the pile mid-depth), in 4 different test beds: Phase Two - test bed 1 and 2 and Phase Three - test bed 3 and 4. Twelve different piles were tested at different eccentricities (e = 0, 1.2, 1.5, 2.5 and 3.5) and different types of loading conditions (rotation and translation) details of which are given in Table 6.1. All of the piles were pushed laterally by a large displacement (15 mm - 30% of the pile diameter) to obtain the ultimate lateral capacity. The effects of moment loading applied at different eccentricities and horizontal loading on piles of aspect ratio of two was examined under extreme loading conditions such as collisions (ice berg and ships) and storm loading.

As mentioned in Chapter 6, T-bar penetrometer tests were carried out before and after each pile test to obtain the strength profile of the clay next to each pile. Since multiple pile tests were carried out in the same clay bed spanning a time of 2 hours (408 days in prototype time), each test was normalized by the appropriate shear strength profile (Refer Section 6.2) to remove the effects of strengthening the clay bed through continued consolidation with time.

6.1 Ultimate lateral capacity

6.1.1 Translational response

The load-deflection curve for the pile tested in pure translation is presented in Figure 6.1 along with the calculated ultimate lateral capacity using methods proposed by Murff and Hamilton (1993), the API method (API, 2000) and finite element analysis carried out by Grajales (2015) for comparison. The lateral head load, H, is normalized by the product of the projected vertical area, LD, and a shear strength profile $s_{u,avg}$ based on the T-bar and water content strength profiles over the depth of pile embedment. The ultimate capacity is

Table 6.1: Monotonic test matrix.

Movement	Eccentricity (e)	Monotonic test	
		first loading	post-cylic
Translation	0	P9	-
Rotation	1.2	P8	P8 test2
			P11
	1.5	P2	P2 test2
			P5
	2.5	P1	P1 test2
		P7	P4
			P7 test2
			P10
	3.5	-	P12

defined as the peak value measured for piles tested in translation. Details on computing the average shear strength, $s_{u,avg}$ based on T-bar and water content data is given in Appendix C.

The pile was pushed horizontally to a displacement equal to 30% of the pile diameter, to maintain a suitable distance between adjacent piles during testing. This was not a limitation to compute the ultimate capacity as 30% lateral strain is considered well above failure. The pile appears to reach its peak value at about 24% displacement amplitude, with the computed horizontal bearing capacity factor (N_h) being equal to 8.7.

As seen from the figure, the ultimate bearing capacity of the pile tested in translation is found to fall in between Murff and Hamilton's empirical upper bound solution for the case of a smooth pile ($\alpha = 0$) with no gap behind the pile and the case of a rough pile ($\alpha = 1$) with the formation of a gap behind the pile. The solution for the case of a rough pile with gapping was found to be 9% higher than the measured ultimate capacity.

The API method was found to be conservative for this aspect ratio by about 42%. FEM analysis for the same aspect ratio, computed for a rough pile assuming no gapping compares well with Murff's solution and was found to be 26% higher than the measured

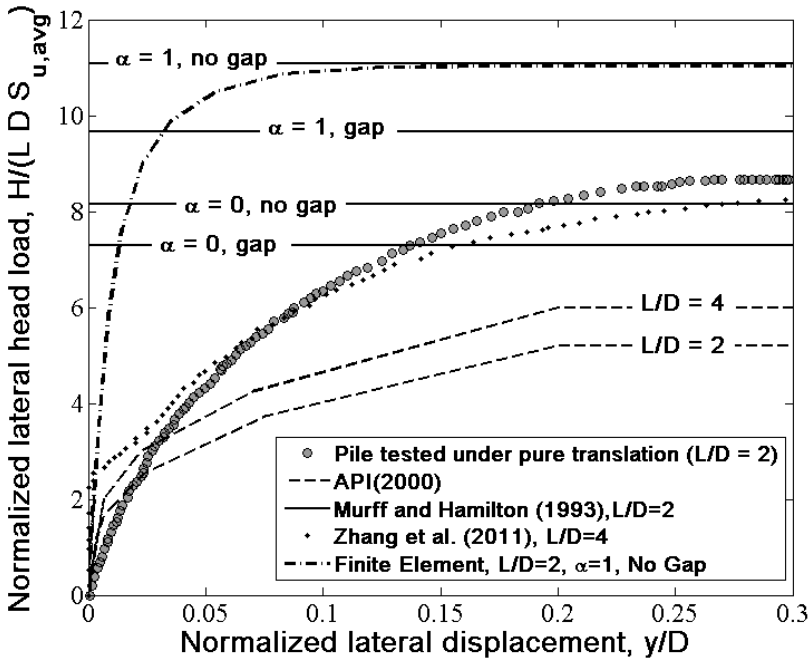

Figure 6.1: Comparison of force-displacement curve and other formulations to compute load.

experimental data (Grajales, 2015). Also seen in Figure 6.1 is the centrifuge test carried out on piles of aspect ratio equal to five (Zhang et al., 2011). The peak capacity for a pile of aspect ratio of 5 is found to be slightly lower than the measured value obtained in this testing program (L/D = 2) by 5.7%.

Formation of gaps was observed between the back of the pile and the soil for each test (Figure 6.8). This gapping depth however could not be measured accurately. A gap was also observed in the centrifuge test carried out by Zhang et al. (2011) at about 50% lateral strain.

6.1.2 Rotational response

The monotonic response of the monopile subject to rotation was examined for four different eccentricities; 1.2D, 1.5D, 2.5D and 3.5D. The load displacement curves for all

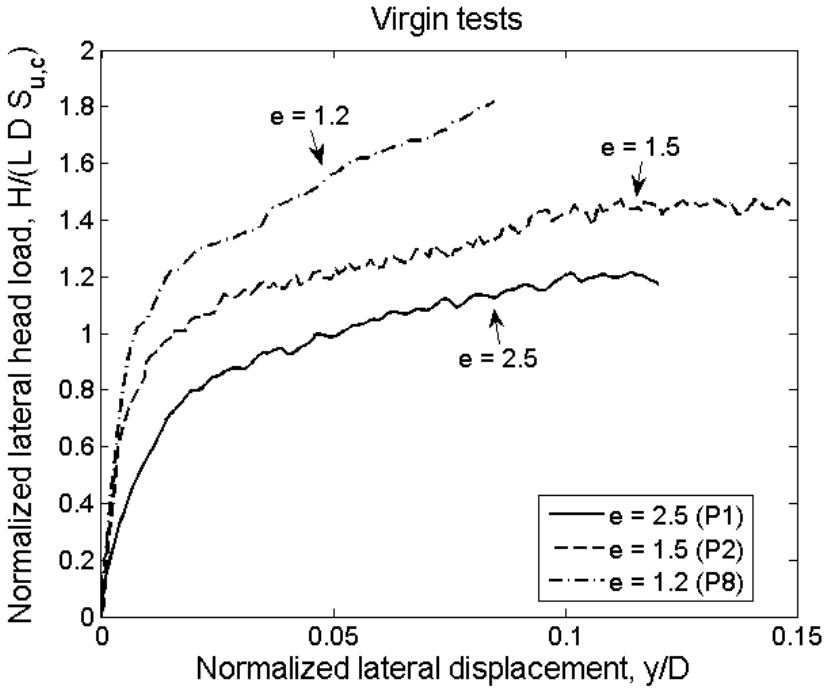

Figure 6.2: Force displacement curve for piles in rotation (first loading)

of the piles tested in rotation is presented in Figures 6.2 (first loading) and 6.3 (post cyclic loading). The lateral head load, H, at the top of the pile cap was computed and normalized by the product of the projected vertical area, LD, and an average shear strength profile over the depth of pile embedment, $s_{u,avg}$. The lateral displacement, y, was computed at the mudline using the tilt and displacement measurements and normalized by the pile diameter, D.

All the piles were pushed laterally at the top of the ball and socket connector to a displacement amplitude equal to 30% of the pile diameter. Thus the pile displacement amplitude at the mudline varied depending on the eccentricity.

As expected the ultimate lateral capacity of the piles decreases with increasing eccentricity for both first loading and post cyclic monotonic loading. Also observed is that the

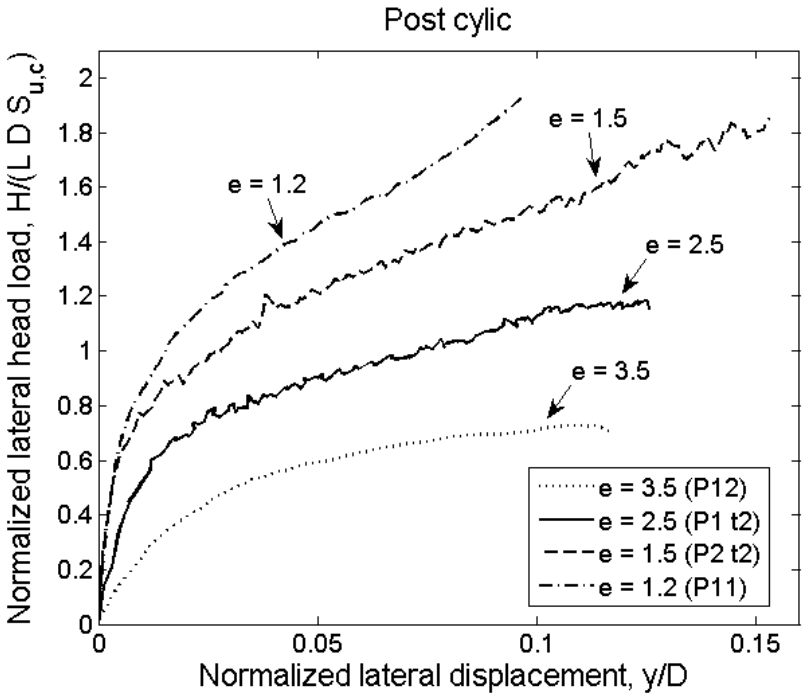

Figure 6.3: Force displacement curve for piles in rotation (post cyclic loading)

piles tested in rotation mobilize increasing strength with increasing displacements due to the rotational failure mechanism of short aspect ratio piles.

Figures 6.4, 6.5 and 6.6 present the primary loading force displacement curves for eccentricities of 1.2, 1.5 and 2.5. Also presented, are the bearing capacity factors computed for a caisson of L/D of 2 with the eccentricities of 1.2, 1.5, and 2.5 and a linear soil strength profiles for each test, based on Aubeny et al. (2003) and Aubeny et al. (2001) plastic limit analysis (Grajales, 2015). The bearing factors were computed for two cases, with gapping at the back of the monopile (no suction) and without gapping at the back of the monopile both with an adhesion factor (α) of 0.7 based on Chen and Randolph (2005).

The experimental bearing factors are bounded by the values predicted using the analysis after Aubeny et al. (2003) for the cases of gapping and no-gapping behind the pile.

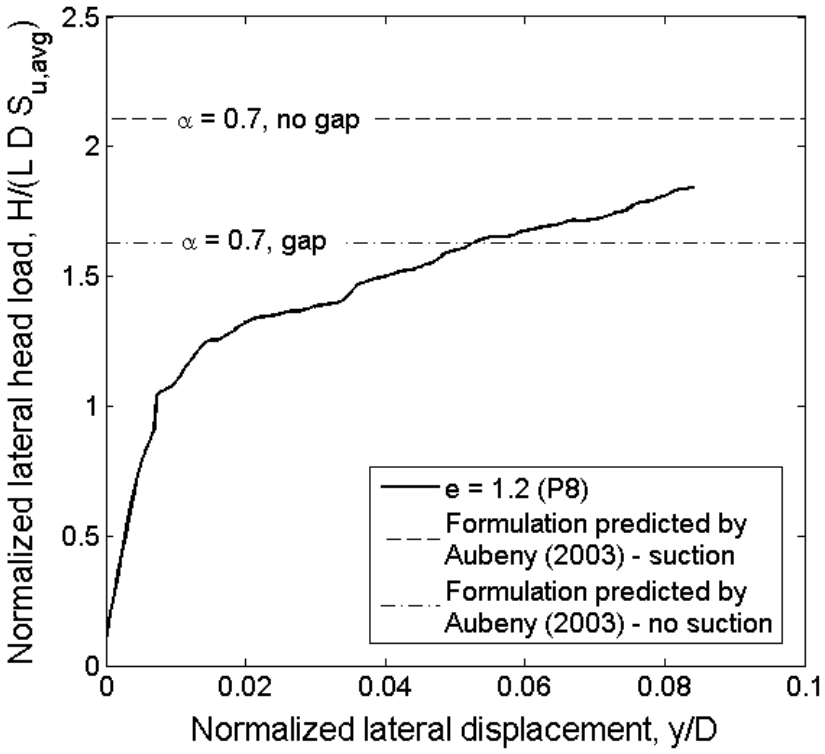

Figure 6.4: Force displacement curve for e = 1.2 (first loading)

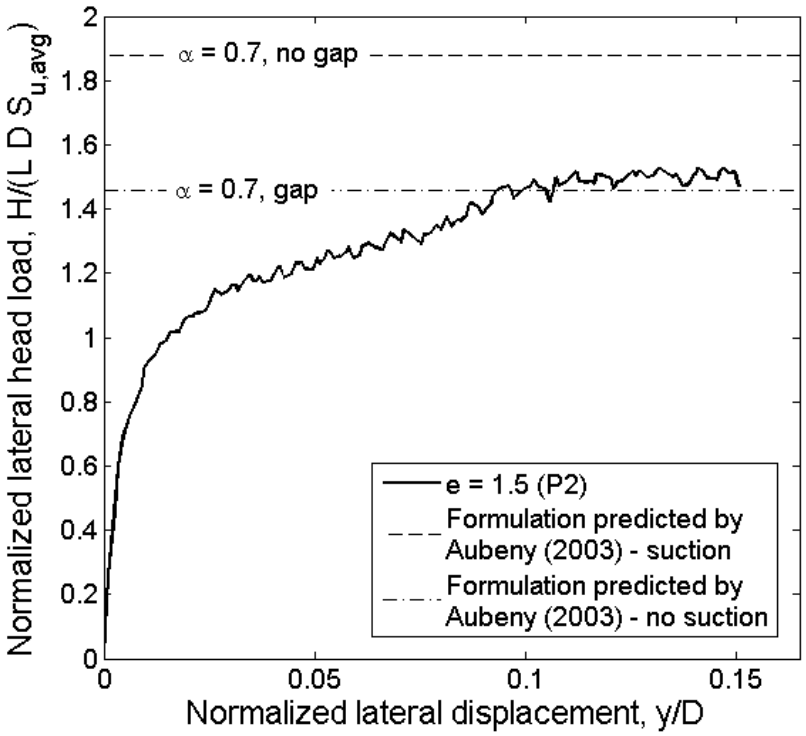

Figure 6.5: Force displacement curve for e = 1.5 (first loading)

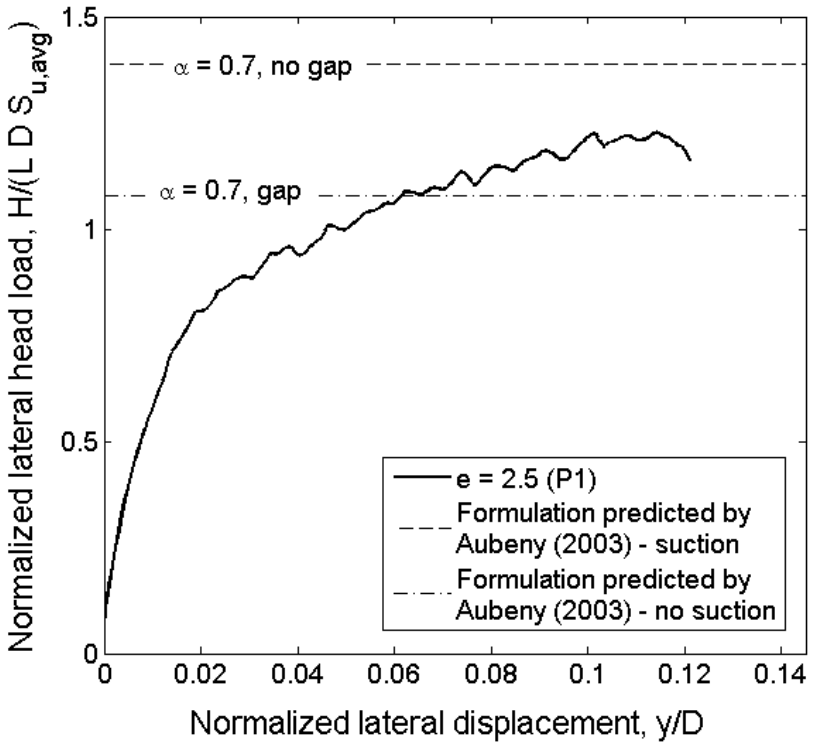

Figure 6.6: Force displacement curve for e = 2.5 (first loading)

The experimental bearing factors for the piles tested at eccentricities of 1.5 and 2.5 compare very well with the formulation predicted for the case of gapping (Refer Figure 6.8). The normalized horizontal load bearing factors, N_h, both experimental and numerical, for these tests are given in Table 6.2.

Figures 6.7 (a), (b), (c) and (d) present the post cyclic loading force displacement curves for eccentricities of 1.2, 1.5, 2.5 and 3.5 along with the bearing capacity factors computed for a caisson of L/D of 2 with the eccentricities of 1.2, 1.5, 2.5 and 3.5 and a linear soil strength profile, based on Aubeny et al. (2003) and Aubeny et al. (2001) plastic limit analysis (Grajales, 2015). Similar to the primary loading curves the bearing factors were computed for two cases, with gapping at the back of the monopile (no suction) and without gapping at the back of the monopile both with an adhesion factor (α) of 0.7.

The slight discrepancies in bearing factors between the experimental and the upper bound plastic limit analysis results are thought to be due to a combination of reasons. A major contributing factor is thought to be due to the combined effect of vertical and moment loading. There was also the presence of gapping at the back of the pile, extended to varying depths along the length of the pile. This depth of gapping could not be quantified for the different model pile tests. Another possible source of error is the plastic coating applied on the piles to prevent corrosion of the strain gages. It was not possible to quantify the adhesion on the sides of the pile.

All the piles tested in rotation appeared to be strain hardening with the lateral load gradually increasing even after failure (Figures 6.2 and 6.3). Murff and Hamilton (1993) discussed collapse mechanisms where a conical wedge forms near the soil surface and is pushed up by the pile. Also mentioned is the bottom kick for short piles. Aubeny et al. (2001) presented a simplified analysis for the tip failure mechanism consisting of a spherical failure surface (Figure 6.9).

Similar to the pile tested in translation, these piles were not constrained vertically and

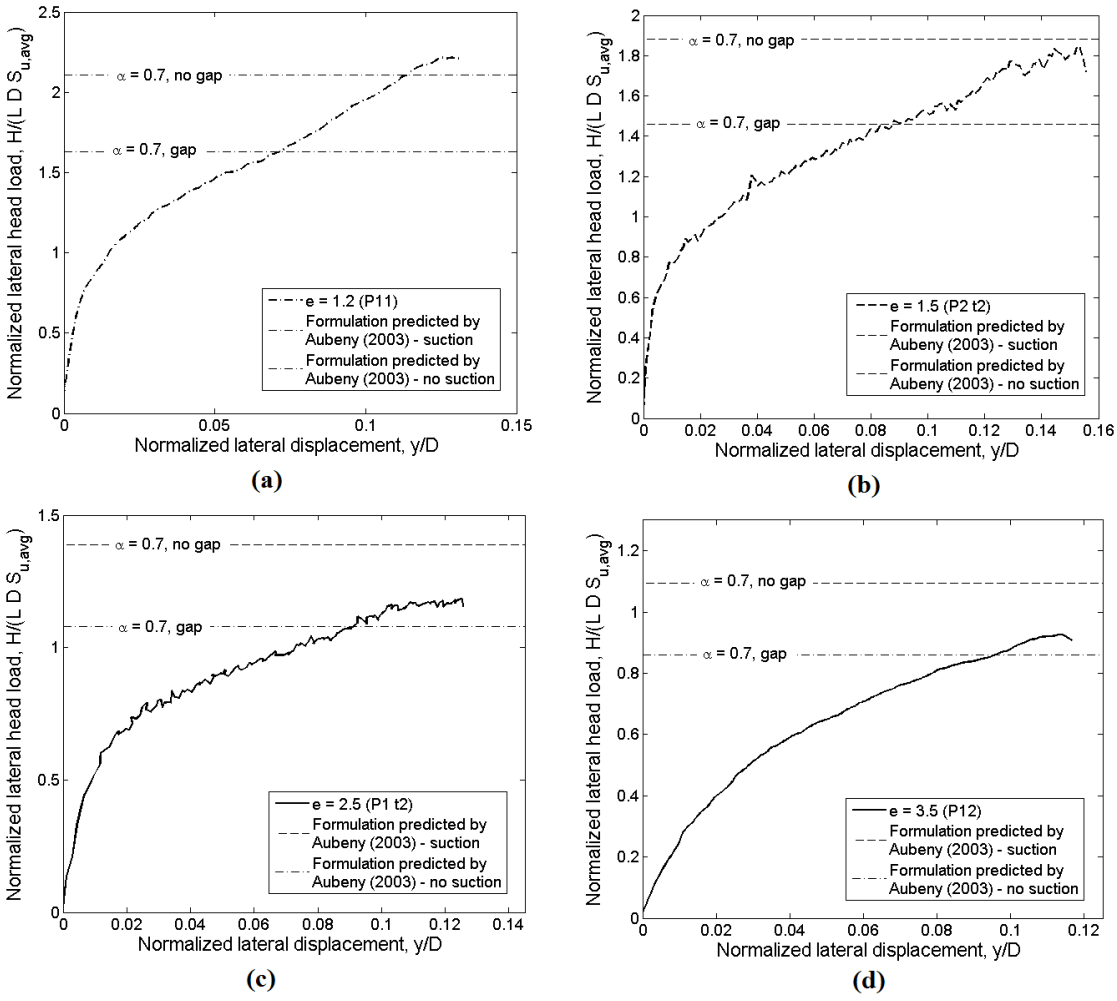

Figure 6.7: Force displacement curve for post cyclic curves (a) e = 1.2; (b) e = 1.5; (c) e = 2.5; (d) e = 3.5

Table 6.2: Normalized lateral load bearing factors

Pile test	e	N_h experimental	N_h - gap (Aubeny et al., 2003)	N_h - no gap (Aubeny et al., 2003)
P12	3.5	0.94	0.859	1.094
P1	2.5	1.25	1.08	1.387
P1 t2	2.5	1.26	1.08	1.387
P2	1.5	1.5	1.46	1.88
P2 t2	1.5	1.8	1.46	1.88
P8	1.2	1.8	1.63	2.11
P11	1.2	2.2	1.63	2.11

Figure 6.8: View of gap observed in a large displacement test

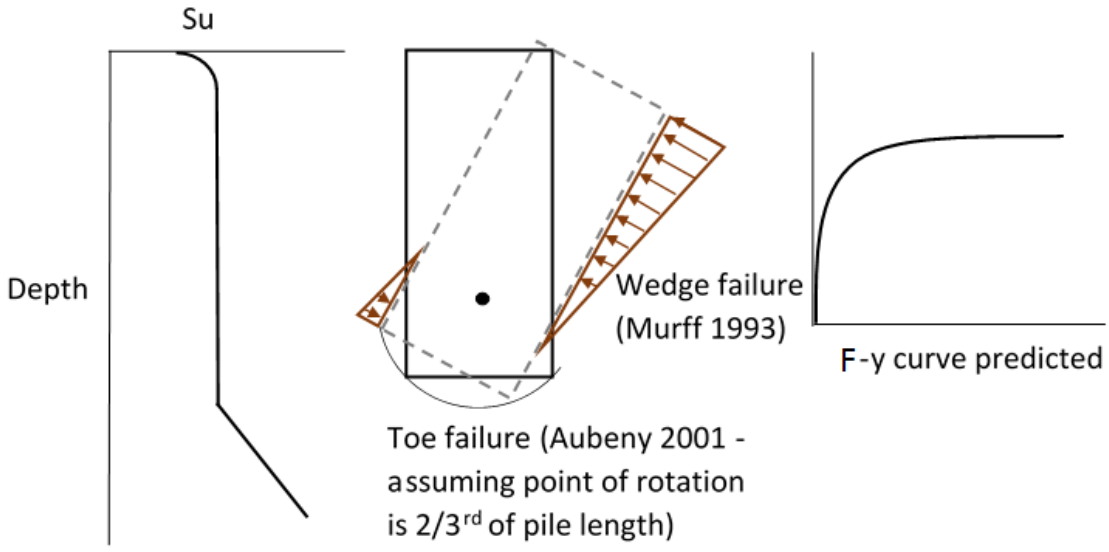

Figure 6.9: Sketch of expected behavior of pile failing in rotation (Not to scale and exaggerated displacements)

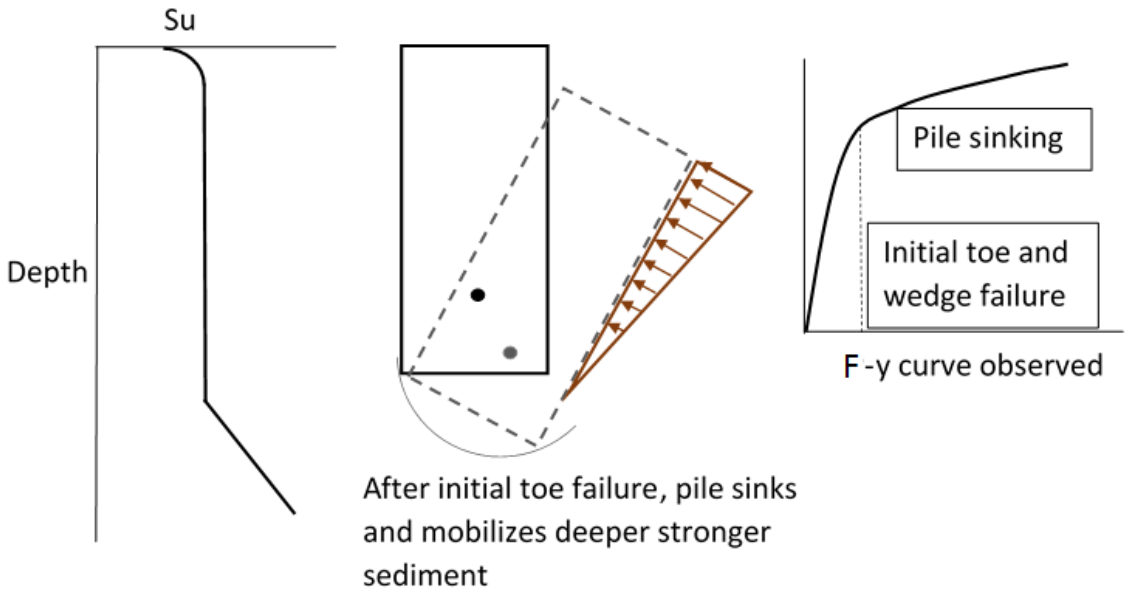

Figure 6.10: Sketch of observed behavior of pile failing in rotation (Not to scale and exaggerated displacements)

were free to move, the combined loading condition of the self weight and the lateral load applied by the robot contributed to settlement or sinking of the pile after the initial wedge and toe failure (Figure 6.10). Figures 6.9 and 6.10 show the sketch of the expected and observed behavior in the pile tests.

A plasticity analysis (refer Section 6.2) was carried out to estimate settlement based on Aubeny et al. (2003) and Aubeny et al. (2001).

6.1.2.1 Comparing first loading and post cyclic loading

Figures 6.11 (a), (b) and (c) compare the normalized ultimate capacity and normalized post cyclic capacity of three eccentricities (1.2, 1.5 and 2.5) tested. From the figures, it appears that post cyclic capacity is slightly lower compared to the ultimate capacity. The post cyclic test has a slightly larger failure strain as compared to the first loading test showing that the failure load is mobilized at a larger displacement amplitude. Also

observed, is that the change in slope is more distinct for the ultimate capacity curves whereas it changes gradually for the post cyclic capacity.

6.1.2.2 Comparing repeat tests

Figure 6.12 (a), (b) and (c) compare identical tests at the same eccentricities carried out in different test beds. The multiple repeat tests compare fairly well with each other. The variation in normalized load for all tests occurs after 3.5% lateral strain (after ϵ_f for each test). This variation is assumed to be due to differences in vertical settlement of each pile test and could not be accounted for accurately in the calculation since vertical settlement of the pile was not monitored.

6.1.3 Ultimate vertical load

Although the focus of this research program was on lateral capacity of monopiles, combined loading of lateral and vertical loads is an important design consideration. In these experiments the self weight of the pile and connectors simulated the constant vertical load of a light structure, while the lateral and moment loads were applied to reproduce the environmental loads on the foundation. The ratio of vertical to horizontal load (V/H) for these pile tests was computed to be in the range of 2.4 to 2.9. Existing values for V/H ratio for offshore wind turbines in the literature are found to be ranging from 2.1 to 5.8 (Argyriadis et al., 2005; Lesney and Wiemann, 2005). Based on Martin (2001)'s vertical bearing capacity factors, for an aspect ratio of 2 and assuming a lower bound analysis for a smooth pile in homogenous soil, approximately 64% of the total vertical bearing capacity was mobilized for pile with e = 1.2 (lowest vertical load) and 80% of the total vertical bearing capacity was mobilized for the pile with e = 3.5 (highest vertical load). See Appendix D for calculations.

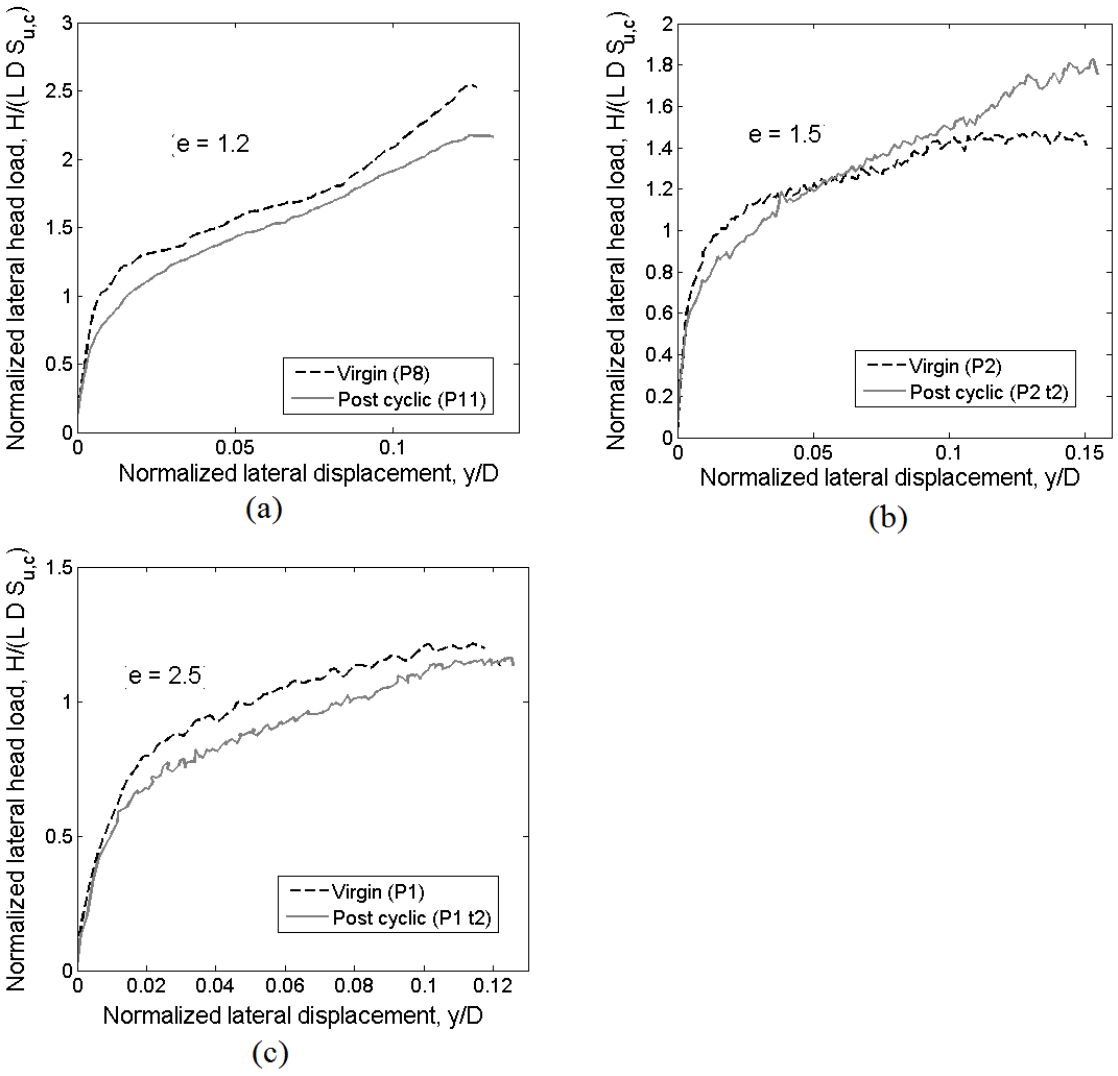

Figure 6.11: F_h-y curves comparing ultimate capacity with post-cyclic capacity

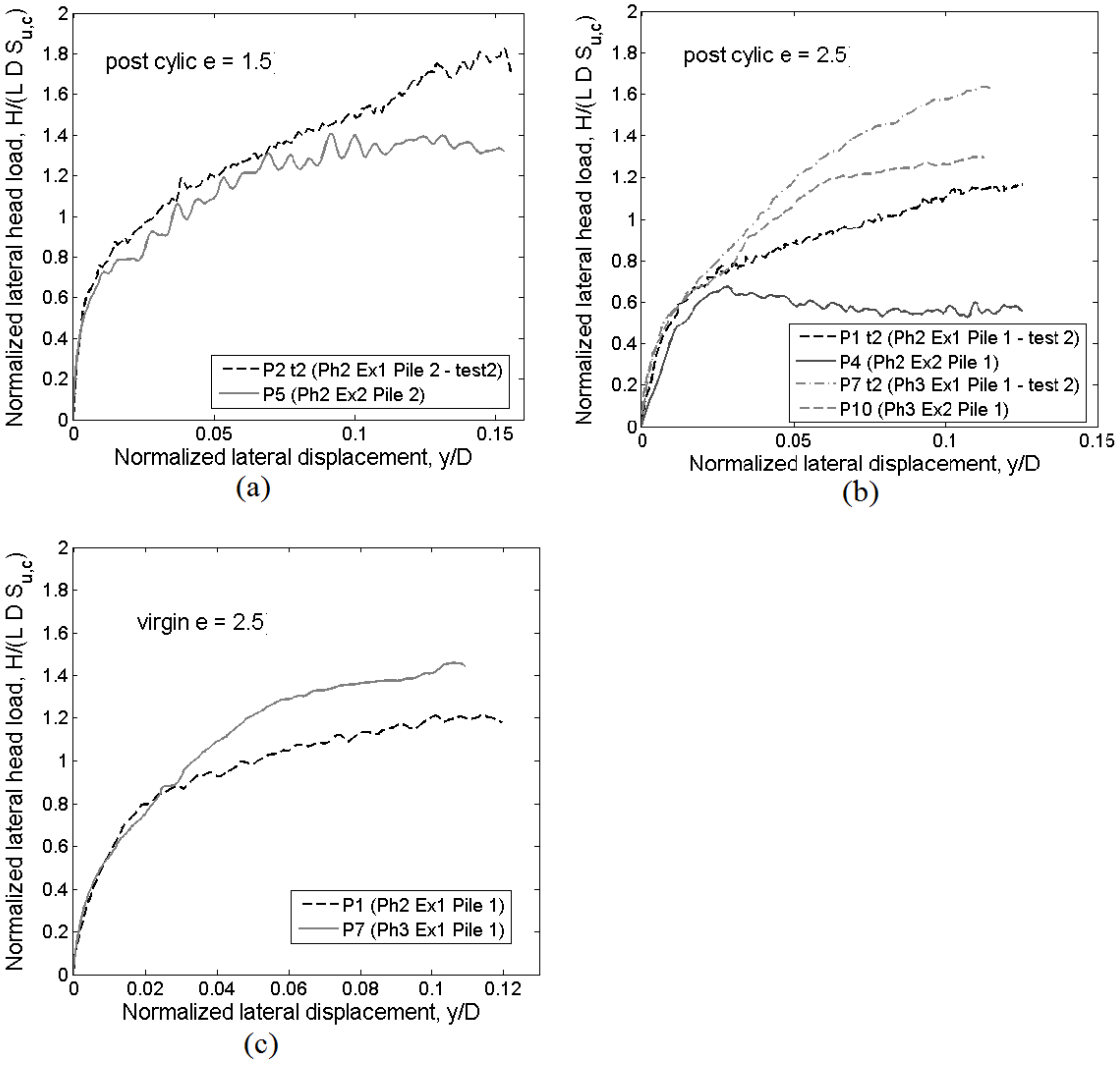

Figure 6.12: F_h-y repeat pile tests

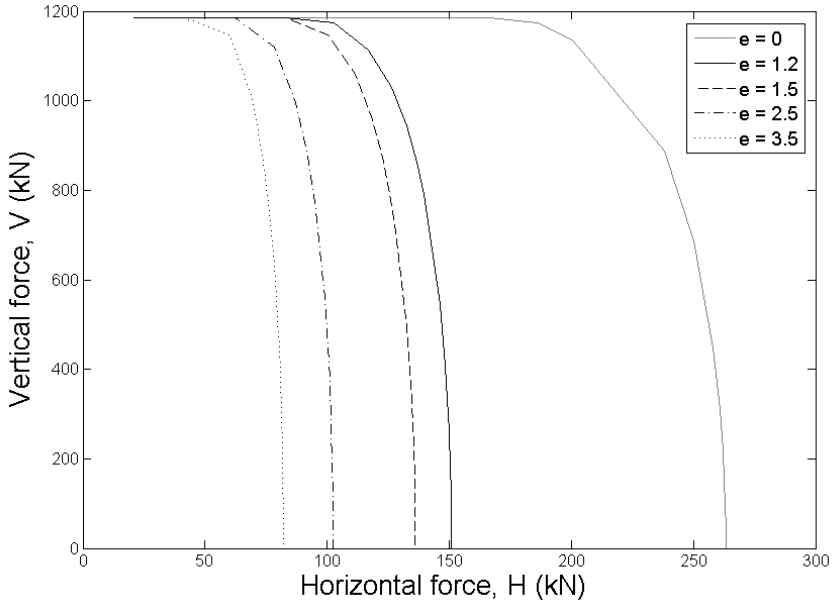

Figure 6.13: Yield envelopes developed using Aubeny et al. (2003)'s upper bound plasticity formulation

6.2 Estimating vertical settlement

Aubeny et al. (2003)'s simplified method of analysis for estimating inclined load capacity of suction caissons based on an upper bound plasticity formulation was used to develop yield envelopes in the V-H (combined vertical and horizontal) load space for a uniform soil strength profile until the tip of pile and then linearly increasing soil strength profile. Different failure envelopes were developed for eccentricities of 0, 1.2, 1.5, 2.5 and 3.5 with caisson dimensions equal to the prototype caisson dimensions (L = 7 m and D = 3.5 m) shown in Figure 6.13.

An empirical curve fit of the form as shown in Equation 6.1 was determined for each of the eccentricities based on Figure 6.13. Vertical settlement and horizontal displacement are given by Equations 6.2 and 6.3 based on the combined load effect. The ratio of vertical settlement to horizontal displacement is given by Equation 6.4 and is plotted in Figure 6.14

for the eccentricities of 0, 1.2, 1.5, 2.5, and 3.5 with increasing V/V_{max}, implying that an increase in the vertical load leads to an increases in the vertical settlement of the pile.

$$f(V,H) = (\frac{V}{V_{max}})^m + (\frac{H}{H_{max}})^n - 1 = 0 \tag{6.1}$$

Where V_{max} and H_{max} are maximum vertical and horizontal loads correspondingly, m and n are empirical exponents for each curve.

$$u_v = \lambda \frac{\partial f(V,H)}{\partial V} = \lambda m (\frac{V}{V_{max}})^{m-1} \frac{1}{V_{max}} \tag{6.2}$$

$$u_h = \lambda \frac{\partial f(V,H)}{\partial H} = \lambda n (\frac{H}{H_{max}})^{n-1} \frac{1}{H_{max}} \tag{6.3}$$

$$\frac{u_v}{u_h} = \frac{m}{n} \frac{(V/V_{max})^{m-1}}{H/H_{max})^{n-1}} \frac{H_{max}}{V_{max}} \tag{6.4}$$

Where, u_v and u_h are vertical settlement and horizontal displacement respectively, and λ is an empirical coefficient.

6.3 Center of rotation

6.3.1 Translation

Tilt sensors were placed on the pile tested in translation enabling the measurement of the rotation point along with the displacement data from the LVDTs. Figure 6.15 shows the variation of the center of rotation below the mudline plotted vs time. As observed in the figure, the monopile does experience some tilt during the initial phase of the test due to compliance of the connector which stabilizes at about 130 mm below the mudline, this rotation point then gradually progresses deeper as the pile is laterally strained during the loading. There is a point when the slope of the drop in rotation becomes a constant,

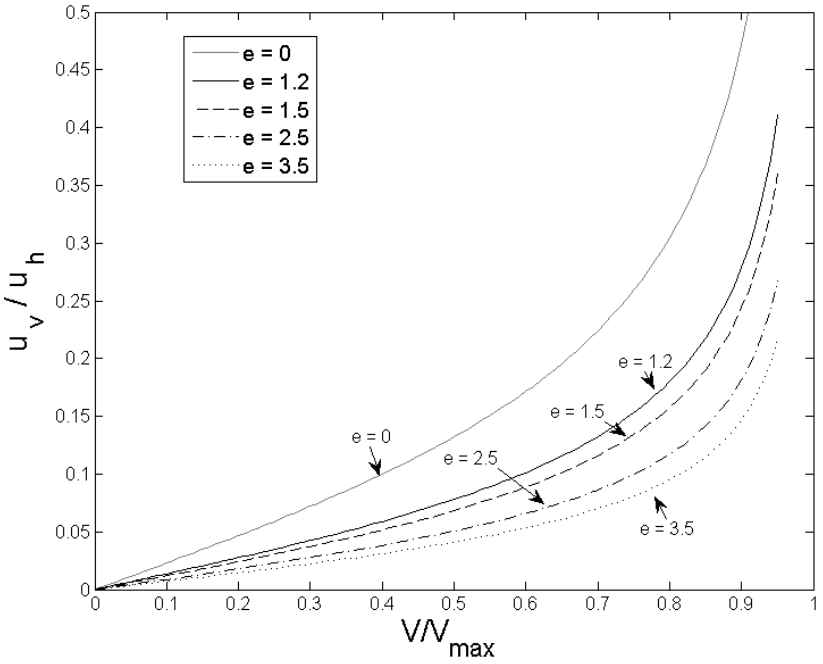

Figure 6.14: Estimated ratio of u_v/u_h vs increasing vertical load.

that is the indication that the pile in pure translation. Theoretically the center of rotation should jump to infinity when the pile starts translating however due to the compliance of the connector that is not practically feasible. The center of rotation is computed quite easily using the displacement (y) measured at the top and the angle (θ) from the vertical, the center of rotation is given by $y/tan(\theta)$.

6.3.2 Rotation

The short rigid monopile rotates about a point without flexing significantly. The variation of the center of rotation as the pile undergoes lateral loading is presented in Figures 6.16 and 6.17 for first loading and post cylic loading respectively. The mudline and the bottom of the monopile are indicated in the figures.

The figures shows that the rotation point drops below the base of the monopile but

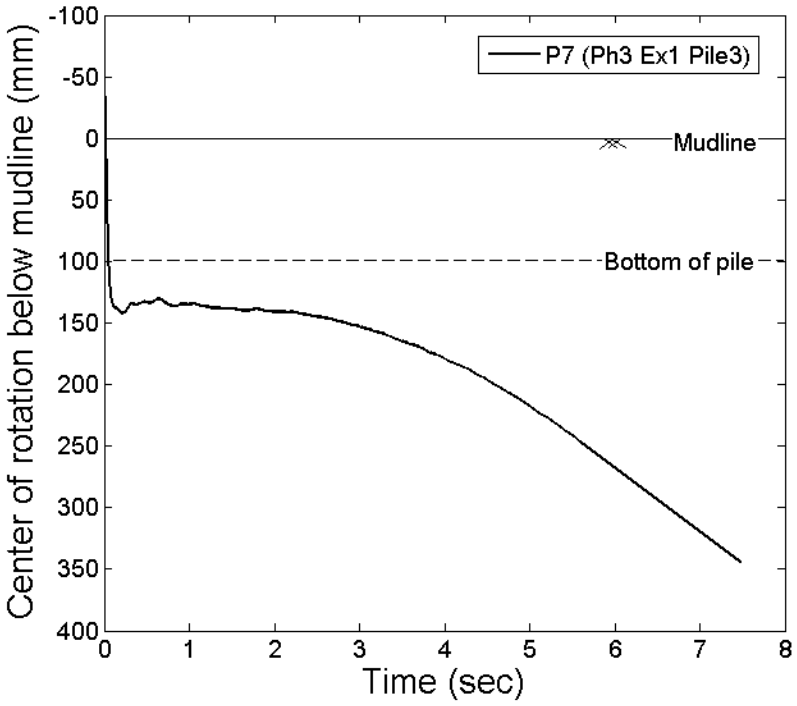

Figure 6.15: Variation of center of rotation (translation pile test)

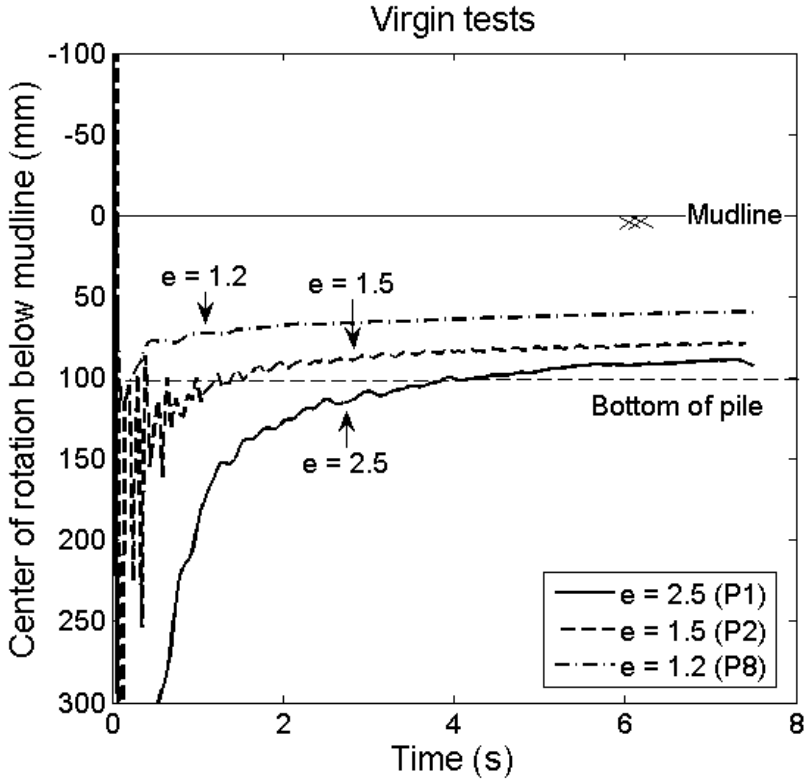

Figure 6.16: Variation of center of rotation (first loading)

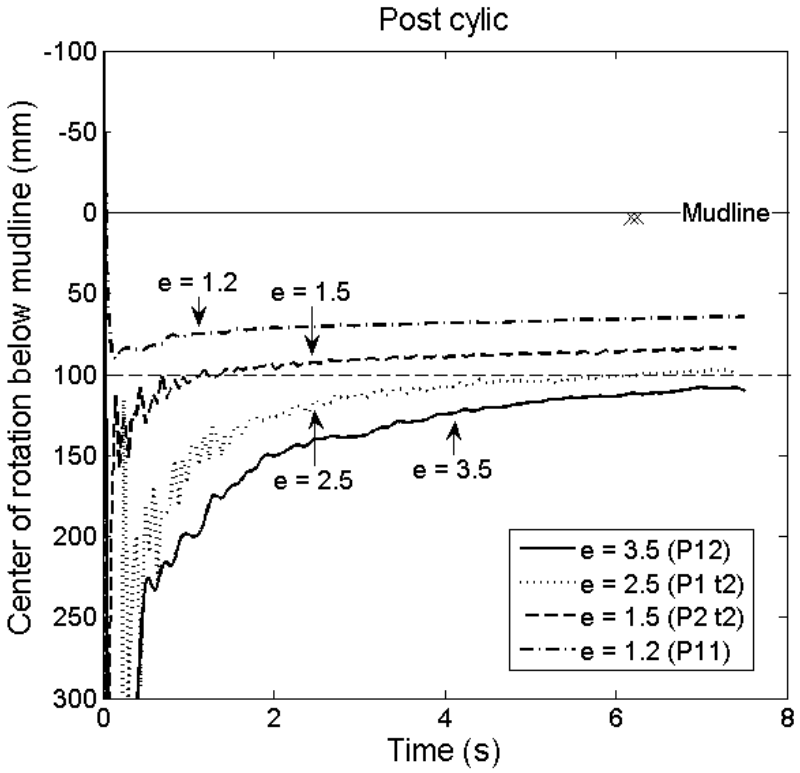

Figure 6.17: Variation of center of rotation (post cyclic loading)

Table 6.3: Center of rotation of all piles

Eccentricity	L_{CoR}/L
3.5	1.1
2.5	0.8 - 1
1.5	0.78 - 0.84
1.2	0.6 - 0.64

quickly stabilizes at a depth ranging between the pile mid-depth and the pile base. Also observed in Figures 6.16 and 6.17 is that the center of rotation moves deeper below the mudline and closer to the pile base with increase in eccentricity. Table 6.3 shows the range of center of rotation normalized by the embedded length of the monopile, L_{CoR}/L, for all the pile tests carried out in this experimental program. Lau et al. (2014) carried out centrifuge testing on monopiles of aspect ratio (L/D) of 5.2 with an eccentricity of 1.5 and experimentally determined their point of rotation to be at a depth of 0.7L below the mudline. This suggests that differing aspect ratio (applicable only to short rigid monopiles) might not influence the center of rotation as much as change in eccentricity or point of loading.

Figure 6.18 shows the center of rotation varying with normalized pile head displacement for 4 representative piles tests. The center of rotation stabilizes much faster with decreasing eccentricity suggesting that the tip failure mechanism consisting of a spherical failure surface (Aubeny et al., 2001) occurs earlier or at a lower normalized displacement for the piles at lower eccentricity.

This is also observed in Figure 6.19 (a), (b) and (c) which shows the rotation points for multiple tests carried out at e = 1.2, 1.5 and 2.5 respectively. The y axis scale is kept constant for comparison. The rotation points for piles tested at e = 1.2 and 1.5 compare really well with each other regardless of first loading or post cyclic loading. The piles tested at e = 2.5 shows some variability with the L_{CoR}/L ratio ranging between 0.8 to 1.

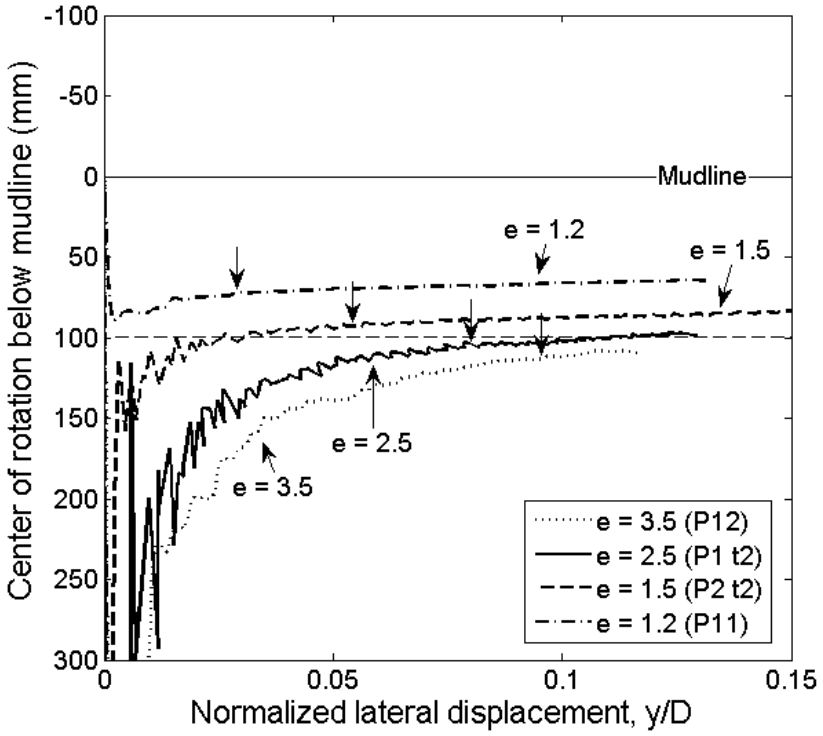

Figure 6.18: Variation of center of rotation with displacement at mudline

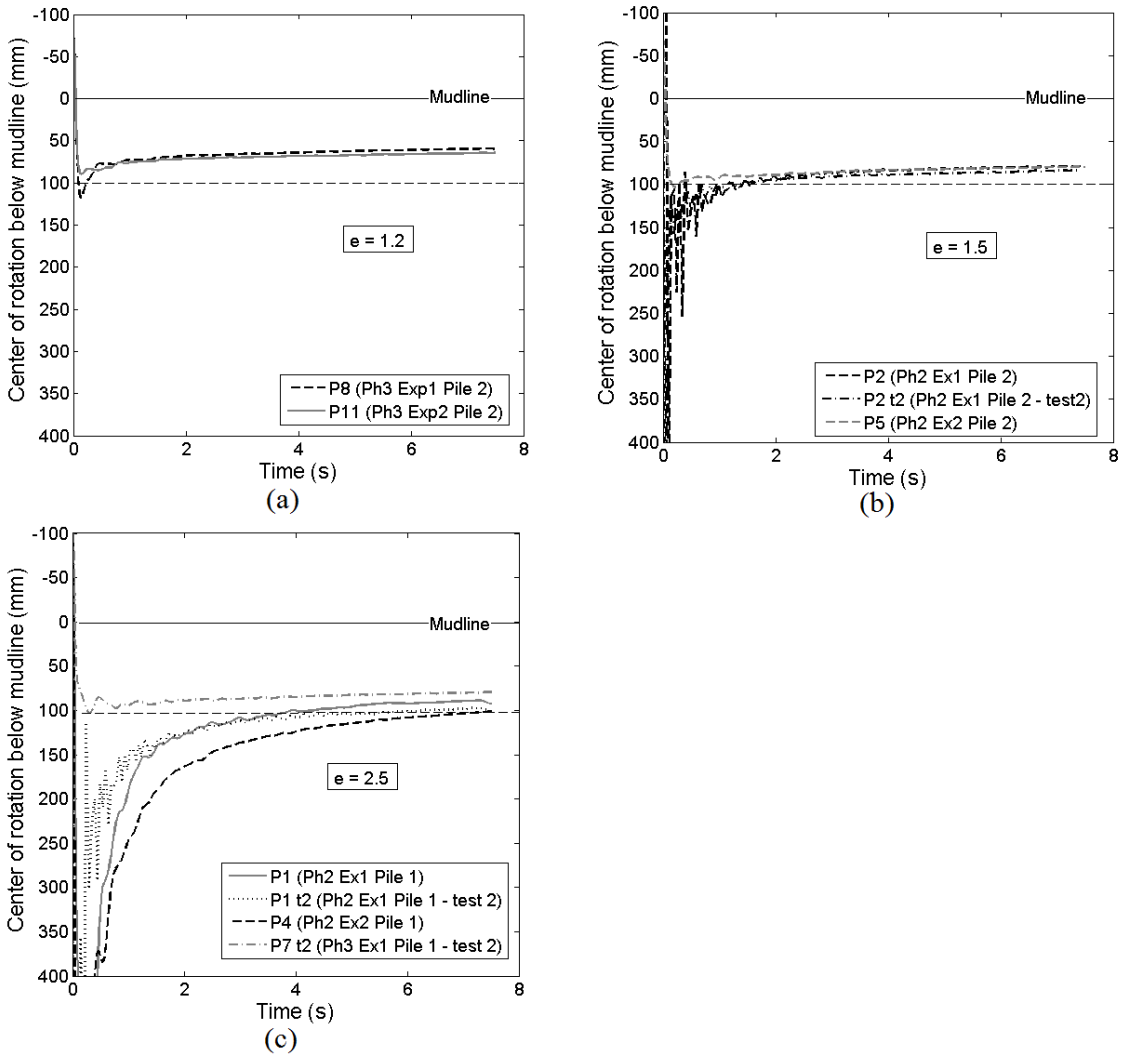

Figure 6.19: Center of rotation for all repeat tests

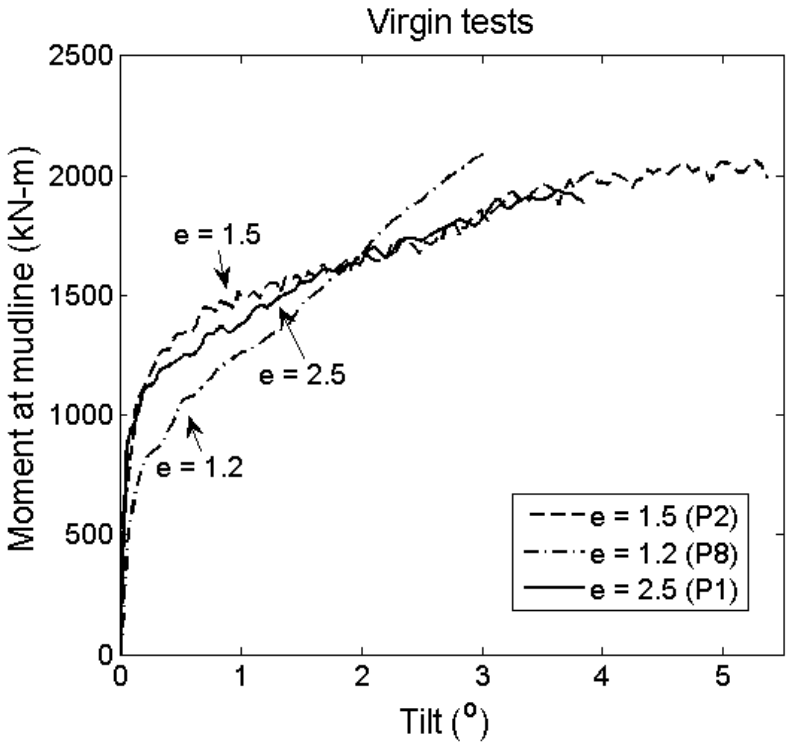

Figure 6.20: Moment theta curves for piles in rotation (first loading)

6.4 Moment-theta curves

The moment-theta curves for all of the piles tested in rotation is presented in Figures 6.20 (first loading) and 6.21 (post cyclic loading). The moment, M, is computed at the mudline for comparison of piles tested at different eccentricities, and tilt or degree of rotation from the vertical axis, θ, is computed using the MEMS sensors (Beemer et al., 2015).

For all the tests except e = 2.5, the moment at the mudline increases with increase in eccentricity as expected. The soil strength profile was relatively low (soil had not consolidated completely) for the test P1 (e = 2.5 first loading) leading to a lower magnitude of moment and the soil strength was higher for test P1 t2 (e = 2.5 post cyclic) giving a

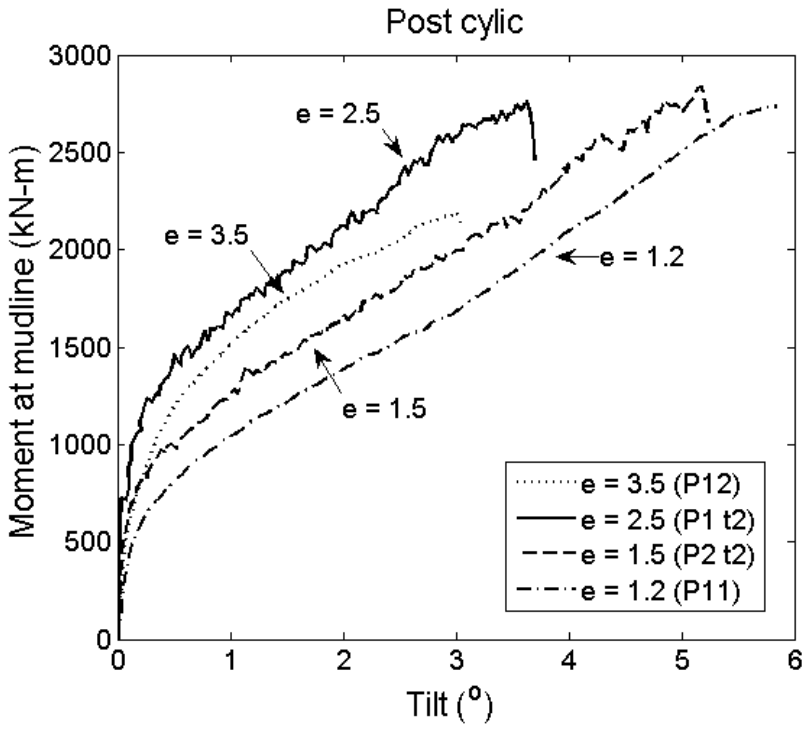

Figure 6.21: Moment theta curves for piles in rotation (post cyclic loading)

slightly higher magnitude of moment. Since the curves are not normalized the influence of the test bed strength is high. Also since the curves are not normalized by $s_{u,c}$ the effect of the pile settling and subsequently mobilizing stronger sediments is seen more clearly in these figures. Using the same failure criteria of change in slope of the moment theta curve, the failure tilt (θ_f) is given in Table 6.4.

Achmus et al. (2009) developed a stiffness degradation model for offshore wind towers based on finite element simulations and an experimental evaluation of drained cyclic triaxial tests on a sandy seabed. They reported a maximum tolerance of 0.5^o of permanent tilt at the mudline for wind towers. All the tests carried out in this research program all failed at very low tilt angles (<0.5%). Although there is no basis for direct comparison as the value reported by Achmus et al. (2009) was for permanent tilt and not static capacity tilt, loading the wind tower beyond the elastic tilt range (or $> \theta_f$) leads to a permanent tilt. The allowable elastic tilt range is found to be very low for these piles which is an important design consideration.

All of the piles were installed by hand in 1 g conditions and the centrifuge spun up to reach the test acceleration. Table 6.4 presents the initial tilt measured by the MEMS sensor at 1 g ($\theta_{in,1g}$) at the time of installation and the tilt after spin up at 75g ($\theta_{in,75g}$) for all the first loading monotonic tests. The initial tilt data is obviously not applicable to the post cyclic monotonic tests. The maximum tilt developed during spin up appears to be for pile P1 with a $\Delta\theta_{spinup}$ of 0.9616^o. This tilt developed during spin up is not assumed to greatly influence the test results.

6.5 Combined loading

The problem of combined loading with respect to offshore foundation behavior has been studied by a number of researchers (Tan, 1990; Murff, 1994; Houlsby and Martin, 1992; Bransby and Randolph, 1998). Plasticity methods have been used to analyze the

Table 6.4: Tilt data for piles tested

Pile	e	θ_f	$\theta_{in,1g}$	$\theta_{in,75g}$	$\Delta\theta_{spinup}$
P1	2.5	0.1	1.327	0.3654	0.9616
P2	1.5	0.11	-1.27	-1.94	0.67
P7	2.5	0.09	0.722	0.3733	0.3487
P8	1.2	0.15	3.5185	3.5007	0.0178
P12	3.5	0.25	-	-	-
P1 t2	2.5	0.2	-	-	-
P2 t2	1.5	0.1	-	-	-
P11	1.2	0.1	-	-	-

yield loci for combined loading response. Curve fits based on empirical centrifuge or 1 g model tests have also been suggested for the shape of the yield locus (Martin, 1994; Murff, 1994; Dean et al., 1992).

In cases where there is no resistance to uplift loading such as flat footings or spudcans, the yield envelope appears as plotted in Figure 6.22 (a) and for footings such as skirted shallow foundations or bucket foundations that provide uplift resistance the yield surface appears as in Figure 6.22 (b) (Bransby and Randolph, 1998; Murff, 1994).

An assumption is made here regarding the short monopiles tested in this research program purely for the ease of presenting the data. The piles were not installed using suction as in the case of suction caissons, but were installed by hand while vented from the top and a plug put in place to seal the pile (Refer Section 5.3). Thus, although in reality the yield surface appears as plotted in Figure 6.22 (c) (with the vertical load in tension, $V_t < V_{max}$), the empirically fitted ellipse to the data representative of the yield surface is computed using $V_t = -V_{max}$ for ease of presenting experimental centrifuge data. Centrifuge test results by Watson and Randolph (1997) also suggest that the ultimate uplift load, $V_t = -V_{max}$.

It is clear from the experimental results that the assessment of failure is subjective and a systematic approach is required to correlate the results from the different tests. As

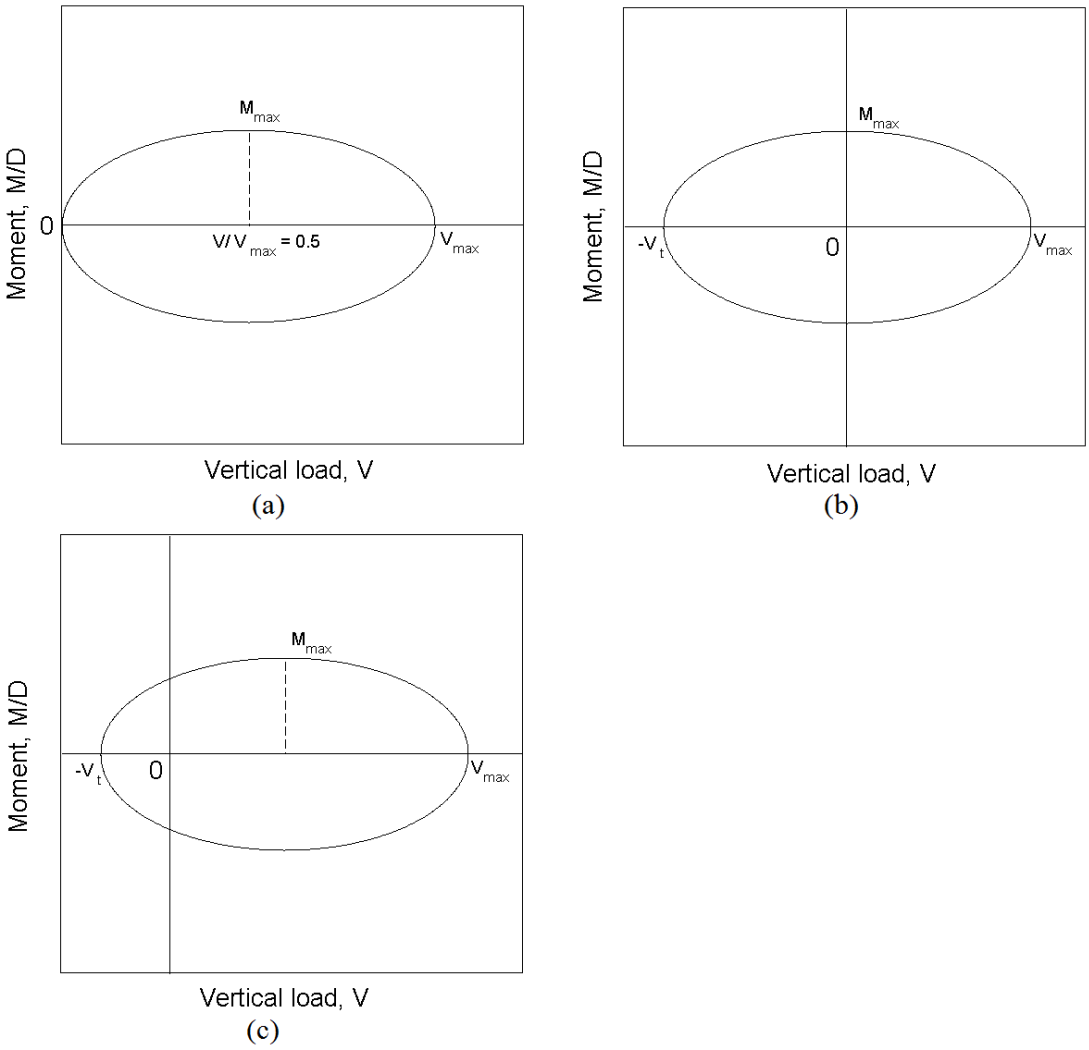

Figure 6.22: Yield envelope after Bransby and Randolph (1998); Murff (1994)

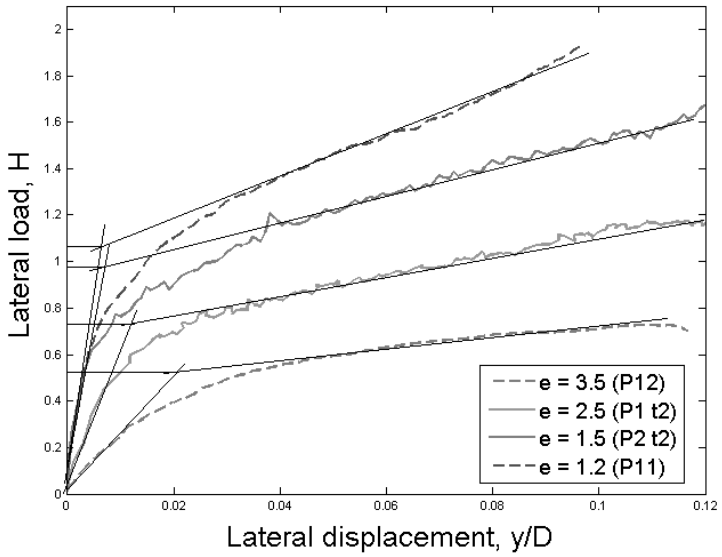

Figure 6.23: Criteria for selecting yield point after Graham et al. (1982); Villalobos et al. (2009)

mentioned previously, the yield point here is determined by the intersection of the two straight lines that best fit the experimental curve at the beginning and at the end of the curve (Graham et al., 1982) as shown in Figure 6.23. This method was also used by Villalobos et al. (2009) who examined a number of failure criteria and determined this to be the most suitable approach.

6.5.1 V - H load space

The load paths for the monotonic tests in the V-H plane is shown in Figure 6.24 where the vertical load (V) is plotted against the horizontal load (H) for the pile tests. An empirically fitted ellipse is also shown in the figure representing the yield surface computed using a least square criteria. The ellipse is computed using the assumption mentioned before, with $V_t = -V_{max}$ (which is ultimate vertical load when M = 0 and H = 0). It is evident from this plot that H and V cannot be directly compared due to differences in the

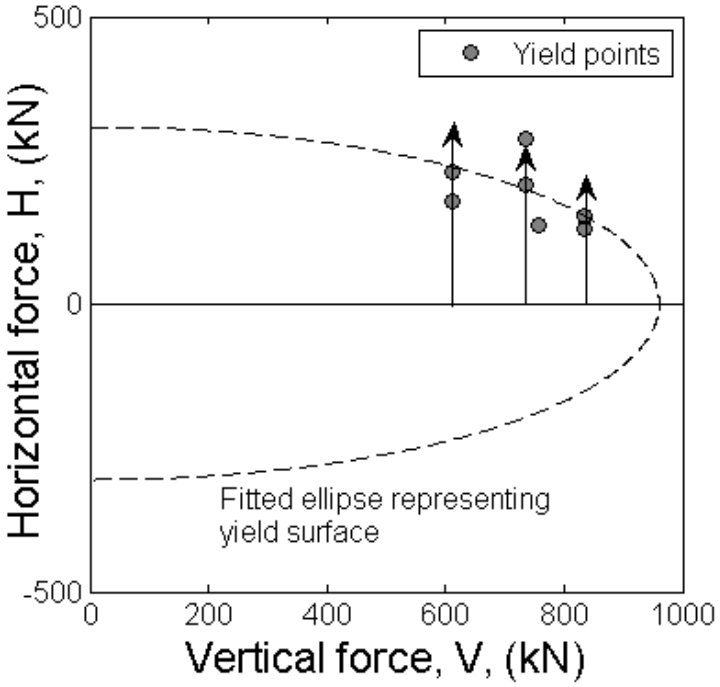

Figure 6.24: Vertical load plotted versus horizontal load

soil strength profile leading to varying H values.

Figure 6.25 shows the horizontal bearing factors, N_h plotted vs the vertical bearing factors, N_v along with the empirical yield surface which was fitted using the yield points from the first loading tests. The yield points obtained from the post cyclic tests lie within the yield surface. The interaction plot shows that the yield surface for first monotonic loading and post cyclic monotonic loading are not perfectly comparable. Based on observing the data points the yield envelope is slightly smaller for the post cyclic loading tests as compared to the first loading tests.

The mathematical representation of the ellipse in the H-V plane is given by Equation 6.5.

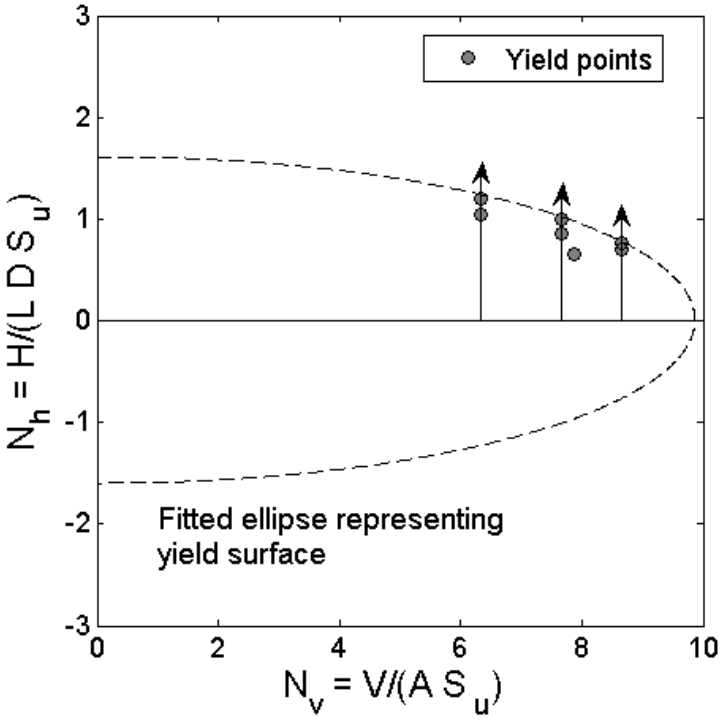

Figure 6.25: Interaction diagram between horizontal and vertical bearing factors.

$$(\frac{N_v - 0.0339}{9.535})^2 + (\frac{N_h - 0.0985}{1.407})^2 = 1 \tag{6.5}$$

6.5.2 M - H load space

Figure 6.26 (a) presents the ultimate bearing factors in the M-H plane (N_m vs N_h) along with a linear fit of the data. It is hard to compare the data in this figure since the yield points presented here are from different slices of the M-H plane along the V axis (i.e varying vertical load, as shown in Figure 6.25).

Figure 6.26 (b) is plotted between N_m and N_h both normalized by V/V_{max}. Also presented in the figure is a linear fit through the data. Byrne et al. (2002) and Villalobos et al. (2009) adopted the mathematical formulation for the yield surface given by an expression

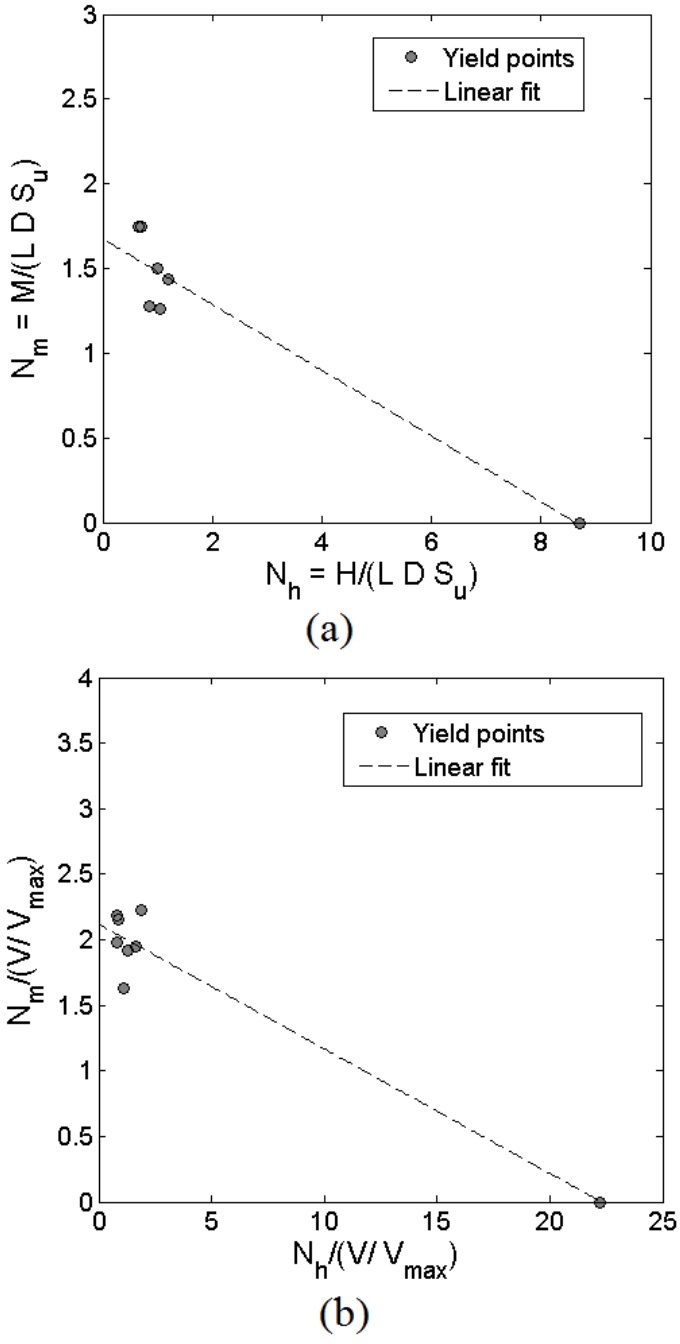

Figure 6.26: Interaction diagram in H-M space; (a) Bearing factors; (b) Normalized bearing factors.

that represents an ellipsoid. This surface was expressed by the Equation 6.6.

$$y = (\frac{H}{h_o V_o})^2 + (\frac{M}{D m_o V_o})^2 - 2e\frac{H}{h_o V_o}\frac{M}{D m_o V_o} - 1 = 0 \tag{6.6}$$

where V_o is the maximum vertical load (when M = H = 0), H/V_o and M/V_o are normalized horizontal and moment loads, h_o and m_o are the x and y intercepts on H/V_o vs M/V_o plot.

An expression of a similar form was used to fit the data tested in this research program given by the Equation 6.7.

$$y = (\frac{N_h}{h_o(V/V_{max})})^2 + (\frac{N_m}{m_o(V/V_{max})})^2 - 2\frac{N_h}{h_o(V/V_{max})}\frac{N_m}{m_o(V/V_{max})} - 1 = 0 \tag{6.7}$$

where $\frac{N_h}{h_o(V/V_{max})}$ and $\frac{N_m}{m_o(V/V_{max})}$ are the horizontal and moment bearing capacity factors normalized w.r.t V/V_{max} as plotted in Figure 6.25 and h_o and m_o are the x and y intercepts in Figure 6.25.

A non-symmetric ellipse is obtained on fitting the experimental data to Equation 6.7 in the normalized M-H ($\frac{N_m}{(V/V_{max})}$ - $\frac{N_h}{(V/V_{max})}$) plane as shown in Figure 6.27. On observing the shape of the ellipse the maximum combined loading capacity occurs when M and H have opposite signs at the apex of the ellipse and the minimum combined loading capacity is found when M and H have the same sign, this is similar to that observed by Villalobos et al. (2009). Since the loading condition usually found offshore is the case where both M and H have the same sign, this tends to control the foundation design.

6.5.3 Comparison with published literature

Kay and Palix (2011) presented results from a 3D finite element program (HARMONY) to develop ellipse/ellipsoidal equations for offshore caisson foundation design

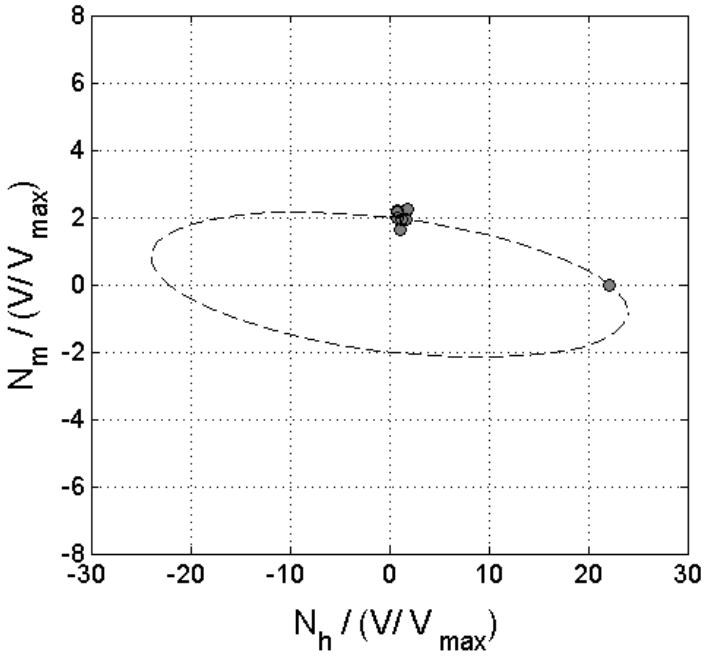

Figure 6.27: Interaction diagram in H-M space along with empirical ellipse.

for a wide range of embedment ratios (L/D = 1.5, 2, 3, 4, 5 and 6) and undrained shear strength profiles (constant, normally consolidated and stepped). Rotated ellipses have the parametric form:

$$N_h(t) = a_{MH}cos(t)cos(\theta_{MH}) - b_{BH}sin(t)sin(\theta_{MH}) \tag{6.8}$$

$$N_m(t) = a_{MH}cos(t)sin(\theta_{MH}) + b_{BH}sin(t)cos(\theta_{MH}) \tag{6.9}$$

Empirical values for θ_{MH}, a_{MH} and b_{MH} were presented in Kay and Palix (2011) varying with soil profile and aspect ratio (L/D). This equation described the M-H yield envelope for the condition where V = 0. Kay and Palix (2011) also extended the work to include a range of vertical load levels (V/V_{max} = 0.6, 0.8, 0.9) since applying vertical load decreases caisson capacity. They accounted for vertical load by using a factor

$H_{max,v}/H_{max,v=0}$ in the Equation 6.9 and Equation 6.10 describing the ellipse in the V-H plane (Supachawarote, 2004).

$$(\frac{H_{max,v}}{H_{max,v=0}})^{a_{VH}} + (\frac{V}{V_{max}})^{b_{VH}} = 1 \tag{6.10}$$

where empirical values for a_{VH} and b_{VH} were presented in Kay and Palix (2011) for varying soil profiles and aspect ratios.

The M-H yield points from the rotational centrifuge tests were plotted along with the M-H ellipsoidal equations developed by Kay and Palix (2011) in Figures 6.28 and 6.29. Figure 6.28 presents the ellipses for V = 0 and V/V_{max} for 0.6 and 0.8 computed for a Normally Consolidated (NC) soil profile. Figure 6.29 presents the same three ellipses computed for a uniform soil profile. As mentioned in Section 6.1.3 the V/V_{max} for these centrifuge tests lie within a range of 0.6 to 0.8 and as seen from the figures the centrifuge data points compare really well with the yield envelopes predicted by the finite element program HARMONY (Kay and Palix, 2011). The data appears to fit the yield envelope for the uniform soil strength profile ($s_u = 10\ kPa$) better than the yield envelope for the normally consolidated profile ($s_u = 1.25z$) given by Kay and Palix (2011).

Although the generalized shear strength profile for the centrifuge test beds is normally consolidated and is given by Equation 6.11, each centrifuge data point was normalized by its individual shear strength profile obtained using T-bar and water content profiles (Refer Section 5.5). The soil strength profiles for all the centrifuge test beds appears to be almost constant or linearly increasing at a low slope until the length of pile (z = 7 m) which is a possible reason as to the centrifuge data points fitting the yield envelope for the uniform soil strength profile better as compared to the yield envelope computed for the NC soil strength profile.

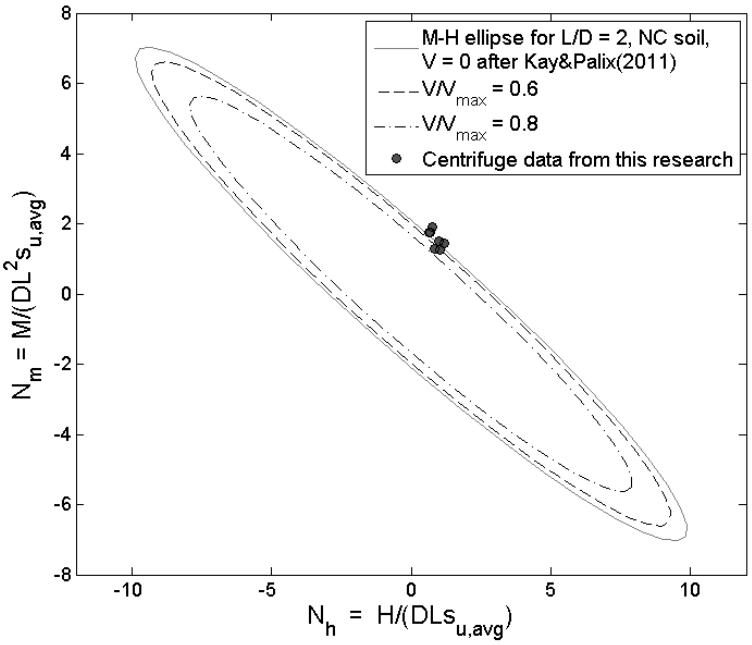

Figure 6.28: M-H ellipse for L/D of 2, NC soil profile after Kay and Palix (2011).

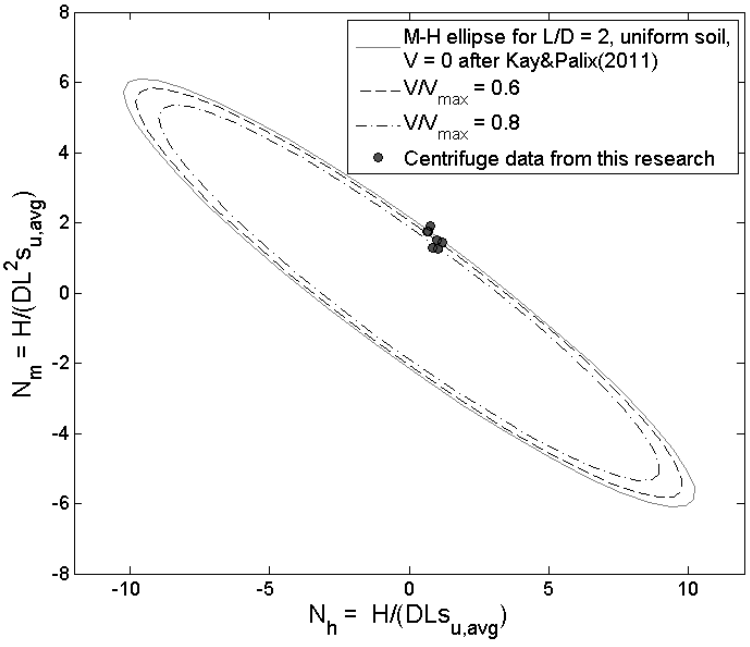

Figure 6.29: M-H ellipse for L/D of 2, uniform soil strength after Kay and Palix (2011).

$$s_u(kPa) = 2 + 1z(m) \tag{6.11}$$

where s_u is the shear strength in kPa and z is the depth below the mudline in units of meters.

The centrifuge monotonic data obtained in this research program appear to be in sync with available FEM models in the literature for soft clays. Due to a limited number of experimental yield points the true shape of the yield locus in the M-H-V space is not obtainable, however the experiments provide a good data set to compare finite element models and theoretical predictions of the yield surface to help designers choose suitable parameters.

7. SUMMARY AND FUTURE WORK

7.1 Summary

This dissertation focussed on contributing to the field of offshore geotechnics in two ways: first, to aid in offshore site characterization by developing a framework for correlating soil strength with geophysical measurements for shallow sediments; and second, to study the ultimate capacity of caisson foundations subjected to loads typically encountered in offshore wind tower installations in water depths up to 30 m.

The research project described a laboratory testing program with 45 CK_oU triaxial tests along with bender element measurements carried out at Texas A&M University for correlation of soil strength with stiffness. It also described a centrifuge testing program where model caisson foundations with aspect ratios of two were tested under combined horizontal and moment loads carried out at Rensselaer Polytechnic Institute.

The following remarks are summarized from the site characterization testing program:
Strength

- The SHANSEP strength parameters (CK_oU compression) for all the clays at low confining pressures (15 kPa to 60 kPa) was experimentally determined and found to lie within the expected range (S = 0.28 to 0.32).

- Stiffness or shear modulus (G_o) for the all the samples was correlated with void ratio, mean effective stress and OCR (for clays) and was found to be comparable with existing literature.

- A new framework for correlating stiffness and strength for all the clays was proposed, based on void ratio and OCR. The formulation provides a convenient way of estimating both absolute value and trends of behavior at different void ratios and

OCRs. It is emphasized again that this equation does not provide a means to directly estimate the undrained shear strength based on geophysical measurements and that suitable site specific correlations will have to be developed for design purposes.

The data obtained from the centrifuge tests was used to understand the ultimate capacity behavior of caisson foundations with the following key points summarized below:

- The ultimate capacity in translation was found to have a bearing factor of 8.7 which falls in between Murff and Hamilton's upper bound solution for the case of a smooth pile ($\alpha = 0$) with no gap behind the pile and the case of a rough pile ($\alpha = 1$) with the formation of a gap behind the pile.

- The rotational capacities of the foundations was slightly below the values predicted by Aubeny et al. (2003), expected to be due to the combined effect of both vertical and moment loading.

- The combined loading also contributed to vertical settlement of all the pile tests to varying levels. Gapping was also observed on all the piles at the end of all tests with varying depths.

- The experimental yield points was compared with the FEM based yield envelope by Kay and Palix (2011) and was found to match relatively well.

7.2 Recommendations for future work

Like any other testing device, the bender element and piezo electric system has its advantages and limitations. Setting up of the device requires a thorough research on the best practices and methods of shielding and signal processing to obtain reliable data. A much larger database on soft clays is required to validate the proposed formulation relating stiffness and strength. Preferably, different methods of obtaining shear modulus and

strength including both in-situ and laboratory methods for clays with a range of PIs should be added to the data set.

The settlement of low aspect ratio foundations requires monitoring when subjected to combined vertical, horizontal and moment loads, especially during centrifuge testing. Since settlement of the pile was not monitored in this testing program, a significant aspect of the foundation behavior cannot be characterized. 1g tests can also be carried out with similar loading sequences to obtain a better sense of the failure mechanism.

REFERENCES

Abdulhadi, N., Germaine, J. T., and Whittle, A. J. (2012). "Stress-dependent behavior of saturated clay." *Can. Geotech. J.*, 49, 907–916.

Achmus, M., Abdel-Rahman, K., and Kuo, Y. (2008). "Design of monopile foundations for offshore wind energy converters." *11th Baltic Sea Geotechnical Conference Geotecnics in Maritime Engineering Gdansk, Poland*, 463–470.

Achmus, M., Kuo, Y., and Abdel-Rahman, K. (2009). "Behavior of monopile foundations under cyclic lateral load." *Computers and Geotechnics*, 35 (5), 725–735.

Airey, D. and Mohsin, A. K. M. (2013). "Evaluation of shear wave velocity from bender elements using cross-correlation." *Geotechnical Testing Journal*, 36 (4), 1–9.

American Petroleum Institute (2000). *Recommended practice for planning, designing and constructing fixed offshore platforms working stress design*. Number API RP 2A-WSD. Washington, DC.

Andersen, K. and Jostad, H. (1999). "Foundation design of skirted foundations and anchors in clay." *Proc. Offshore Technology, Houston, USA, OTC 10824*.

Andersen, K., Murff, J., Randolph, M., Clukey, E., Erbrich, C., Jostad, H., Hansen, B., Aubeny, C., Sharma, P., and Supachawarote, C. (2005). "Suction anchors for deepwater applications. keynote lecture." *Proceedings of the International Symposium on Frontiers in Offshore Geotechnics, Perth, Western Australia.* (September).

Andrus, R.D., S. K. I. (2000). "Liquefaction resistance of soils from shear-wave velocity." *Journal of Geotechnical and Geoenvironmental Engineering*, 126 (11), 1015–1025.

API (2000). "Recommended practice for planning, designing, and constructing fixed offshore platforms - working stress design." American Petroleum Institute.

Argyriadis, K., Gill, L., and Schwartz, S. (2005). "Loads for offshore wind turbines: the

second edition of the gl wind turbine." *Report no.*, GL Wind turbine.

Arulnathan, R., Boulanger, R. W., and Riemer, M. F. (1998). "Analysis of bender element tests." *Geotech. Test. J.,*, 21-2, 120–131.

Associazione Geotechnica Italiana (1991). "Geotechnical characterisation of fucino clay." *Proc. 10th European Regional Conf. on SMFE, Florence*.

ASTM Standard D4186 (2006). *Standard Test Method for One-Dimensional Consolidation Properties of Saturated Cohesive Soils Using Controlled-Strain Loading*. ASTM International.

ASTM Standard D4318 (2010). *Standard Test Methods for Liquid Limit, Plastic Limit, and Plasticity Index of Soils*. ASTM International.

ASTM Standard D4767 (2011). *Standard Test Method for Consolidated Undrained Triaxial Compression Test for Cohesive Soils.* ASTM International, <www.astm.org>.

ASTM Standard D854 (2010). *Standard Test Methods for Specific Gravity of Soil Solids by Water Pycnometer*. ASTM International, <www.astm.org>.

Atkinson, J. H., Richardson, D., and Robinson, P. J. (1987). "Compression and extension of ko normally consolidated kaolin clay." *Journal of Geotechnical Engineering*, 113(12).

Aubeny, C., Han, S., and Murff, J. (2003). "Inclined load capacity of suction caissons." *Int. J. Numer. Anal. Meth. Geomech.*, 27, 1235–1254.

Aubeny, C., Moon, S., and Murff, J. (2001). "Lateral undrained resistance of suction caisson anchors." *Intl. J. Offshore and Polar Engineering*, 11 (3), 211–219.

Bates, C. (1989). "Dynamic soil property measurement suring triaxial testing." *Géotechnique*, 39, 721–726.

Beemer, R., Murali, M., Biscontin, G., and Aubeny, C. (2015). "Theory on measuring orientation with mems accelerometers in a centrifuge." *International Foundations Congress and Equipment Expo, San Antonio, TX*.

Beemer, R. D. (2015). "Global stiffness of offshore monopile and its behaviour under cyclic conditions." Ph.D. thesis, Texas A&M University, Texas A&M University.

Berre, T. and Bjerrum, L. (1973). "Shear strength of normally consolidated clays." *Proc. 8th Intl. Conf. on Soil Mech. and Found. Eng., Moscow*, 1, 39–49.

Bishop, A. and Henkel, D. (1962). *The Measurement of Soil Properties in the Triaxial Test. 2nd Ed.* Edward Arnold Ltd., London.

Bishop, A. and Wesley, L. (1975). "A hydraulic triaxial apparatus for controlled stress path testing." *Géotechnique*, 25 Issue:4, 657–670.

Bonal, J., Donohue, S., and McNally, C. (2012). "Wavelet analysis of bender element signals." *Géotechnique*, 62 (3), 243–252.

Bransby, M. F. and Randolph, M. (1998). "Combined loading of skirted foundations." *Géotechnique*, 48 (5), 637–655.

Brignoli, E., Gotti, M., and Stokoe, K. (1996). "Measurement of shear waves in laboratory specimens by means of piezoelectric transducers." *Geotech. Test. J.*, 19, 384–397.

Broms, B. B. (1964). "Lateral resistance of piles in cohesive soils." *Journal of the Soil Mechanics and Foundations Division*, 90, 27–63.

Bruijne, R., Van der Palen, L., Nielsen, S., Lemming, J., Overton, J., Payne, M., Snodin, H., O Donnell, M., McCarthy, A., Bruns, E., Steinhauer, I., Bjorck, A., Persson, S., Michalowska-Knap, K., Palmers, G., and Woyte, A. (2005). "General information: Principal findings 2003-2005." *Report no.*, Concerted Action for Offshore Wind Deployment.

Burland, J. (1989). "Small is beautiful-the stiffness of soils at small strains." *Ninth Laurits Bjerrum Memorial Lecture*.

Burland, J. and Georgiannou, V. N. (1991). "Small strain stiffness under genegeneral stress changes." *Deformation of soils and displacements of structures: Proceedings of the tenth European conference on Soil Mechanics and Foundations Engineering*, 1, 41–

44.

Byrne, B. and Houlsby, G. (2003). "Foundations for offshore wind turbines." *Phil. Trans. R. Soc. Lond. A*, 361, 2909–2930.

Byrne, B. and Houlsby, G. (2005). "Investigating 6 degree-of-greedom loading on shallow foundations." *International Symposium on Frontiers in Offshore Geotechnics, Perth, Australia*, 477–482.

Byrne, B. and Houlsby, G. (2006). "Assessing novel foundation options for offshore wind turbines." *World Maritime Technology Conference, London*.

Byrne, B., Houlsby, G., Martin, C., and Fish, P. (2002). "Suction caisson foundations for offshore wind turbines." *Wind Engineering*, 26 (3), 145–155.

Campbell, K. and Hough, J. (1986). *Planning and design of fixed offshore platforms*. Van Nostrand Reinhold Company.

Casagrande, A. (1936). "The determination of the pre-consolidation load and its practical significance." *Proceedings of the 1st International Conference on Soil Mechanics and Foundation Engineering, Cambridge, MA*, Vol. 3, 60–64.

Chan, K. H., Boonyatee, T., and Mitachi, T. (2010). "Effect of bender element installation in clay samples." *Géotechnique*, 60 (4), 287–291.

Chen, W. and Randolph, M. F. (2005). *Centrifuge tests on axial capacity of suction caissons in clay*. Taylor & Francis, Chapter 19, 243 – 249.

Clayton, C. and Heymann, G. (2001). "Stiffness of geomaterials at very small strains." *Géotechnique*, 51, 245–255.

Dakoulas, P. and Yuanhui, S. (1992). "Fine ottawa sand: Experimental behavior and theoretical predictions." *Journal of Geotechnical Engineering*, 118(12).

Dean, E. R., James, R., Schofield, A. N., Tan, F., and Tsukamoto, Y. (1992). "The bearing capacity of conical footings on sand in relation to the behaviour of spudcan footing of jackups." *Proceedings of the Wroth Memorial Symposium 'Predictive soil mechanics'*,

230–253.

DeJong, J. T., Yafrate, N. J., and DeGroot, D. J. (2011). "Evaluation of undrained shear strength using full-flow penetrometers." *Journal of geotechnical and geoenvironmental engineering*, 137 (1), 14–26.

Diaz-Rodrigues, J. and Lopez-Flores, L. (1997). "Effect of soil microstucture on the dynamic properties of mexico city clay." *Proc., 14th Int. Conf. on Soil Mechanics and Foundation Engineering, Hamburg, Germany*, Vol. 1, 275–278.

Dyvik, R. and Madshus, C. (1985). "Lab measurements of gmax using bender element." *Proc., ASCE Convention on Advances in the Art of Testing Soils under Cyclic Conditions*, 186–196.

Edil, T. and Luh, G. (1980). "Microstructural effects on dynamic response of clays." *Proc., 7th World Conf. on Earthquake Engng., Turkish National Committee on Earthquake Engineering, Istanbul, Turkey*, Vol. 3, 133–140.

Einav, I. and Randolph, M. F. (2005). "Combing upper bound and strain path methods for evaluating penetration resistance." *Int. J. Numer. Methods Eng.*, 63(14), 1991–2016.

Frye, J. (2011). "Design of scale-model floating wind turbine: spar buoy." M.S. thesis, Worcester Polytechnic Institute, Worcester Polytechnic Institute.

Garnier, J. and Gaudin, C. (2007). "Catalogue of scaling laws and similitude questions in centrifuge modelling. International Technical Committee TC2 (Physical Modelling in Geotechnics, PMG).

Germaine, J. T. (1982). "Development of the directional shear cell for measuring cross-anisotropic clay properties.." M.S. thesis, Massachussets Institute of Technology, Cambridge, MA.

Germaine, J. T. and Ladd, C. (1988). "Triaxial testing of saturated cohesive soils." *Advanced triaxial testing of soil and rock, ASTMSTP 977*, ASTMSTP 977, 421–459.

Gordon, M. and Clayton, C. R. I. (1997). *Measurement of stiffness of soils using small*

strain triaxial testing and bender elements, Vol. Geological Society Engineering Geology Special Publication No. 12.

Gourvenec, S. (2007). "Failure envelopes for offshore shallow foundations under general loading." *Géotechnique*, 57 (9), 715–727.

Graham, J., Pinkney, R. B., Lew, K. V., and Trainor, P. G. S. (1982). "Curve fitting and loaboratory data." *Canadian Geotechnical Journal*, 19, 201–205.

Grajales, F. (2015). "Undrained capacity of short piles and caissons on cohesive soils." Ph.D. thesis, Texas A&M University, Texas A&M University.

Gu, X., Yang, J., and Huang, M. (2013). "Laboratory measurements of small strain properties of dry sands by bender element." *Soils and Foundations*, 53 (5), 735–745.

Guldur, B. (2010). "Implementation of bender elements in an automated triaxial testing system for measuring clay structure restoration by consolidation." M.S. thesis, Northeastern University, Boston, Massachusetts, Northeastern University, Boston, Massachusetts.

Hamilton, J., Phillips, R., Dunnavant, T., and Murff, J. (1991). "Centrifuge study of laterally loaded piles in soft clay." *Proc Int Conf Centrifuge 1991, ISSMFE*.

Hardin, B. O. (1978). "The nature of stress strain behavior of soils." *Proc. Geotech. Eng. Div. Speciality Conf. on Earthquake Eng. and Soil Dynamics*, Vol. 1, Pasadena, 3–90.

Hardin, B. O. and Black, W. L. (1968). "Vibration modulus of a normally consolidated clay." *Journal of the SMF Div. Proc., ASCE*, 95, 1531–1537.

Hardin, B. O., Drnevich, V. P., Wang, J., and Sams, C. E. (1994). "Resonant column testing at pressures up to 3.5 mpa (500 psi).." *Dynamic geotechnical testing II*.

Hardin, B. O. and Richart, F. E. J. (1963). "Elastic wave velocity in granular soils." *Journal of soil mechanics and foundation division, ASCE*, 89(1), 33–65.

Head, K. H. (1998). *Manual of soil laboratory testing. Volume 3: Effective stress tests*. John Wiley & Sons, New Jersey.

Hight, D. W., Bond, A. J., and Legge, J. D. (1992). "Characterisation of bothkennar clay: an overview.." *Géotechnique*, 42, 303–347.

Ho, E. W. L. (1985). "Undrained compression and extension tests on reconstituted specswhite kaolin consolidated under ko conditions with particular reference to the effects of perfect sampling." *Report no.*, Geotechnical Engineering Research Center Report, City University, London, England.

Houlsby, G. T. and Martin, C. M. (1992). "Modelling of the behaviour of foundations of jack up units on clay.." *Proceedings of the Wroth Memorial Symposium 'Predictive soil mechanics'*, 339–358.

Houlsby, G. T. and Wroth, C. P. (1991). "The variation of shear modulus of a clay with pressure and over consolidation ratio.." *Soils Fdns*, 31 No. 3, 138–143.

Hvorslev, M. J. (1949). "Subsurface exploration and sampling of soils for civil engineering purposes." *Report no.*, Department of the Army, Waterways Experiment Station, Corps of Engineers, Geotechnical Laboratory, Vicksburg, MS.

Jamiolkowski, M., Lancellotta, R. H., and Lo Presti, D. C. F. (1994). "Remarks on the stiffness at small strain of six italian clays." *Pre-failure deformation of geomaterials*, Vol. 2, 817–836.

Jamiolkowski, M., Leroueil, S., and Lo Presti, D. C. F. (1991). "Design parameters from theory to practice." *Proc., Int. Conf. on Geotechnical Engineering for Coastal Development: Geo-Coast 1991*.

Janbu, N. (1963). "Soil compressibility as determined by oedometer and triaxial tests." *Proceedings of 3rd European Conference on Soil Mechanics*.

Jeanjean, P. (2009). "Re-assessment of p-y curves for soft clays from centrifuge testing and finite element modeling." *Proc. Offshore Technology Conf., Paper OTC20158, Houston.*

Jenner, C., Finch, M., Finlayson, K., and Harker, G. (2002). "Optimising integrated site investigations for offshore wind farm projects." *Offshore Site Investigation and Geotech-*

nics 'Diversity and Sustainability'; Proceedings of an International Conference.

Jones, C. D. (2009). "Investigation into the behavior of high quality samples of a soft offshore clay and the factors influencing g_{max}." M.S. thesis, University of Massachusetts Amherst, Amherst, MA, University of Massachusetts Amherst, Amherst, MA.

Jovicic, V., Coop, M. R., , and Simic, M. (1996). "Objective criteria for determining g_{max} from bender element tests." *Géotechnique*, 46-2, 357–362.

Jovicic, V. and Coop, M. R. (1997). "Stiffness of coarse grained soils at small strains." *Geotechnique*, 47(3), 545–561.

Jovicic, V. and Coop, M. R. (1998). "The measurement of stiffness anisotropy in clays with bender element tests in the triaxial apparatus." *Geotech. Test. J*, 21 Issue 1, 3–10.

Kay, S. and Palix, E. (2011). "Caisson capacity in clay: Vhm resistance envelope - part2: Vhm envelope equation and design procedures." *Frontiers in Offshore Geotechnics II*, Taylor & Francis Group, London.

Ladd, C. and Foott, R. (1974). "New design procedure for stability of soft clays." *J.Geotech. Engng. Div., ASCE*, 100(GT7), 763–786.

Ladd, C., Foott, R., Ishihara, K., Schlosser, F., and Poulos, H. (1977). "Stress deformation and strength characteristics." *Report no.*, State of the Art Report, Proc. of IX ICSMFE, Tokyo.

Landon, M., DeGroot, D., and Sheahan, T. (2007). "Nondestructive sample quality assessment of a soft clay using shear wave velocity." *Journal of Geotechnical and Geoenvironmental Engineering*, 133, No. 4, 424–432.

Lau, B., Lam, S., Haigh, S. K., and Madabhushi, S. P. G. (2014). "Centrifuge testing of monopile in clay under monotonic loads." *Physical Modelling in geotechnics*, Gaudin and White, eds., Taylor & Francis Group, London.

Lee, K. L. and Seed, H. B. (1967). "Drained strength characteristics of sand." *Journal for soil mechanics and foundation division*, 93(SM6), 117–141.

Lefebvre, G., Leboeuf, D., Rahhal, M. B., LaCroix, A., Warde, J., and Stokoe, K. H. (1994). "Laboratory and field determination of small strain shear modulus for a structured champlain clay." *Can. Geotech. J.*, 31 (1), 61–70.

Lesney, K. and Wiemann, J. (2005). "Design aspects of monopiles in german offshore wind farms,." *International Symposium on Frontiers in Offshore Geotechnics, Perth, Australia*, 383–389 (September). Perth, Australia.

Lo Presti, D. C. F., Pallara, O., Lancellotta, R., and Maniscalco, R. (1993). "Monotonic and cyclic loading behavior of two sands at small strains.." *Geotech. Test. J.*, 16(4), 409–424.

Lohani, T., Imai, G., and Shibuya, S. (1999). "Determination of shear wave velocity in bender element test." *Proceedings of the 2nd International Conference on Earthquake Geotechnical Engineering*, 101–106.

Lunne, T. and Andersen, K. H. (2007). "Soft clay shear strength parameters for deepwater geotechnical design." *Proceedings of the 6th International Offshore Site Investigation and Geotechnics Conference: Confronting New Challenges and Sharing Knowledge*.

Lunne, T. O., Eide, J., and de Ruiter, J. (1976). "Correlations between cone resistance and vane shear strength in some scandinavian soft to medium stiff clays.." *Can. Geotech. J.*, 13-4, 430–441.

Malhotra, S. (2009). "Design considerations for offshore wind turbine foundations in the united states." *Proceedings of the Nineteenth (2009) International Offshore and Polar Engineering Conference, Osaka, Japan, June 21-26*, <ISBN 978-1-880653-53-1>.

Marcuson, W. G. and Wahls, H. E. (1972). "Time effects on dynamic shear modulus of clays." *Proc. Am. Soc. Civ. Engrs*, Vol. 97, No. SM1, 1359–1373.

Martin, C. M. (1994). "Physical and numerical modelling of offshore foundations under combined load." Ph.D. thesis, University of Oxford, University of Oxford.

Martin, C. M. (2001). "Vertical bearing capacity of skirted circular foundations on tresca

soil." *Proc. 15th Int. Conference on Soil Mechanics and Geotechnical Engineering, Istanbul*, 743–746.

Martin, C. M. and Randolph, M. F. (2006). "Upper bound analysis of lateral pile capacity in cohesive soil.." *Geotechnique*, 56(2), 141–145.

Matlock, H. (1970). "Correlations for design of laterally loaded piles in soft clay." *Proc. Offshore Technology Conference, OTC 1204, Houston.*

Moe, G., Niedzwecki, J., Long, H., Lubbad, R., and Breton, S. (2007). "Technology for offshore wind turbines." *Report no.*, WIT Press (060207).

Murali, M. (2011). "Characterisation of gulf of mexico clay." M.S. thesis, Texas A&M University, Texas A&M University.

Murff, J. and Hamilton, J. (1993). "P-ultimate for undrained analysis of laterally loaded piles.." *ASCE Journal of Geotechnical Engineering*, 119 (1), 91–107.

Murff, J., Randolph, M., Elkhatib, S., Kolk, H., Ruinen, R., Strom, P., and Thorne, C. (2005). "Vertically loaded plate anchors for deepwater applications." *Proceedings of the International Symposium on Frontiers in Offshore Geotechnics, Perth, Western Australia.* (September).

Murff, J. D. (1994). "Limit analysis of multi footing foundation systems." *Proc. 8th International conference of computational methods and advanced geomechanics.*, 223–244.

NAVFAC (2011). "Lab results and a preliminary analytical framework to assess the magnitude and uncertainty in geotechnical properties estimated from the results of offshore geophysical surveys (December).

nees.rpi.edu. "Center for earthquake engineering simulation, <http://www.nees.rpi.edu/>.

Ni, S. H. (1987). "Dynamic properties of sand under true triaxial stress states from resonant column/torsion shear tests." Ph.D. thesis, University of Texas, Austin, University of Texas, Austin.

Pennington, D., Nash, D., and Lings, M. (2001). "Horizontally mounted bender elements

for measuring anisotropic shear moduli in triaxial clay specimens." *Geotechnical Testing Journal*, 24(2), 133–144.

Pestana, J. M. and Salvati, L. A. (2006). "Small-strain behavior of granular soils; (a) model for cemented and uncemented sands and gravels." *Journal of Geotechnical and Geoenvironmental Engineering*, 132(8).

Pestana, J. M. and Whittle, A. J. (1995). "Compression model for cohesionless soils." *Geotechnique*, 45(4), 611–631.

Randolph, M. F. (2004). "Characterisation of soft sediments for offshore applications." *Proc. 2nd Int. Conf. on Site Characterisation, Millpress, Rotterdam, Netherlands*, 209–231.

Randolph, M. F. and Andersen, K. H. (2006). "Numerical analysis t-bar penetration in soft clay." *Int. J. Geomech.*, 6(6), 411–420.

Randolph, M. F. and Houlsby, G. T. (1984). "The limiting pressure on a circular pile loaded laterally in cohesive soil." *Géotechnique*, 34(4), 613–623.

Reese, L. C., Cox, W. R., , and Koop, F. (1975). "Field testing and analysis of laterally loaded piles in stiff clay." *Proceedings, Offshore Technology Conference, OTC 2312, Houston, Texas*, 671–690.

Reimer, M., Gookin, W., Bray, J., and Wartman, J. (1998). "Using reflected shear waves to measure small strain dynamic properties." *Proceedings of the 5th CALTRANS Seismic Research Workshop.*

Richart, F., Hall, J., and Woods, R. (1970). *Vibrations of Soils and Foundations*. Prentice-Hall, Englewood Cliffs, New Jersey.

Roesler, S. K. (1979). "Anisotropic shear modulus due to stress anisotropy." *J. Geotech. Eng. Div. ASCE*, 105 No GT 7, 871–880.

Rowe, P. W. (1971). "Theoretical meaning and observed values of defomation parameters for soils." *Stress-strain behaviour of soils*, 1, 143–194.

Rutherford, C. (2011). "Development of multi directional simple shear testing device for characterization of the cyclic shear response of marine clays." Ph.D. thesis, Texas A&M University, College Station, TX.

Saigal, R., Dolan, D., Der Kiureghian, A., Camp, T., and Smith, C. E. (2007). "Comparison of design guidelines for offshore wind energy systems." *Offshore Technology Conference*, Houston, TX (30 April - 3 May).

Salvati, L. A. (2002). "Seismic response and cyclic behavior of sands." Ph.D. thesis, Univ. of California, Berkeley, California, Univ. of California, Berkeley, California.

Sanchez-Salinero, I., Rosset, J., and Stokoe, K. (1986). "Analytical studies of body wave propagation and attenuation." *Report no.*, Rep. No. GR-86-15, Univ. of Texas, Austin, Tex.

Santagata, M., Germaine, J., and Ladd, C. (2005). "Factors affecting the initial stiffness of cohesive soils." *Journal of Geotechnical and Geoenvironmental Engineering*, 131(4), 430–441.

Santamarina, J., Klein, K., and Fam, M. (2001). *Soils and Waves*. J. Wiley & Sons, Inc., New York, NY.

Schneider, J., Hoyos, L., J., Mayne, P., Macari, E., and Rix, G. (1999). "Field and laboratory measurements of dynamic shear modulus of piedmont residual soils." *Report no.*, Behavioral Characteristics of Residual Soils, GSP 92, ASCE, Reston, VA, pp. 12-25.

Seed, H. B. and Idriss, I. M. (1970). "Soil moduli and damping factors for dynamic response analysis." *Report No. Rep. UCB/EERC-70/10,*, Univ. of California, Berkeley, Calif.

Shibuya, S., Hwang, S. C., and Mtachi, T. (1997). "Elastic shear modulus of soft clays from shear velocity measurement." *Géotechnique*, 47, 593–601.

Shibuya, S., Mitachi, T., Hosomi, A., and Hwang, S. C. (1996). *Strain rate effects on stress strain behavior of clay as observed in monotonic and cyclic triaxial tests*. Number

ASCE GSP No.61.

Shirley, D. J. and Hampton, L. D. (1978). "Shear wave measurements in laboratory sediments." *Journal of Acoustic Society of America*, 63(2), 607–613.

Skempton, A. (1960). *From theory to practice in soil mechanics*. John Wiley & sons, Chapter Significance of Terzaghi's concept of effective stress.

Stewart, D. P. and Randolph, M. F. (1991). "A new site investigation tool for the centrifuge." *Proc. Int. Conf. On Centrifuge Modelling, Balkema, Rotterdam, Netherlands*, 531–538.

Stokoe, K. H., Hwang, S. K., and Lee, J. N. K. (1994). "Effects of various parameters on the stiffness and damping of soils at small to meadium strain." *Pre-failure deformation of geomaterials*, Vol. 2, Rotterdam, 785–816.

Supachawarote, C., R. M. G. S. (2004). "Inclined pull out capacity of suction caissons." *Proc. Fourtheenth Int. Offshore and Polar Engineering Conference, ISOPE*.

Tan, F. (1990). "Centrifuge and theoretical modelling of conical footings on sand." Ph.D. thesis, University of Cambridge, University of Cambridge.

Taylor, R. N. (ed.) (1995). *Geotechnical Centrifuge Technology*. CRC, London.

Tessari, A. (2012). "Centrifuge modeling of the effects of natural hazards on pile-founded concrete floodwalls." Ph.D. thesis, Rensselaer Polytechnic Institute, Rensselaer Polytechnic Institute.

Tjelta, T. (2001). "Suction piles: their position and applications today." *Proceedings of the 11th International Offshore and Polar Engineering Conference, Stavanger, Norway, June 17-22, Vol 2*.

Toolan, E. (2001). "Geophysical & geotechnical techniques for the investigation of near-seabed soils and rocks." *Report no.*, Fugro NV.

Tuttle, M. E. (1981). "Load measurement in a cylindrical column or beam using three strain gages." *Experimental Techniques*, 5, 19–20.

Van Randeraat, J. and Setterington, R. (1974). "Piezoelectric ceramics.

Viggiani, G. and Atkinson, J. H. (1995a). "Interpretation of bender element tests." *Géotechnique*, 45, 149–154.

Viggiani, G. and Atkinson, J. H. (1995b). "Stiffness of fine grained soil at very small strains." *Géotechnique*, 45 Issue 2, 249–265.

Villalobos, F. A., Byrne, B. W., and Houlsby, G. (2009). "An experimental study of the drained capacity of suction caisson foundations under monotonic loading for offshore applications." *Soils and Foundations*, 49, No 3, 477–488.

Waanders, J. W. (1991). "Piezoelectric ceramics: Properties and applications.

Watson, P. G. and Randolph, M. (1997). "A yield envelope design approach for caisson foundations in calcareous sediments." *Proceedings of BOSS '97 Eighth International Conference on the Behaviour of Offshore Structures*, Vol. 1, 259–273.

Webb, D. L. (1967). "The mechanical properties of undisturbed samples of london clay and pierre shale." Ph.D. thesis, University of London, University of London.

Westgate, Z. J. and DeJong, J. T. (2005). "Geotechnical considerations for offshore wind turbines." *Report no.*, US Offshore Wind Collaborative.

White, D. J., Gaudin, C., Boylan, N., and Zhou, H. (2010). "Interpretation of t-bar penetrometer tests at shallow embedment and in very soft soils." *Can. Geotech. J.*, 47(2), 218–229.

Yafrate, N. J. and DeJong, J. T. (2007). "Influence of penetration rate on measured resistance with full-flow penetrometers in soft clay." *Proc., Advances in Measuring and Modeling of Soil Behavior, GeoDenver, Geotechnical Special Publication 173, ASCE.*

Yang, J. and Yan, X. (2009). "Site response to multi-directional earthquake loading: a practical procedure." *Soil Dynamics and Earthquake Engineering*, 29 (4), 710–721.

Youn, J., Choo, Y., and Kim, D. (2008). "Measurement of small strain shear modulus g_{max} of dry and saturated sands by bender element, resonant column, and torsional

shear tests." *Canadian Geotechnical Journal*, 45(10), 1426–1438.

Zhang, C., White, D., and Randolph, M. (2011). "Centrifuge modeling of the cyclic lateral response of a rigid pile in soft clay." *Journal of Geotechnical and Geoenvironmental Engineering*, 137(7), 717–729.

APPENDIX A

BENDER ELEMENT SIGNAL ANALYSIS

A.1 Description of Bender elements

Bender elements consist of two thin piezoceramic plates rigidly bonded to a central metallic plate. Two thin conductive layers, electrodes, are glued externally to the bender. The polarization of the ceramic material in each plate and the electrical connections are such that when a driving voltage is applied to the element, one plate elongates and the other shortens. The net result is a bending displacement. On the other hand, when an element is forced to bend, an electrical signal can be measured through the wires leading to the element.

There are two possible versions, differing only in the electrical connection of the two polarized plates: a series or a parallel connection (Figure A.1). The series version gives a higher output for a given distortion and is better used as a receiver. The parallel version has an additional electrode between the piezoceramic plates and is better used as transmitter because it gives the largest distortion for a given input (Dyvik and Madshus, 1985).

A transmitter and receiver element can be placed in various soil testing devices, such as oedometer, simple shear test device or, as in this project, in the bottom and top cap of a conventional triaxial device. Although a combination of a parallel element as sender and a serial element as receiver would improve the signal quality, in the frame of this research only series connected elements are used. This gives the opportunity to change the pulse direction in the sample without the element configuration influencing the receiving signal. It means the received signals should have the same shape independently of the sending direction.

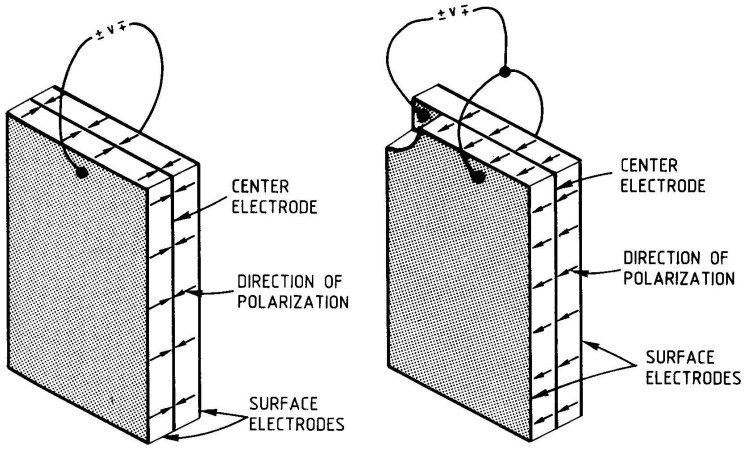

Figure A.1: (a) Series and (b) parallel connected piezoceramic element (Dyvik and Madshus, 1985).

A.2 Signal generation and measurement

The equipment to perform pulse bender element tests is given in Figure A.2.

A Tectronix arbitrary function generator AFG320 provides a burst sine output signal. The frequency for these tests is 50 kHz. This was selected as 50 kHz gave the least amount of electrical interference with the other devices in the laboratory. The amplitude of the signal is limited to 10 V peak-to-peak. The driving signal is amplified by a Piezosystems PiezoLinear Amplifier by a gain of 20 (200 V peak-to-peak amplitude). This amplified signal is the input for the bottom cap bender element. The receiver signal is sampled by Tectronix oscilloscope TD3014B. This digital oscilloscope is able to capture and record signals at four channels. In this setup the first channel is output from the compression wave crystal (p wave reading), the second channel reads the output from the shear wave crystal (s wave reading), the fourth channel records the input signal or the driving signal from the wave generator. The data is recorded from the oscilloscope by the means of a USB flash drive. A function of the oscilloscope to average repetitions of the receiver signal is used to

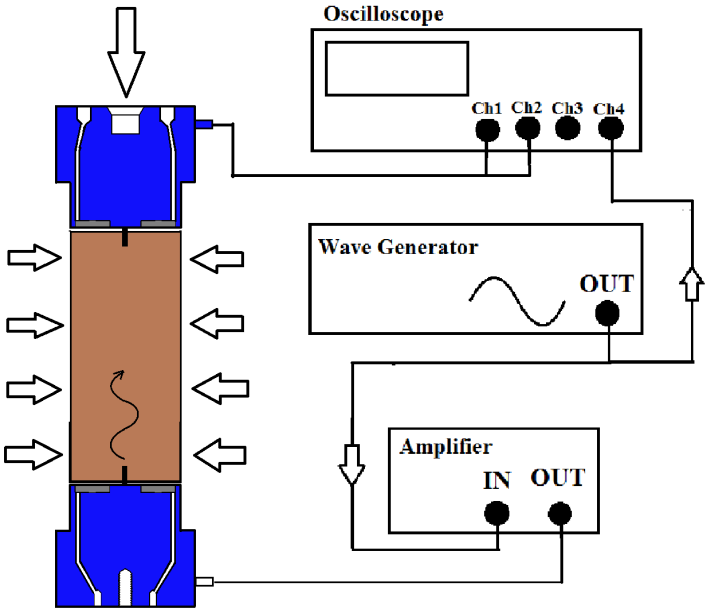

Figure A.2: Schematic test setup along with triaxial sample.

reduce the signal noise during the pulse tests. Usually 64 single pulses are averaged and summarized to one signal for interpretation.

Figure A.3 shows a cross-section of the triaxial caps with the bender elements and p and s wave piezoelectric crystals. The mass of the metal top cap was about 400 g and had to be accounted for in the seating load calculations. Since the sample had to be placed inside the triaxial chamber with the weight of the top cap on it, it was very important to make sure the sample prepared from slurry had dissipated the excess pore pressure during the consolidation outside the chamber.

It was very useful to connect the electrical ground of all components of the measuring system to the metal parts of the cell housing.

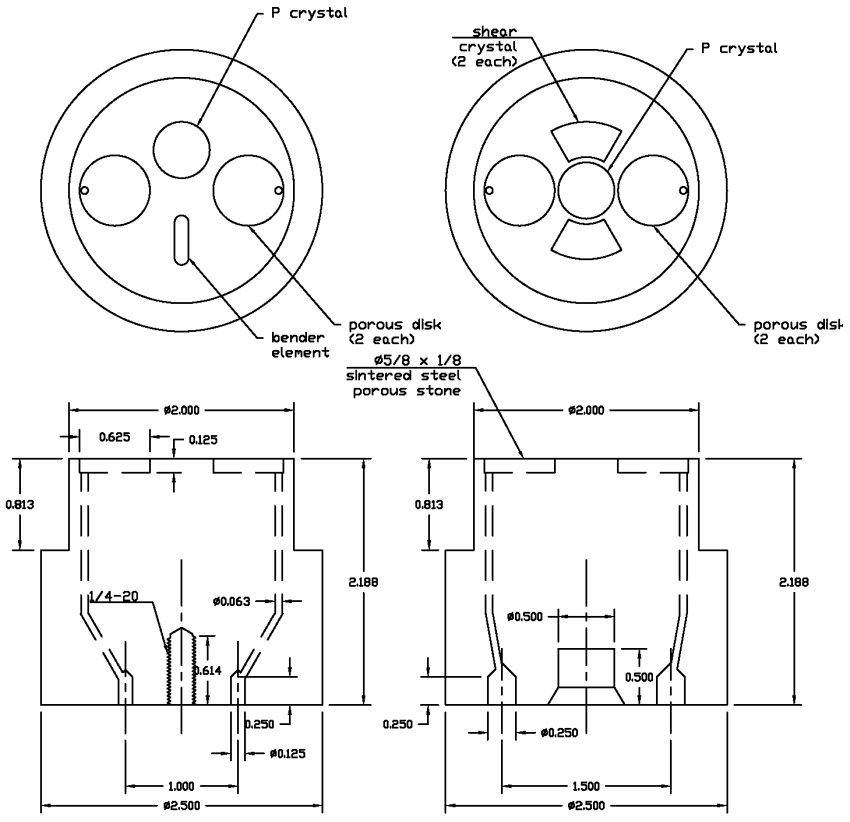

Figure A.3: Drawings of triaxial caps with placement of bender elements and p and s piezoelectric crystals.

A.3 Signal Analysis

The smallest distance between the bender elements is assumed to be the length of the wave travel path needed for the calculation of the wave velocity. This is the distance between the tip of the transmitter element and the tip of the receiver element called the tip-to-tip distance. This assumption is based on the work of Dyvik and Madshus (1985), confirmed by Brignoli et al. (1996), who carried out studies using different element penetration depths.

Although pulse tests with bender elements started with a step function, as seen in Dyvik and Madshus (1985), a sine pulse with a shape of a single sine cycle is now most commonly used. The single sine wave function helps in studying the influence of frequency on the signals. Occasionally input signals consisting of several sine cycles and deformed sine cycles, as suggested by Jovicic et al. (1996), are used to simplify the identification of the s-wave arrival.

Figure A.4 shows a typical receiver signal obtained from a bender test using a single sine pulse of 50 kHz for a sample of natural Gulf of Mexico. The arrival time corresponds with the first inflection at point D1. The example time record clearly displays a second and a third wave arrival, in addition to the first arrival. However, in the majority of bender element measurements it is not possible to clearly identify such multiple arrivals.

Methods for the determination of the travel time of the shear and compression wave through the sample are summarized and the reasons for choosing particular data reduction techniques are stated. Because the s-wave and p-wave velocity do not change with frequency, the simple visual interpretation of the receiver signal is still the most commonly used technique. Sanchez-Salinero et al. (1986) developed an analytical solution for the time record at a monitoring point that would result from a transverse sine pulse of a point source within an infinite isotropic medium. Jovicic et al. (1996) made finite element cal-

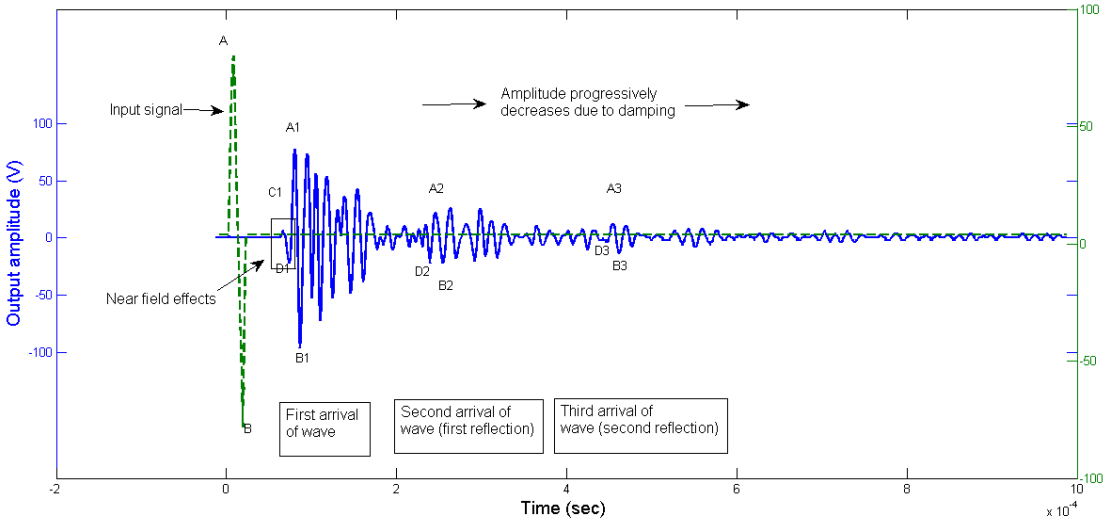

Figure A.4: Bender element time record of Natural Gulf of Mexico sample.

culations confirming the analytical results. The essential findings are the definition of a phenomenon called near field effect, explained in detailed later in this section, which is the reason for a deflection, as labeled in Figure A.4, in front of the arrival point. Viggiani and Atkinson (1995a) and Jovicic et al. (1996) concluded from their laboratory work and from the numerical study that the most consistent results are obtained by assuming that the compression wave arrival is marked by this first infliction labeled as D1. Therefore in the framework of this research this point is chosen in all cases as the arrival point of the compression wave, if it is identifiable. Additionally the frequency of the sine pulse is varied to check if the selected point is not moving with frequency. The test was repeated at 30, 40, 50 and 60 kHz sine pulse frequency. Once this was established all the consecutive tests were carried out at 50 kHz frequency.

A.3.1 Travel time by direct arrival

The travel time can be estimated as the time between the start of the input voltage pulse to the sending bender and the first deflection in the output signal from the receiver bender

(between point C1 and D1). Depending on the clarity of the bender element signals, the identification of the first deflection point can be straightforward or difficult.

This method of direct arrival is used only for the compression wave front as the arrival point of the shear wave front can be masked by faster traveling p-wave components, the described near near phenomenon and by an inductive coupling between the sender and receiver channels.

A.3.2 Travel time between characteristics points in a signal

The travel time of an impulse wave between two points in space may be taken as the time between characteristic points in the signals recorded at these two points. Two measured receiver signals are needed for this approach.

In the case of a bender element test only one actual receiver signal is available, it has to be assumed that the input signal to the transmitting element has the same shape as a fictitious receiver signal at the source. The input signal is then used as the first receiver signal.

This assumption is questionable because of two reasons. The first is the capability of the bender elements to follow the driving signal. Studies of different authors for instance by Jovicic et al. (1996), applied self-monitoring elements, showing that the ability of the bender elements to follow the driving signal decreases in the very high frequency range. This is no problem for single and multiple excitation sine pulses since the commonly used frequencies are below this range. But if rectangular step function are used, such high frequencies are reached.

The second problem is related to the transfer characteristic element soil and the attenuation in the soil itself. Even though the transfer characteristic mechanism is not well understood it can be seen from practical tests that both phenomena cause a change of the frequency content of the signal. The compared signals, i.e. driving signal and one receiver

signal, show therefore a different shape also in the time domain. This again makes the picking of comparable points at the two signals often erroneous. The method is therefore not used.

A.3.3 Travel time by cross correlation of input and output signals

Another way for the determination of the travel time between sender and receiver element is the calculation of the cross correlation between sender and receiver signal. The equation for the cross correlation is given by

$$r_{RS} = \int \int s_R(t) s_S(t+\tau) dt \tag{A.1}$$

where s_S is the sender signal, s_R the receiver signal and t the time. r_{RS} will reach a maximum value for the time shift that equals the travel time of the impulse from source to the receiver.

This method worked very well for the shear wave front and the time of arrival was determined by cross correlating the input signal with the output signal.

A.3.4 Travel time using multiple arrivals in the output signal

Output signals show in some cases a clear second arrival or even multiple arrivals of the input wave. The second arrival is the input wave after it reflects from the receiver cap, travels back to the transmitter cap where it reflects again and then returns to the receiver cap a second time. Arrivals of a higher order are caused by successive refections on receiver and top cap. Assuming plane wave propagation, the time between the multiple arrivals in the output signal is equal to multiples of the double of the travel time from cap to cap.

The travel time may be determined using either characteristic peaks or the cross correlation method. Possible characteristic points in the example time record are A1-A2-A3,

B1-B2-B3 or D1-D2-D3. The cross correlation of the output signal with itself, also called an auto-correlation, is in principle sufficient to determine the travel time. If the different arrivals are not very well separated it is useful to create, by windowing, for each wave arrival a dummy signal, where all parts outside the time window containing the arrival, are set to zero. The dummy signals are than cross-correlated which each other. Arulnathan et al. (1998) found this method helpful in their studies.

The advantage using multiple arrivals in opposite to the comparison of sender and receiver signal is the avoidance of the assumption that the electrical input signal is transferred perfectly into a mechanical oscillation of the bender tip. However, multiple arrivals are not very often observed in the bender element output signal. Therefore the field of application is quite restricted.

A.4 Difficulties in determining travel time

A.4.1 p wave interference

Although these bender elements contained 2 piezo crystals one to generate and receive compression waves and one to generate and receive shear waves, the shear wave wave crystals or bender elements generate a certain amount of compression waves, traveling with p-wave velocity. This velocity is faster than the s-wave and can reach the compression wave velocity of the pore water if the sample is fully saturated. Therefore these wave components arrive before the s-wave and their reflections might overlap with the actual s-wave arrival.

A.4.2 Inductive coupling

It was observed that the output signal was superimposed with a signal of the same shape as the input signal and with no shift in time to the input signal. This behavior is caused by capacitive coupling between input and output signal inside the measurement apparatus. The phenomenon is found at all kinds of shapes of the input signal. Especially

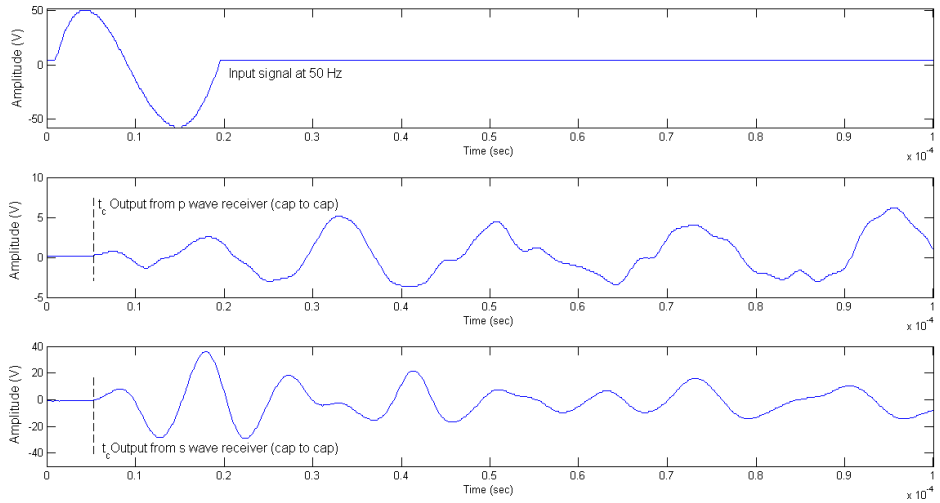

Figure A.5: Calibration record of the ultrasonic caps.

the results from the set-up of Dyvik and Madshus (1985) with a step-pulse excitation show the effect significantly. A careful grounding of all involved devices, including the housing of the testing cell, can reduce part of the effect.

A.5 Calibration of ultrasonic and bender elements

Calibration of the ultrasonic and bender element system was necessary so that any delay time introduced in the system by the electronics, ceramics and coating materials can be determined (Brignoli et al., 1996). This was carried out by placing the two caps in direct contact and measuring the time interval between the initiation of the electrical signal sent to the transmitter and the initial arrival of the waveform recorded at the receiver.

Figure A.5 shows the input signal and the measured wave form of the receiving signal when the ultrasonic caps are placed cap to cap. This time interval (t_c) is corrected for while determining travel time for other samples placed in between the caps.

It was also required to check if the ultrasonic caps give reasonable values of compression and shear wave velocities when a material with known parameters is placed in

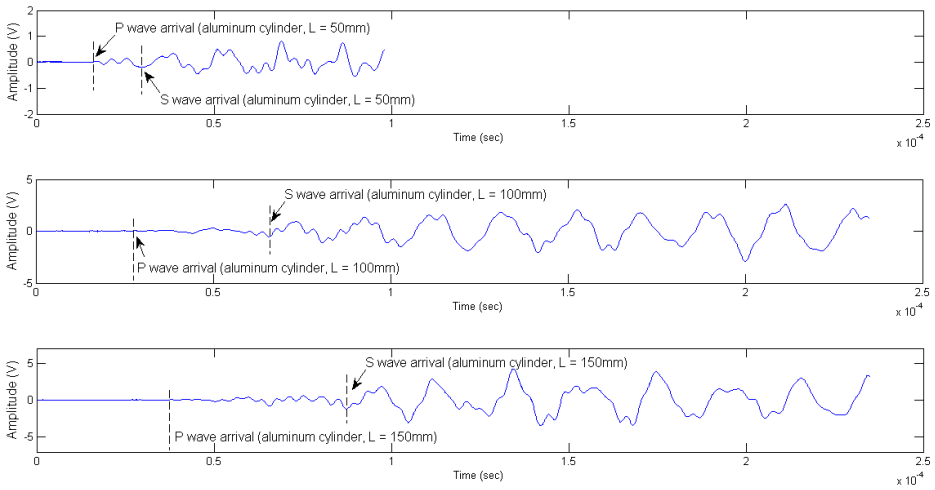

Figure A.6: Calibration record of the ultrasonic caps using aluminum.

between. Aluminum and nylon cylinders of varying lengths were placed in between the ultrasonic caps and the compression and shear wave velocity through the two materials were computed. The time of arrival of the compression wave was easily identified as they are the first set of waves to reach the receiver. The time of arrival of the shear wave is more complicated to identify as the receiving signal is a composition of both shear waves and reflected compression waves.

Figure A.6 shows the measured wave form of the receiving signal for Aluminum cylinders of differing lengths placed between the caps. The p wave and s wave arrival time was identified in accordance with Brignoli et al. (1996) where he identifies 6 types of wave forms for bender and ultrasonic output signals and specifies the arrival of the s wave for each form.

Figure A.8 shows the measured wave forms of the receiving signal for nylon cylinders placed within the caps. The p wave arrival is determined by direct arrival (Figure A.7). The s wave arrival (Figure A.8) for nylon specimens is determined by cross-correlating

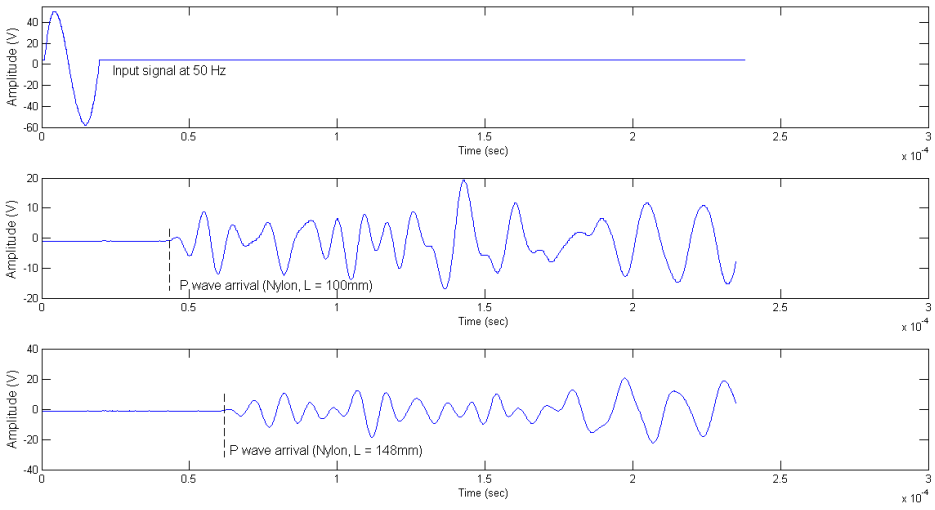

Figure A.7: Calibration record of the ultrasonic caps using nylon.

the output signal with the input and identifying the maximum amplitude in the set of peaks (Viggiani and Atkinson, 1995a). The peak with the highest amplitude is chosen as it signifies the arrival of the s wave in resonance with the reflections of the p wave.

The calibration process was carried out with the exact same setup as is used along with the triaxial device. An ultrasonic couplant Sonotrace GR-30 was used as a medium between the two caps to eliminate the air gap. Table A.1 lists the values of shear wave and compression wave velocities of aluminum and nylon calculated based on the methods stated above.

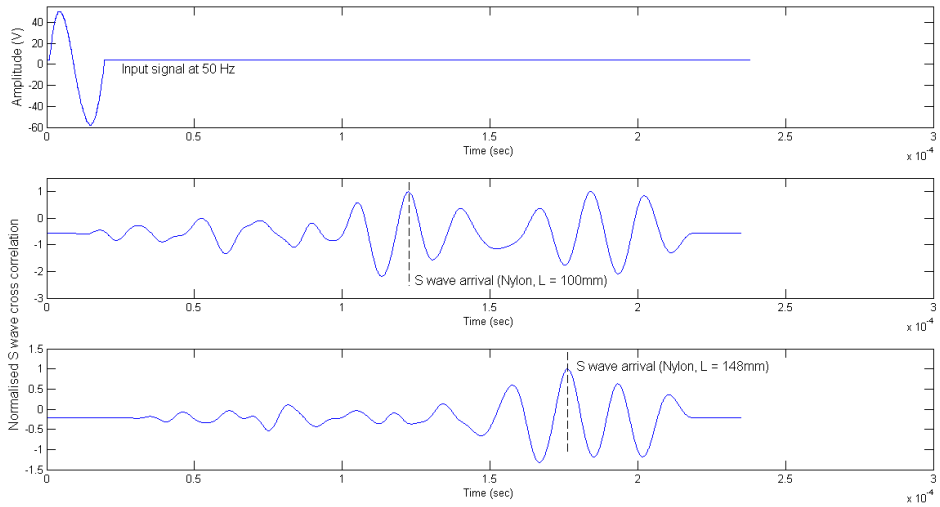

Figure A.8: Normalized cross correlation of calibration record of the ultrasonic caps using nylon.

Table A.1: Summary of bender and ultrasonic tests calibration tests using Aluminum and Nylon

Material	Density (kg/m^3)	Length (m)	V_s calculated (m/s)	V_p calculated (m/s)
Aluminum	2700	0.05	2994	5154
		0.1	3048	5076
		0.15	3012	5050
Nylon	1150	0.048	926	2874
		0.1	1002	2583
		0.148	968	2610

APPENDIX B

CONSOLIDATION IN THE CENTRIFUGE

The consolidation calculations for Phase two of the centrifuge tests is given in this appendix.

B.1 Calculating optimum initial height and initial water content

The final height of the clay test bed is required to be 20 cm to give room for the deeper aspect ratio piles to be tested without considerable boundary effects. Also the average final water content of clay layer is required to be approximately 50% to generate a similar shear strength profile as found in the seabed.

With these limitations, the optimum initial height of the clay layer was found to be 32 cm. Figure B.1 shows the plot of initial water content vs settlement and initial water content vs final water content. By selecting an initial water content of 77%, the total settlement is found to be approximately 8 cm and the final average water content is found to be approximately 50%.

The matlab program that was used to plot this graph is attached at the end.

B.2 Effective stress calculation at various g levels

Known parameters:

Large rigid box dimensions at RPI: 88 cm x 39 cm x 36 cm (L x W x D)

Height of clay layer before consolidation: 32 cm

Final height of clay layer after consolidation: 20 cm

Density of clay, ρ_{kaolin} = 1580 kg/m^3

Density of sand, ρ_{sand} = 1600 kg/m^3

Centripetal acceleration: N

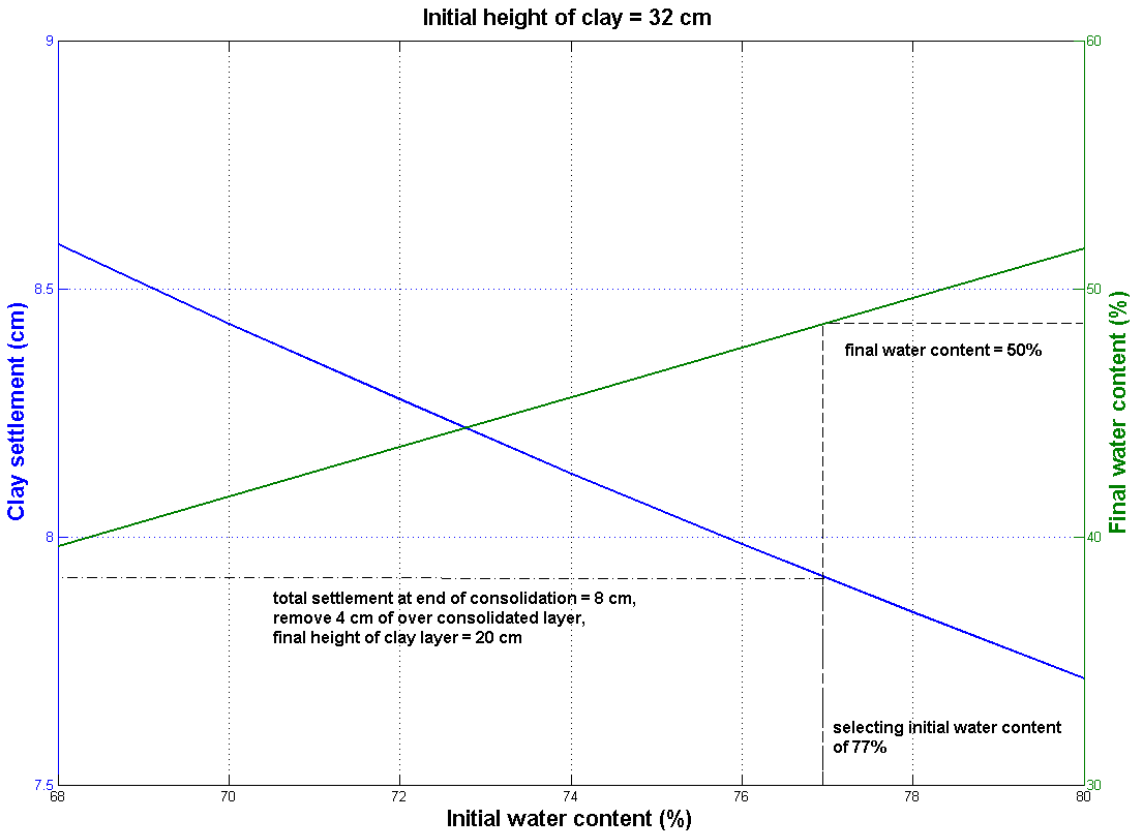

Figure B.1: Initial water content plotted against settlement and final water content.

At 1g (N = 1):

$$\sigma_i = h\rho_{kaolin}g = 0.16 * 1580 * 9.81 = 2.5\ kPa \tag{B.1}$$

$$u_i = h\rho_{water}g = 0.16 * 1000 * 9.81 = 1.5\ kPa \tag{B.2}$$

$$\sigma_i' = \sigma_i - u = 1\ kPa \tag{B.3}$$

Where σ_i is initial total stress, u_i is the initial pore pressure and σ_i' is the initial effective stress.

At 70g (N = 70):

$$\sigma_f = h\rho_{kaolin}gN = 0.1 * 1580 * 9.81 * 70 = 108.5\ kPa \tag{B.4}$$

$$u_f = h\rho_{water}gN = 0.16 * 1000 * 9.81 = 68.67\ kPa \tag{B.5}$$

$$\sigma_f' = \sigma_f - u = 39.83\ kPa \tag{B.6}$$

Where σ_f is final total stress, u_f is the final pore pressure and σ_f' is the final effective stress.

When the test bucket is spun from 1g to 70g, the change in effective stress is approximately 40 kPa ($\sigma_f' - \sigma_i'$). Thus to avoid consolidation during testing of the piles we require 40 kPa of excess pore pressure to be dissipated.

At 100g (N = 100) with 3 cm of sand on top of the clay layer (preload):

$$\sigma_{100} = h\rho_{kaolin}gN + h_{sand}\rho_{sand}gN = 295.08\ kPa \tag{B.7}$$

$$u_{100} = h\rho_{water}gN = 0.16 * 1000 * 9.81 = 156.96\ kPa \tag{B.8}$$

$$\sigma'_{100} = \sigma_f - u = 138.12\ kPa \tag{B.9}$$

Where σ_{100} is total stress generated at 100g, u_{100} is the pore pressure at 100g and σ'_{100} is the effective stress at 100g.

B.3 Calculating consolidation spin time

By spinning the test bucket at 100g with preload, the time taken to dissipate the same amount of pore pressure (40 kPa) decreases. The progress of consolidation (U_z) at any depth, z can be related to the pore pressure at that depth.

$$U_z = (\sigma' - \sigma'_i)/\Delta\sigma' = (u_{dissipated})/\Delta\sigma' = 40/138.12 = 0.289 \tag{B.10}$$

Where $u_{dissipated}$ is the pore pressure dissipated at depth, z (40 kPa to be dissipated), $\Delta\sigma'$ is the change in effective stress (132 kPa at 100g)

Therefore, at 100g with a preload of 3 cm of sand the consolidation ratio (U_z) is approximately 29%. At the center of the test bed, with two way drainage, the time factor (T) corresponding to the U_z is 22%.

$$t = T * H_{dr}^2/C_v = 0.22 * 0.16^2/(1.6 * 10^{-7}) = 586\ min = 9.7\ hr \tag{B.11}$$

The total consolidation spin time at 100g for the current model is approximately 9.7 hr.

APPENDIX C

DATA PROCESSING METHODS

This appendix shows how the raw centrifuge data was reduced to obtain all the variables of interest. Figure C.1 shows a side view of a single pile setup with the location of all the sensors (momentless connector with e=3 is used as an example).

Table C.2 shows the scaling laws applied for all the quantities calculated in this appendix. N is the centrifugal acceleration and is equal to 70gs in these tests.

C.1 Lateral load at stem top

The stem is assumed to bend as a cantilever beam, fixed at the soil surface, with a point load at the free end (stem top). The following equations are applicable (Housner&Vreeland 1991) for a cantilever beam:

$$\epsilon_{bending} = Momentstress/E_{steel} \tag{C.1}$$

$$Momentstress = M_b/Z = P_h * l_{top/bot}/Z \tag{C.2}$$

where $\epsilon_{bending}$ is the strain measured by the strain gage placed on the stem along the direction of loading, E_{steel} is the modulus of elasticity of steel (200 GPa), M_b is the bending moment at the location of the strain gage, $l_{top/bot}$ is the height of the application of load from the strain gage level (Figure C.1), Z is the sectional modulus at that cross-section and P_h is the lateral load applied at the top.

Thus, lateral load (P_h) on the prototype is given by:

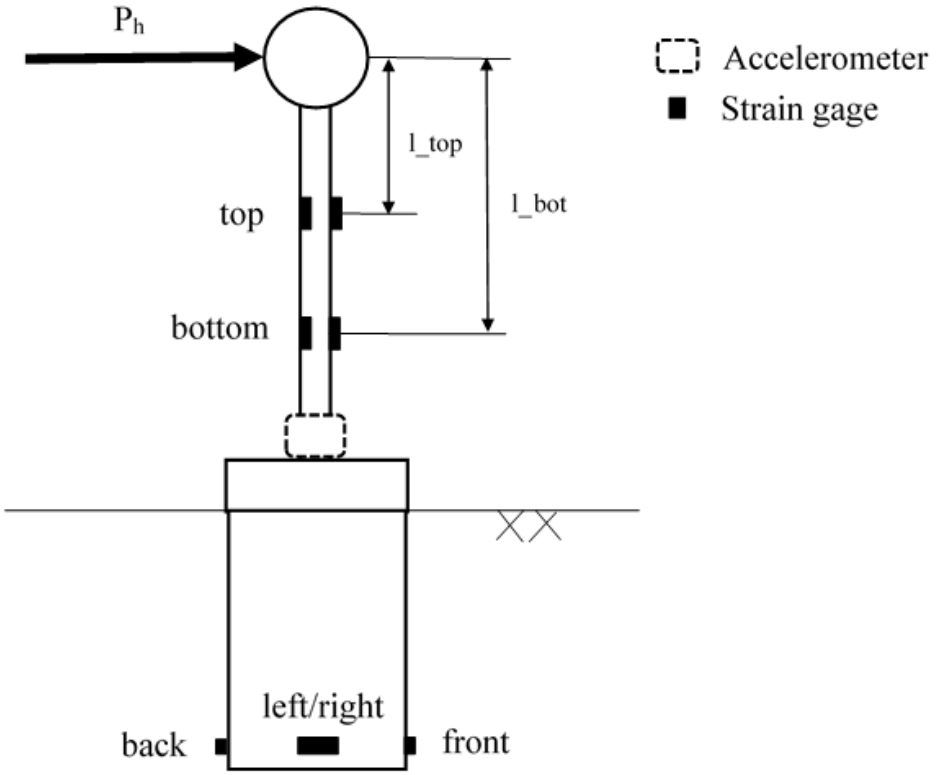

Figure C.1: Single pile setup with sensors.

$$P_h = \epsilon_{bending} * 10^{(-6)} * E_{steel} * Z * N^2 / l_{top/bot} \tag{C.3}$$

where N is the centrifugal acceleration (70g), E_{steel}, $l_{top/bot}$ and Z are defined as given in equation C.2. The strain gage records all readings in micro strain ($\mu\ \epsilon$), thus $\epsilon_{bending}$ is multiplied by $10^{(-6)}$.

C.2 Displacement at soil surface

Figure C.2 shows the displacements (not to scale) for both the momentless and rigid connectors. Ideally, in the tests with the momentless connector, there is only pure rotation and in the tests with the rigid connector, there is only pure translation. However in reality, a combination of bending, rotation and translation takes place.

The total displacement (x) for each test at the stem top is given by the robot motion for each test (Figure C.2), this robot displacement is a combination of bending of the stem (δ_{bend}) and rotation of the pile setup (δ_{rotate}) for the momentless tests and a combination of bending of the stem (δ_{bend}) and translation of the rigid connector ($\delta_{translate}$).

$$x = \delta_{rotate/translate} + \delta_{bend} \tag{C.4}$$

The deflection at the stem top (model scale) due to bending of the stem (δ_{bend}) is calculated using the lateral load on stem top, P_h (Section C.1) by assuming the stem behaves as a cantilever beam fixed at the soil surface.

$$\delta_{bend} = (P_h * y^3)/(3 * E_{steel} * I) \tag{C.5}$$

The table C.1 shows the total displacement of the three monotonic tests separated into its deflection (δ_{bend}) and displacement ($\delta_{translate/rotate}$) components.

Neglecting the deflection due to bending of the stem, the displacement of the pile at

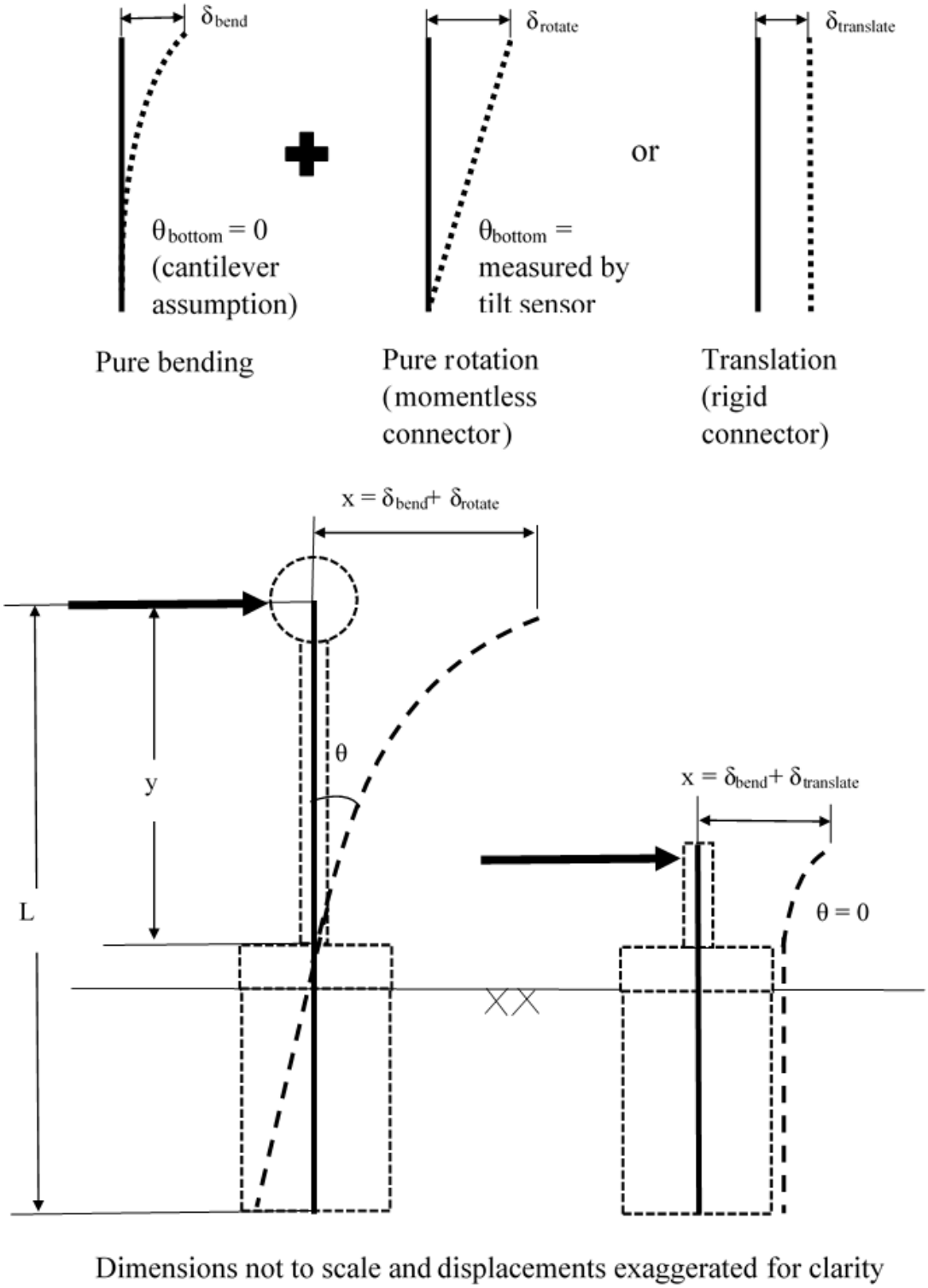

Figure C.2: Sketch showing displacement for momentless and rigid connectors.

Table C.1: Peak displacements for monotonic tests

Pile test number	Robot displacement	Deflection of stem	Movement
17 - momentless	50 mm	0.16 mm	49.84 mm
18 - momentless	58.33 mm	0.11 mm	58.22 mm
19 - rigid	not in robot log	No gage (R1 disconnected)	-
7 - momentless	30 mm	2.1 mm	27.9 mm
8 - momentless	41.17 mm	0.8 mm	40.37 mm
9 - rigid	not in robot log	0.5 mm	-

Table C.2: Centrifuge scaling relationships

Quantity	Dimensions	Model (at Ng's)	Prototype
Length	L	1	N
Area	L^2	1	N^2
Mass	M	1	N^3
Sectional modulus (Z)	L^3	1	N^3
Force	MLT^{-2}	1	N^2
Stress	$ML^{-1}T^{-2}$	1	1
Strain	-	1	1
Unit weight	$ML^{-2}T^{-2}$	1	N^{-1}
Modulus of elasticity (E)	$ML^{-1}T^{-2}$	1	1
Dynamic time	T	1	N
Acceleration	LT^{-2}	1	N^{-1}

the soil surface is computed using the accelerometer placed on the top of the caisson.

As the pile is being moved by the robot, the center of rotation moves vertically about the axis of the pile setup, however to keep the calculation consistent, a reference is chosen. The center of rotation of the pile setup (y in Figure C.3) is calculated using equation C.6

$$y_{ref} = x_{peak}/tan(\theta_{max}) \tag{C.6}$$

Thus the displacement on the soil surface (x' in Figure C.3) is computed with this y_{ref} using trigonometry.

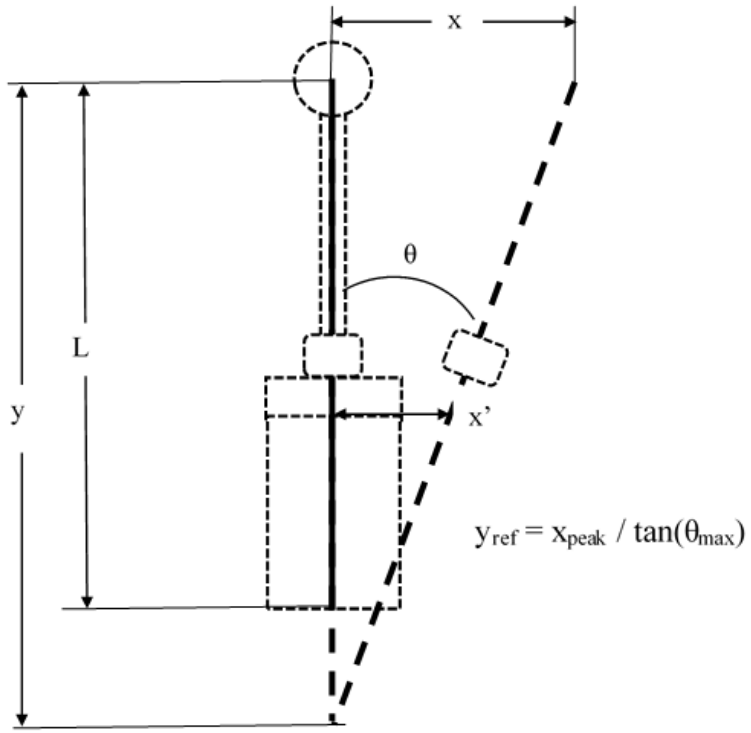

Figure C.3: Sketch showing displacement calculation for momentless connector at soil surface.

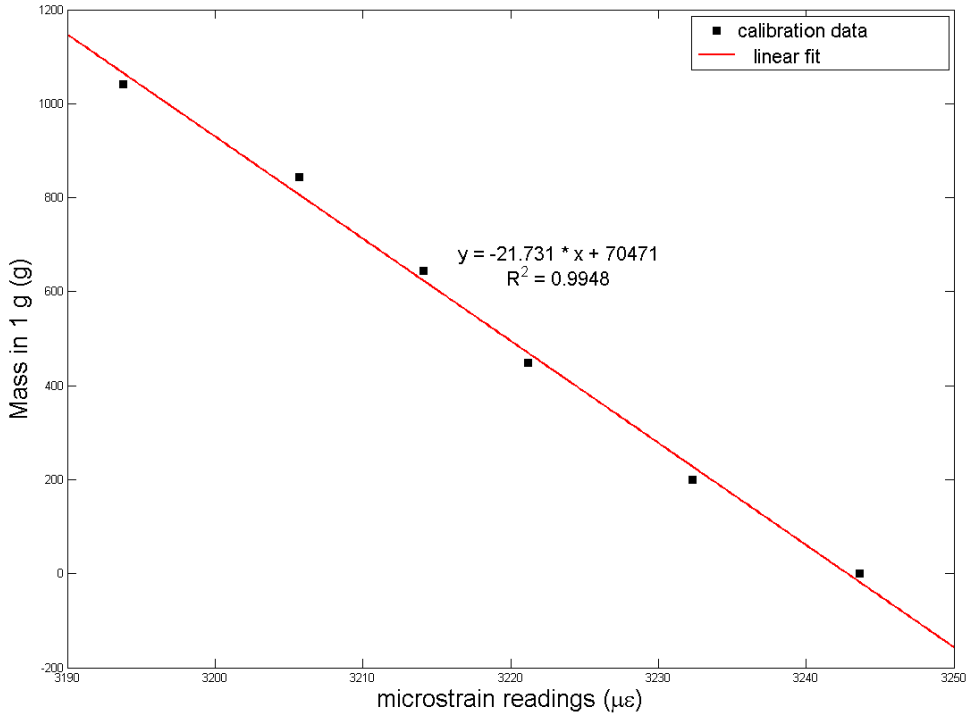

Figure C.4: T bar calibration.

C.3 T bar data reduction

This section shows how raw strain gage data vs time from the T bar was reduced to obtain the T-bar penetration resistance and an estimate of the undrained shear strength vs depth of the sample.

The T-bar was calibrated in 1g conditions using mass (g) plotted in Figure C.4.

The equations C.7 to C.10 were used to compute the T-bar penetration resistance and undrained shear strength.

$$mass_{1g}(g) = CalibrationFactor * \mu strain \tag{C.7}$$

$$Force(N) = mass(g)/1000 * N * g \tag{C.8}$$

$$q_{tbar}(MPa) = Force(N)/A(mm^2) \tag{C.9}$$

$$S_u = q_{tbar}(MPa)/N_b \tag{C.10}$$

Where N is the centrifugal acceleration of the centrifuge (70 in this case), g is the acceleration due to gravity, A is the surface area of the T-bar without including the ends and N_b is the bar factor dependent on the surface roughness of the T-bar described by the adhesion factor (α). Randolph and Houlsby (1984) suggest using a bar factor of 10.5 for most cases.

The depth was obtained by using the raw time data and velocity and acceleration values of the robot moving the T-bar. The depth in prototype scale was computed using the equations of motion (Figure C.5).

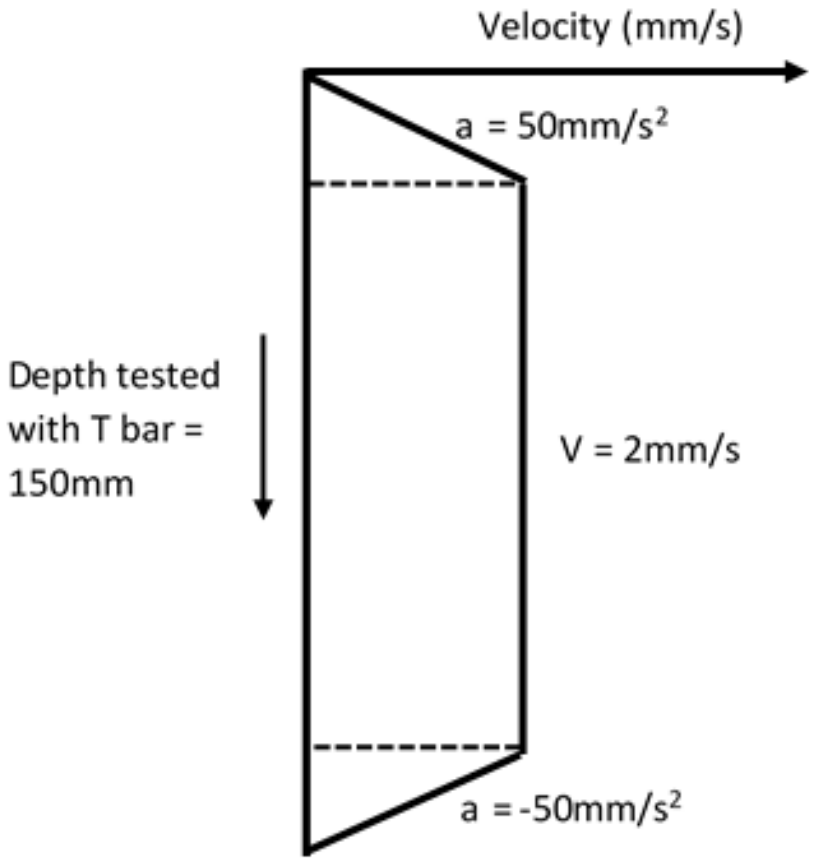

Figure C.5: Sketch to explain computation of T-bar depth.